Ana Lúcia Rebelo do Rosário

BSc Microbiologia

Functional and Structural Studies of Two Enzymes: Membrane Bound Kinase and Z-DNA/Z-RNA-Binding Protein.

Dissertação para obtenção do Grau de Doutor em

Sistemas de Bioengenharia

Orientador: Margarida Archer, Investigador Auxiliar, ITQB-UNL

Co-orientador: Li-Huei Tsai, Investigador/Director, PILM-MIT

Júri:

Presidente: Prof. Doutor Manuel Luís Magalhães Nunes da Ponte

Arguentes: Prof. Doutor Domingos Manuel Pinto Henrique

Prof. Doutor Luis Miguel Gales Pereira Pinto

Vogais: Prof. Doutora Maria Arménia Abreu Fonseca Carvalho T. Carrondo

Prof. Doutor Shabir Husein Najmudin

FACULDADE DE CIÊNCIAS E TECNOLOGIA
UNIVERSIDADE NOVA DE LISBOA

Dezembro de 2013

Functional and structural studies of two enzymes: membrane bound kinase and Z-DNA/Z-RNA-binding protein.

18th November 2013, ITQB, Oeiras, Portugal
First edition, November 2013

ISBN 978-989-20-4348-7

Foreword

The present dissertation represents a joint effort to unravel the role and regulatory function of *h*TAOK2α and of Z-DNA/Z-RNA, two distinct biological molecules.

The thesis is organized in two main chapters - 1 and 2.

Chapter 1 is then divided in section 1, which tells us the role of TAOK2α in brain development. This work was developed at the laboratory of Prof Li-Huei Tsai (co-supervised by Dr. Froylan Calderon de Anda), at the Picower Institute for Learning and Memory, Massachusetts Institute of Technology, Cambridge, USA. Section 2 of this chapter, describes the work developed to characterize *h*TAOK2α biochemical and structurally by X-ray crystallography. The work herein described was carried out at the Membrane Protein Crystallography laboratory at ITQB, under the supervision of Dr Margarida Archer and in collaboration with Dr Gonçalo Real and Dr. Marco Patrone (Animal Cell Technology Unit, IBET).

Chapter 2 describes the data obtained when studying Z-RNA and Z-DNA junctions when nucleic acid oligomers bind to the ADAR1 Zα domain. This was a joint collaboration between the Macromolecular Crystallography Unit at ITQB (Dr Margarida Archer and Prof. M. Arménia Carrondo), the Protein-Nucleic Acids Interactions group at IGC (Dr. Alekos Athanasiadis) and Prof. Alexander Rich, from the MIT Biology Department.

Acknowledgments

I owe a great deal of thanks to a great many people. Saying this I want to aknowledge:

First of all, Doctor Margarida Archer for all her support and confidence, for accepting me in her laboratory, giving me the conditions to do my work, and making it possible to work in such different fields. Dra Margarida Archer was always able to motivate me in decisive moments, to advice me in the right directions, to make me understand my possibilities, and for making me believe it was possible to go further. To her, my most sincere thanks. It was a pleasure and a privilege to do my PhD under your supervision. In second, I want to aknowledge Prof Maria Arménia Carrondo, for receiving me in the crystallography unit at ITQB, for all your support and motivation, thank you.

Professor Li-Huei Tsai, for receiving me in your laboratory, for the challenge of working and debating with you my work. It made me stronger! I want to particular thank Froylan, my mentor at MIT, my friend for life. You taught me so many things that are immeasurable. You helped me to construct a critical spirit in my work, to think outside the box, to wonder at our findings and, when looking at a neuron for the thousand time, we would see it for the first. It was a pleasure to learn with you. Konstatinos, for working with me and making me a litle easier with details on experiments, you're always saying "*Ana, this is not rocket science".* I want to thank all the people from the Tsai lab and from the Picower Institute that helped me and worked with me during my stay. A special thanks to all my colleagues from the MIT-Portugal program that were in Boston at the time. We had great moments together.

My colleagues from the crystallography unit at ITQB, all of you have made my life easier. A special thanks to Dr Pedro Matias and Dr Carlos Frazão, always prepared to help me when collecting data at synchrotrons and *in-house*. Dr Colin McCvey for all your help, support and suggestions with my purification experiments. I want to thank my colleagues from the Membrane Protein Crystallography Laboratory. A special thanks to José Brito for your capacity in getting everything we need in time, your support and friendship in the lab. A very very special thanks to Tânia, for all your help and support, our discussions about the work, your tips and tricks in crystallization, for all your friendship in the hard times of thesis "depression". For all your good mood and patience, I thank you deeply. To Dr Alekos Athanasiadis and Matteo, for working with me in the begining of my PhD, for your hard questions, you taught me so much in the laboratory and made me so much more independent. Gonçalo Real and Marco Patrone, for your patient working with our TAO Kinase, for baring with my 96 experimental conditions, it was pleasure to work with you.

I am greatfull for having such good friends Nuno, Rita, José, Ricardo and Emanuel. We have been together since university and it has been a pleasure to be your friend and part of your life. I wish you all the best in life and thank you for all the good laughs we have.

Finalmente, mas não menos importante. Quero agradecer a toda a minha família. O meu porto de abrigo, onde a palavra casa, amizade e amor tem um significado imenso. Aos meus pais, António e Mabília, foram sempre meus amigos e companheiros. Deram-me tudo o que eu precisei e muito mais, é por vocês que sou assim, e que estou hoje a escrever estas palavras. Aos meus avós, que sempre fizeram parte da minha vida e ajudaram em tudo. À minha irmã e ao meu afilhado, Vera e Mateus, porque o simples facto de fazerem parte da minha vida, já a torna mais preenchida, cheia de significado, e muito mais rica. Sem vocês, tudo faria menos sentido, e eu seria pobre.

Um agradecimento muito especial a ti, Bruno, porque estás aqui novamente comigo, neste momento. A tua companhia e amizade, o teu amor, a tua persistência, o teu bom humor torna tudo mais colorido. Obrigada.

Fundação para a Ciência e Tecnologia (FCT) for financial support, PhD grant reference SFRH / BD / 37676 / 2007.

Dissertation Abstract

The neocortex is a unique structure designed for higher cognitive and associative functions. Herein, we will refer to the work performed to assess the role of TAOK2α, a specific membrane bound kinase, in the mammalian neocortical development. The results obtained, delineate a pathway whereby Semaphorin3A and Neuropilin1 transduce signals through TAOK2α and c-Jun N-terminal Kinase to regulate basal dendrite development and migration in cortical neurons. This work represents the first approach aimed at understanding the mechanisms responsible for the delineation of basal and apical dendrites during pyramidal neuron development in the embryo, and how such mechanism may evolve to neocortical disconnection disorders. Additional work performed on *human*TAOK2α focused at the determination of its three-dimensional structure by X-ray crystallography to elucidate its regulatory mechanism.

The 20th century exciting discovery of the DNA left-handed conformation, and the fact it binds to certain classes of proteins with high affinity and specificity, indicated a biological role to it. However, a full function is still to be elucidated. The human double-stranded RNA adenosine deaminase (ADAR1) is the best characterized of all Z-DNA binding proteins, where Zα domain binds and stabilizes Z-DNA/Z-RNA forms upon binding. The second part of this thesis describes the work on the $Zα_{ADAR1}$ domain that binds to Z-RNA/Z-DNA. When a section of a DNA or RNA molecule forms a left-handed Z-DNA/Z-RNA segment, two B-Z/A-Z junctions are formed. Herein, we describe the study carried out on the formation of Z-Z junctions from DNA and, also, the approach on trying to describe the Z-Z junction for RNA when interacting with $Zα_{ADAR1}$. The structure of the Z-Z-DNA junction consists of a single base pair that leads to partial or full disruption of the helical stacking. The junction region allows intercalating agents to insert themselves into the left-handed helix, which is otherwise resistant to intercalation.

Keywords: neocortical development, humanTAOK2α, Z-DNA/Z-RNA, $Zα_{ADAR1}$

Resumo da Dissertação

O neocortex é uma estrutura única, projectada para realizar complexas funções associativas e cognitivas. Nesta tese descrevemos o trabalho realizado para elucidar o papel da TAOK2α no desenvolvimento neocortical dos mamíferos. Os resultados obtidos revelam uma trajetória na qual a Semaphorin3A e Neuropilin1 transduzem sinais através da TAOK2α e da quinase c-Jun N-Terminal para regular o desenvolvimento de dendrites basais e a migração de neurónios corticais. Este estudo representa a primeira tentativa para compreender os mecanismos responsáveis pela delienação entre dendrites basais e apicais no densenvolvimento dos neurónios piramidais, e de que forma esses mecanismos podem resultar em doenças de disconecção cortical. Apresentamos também o trabalho realizado no âmbito da determinação da estrutura tridimensional da *humana*TAOK2α por cristalografia de raios-X, para esclarecer o seu mecanismo de regulação.

O ADN de rotação contrária (Z-ADN), foi uma importante descoberta do século XX. O facto do Z-ADN se ligar a determinadas classes de proteínas com alta afinidade e especificidade auspiciou uma função biológica para o mesmo. No entanto, a sua função continua por identificar. A ARN de dupla-cadeia adenosine deaminase humana (ADAR1) é a mais bem caracterizada de todas as proteínas de ligação ao Z-ADN, onde o domínio Zα se liga e estabiliza a forma Z-ADN/Z-ARN. Sempre que uma secção de ADN/ARN forma um segmento Z-ADN/Z-ARN, dá-se a formação de duas junções, B-Z/A-Z respectivamente. Nesta tese, descrevemos o trabalho realizado no estudo da formação de junções Z-Z-ADN, de forma concomitante ao estudo realizado da junção Z-Z-ARN, aquando em interacção com o $Zα_{ADAR1}$. A determinação da estrutura da junção Z-Z-ADN, permitiu verificar que um único par de bases é responsável pela disrupção parcial ou total do empilhamento da dupla hélice. Esta região da junção permite a inserção de agentes de intercalação na hélice de rotação contrária que, de outra forma, é resistente à intercalação.

Palavras-chave: desenvolvimento neocortical, TAOK2α humana, Z-DNA/Z-RNA, $Zα_{ADAR1.}$

Abbreviations

A	Adenosine
Ă	Angstrom
aa	amino acid
ADAR1	double-stranded RNA adenosine deaminase type I
ASDs	Autism Spectrum Disorders
BPs	Basal progenitors
CD	Circular Dichroism
CNS	Central Nervous System
CP	Cortical Plate
DNA	Deoxyribonucleic acid
et al.	and other people
e.g.	for example
F-GFP	Membrane-bound GFP
G	Guanine
GFP	Green Fluorescent Protein
HEPES	2-[4-(2-hydroxyethyl)piperazin-1-yl]ethanesulfonic acid
I	Inosine
i.e.	in other words/that is
IFN	Interferon
IMAC	Immobilized affinity chromatography
INM	Interkinetic nuclear migration
IZ	Intermediate Zone
JNK	c-Jun N terminal kinase
kDa	kiloDalton
Ni-NTA	Nickel-nitrilotriacetic acid
MALDI	Matrix Assisted Laser Desorption/Ionization
MAP2K	Mitogen-activated protein kinase kinase
MAP3K	Mitogen-activated protein kinase kinase kinase
MAPK	Mitogen-activated protein kinase
MP(s)	Membrane Protein(s)
MTs	Microtubules
NMR	Nuclear Magnetic Resonance
PAGE	Polyacrylamide gel electrophoresis
PDB	Protein Data Bank
PEGs	Polyethyleneglycol(s)
PSK	Prostate-derived STE20-like kinase
RGCs	Radial Glial Cells
RNA	Ribonucleic acid

SDS	Sodim Dodecyl Sulphate -
SEC	Size-exclusion chromatography
shRNA	Short-hairpin RNA
SVZ	Subventricular Zone
T	Thymine
TAOK2α	Thousand-and-one amino acid 2 kinase isorform 1
TOF	Time of Flight
TM(s)	Transmembrane Helice(s)
VZ	Ventricular Zone
$Zα_{ADAR1}$	ADAR1 Zalpha domain
Z-DNA/Z-RNA	Left-handed DNA/left-handed RNA

Table of Contents

Chapter 1 – Section 1 The role of TAOK2α in neocortical development

1.1.1. Abstract 6

1.1.2. Introduction 7

Mammalian Brain Development 7

Neuronal Migration 9

Neuronal polarity: axon and dendrites 12

Axon Elongation 14

Dendritic arborization mechanims 15

Semaphorin3A signaling in cortical development 16

The TAOK2 protein 18

1.1.3. Material and Methods 20

1.1.4. Results and Discussion 25

1.1.5. Conclusion 55

1.1.6. References 59

Chapter 1 – Section 2 Deciphering *human* TAOK2α structure – an unfinished business

1.2.1. Abstract 70

1.2.2. Introduction 71

The biological membrane 71

From Gene to Protein – recombinant DNA 72

Studying Membrane Proteins 73

Overexpression of membrane proteins 75

Detergent-based crystallization of membrane proteins 77

TAOK2 secondary structure predictions 79

1.2.3. Material and Methods 82

1.2.4. Results and Discussion 88

1.2.5. Conclusion 110

1.2.6. References 112

Chapter 2 **Structural Studies on Z-RNA and Z-DNA Junctions**

2.1. Abstract 118
2.2. Introduction 119
Nucleic Acids 119
DNA – *Deoxyribonucleic Acid* 119
The discovery of Z-DNA, the left-handed conformation of nucleic acids 121
RNA - ribonucleic acid 123
Proteins that bind Z-DNA/Z-RNA 127
ADAR1 127
ADAR1 Zalpha Domain 129
Other proteins that bind Z-DNA/Z-RNA 133
The biological role of Z-DNA 134
2.3. Materials and Methods 136
2.4. Results and Discussion 140
2.5. Conclusion 159
2.6. References: 160

Chapter 3 **General Conclusions**

General Conclusions 168

Appendix

List of Figures

Figure 1.1.2.1. Different types of neurons. 8
Figure 1.1.2.2. Modes of cell division in the mammalian neocortex. 10
Figure 1.1.2.3. The model of radial glial migration in the mammalian cortex. 11
Figure 1.1.2.4. Schematic depiction of a developing hippocampal neuron during neuronal polarization. 13
Figure 1.1.2.5. Semaphorins and their receptors, plexins and neuropilins, present in vertebrates. 17
Figure 1.1.4.1. Distribution of TAOK2 and activated TAOK2 (pTAOK2) in cultured neurons. 25
Figure 1.1.4.2. Distribution of TAOK2 and activated TAOK2 in the developing cerebral cortex. 26
Figure 1.1.4.3. Distribution of TAOK2 in the early cortical embryonic mouse brain. 26
Figure 1.1.4.4. *Taok2* shRNA's specifically down-regulate TAOK2 expression in dissociated cortical neurons and Ht22 cells. 28
Figure 1.1.4.5. TAOK2 down-regulation or overexpression affects the differentiation of isolated cortical neurons. 29
Figure 1.1.4.6. TAOK2 down-regulation or overexpression affects axon elongation of isolated cortical neurons. 31
Figure 1.1.4.7. TAOK2 down-regulation or overexpression affects basal dendrite arborization in layer V neurons in the developing cortex. 33
Figure 1.1.4.8. TAOK2 down-regulation or overexpression affects basal dendrite arborization in layer II-III neurons in the developing cortex. 34
Figure 1.1.4.9. TAOK2 down-regulation affects callosal axon projection in the developing cortex. 35
Figure 1.1.4.10. TAOK2 overexpression affects axonal projection at the corpus callosum in the developing cortex. 36
Figure 1.1.4.11. TAOK2 interacts with Nrp1. 36
Figure 1.1.4.12. TAOK2 interacts with Nrp1 at the intermediate zone and cortical plate in the developing cortex. 37
Figure 1.1.4.13. TAOK2 interacts with Nrp1 to modulate TAOK2 phosphorylation. 38
Figure 1.1.4.14. TAOK2 and Sema3A modulate the activity of JNK1: TAOK2 down-regulation descreases JNK1 signal in isolated neurons. 40
Figure 1.1.4.15. TAOK2 and Sema3A modulate the activity of JNK1: Sema3A treatment of isolated neurons increases JNK1 signal. 41
Figure 1.1.4.16. TAOK2 and Sema3A modulate the activity of JNK1: Nrp1 knock-out mouse has decreased activity of JNK1. 42
Figure 1.1.4.17. TAOK2 counteracts the dendritic arborization deficit in neurons expressing a deficient Nrp1 receptor. 43
Figure 1.1.4.18. Nrp1 shRNA specifically down-regulates Nrp1-mCherry expression in HEK293Tcells. 44
Figure 1.1.4.19. TAOK2 counteracts the dendritic arborization deficit in neurons with Nrp1 down-regulation. 45
Figure 1.1.4.20. Activated JNK1 predominates in basal dendrites. 46
Figure 1.1.4.21. Activated JNK1 ameliorates deficient basal dendrite formation following TAOK2 down-regulation. 47
Figure 1.1.4.22. Activated JNK1 ameliorates axonal projection deficits following TAO2 down-regulation. 48
Figure 1.1.4.23. TAOK2 down-regulation affects neuronal migration in the developing cortex, while the overexpression of MKK7-JNK1 partially rescues the phenotype 50
Figure 1.1.4.24. TAOK2 downregulation affects cortex layering. 51
Figure 1.1.4.25. The overexpression of the constituve active form MKK7-JNK1 rescues the cortial layering defect. 52
Figure 1.1.4.26. TAOK2 down-regulation affects in vivo cell body movement speed and displacement. 54
Figure 1.1.4.27. TAOK2 modulates the formation of basal dendrites and axonal elongation in pyramidal neurons. 57

Figure 1.2.2.1. Model of fluid mosaic membrane first described by Singer and Nicolson. 71
Figure 1.2.2.2. Recombinant DNA technology. 73
Figure 1.2.2.3. Number of unique membrane protein structures. Currently, 427 unique membrane protein structures are present at the 'Membrane protein of known 3D structure' database (http://blanco.biomol.uci.edu/mpstruc/). 74
Figure 1.2.2.4. Schematic diagram of detergent-based crystallization of membrane proteins. 78
Figure 1.2.2.5. Schematic diagram of secondary structure predictions for *human*TAOK2. 80
Figure 1.2.2.6. Crystal structure of the TAOK2 kinase domain. 81

Figure 1.2.4.1. pOPIN vector used at the OPPF laboratory for high-throughput screening of *h*TAOK2 in *Escherichia coli* strains. 89
Figure 1.2.4.2. OPPF constructs of *h*TAOK2-GFP tested in HEK293T cells. 92
Figure 1.2.4.3. OPPF construct, full length *h*TAOK2-GFP, tested in different *Escherichia coli* strains. 93
Figure 1.2.4.4. Small scale expression and purification of *h*TAOK2 constructs. 93
Figure 1.2.4.5. Schematic diagram of full-length constructs designed *in house.* 94
Figure 1.2.4.6. HEK293T cells 48 hours after transfection with the different constructs. 95
Figure 1.2.4.7. His-GFP-*h*TAOK2 overexpression evaluated by western blot. 95
Figure 1.2.4.8. *E. coli* strains 48 hours after transfection with the different constructs. 96
Figure 1.2.4.9. Western blot of BL21(DE3) and C43(DE3) probed for αTAOK2 polyclonal antibody. 96
Figure 1.2.4.10. Affinity chromatography (Ni-NTA) for *h*TAOK2 overexpressed in HEK293T cells. 98
Figure 1.2.4.11. Time-course expression screening of His-GFP-*h*TAOK2 and strep-GFP-hTAOK2 in Baculovirus-infected insect cell lines 99
Figure 1.2.4.12. Hi5 cell cultures were infected with the indicated recombinant Baculoviruses. 100
Figure 1.2.4.13. Microscale Ni-NTA from Hi5 cells infected with His-GFP-*h*TAOK2 expressing recombinant Baculovirus. 101
Figure 1.2.4.14. Immunoblot with α-TAOK2 polyclonal antibody. 102
Figure 1.2.4.15. Initial solubilization tests performed on overexpressed His-GFP-*h*TAOK2 in HEK293T cells. 103
Figure 1.2.4.16. Western blot of soluble samples extracted from the membranes of Hi5 cells with higher yields. 105
Figure 1.2.4.17. Western blot of soluble samples extracted from the membranes of HEK293T cells with higher yields 106
Figure 1.2.4.18. Graphical representation of detergent solubilization capacity of His-GFP-*h*TAOK2 construct when expressed in HEK293T cells. 107
Figure 1.2.4.19. Western blot analysis after manual affinity chromatography of strep-GFP-*h*TAOK2. 108
Figure 1.2.4.20. Analytical SEC of eluted fractions from affinity column Ni-NTA. 109
Figure 2.2.1: Diagram of DNA structure as proposed by Watson and Crick in 1953. 119
Figure 2.2.2. The chemical structure of DNA. 120
Figure 2.2.3. Representative double-helical structures of DNA. 121
Figure 2.2.4. B to Z-DNA transition. 122
Figure 2.2.5. The chemical structure of RNA. 123
Figure 2.2.6. First structure of Z-RNA by NMR. 125
Figure 2.2.7. Full-turn model of the Z-RNA helix (12.4 bp per turn) (left) compared to the 12 bp per turn models of Z_I- (middle) and Z_{II}-DNA (right). 126
Figure 2.2.8. The ADAR family protein. 128
Figure 2.2.9. Model for regulation of ADAR1 activity by Z-DNA. 129
Figure 2.2.10. Crystal structure of $Z\alpha_{ADAR1}$:Z-DNA complex (PDB ID 1QBJ). 130
Figure 2.2.11. Crystal structure showing a B-Z-DNA junction (PDB ID: 2ACJ). 131
Figure 2.2.12. Crystal structure showing a $Z\alpha_{ADAR1}$:Z-RNA complex (PDB ID 2GXB). 132
Figure 2.2.13. Base Stacking and Backbone Hydration of two Z-RNA Conformations one Z-DNA. 132
Figure 2.2.14. Proteins containing a Zα domain. 133

Figure 2.4.1. SDS-PAGE after His-tag cleavage and ion-exchange chromatography. 140
Figure 2.4.2. Crystals for $Z\alpha_{ADAR1}$:Z-Z-RNA (a-f) and for $Z\alpha_{ADAR1}$:A-Z-RNA (g-l). 141
Figure 2.4.3. CD measurements on A-Z-RNA oligonucleotide incubated with different concentrations of $NaClO_4$. 142
Figure 2.4.4. A-Z-RNA oligonucleotide incubated with $Z\alpha_{ADAR1}$. 144
Figure 2.4.5. Z-Z-RNA oligonucleotide incubated with $NaClO_4$. 144
Figure 2.4.6. MS spectra of A-Z oligos (a and b), purified $Z\alpha_{ADAR1}$ (c), and crystals from the A-Z-RNA complex (d). 147
Figure 2.4.7. Data processing of Z-Z-RNA dataset showing A-dsRNA. 148
Figure 2.4.8. Overall structure of a Z-Z junction. 150
Figure 2.4.9. Circular dichroism spectra of the Z-Z DNA duplex and its titration with Zα. 151
Figure 2.4.10 .Conservation of the protein–DNA interactions in the $Z\alpha_{ADAR1}$:Z-Z DNA complex. 152
Figure 2.4.11.The Z-Z junction structure in the presence of Hepes. 155
Figure 2.4.12. The Z-Z junction structure and its comparison with a B-Z junction. 156

List of Tables

Table 1.2.2.1. Predicted transmembrane helices (TMs) for *human*TAOK2α. 79
Table 1.2.3.1. PCR primers list for In-Fusion protocol to obtain the His-GFP-hTAOK2 and the strep-GFP-hTAOK2 constructs for Baculovirus expression. 84
Tabel 1.2.4.1. List of the 47 *h*TAOK2 constructs tested at OPPF-UK 91
Tabel 1.2.4.2. Detailed information of the 96 detergent screen. 104

Table 2.4.1. X-ray diffraction data collection and processing statistics of putative RNA oligonucleotides in complex with $Z\alpha_{ADAR1}$ 145
Table 2.4.2. Data collection and refinement statistics. 149
Table 2.4.3. Selected conformational parameters for the Z-Z junction in Tris buffer; DNA conformational parameters as determined by using 3DNA (Lu and Olson, 2003). 153
Table 2.4.4. Detailed conformational parameters of a Z-Z junction in Hepes buffer; local base-pair step parameters as calculated by using 3DNA (Lu and Olson, 2003). 153
Table 2.4.5. Detailed conformational parameters of a Z-Z junction in Tris buffer; local base-pair step parameters as calculated by using 3DNA (Lu and Olson, 2003). 154
Table 2.4.6. B factors and occupancy of the intercalating Hepes molecule. 155

Chapter 1

Functional and structural studies of the membrane bound kinase – TAOK2α

Chapter 1 - Section 1

The role of TAOK2α in neocortical development

Nothing in biology, it is said, makes sense unless viewed in light of evolution. Thus the mechanisms underlying expansion of the cerebral cortex are central to understanding the potential and limits of our mental capacity.

- Pasko Rakic

This work is/will be published in the following manuscripts:

Froylan Calderon De Anda, **Ana Lúcia Rosário**, Omer Durak, Tracy Tran, Johannes Gräff, Kostantinos Meletis, Damien Rei, Takahiro Soda, Ram Madabhushi, David D Ginty, Alex L Kolodkin & Li-Huei Tsai, 2012. Autism spectrum disorder susceptibility gene TAOK2 affects basal dendrite formation in the neocortex. *Nature Neuroscience* 15, 1022–1031.

Froylan Calderon De Anda, **Ana Lúcia Rosário**, Omer Durak, Konstantinos Meletis & Li-Huei Tsai. TAOK2 acts as player on pyramidal neuron migration from the mouse neocortex. *In preparation.*

This study was designed, directed and coordinated by F.C.d.A. and L.-H.T. L.-H.T., as the principal investigator, provided conceptual and technical guidance for all aspects of the project. F.C.d.A. planned and performed the *in utero* electroporations and analyzed the data with A.L.R. and O.D. F.C.d.A. performed and analyzed the immunohistochemistry experiments. K.M. generated and characterized the shRNA constructs. K.M., A.L.R. and D.R. contributed to the neuronal cultures. T.T. performed and analyzed the data from the neuronal cultures of *Nrp1*$^{Sema-}$ mice. A.L.R., O.D., J.G. and R.M. contributed to the biochemistry experiments. T.S. generated the lentiviral shRNA construct and produced the virus particles. D.D.G. and A.L.K. provided the *Nrp1*$^{Sema-}$ mouse brains and suggested and commented on the design of the experiments. The manuscript was written by F.C.d.A. and L.-H.T. and commented on by all authors.

1.1.1. Abstract 6

1.1.2. Introduction 7

Mammalian Brain Development 7

Neuronal Migration 9

Neuronal polarity: axon and dendrites 12

Axon Elongation 14

Dendritic arborization mechanims 15

Semaphorin3A signaling in cortical development 16

The TAOK2 protein 18

1.1.3. Material and Methods 20

1.1.4. Results and Discussion 25

Expression profile of TAOK2 in cultured cortical neurons and in the developing cerebral cortex. 25

TAOK2 impacts neuronal differentiation in cultured cortical neurons. 27

TAOK2 affects basal dendrite formation and axon elongation in vivo. 32

TAOK2 interacts with the Neuropilin 1 receptor to modulate neuronal differentiation. 36

TAOK2 and Sema3A modulate the activity of JNK in cortical neurons. 39

TAOK2 modulates basal dendrite formation downstream of Sema3A-Nrp1. 43

Activated JNK modulates basal dendrite formation downstream of TAOK2. 45

TAOK2 down regulation affects cortical neuronal migration, JNK1 rescues the phenotype 48

TAOK2 down-regulation afects in vivo leading process displacement and speed of migration 53

1.1.5. Conclusion 55

The Sema3A-Nrp1 signaling cascade is coupled to TAOK2-JNK1 to modulate differentiation of cortical pyramidal neurons. 55

TAOK2 and Autism Spectrum Disorders. 58

1.1.6. References 59

1.1.1. Abstract

How neurons develop their morphology is an important and challenging question in neurobiology. Little is known concerning the establishment of distinct neuronal dendritic architectures. Specifically, how different molecular pathways define distinct compartments, including apical versus basal dendrites in pyramidal neurons, remains to be elucidated.

In this chapter is described a novel pathway that specifically affects the formation of basal dendrites and axonal projections in cortical pyramidal neurons, which had a simultaneous role in the migration of pyramidal cortical neurons. TAOK2α kinase (thousand-and-one amino acid 2 kinase isorform 1), the product of an Autism Spectrum Disorder susceptibility gene, plays an essential role in dendrite morphogenesis and axonal projection. TAOK2α down-regulation impairs basal dendrite formation *in vivo* without affecting apical dendrites. Moreover, TAOK2α interacts with Neuropilin 1 (Nrp1), a receptor protein that binds the secreted guidance cue Semaphorin 3A (Sema3A), which has previously been associated with basal dendrite morphogenesis and axon elongation. TAOK2α overexpression restores dendrite formation in primary cortical neurons cultured from *Nrp1*$^{Sema-}$ mice, which express an Nrp1 receptor incapable of binding Sema3A. TAOK2 overexpression also ameliorates the basal dendrite impairment resulting from Nrp1 down-regulation *in vivo*. Finally, Sema3A and TAOK2 modulate the formation of basal dendrites and axonal elongation through the activation of the c-Jun N-Terminal Kinase (JNK). The TAOK2 pathway through JNK is also associated with the pyramidal neuron migration during development.

The presented results delineate a pathway whereby Sema3A and Nrp1 transduce signals through TAOK2 and JNK to regulate basal dendrite development and axonal elongation in cortical neurons.

1.1.2. Introduction

Mammalian Brain Development

The human brain contains more than 10^{11} neurons, each of which, on average, has to make connections with a thousand others, according to a regular and predictable wiring plan. Contrary to a man-made computer, the wiring between neurons is not so precise, simply because brains don't work as computers and are much more tolerant to failures in wiring between its components. Nevertheless, the brain outstrips all other biological structures in its organized complexity (Alberts et al., 2002a).

The adult brain has a diversified and elaborated architecture, a product of genes, signaling mechanism and, eventually, the external world. The first stages of brain development occur prior to synaptic activity. Those include the establishment of primordial nervous system in the embryo; the first born neurons from precursor cells, the migration of neurons from their origin towards their final position and the formation of brain regions. If any of these processes goes awry, the consequences can be disastrous, as most of the congenital brain defects result when an event – genetic mutation, disease, exposure to toxic agent – interferes with these normal mechanisms of development.

Early in the generation of the embryo, the cells that will give rise to the brain become distinct quite early. Neurulation in vertebrates, the first event in organogenesis, results in the formation of the neural tube which gives rise to the spinal cord and the brain. Neural crest cells, also born during neurulation, lie between the neural tube and the overlying epidermis, migrate away from the neural tube and will give rise to the diversity of cells present in the brain, including neurons.

Three different events take place for the formation of the central nervous system (CNS). The neural tube and its lumen bulge and constrict to form the chambers of the brain and spinal cord. At the cellular level, the neuroepithelial cells differentiate into numerous types of neurons and glia present in the brain. Simultaneously, at tissue level, there is a rearrangement of the cell populations present in the wall of the neural tube leading to a formation of different functional regions of the brain and spinal cord (Alberts et al., 2002a).

Neurons also differ in their developmental origins; they have different genomic expression and electrophysiology patterns, however morphological differences are valuable tools for neuronal identification (Figure 1.1.2.1). Branching patterns of dendrites are extremely diversified (Ramón y Cajal, 1952).

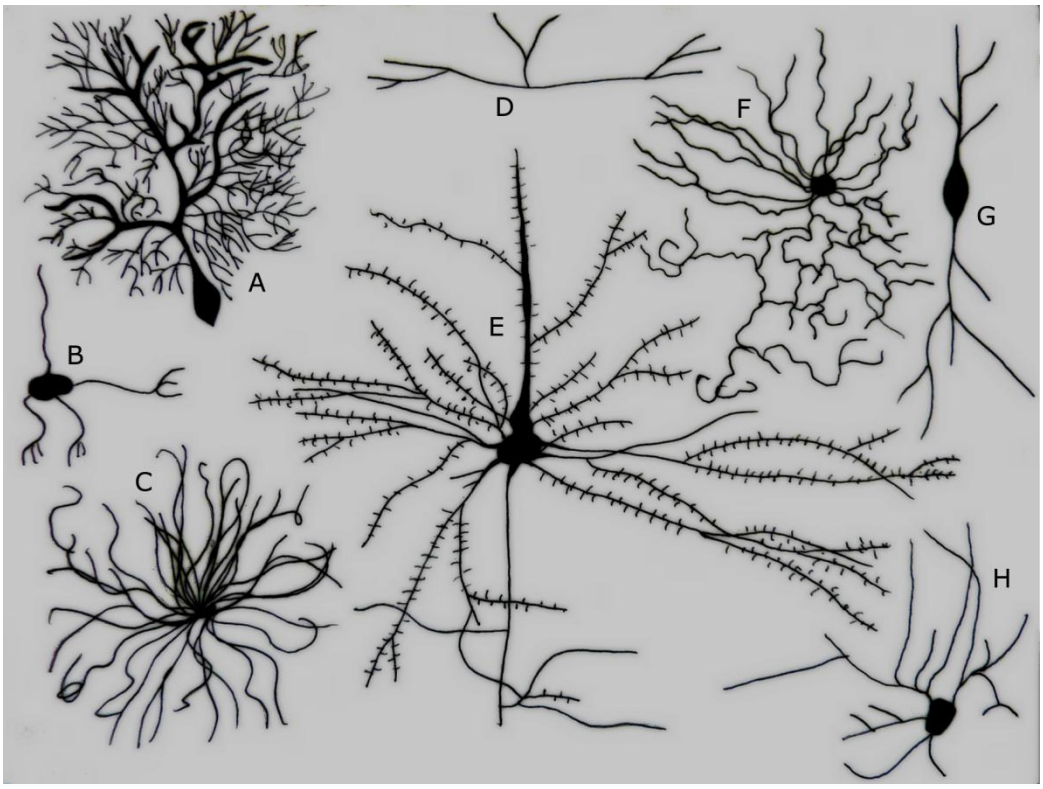

Figure 1.1.2.1. Different types of neurons.

A. Purkinje cell B. Granule cell C. Motor neuron D. Tripolar neuron E. Pyramidal Cell F. Chandelier cell G. Spindle neuron H. Stellate cell [Credit: Ferris Jabr; based on reconstructions and drawings by Ramon y Cajal (from Jabr, 2012)].

The mammalian neocortex is a unique structure, an evident hallmark in evolutionary biology. Thoughts, consciousness, resolution of intricate mathematical problems, writing an opera or simply reading a thesis are high cerebral cognitive and associative functions, all seating in the neocortex. The vertebrate cortex is organized in six layers and tangentially subdivided – arealization - into functional areas deputed to the elaboration of sensory information, association between different stimuli, and selection and triggering of voluntary movements. Each area of the cortex is associated with a peculiar function, possesses unique connectivity and cytoarchitecture. In mammals, there is an extreme conservation of the neocortical areas, their conserved position and wiring within the brain suggested an identical genetic program governing the neocortical patterning (Alfano and Studer, 2013).

With increased microscopical power, the last five decades are sprouted with milestones in the field. Raskic and colleagues followed the pioneer work of Poliakov (Poliakov, 1961) and together they established the current models of cortical arealization - the neocortex subdivisions, i.e. the different functional areas which have unique cytoarchitecture and connectivity patterns; and neuronal migration – as most neurons are generated at different sites from those in which they permanently reside, they demonstrated that 80 to 90 % of neuronal precursors in the cortex migrate along radial glial cells (RGCs) (Angevine and Sidman, 1961; Rakic, 1972, 1974, 1990; Sidman and Rakic, 1973). Also, in the recent years, a large diversity

of transcription regulators of neuronal polarity and migration had been studied. An intimate knowledge of the existing balance between specific transcription factors and highly-regulated GTPases is described (Fukata et al., 2003). However, despite the enormous amount of studies, little is known about the process of brain development. But certainly, not only neuronal intrinsic factors play a role in cortical development, as the sensing of extrinsic molecules is essential during development to the establishment of the complex network of connections in the central nervous system.

Neuronal Migration

Motility is one of the primordial features of prokaryotic and eukaryotic cells. A key feature in the developing nervous system is neuronal migration. Understanding its molecular mechanisms is a milestone for neuroscientists in part because, direct or indirectly, many human disorders are related with abnormal migration. Neuronal migration defects have been associated with multiple disorders related with development, Autism Spectrum Disorder (ASDs), schizophrenia, epilepsy, lissencephaly, between others (Liu, 2011; McManus and Golden, 2005; Murray et al., 1991).

Neuronal migration occurs during neurogenesis and consists in an accurate execution of sequentially molecular processes that confer identity and positioning to neuronal cells with subsequent maturation and connection between those cells. A neuron needs to be in the right place at the right time for differentiation and integration in a circuit that mediates behavior. However, once neurons reach a final position, cell death occurs and there is a decrease in number of neurons due to histogenetic cell death mechanisms (Finlay and Slattery, 1983). Histogenesis events are extended in time; proceed widely in all areas of the brain, comprising structural diversity with unique properties. In the neocortex, cell death is not uniform, e.g. it occurs in several of the areas from cyngulate and frontal cortex lack layer IV neurons, while the primary visual and sensory cortex have highly developed layer IV; cell loss has been suggested to determine local features of cortical differentiation (Finlay and Slattery, 1983). Yet these events are coordinated to arrive at a neuronal density that is approximately the same from region to region of the same brain and in the brains of diverse mammalian species (Rockel et al., 1980; Schüz and Palm, 1989).

Before the onset of neurogenesis, neuroepithelial cells, the primary stem/progenitor of neuronal cells present in the neuroepthelium, expand via symmetric divisions. With the onset of neurogenesis, neuroepithelial cells switch the pattern of gene expression to invoke the differentiation potential and allow for asymmetrical cell division to happen, generating secondary stem and progenitor cells (radial glia cells and basal progenitors) and neurons. Neuroepithelial progenitors and RGCs are considered apical progenitors, as they undergo mitosis at the apical, ventricular surface (Farkas and Huttner, 2008). Neurogenesis comprehends a combination of modes of cell division: symmetrical progenitor cell division (expansion of secondary precursor

cells), asymmetrical progenitor divisions (one daughter cell arises as a neuron, the other as a progenitor) (Chenn and McConnell, 1995) and symmetrical terminal divisions (generation of two neurons – terminally differentiated) (Takahashi et al., 1996).

The first phenotypic change occurs at E9/E10 of the mouse telenchephalon. With the onset of neurogenesis at the telenchephalon germinal zones – the ventricular zone (VZ, also known as proliferative zone or germinal matrix, a pseudostratified columnar neuroepithelial region lining the lateral ventricles). At the VZ, neuroepithelial cells start to express glial markers, forming RGCs (Götz and Huttner, 2005; Kriegstein and Götz, 2003). RGCs are non-neuronal cells present in the developing brain which serve as molecular scaffolds for the migration of future neurons due to the particularity that these cells have their body in the VZ but extend processes to the pial (apical process) and ventricular surface (basal process), covering vertically, all length of the nascent cortex (for revision see Campbell and Götz, 2002). As neurons, RGCs also perform interkinetic nuclear migration (INM), whereas their nucleus travels within the VZ. RGCs are regarded as neural stem cells (Figure 1.1.2.2); they undergo self-renewal by symmetric division or give rise to neurons or secondary progenitors by asymmetric divisions (Noctor et al., 2001, 2004, 2008). Also, there is supporting evidence of an existing lineage relationship between neurons and the proliferative RGC, reporting that clonally related neurons migrate along radial glial fibers to form functional cortical columns, the radial organization of the neocortex (Noctor et al., 2001).

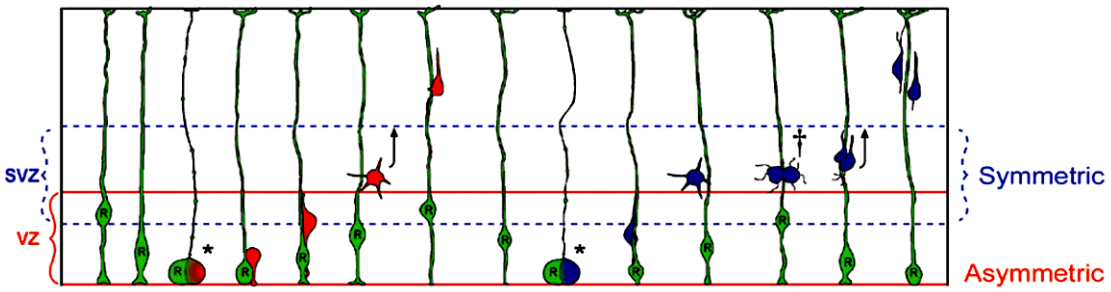

Figure 1.1.2.2. Modes of cell division in the mammalian neocortex.

Radial glial cells divide asymmetrically in the ventricular zone (VZ), and intermediate progenitor cells divide symmetrically in the subventricular zone (SVZ). A radial glial cell (green) divides asymmetrically at the ventricular surface to generate a daughter neuron (red). The radial glial cell remains mitotic to generate another daughter cell. Radial glial cells (green) also generate intermediate progenitor cells (blue) that divide symmetrically in the SVZ to generate two daughter cells, neurons (blue) that migrate toward the cortical plate (CP). Terminal symmetric divisions occur in the SVZ (from Noctor et al., 2004).

Basal (intermediate) progenitors (BPs) translocate their nucleus to the basal region of the VZ to form a second germinal layer, or subventricular zone (SVZ). BPs retract their basal and apical processes and undergo mitosis at the basal SVZ, a region that overlaps the VZ and extend into the intermediate zone (IZ) (Boulder Committee, 1970), producing two neurons. It is possible that in rodents, BPs can expand their pool by proliferative asymmetric divisions (Kowalczyk et al., 2009; Noctor et al., 2004, 2008).

Postmitotic neurons undergo migration towards the developing cortical plate to reach their final destination. Newly generated neurons reach the developing cortex either by somal translocation, whereby a neuron cell body travels within a pial contacting radial process, or by locomotion, a process by which newborn neurons develop leading and trailing processes and migrate along radial glial fibers (for revision see Noctor et al., 2004).

The distance a population of neurons migrates varies with neuronal type and brain region. In the human cerebral cortex, pyramidal neurons migrate radially about 2 cm, to those that travel tangentially the distance may be several fold increased (Tsai and Gleeson, 2005).

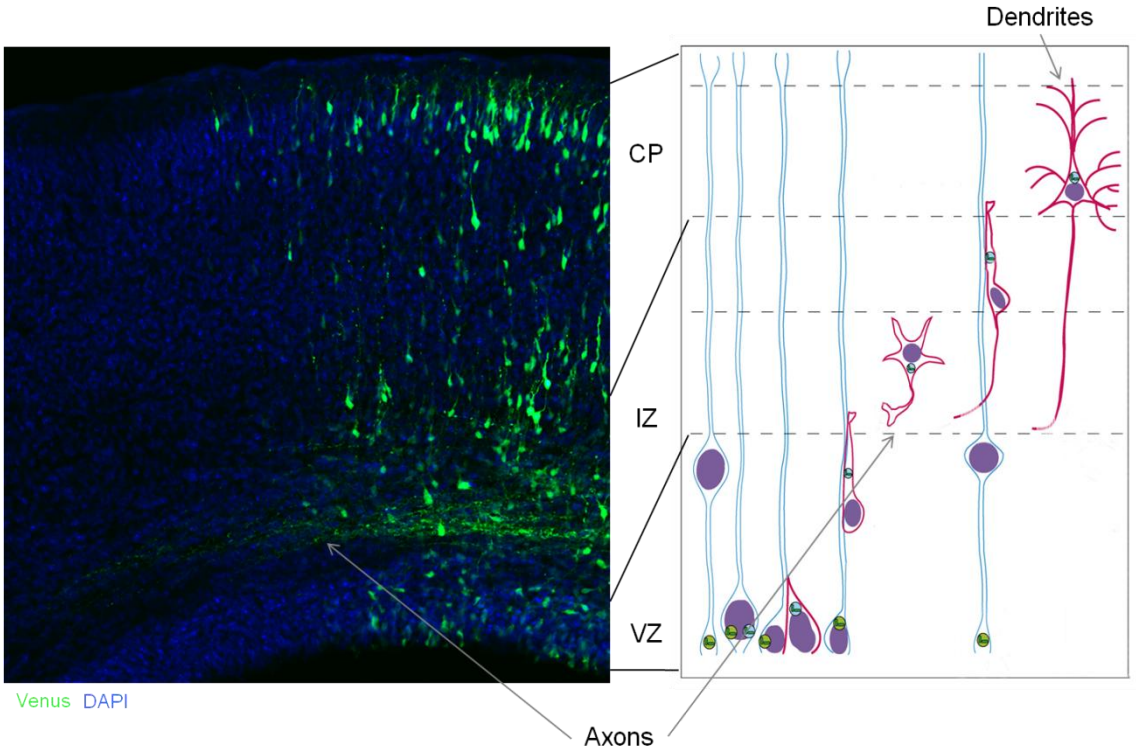

Figure 1.1.2.3. The model of radial glial migration in the mammalian cortex.

Microscopical picture of the mouse neocortex evidanciating the different cortical layers (left). Scheme depicting a neuron (red) undergoing the migration along a radial glial fiber (blue): initial radial migration at the VZ, SVZ arrest, establishment of neuronal polarity, second phase of migration until final destination and maturation of the neuron (right; credits of picture to Froylan Calderon de Anda).

The earliest generated cortical neurons form a transient structure, the preplate. The next cohort of cells will intercalate in the preplate, splitting these structure in the marginal zone (MZ or layer I) and in the deeper layer, the subplate. Together they form the cortical plate (CP) that is populated by arising neurons forming a total of six horizontal cortical layers (L1-L6) that are distinguished cytoarchitectonically and functionally. Neurons of layers II-VI migrate according to the inside-first, outside-last manner; earlier neurons migrate and populate the deepest layer

followed by a sequential wave of migrating neurons that will occupy a more superficial layer (Berry and Rogers, 1965; Rakic, 1972; Sidman and Rakic, 1973; SIDMAN et al., 1959). Cortical layers are populated by arising neurons and each layer is constituted by a specific subset of approximately three quarters of pyramidal neurons (glutamatergic excitatory projection neurons) and the remaining are interneurons (GABAergic inhibitory neurons) (Jones, 1986). Deep layer and subplate neurons (L5-L6) project mainly to other areas of the nervous system, as spinal cord, thalamus and striatum, and other subcortical structures. More superficial neurons (L2-L4) are cortical projection neurons. Projection neurons are responsible for connections within the cortex: interhemispheric or contralaterally, mostly trough the corpus callosum, and intrahemispheric connections (Berry and Rogers, 1965; Rakic, 1972; Sidman and Rakic, 1973; SIDMAN et al., 1959).

During migration, neurons establish interactions between other migrating neurons and the surfaces of neighboring cells. Such interactions play a pivotal role in the appropriate selection of migratory pathways, as well in orientation, navigation and conclusion of neuronal movement in their final destination, where neuronal maturation takes place (Hatten, 2002; Pearlman et al., 1998).

The migration of neurons progresses in a way where two consecutive events are repeated, those events underlie at first an extension and retraction of the leading neurite, oriented forward, together with the centrosome, followed by nuclear displacement (Bellion et al., 2005; Gregory et al., 1988; Rakic, 1972). This migratory fashion requires major alterations in the cellular cytoskeleton, both in actin and microtubules (MTs), and action of very specialized molecules. The leading process is composed of several organelles and usually terminates in several protrusions oriented toward the cortical plate that by sensing the extracellular environment will determine the migratory pathway. Alteration to this dynamics usually is impairment for migration in cortical development studies.

The precise regulation of neuronal migration is responsible for cortical lamination and critical for proper development of the brain architecture. Therefore, its deregulation has a huge impact in the whole development of the neocortex causing a diversity of disorders (Dobyns and Truwit, 1995). The establishment of neuronal polarity with axon development and growth is crucial for the migration of neurons. Also, it is well accepted that cytoskeleton dynamics enables the movement of the growth cone, determining its direction, and regulating axon elongation during migration (Lowery and Van Vactor, 2009).

Neuronal polarity: axon and dendrites

In one neuronal cell, differentiation occurs during neurogenesis with a dramatic change in neuronal shape – in the establishment of neuronal polarity, two distinct morphological and functional compartmentalized structures composed of different proteins and organelles, axon and dendrites, become evident. Axons are long and thin, with a uniform thickness through their

whole length. Dendrites are short and become thinner with increased distance and undergo Y-shaped branching, they contain sites of membrane protrusion called dendritic spines the major excitatory synaptic site, a specialized structure full of neurotransmitter receptors in order to receive information. During the transmission of neuronal information, dendrites receive a synaptic input from other neuron through the dendritic spine. The information is integrated at the cell body and propagates down to the axon to the presynaptic terminal, and is transferred to other neurons. Hence, polarization is an indispensable event during neuronal development and a pre-requisite for the integration and transmission of information within the brain (Neukirchen and Bradke, 2011). Axon formation is the key event for the initiation of neuronal polarization. Banker and colleagues developed a culture system, of embryonic rat hippocampal neurons, for the observation in living CNS neurons. With those, they could observe the morphological events taking place during differentiation from a neuroblast to a polarized cell (Dotti et al., 1988). This *in vitro* model is a powerful tool to uncover the developmental mechanism of neurons and most of the knowledge comes from it, *in vivo* studies are then necessary for the validation of the proposed mechanism.

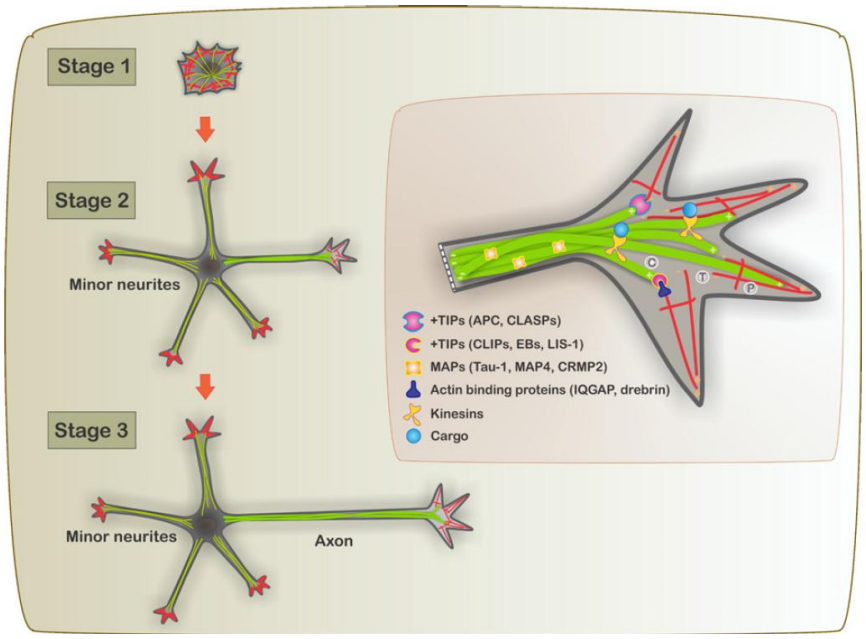

Figure 1.1.2.4. Schematic depiction of a developing hippocampal neuron during neuronal polarization.

After dissociation and plating, the neuron attaches to the substrate as a round sphere surrounded by lammellipodia and filopodia (Stage 1). During neuritogenesis, growth cones form by the condensation of lamellipodia and induce the establishment of several short protuberant processes, called minor neurites (Stage 2). At this stage, the neuron remains symmetric and unpolarized. One minor neurite strarts to enlogate rapidly and becomes the axon while the other neurites remain short, breaking the neuronal symmetry (Stage 3). At this stage, polarity is established. With neuronal maturation, minor neuritis become dendrites at a later stage (Stage 4).The enlarged view shows an axonal growth cone. Microtubules (green) enter the growth cone and interact with the actin cytoskeleton (red). Microtubule associated proteins (MAPs) bind along the microtubule lattice or at the growing ends of microtubules (+TIPs), where they interact with actin binding proteins. C: central domain; T: transition zone; P: peripheral domain; polymerizing or depolymerizing ends are labeled with + or −, respectively (from Neukirchen and Bradke, 2011).

The role of localized instability of the actin network in specifying axonal fate was examined by Bradke and Dotti in 1999 (Bradke and Dotti, 1999) with the use of rat hippocampal neurons in culture. They proved that local instability of actin, restricted to a single growth cone, present in one of the neurites, is a physiological signal specifying neuronal polarization. Disruption of the actin network in the growth cone induces axon elongation. From the observation of cultured hippocampal neurons, different developmental stages were identified during polarization (Figure 1.1.2.4.): born as an unpolar and symmetric sphere, neurons end up mature when achieving a highly polarized structure.

Defining the mechanism that regulate growth, guidance and branching of axons will tell us how the cerebral cortex becomes wired to appropriate targets during development. In the mammalian nervous system, axons establish connections through the activity of the growth cone and by extending branches towards a cell target from the collateral primary axon shaft branches (Kalil et al., 2000). Once the connectivity is incorrect or damaged; the brain's ability to work normally is severely incapacitated.

Axon Elongation

The growth cone responds to attractive cues by turning toward the source of a positive guidance cue, in contrary, inhibitory guidance cues repel axons away (Huber et al., 2003). It is now clear that the response to attraction versus repulsion is not due to the properties of a specific cue, but due to the intrinsic properties of the growth cone – the receptors engaged in the growth cone, and its signaling milieu. The growth cone comprises the necessary elements to determine how environmental direction lead to a given guidance response during axon "navigation" (Chilton, 2006). Neuronal growth cones adhere to extracellular substrates: cell adhesion molecules (CAMs) or extracellular matrices, in order to properly migrate towards their final destination. Microtubules play an important role, as they are responsible for the connectivity between the growth cone and the extracellular substrates, possibly acting as guidance sensors, i.e. introducing an adhesive molecule leads to an increase in exploratory MTs (Lee and Suter, 2008).

Microtubules provide structure and rigidity to the axon shaft. When the axon is elongating, microtubules populate the central domain of the growth cone and polymerize into the direction of the leading edge, transporting vesicles and organelles towards it (Lowery and Van Vactor, 2009). However, the peripheral domain of the growth cone is composed of actin filaments, existing in the form of filopodia (packed actin bundles) or lamellipodia (sheet like actin meshwork). Actin forms a meshwork inveil-like lamellipodia and boundless in finger like filopodia that protrude from the highly motile lamellipodia towards a leading edge. Actin structures and its dynamics shape and direct the growth cone propagation in the surrounding environment. Actin and microtubules interact in the transition zone, between the central and peripheral domain, which is fundamental for axon extension (Lowery and Van Vactor, 2009). Axon extension happens by extending the axon shaft, due to transformation of the C-domain (Figure 1.1.2.4),

allowing the growth cone to advance. So, extension underlies a complex rearrangement of the cytoskeleton. Polymerization of actin filaments causes extension and protrusion of the growth cone – the growing end points to the distal membrane and creates a force that pushes the actin network and the closely linked membrane backwards. Myosin-II, a molecular motor that generates forces on F-actin, supports the retrograde flow by contraction of actin filaments in the T-zone, and generates actin arcs (Medeiros et al., 2006; Schaefer et al., 2008). Actin arcs orient perpendicular to the axis of filopodia and hinder the invasion of microtubules into the P-domain. So, while actin functions as a steric hindrance for microtubules, microtubules push the actin arcs cytoskeleton towards the growth direction, creating an area free of actin, enabling microtubules engorgement and delivery of proteins (Forscher and Smith, 1988). Finally, the actin cytoskeleton depolymerizes at the neck of the growth cone and microtubules bundle, enabling the proximal part of the growth cone to assume a cylindrical shape, becoming part of the axonal shaft (Bradke and Dotti, 1999; Lowery and Van Vactor, 2009; Neukirchen and Bradke, 2011).

Interstitial branching mechanism occurs from the axon shaft after the growth cone has extended past the target. Such mechanism are extremely important, those possibilitate the wiring of the cortical neurons to distinct targets, e.g. spinal cord (efferent corticospinal) and contralateral cortex (callosal axons) (Bastmeyer and O'Leary, 1996; Halloran and Kalil, 1994; O'Leary et al., 1990).

Dendritic arborization mechanims

Dendrites are the neuronal processes specialized in the input of information, differing morphologically and functionally from the axons (Craig and Banker, 1994). The main excitatory synaptic sites, spines, are only present in dendrites. Different types of neurons meet different requirements accordingly with their physiological function. They are so readily classified based on their dendritic field dimensions and dendrite branching patterns (Ramón y Cajal, 1995).

The dendritic field is the region occupied by one neuron dendrites and determines the extent of sensory or synaptic inputs to that neuron. The field complexity and circuitry assembly influences the range of inputs received by the neuron. On the other hand, the morphological features of the dendritic arbor impacts processing and integration of the electrical signals (London and Häusser, 2005). The innervation of particular regions of the nervous system out of many possible targets will determine the input that a neuron receives and its function in specific circuits. Dendritic guidance and targeting programs are controlled primarily by intrinsic programs liked to cell lineage and identity. In turn, those intrinsic programs dictate how dendrites respond to extrinsic factors – attractive and repulsive cues from the environment. Local interactions between dendrites help to define and refine dendritic target boundaries. Dendrites need to have the flexibility for adjustment in development and in response to experience. For example, by

dynamic microtubule invasion of spines and NMDA (N-methyl-D-aspartarte) receptor mediates signaling that affects dendrite organization in the somatosensory cortex during development and in the mature nervous system.

The development of dendritic branch diversity though guidance and targeting, happens in a cell-type specific way, where the first level of control arises from intrinsic programs that are linked to cell lineage and identity controlling how dendrites respond to attractive and repulsive cues in their environment (Kelsch et al., 2007; Komiyama and Luo, 2007). Local interactions between dendrites help to define and refine dendritic target boundaries. Later dendritic branching is thought to be associated with neuronal activity. As primary dendrites form first, side branches emerge later from the shaft of the primary dendrite, first as transient slender projections, or filopodia – highly dynamic actin structures. Those transient projections, if stabilized, will become a secondary dendritic branch. Stabilization occurs at the formation of a synapse, so, postsynaptic signaling may influence such process, at the same time that a dendritic spine is stabilized, likely, due to the involvement of calcium signaling (Konur and Ghosh, 2005). Side branching formation requires dynamic actin for the formation and remodeling of filipodia, followed by actin stabilization as the secondary branching pattern develops. RhoGTPases are the best studied molecules that provide regulation of actin dynamics in neuronal development (Etienne-Manneville and Hall, 2002). *In vitro* studies have shown that Rho inhibits dendrite growth and branching, while Rac1 play as inducer (Govek et al., 2005). Cdc42, another RhoGTPase involved in branching and cell polarity, is thought to be activated more in some layers of the cortex than in others, revealing a layer-specific environmental signaling, which is thought to interact with other players to determine the dendritic arborization at a specific cortical layer (Rosário et al., 2012; Simó and Cooper, 2012).

Recent genetic studies revealed a complex network of intrinsic and extrinsic regulators, transcription factors and ligands for cell surface receptors, respectively, that are needed to produce the distinct morphology of the four classes of larval dendritic arborization neurons in *Drosophila melanogaster* peripheral nervous system (revised in Corty et al., 2009).

Semaphorin3A signaling in cortical development

First characterized as repulsive guidance cues (Kolodkin et al., 1992), semaphorins (Semas) are their largest family (20 members), comprising both secreted and membrane-bound proteins. In vertebrates, the major receptors of semaphorins are plexins (Plex) and neuropilins (Nrps), and all are subdivided in subfamilies (Figure 1.1.2.5).

Plexins, neuropilins and semaphorins are extremely important, has by their discovery in diverse biological systems (Goshima et al., 2002): nervous (McCormick and Leipzig, 2012; Tillo et al., 2012), epithelial (Fujii et al., 2002; Miao et al., 1999), and immune systems (Kumanogoh and

Takamatsu, 2012) as well as diverse cell processes including angiogenesis (Serini et al., 2009), embryogenesis (Perälä et al., 2012), and cancer (Micucci et al., 2010; Potiron et al., 2009).

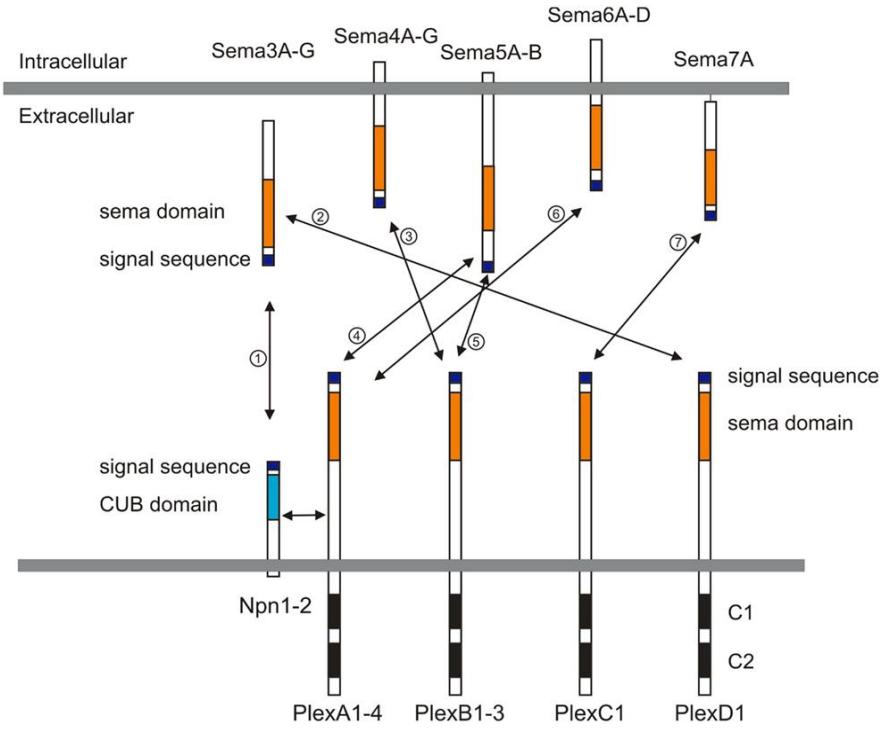

Figure 1.1.2.5. Semaphorins and their receptors, plexins and neuropilins, present in vertebrates.

Semaphorins are secreted (Sema3A-G), glycosylphosphatidylinositol (GPI)-anchored (Sema7), or transmembrane (Sema4A-G, Sema5A-B and Sema6A-D) family members. Neuropilins consist of two transmembrane molecules (Nrp1–2), and plexins consist of transmembrane A (1–4), B (1–3), C1, and D1 family members. Most class 3 semaphorins require an obligate neuropilin co-receptor. Sema3E binds to PlexD1 without neuropilins. Class 4 and 5 semaphorins interact with plexinBs. Class 6 semaphorins interact with plexinAs. Sema7A interacts with PlexC1. CUB indicates complement binding. One to seven indicate the interactions between semaphorins and their receptors; 1: class 3 semaphorins and neuropilin1/2, 2: Sema3E and PlexD1, 3: Sema4D and PlexB1/B2 or Sema4C/4G and PlexB1, 4: Sema5A/5B and PlexA1/A3, 5: Sema5A and PlexB3, 6: Sema6A/6B and PlexA2/A3 or Sema6C/6D and PlexA1, 7: Sema7A and PlexC1. Other sematherins classes (e.g. Class 8, viral semaphorin) are not here respresented, because they are absent in vertebrate (from Yoshida, 2012).

Plexins and semaphorins are transmembrane proteins that share a conserved extracellular semaphorin domain (Hota and Buck, 2012). The plexins and semaphorins are divided into four and eight subfamilies respectively based on their structural homology. Semaphorins are relatively small proteins containing the extracellular semaphorin domain and short intracellular tails. Plexins contain the semaphorin domain and long intracellular tails (Hota and Buck, 2012). The majority of plexin and semaphorin research has focused on the nervous system, particularly the developing nervous system, where these proteins are found to mediate many common neuronal cell processes including cell movement, cytoskeletal rearrangement, and signal transduction (Choi et al., 2008; Takamatsu et al., 2010).

Most class 3 semaphorins (Sema3) bind to Nrps. Plexin A family members associate to Nrps to transduce Sema3 signals across the neuronal membrane (Takahashi et al., 1999; Tamagnone et al., 1999) Sema3A and Nrp1 are known to play an important role in motor axon fasciculation and branching during embryogenesis (Behar et al., 1996; Gu et al., 2003; Kitsukawa et al., 1997; Taniguchi et al., 1997). Huber and colegueas have found that Sema3A regulates the timing motor axons ingrow to the limb (Huber et al., 2005).

Extensive studies to unravel the role of Sema3A, in the mouse neocortex, showed that Sema3A signaling is important for the developmental of axon and dendrites during development. Polleux and colleagues show that Sema3A repels axons but attracts dendrites in cortical neurons, so Sema3A promotes dendrite formation (Polleux et al., 2000). Quite recently, those findings were further proved by several studies (Nishiyama et al., 2011; Shelly et al., 2011). Sema3A signaling results in inhibition of PKA activity, and consequently to decreased activity of axon-promoting kinases. However, Sema3A knockout mice do not display defects in neuronal polarity, suggesting that alternative mechanism may also regulate axon and dendrite specification.

The TAOK2 protein

Thousand-and-one-aminoacids kinase 2 (TAOK2), a close relative of TAOK1, was first described the group of Melanie H. Cobb (Chen et al., 1999), and simultaneously by Moore and colleagues (Moore et al., 2000) under the name of PSK (Prostate-derived STE20-like kinase 1), as a member of the mitogen-activated protein kinase kinase kinase (MAP3K) family of signaling modules, ubiquitous to eukaryotic cell regulation.

The human *Taok*2 gene is encoded on the 16p11.2 chromosome, a genomic region associated with developmental and psychiatric disorders, where TAOK2 misregulation has been associated with Autism Spectrum Disorders (Battaglia et al., 2009; Tabet et al., 2012; Weiss et al., 2008), Depression (Degenhardt et al., 2012), Fragile X syndrome (Darnell et al., 2011), Schizophrenia (McCarthy et al., 2009) and Alzheimer Disease (Tavares et al., 2013). TAOK2 is subjected to alternative splicing to produce the TAOK2α (140KD) and TAOK2β (120KD) isoforms (Yasuda et al., 2007).

TAOK2 has a serine/threonine kinase domain present at the N-terminus, a long C-terminal domain composed of 690 residues, possibly containing a nucleotide binding site, a serine, proline and leucine-rich region, and an unbroken stretch of 17 glutamic acid residues (Chen et al., 1999). STE20-like kinases usually contain a small G protein binding consensus motif, not found at TAOK2 (Burbelo et al., 1995).

Moore and colleagues have identified TAOK2α as a MAP3K signaling molecule that selectively activates the c-Jun N terminal kinase mitogen activated protein kinase (JNK MAPK) pathway through the activation of MKK4 and MKK7 (MAP2Ks) and induces loss of actin stress fibers.

These data suggests a role in actin cytoskeleton organization, by coordinating such event TAOK2α most likely plays a role in the regulation of stress response and cell migration (Moore et al., 2000). Further microscopically studies show that TAOK2α staining in cells had tubulovesicular morphology, a clue that the kinase constitutively associates with vesicular compartments present in the cytoplasm. This specific morphological phenotype was only visible for the full-length protein, where a truncated version TAOK2α (1-349), constituted of kinase domain only, shows a diffusive cytoplasmic localization, showing the relevance of the unknown C-terminal domain to the regulatory pathway and function of TAOK2α in the cells.

TAOK2 was later shown to activate other signaling pathways, e.g. p38 and ERK family members (Chen et al., 1999, 2003), however those pathways are activated by the smaller isoform of TAOK2 – TAOK2β. TAOK2β endogenous activity is activated by the muscarinic agonist carbachol.

Several other studies reveal the involvement of TAOK2α in regulating cytoskeleton properties during stress-like conditions and demonstrate that TAOK2α colocalizes with microtubules (MTs) for their stabilization in a kinase independent fashion, producing stabilized perinuclear MTs with increased levels of acetylated α-tubulin (Chen and Cobb, 2001; Mitsopoulos et al., 2003). So it is possible that TAOK2α is responsible for the stability of actin, playing a major role in the dynamics of microtubules.

TAOK2α is sensitive to cleavage, removing the C-terminal domain (MTs binding domain), enabling the N-terminal catalytic region to relocate from the cytoplasm to the nucleus for the up regulation of apoptotic morphology (Moore et al., 2000; Zihni et al., 2007).

In *Drosophila melanogaster* a homologous protein of TAOK2 is present, Tao-1, that regulates dynamic interactions between growing MT plus ends and actin rich cortex, inhibiting MT growth when in contact with actin (Liu et al., 2010). This suggests a role of TAOK2 on actin-induced changes in MT dynamics directly. Such mechanisms are usually present for the regulation of cell shape and spindle centralization during mitosis.

1.1.3. Material and Methods

shRNA and fluorescent proteins.

The *Taok2* shRNA sequences used in this study are:

Taok2 shRNA 1 = CGAGAGGACTTGAATAAGAAA.

Taok2 shRNA 2 = GCATCCTAATACCATTCAGTA.

Taok2 shRNA 3 = GTTCCAGGAGACGTGTAAGATCC.

Taok2 shRNA 1 and 2 were primarily throughout the study. The *Taok2* shRNA 1-resistant construct (pCMV human *TAOK2*) is from imaGenes (Berlin, Germany), Clone: IRATp970E03140D. The sequence for the Nrp1 shRNA is: AGAGAAGCCAACCATTATA (Chen et al., 2008). The shRNAs sequences used in the experiments were inserted into a pSilencer vector. A pSilencer vector containing a random sequence hairpin insert was used as a control for the shRNAs. The Venus (pCAGIG) and mCherry (pCAGIG) plasmids were kindly provided by Dr. Z. Xie (Boston University). The F-GFP (pCAGIG-GAP 43-GFP) construct was a gift from Dr. A. Gartner (University of Leuven, Belgium). The Myc-TAOK2 (pCMV rat *TaoK2*) was kindly provided by Dr. M. H. Cobb (University of Texas Southwestern Medical Center). The Nrp1-mCherry (plasmid 21934) and the MKK7-JNK1 (Plasmid 19726) are from Addgene (Cambridge, MA).

Lentiviral production.

Production of plentilox3.7 *Taok2* shRNA

Taok2 shRNA was cloned into the plentilox 3.7 vector (Addgene plasmid 11795) as previously described (Mao et al., 2009). Briefly, complimentary 5' phosphorylated oligonucleotides FC_TAO2 sh3pllf and FC_TAO2 sh3pllr with the sequences: TGCGAGAGGACTTGAATAAGAAATTCAAGAGATTTCTTATTCAAGTCCTCTCGTTTTTTC; TCGAGAAAAAACGAGAGGACTTGAATAAGAAATCTCTTGAATTTCTTATTCAAGTCCTCTCG CA, respectively, were annealed, digested with XhoI, and ligated into the plentilox 3.7 vector that had been digested with HpaI and XhoI. Proper insertion and orientation of the sequence downstream of the U6 promoter was confirmed using a sequencing primer with the sequence CAGTGCAGGGGAAAGAATAGTAGAC.

Production and titration of virus.

Lentiviral particles were made as previously described (Mao et al., 2009). Briefly, HEK-293Tcells were plated on 10 cm dishes in 10% FBS-DMEM and transfected at 95% confluency with 8 µg plenti 3.7, 6ug pCMV-ΔR8.9, and 5 µg pCMV-VSV-G per dish. The culture medium was switched to 30% FBS DMEM 12 hours after transfection and viral supernatant was collected 48 and 96 hours later. Viral supernatant was filtered through a 0.45 µm cellular acetate vacuum filter (Corning 431155), and concentrated by ultracentrifugation at 25,000 x g for 90 minutes. Viral pellets were resuspended in DPBS+0.1% glucose and stored at - 80 °C. Viral titers were determined on HEK293T cells plated at 2x105 cells / well in 6-well plates, and serial dilutions of 1:200, 1:2000, and 1:20,000 were used to determine viral titer. After 48 hours of viral supernatant application, percentage of infected cells were determined by determining the percentage of fluorescent cells divided by the total number of cells by visual inspection. Four fields of view were counted per well, and three wells were inspected per dilution. Infection was performed with MOI =10.

Antibodies.

The following antibodies were used in these studies: mouse anti-acetylated tubulin (Sigma, immunocytochemistry, 1:1000), goat anti-TAOK2 (K-16, Santa Cruz Biotechnology, western blot (WB) 1:2000; immunocytochemistry, 1:100), rabbit anti-pTAOK2 (Ser 181; sc-135712; Santa Cruz Biotechnology, western blot (WB) 1:250; immunocytochemistry, 1:100), rabbit anti-pJNK1/2 (Promega, immunocytochemistry, 1:200) mouse anti-pJNK1/2 (Promega, immunocytochemistry, 1:200), mouse anti-pan-JNK (BD Transduction Laboratories; WB, 1:500); goat anti-rat Neuropilin-1 (R&D Systems, WB, 1:500) rabbit anti-FAK (clone C-20, Santa Cruz Biotechnology, WB, 1:500); anti-mCherry (Clontech Cat no: 632543, WB, 1:1000); anti-RFP (ABcam, ab62341, WB, 1:400); anti-actin (WB, 1:2000) and anti-GAPDH (WB, 1:500). Nucleic acid were visualized with Hoechst (Invitrogen) and F-actin with phalloidin (Molecular Probes). Alexa conjugated secondary antibodies (Jackson Immunoresearch, 1:1000) were applied for 1-2 hr at 25ºC.

Cell transfection and western blot analysis.

HEK293T and Ht22 cells (ATCC) were grown under standard cell culture conditions and transfected with plasmids using Lipofectamine 2000 according to the manufacturer's protocol (Invitrogen). Proteins from cell lysates were separated on 8% or 12% SDS-polyacrylamide gels at 60V and transferred onto Immobilon-P PVDF membranes (Millipore). Membranes were blocked in TBS-T (50 mM Tris-HCl pH 7.4, 150 mM NaCl, 0.1% Tween-20) with 5% non-fat dried milk for 1 h at room temperature and then incubated with primary antibody for 2 hours to overnight at 4 °C. Membranes were washed for 30 minutes in TBS-T and incubated for 1 hour at room temperature with horseradish peroxidase conjugated secondary antibodies (GE) and

then washed for 30 minutes in TBS28 T. Immunoreactivity signals were detected by enhanced chemiluminescence (Perkin Elmer).

Immunoprecipitation.

HEK293T cell lysates: For transient transfection, HEK293T cells were cotransfected with equal amounts of overexpression plasmids carrying myc-*Taok2* and *mCherry-Nrp1* cDNA. The total amount of transfected DNA was between 3.5 – 4.0 µg / 35 mm plate. The cells were allowed to express the constructs for 24 h before lysis and analysis. Transfected cells were washed once with ice-cold 1X PBS and immediately lysed in 1X lysis buffer with protease inhibitors. The Bio-Rad assay kit was used to determine protein concentration. For TAOK2 and Nrp1 immunoprecipitation assays, lysates were incubated with protein A sepharose conjugated to anti-mCherry antibodies overnight at 4 °C. Lysates containing 0.5 mg of protein were used for each condition. The beads were then washed with RIPA buffer twice to remove nonspecific proteins, and then washed 5 times with 1X lysis buffer before boiling in Laemmli sample buffer. Following SDS-PAGE to separate the proteins, blots were incubated with anti-TAOK2 antibodies.

Cortical brain lysates: cortices from P0 Swiss Webster mice were dissected and homogenized in 350 µl of sterile-filtered 50 mM Tris-Cl pH 7.4, 120 mM NaCl, 0.5% NP-40 containing proteinase inhibitors (Roche) using a 26G-syringe, followed by a 15 min centrifugation at 14000 rpm at 4 °C and the collection of the supernatant. Following a 60 minutes incubation with 1-2 µg of the corresponding antibodies, 20 µl of protein G Sepharose (GE Healthcare) was added to the lysates and incubated for 45 min at 4 °C. The bound immune complexes were then collected at 8000 rpm for 3 min followed by one wash each in sterile-filtered 50 mM Tris-Cl, pH 7.4, 500 mM NaCl, 1% NP-40, and sterile-filtered 50 mM Tris-Cl pH 7.4, 120mM NaCl, 0.5% NP-40. Samples were boiled for 5 min at 95 °C, run on a 10% SDS gel and analyzed with the same primary antibodies used for the immunoprecipitation.

Cortical cultures.

Neurons were transfected by *in utero* electroporation at E15 and the transfected cortices were dissected two days later. Cortical neurons were isolated in 1X HBSS (Invitrogen) containing papain and DNase at 37 °C (Worthington). Papain was inhibited by the addition of ovomucoid (Worthington). Neurons were plated on poly-D-lysine and laminin pre-coated glass coverslips in Neurobasal / B27 medium (Invitrogen), maintained in culture for 48 hr, and then fixed for immunofluorescent analysis. Neurons treated with Sema3A were dissected from brains harvested at E17 and cultured as above. Sema3A (R&D Systems) was applied 48 hr later at a final concentration of 2 µg/ml. Cells were fixed as described, for immunofluorescence studies, or lysed with cold RIPA buffer supplemented with phosphatase and protease inhibitors (Roche) for western blot analysis.

Quantitative immunofluorescence of pTAO2, pJNK, tubulin, and MAP2 in neuritis of cultured cortical neurons.

Neurons were cultured for 2 DIV and 7 DIV after plating and then fixed as described (see *immunofluorescence*). pTAO2, pJNK, tubulin, and MAP2 were visualized by indirect immunofluorescence. The mean intensity gray value of a line drew along the neurites was measured using ImageJ.

Sholl analysis.

All GFP-positive image stacks from transfected cortical neurons were taken as described (see *Confocal imaging*). All Sholl analyses use cortices that displayed relatively low transfection efficiencies in order to be able to select and analyze isolated transfected neurons in the cortex. Sholl analysis was performed by drawing concentric circles centered on the cell soma using Adobe Illustrator CS3. The starting radius was 15 µm and the ending radius was 55-100 µm; the interval between consecutive radii was 5 µm. All analyses were performed blindly.

***In utero* electroporation.**

The Institutional Animal Care and Use Committee of Massahusetts Institute of Technology approved all experiments. Pregnant Swiss Webster mice were anesthetized by intraperitoneal injection of Ketamine 1% / Xilazine 2 mg/mL (0,01 µl/g body weight), the uterine horns were exposed, and plasmids mixed with Fast Green (Sigma) were microinjected into the lateral ventricles of embryos. The shRNA plasmid concentration was 2 to 3-fold higher than that of mCherry, Venus, or F-GFP. Five current pulses (50 ms pulse / 950 ms interval; 35-36V) were delivered across the head of the embryo.

Immunofluorescence.

Dissociated neurons: Neurons were fixed with 4% formaldehyde (FA) at 37 °C for 2 min followed by fixation for 3 min in methanol at -20 °C. After blocking in goat serum (Zymed), neurons were incubated with the primary antibodies. *Cortical sections*: Brains were removed and fixed overnight in 4% FA and thereafter transferred to 30% sucrose/PBS (4 °C, overnight). Brains were embedded in OCT compound and sectioned in a cryostat. The 20-30 µm cryosections were incubated overnight at 4 °C with the primary antibodies.

Confocal imaging.

Images were taken with a Zeiss LSM 510 confocal microscope. Z-series images were collected with 1 µm steps. To perform 3D reconstructions on stacks of images of transfected cells, only Z sections in the same focal plane as GFP were used for analysis and for producing figures. 3D reconstructions and Z-stack analyses were produced using ImageJ software. The adjustment of brightness and contrast was performed on images.

Quantitative phalloidin-fluorescence determination in growth cones.

Neurons were cultured for 2DIV after plating and then fixed as described above (see immunofluorescence). F-actin was visualized by the binding of fluorescentlylabeled phalloidin. The mean intensity gray value of phalloidin in the growth cone area was measured using ImageJ.

Organotypic slice cultures.

Mouse embryos were electroporated at embryonic day 15 (E15), and acute coronal brain slices (240 µm) were prepared at E17 and E18 (at which time TAOK2 was downregulated via shRNA). Slices were transferred onto slice culture inserts (Millicell) in cell culture dishes (35 × 10 mm; Corning) with Neurobasal medium (Invitrogen) containing the following: B27 (1%), glutamine (1%), penicillin/streptomycin (1%), horse serum (5%), and N2 (1%). Slices were used for imaging (1–2 h after slicing) or for pharmacological treatments (incubated at 37°C in 5% CO_2, for 1–2 d).

Time-lapse imaging.

GFP- and RFP-positive cells were imaged on an inverted Nikon microscope (TE 2000-S) with a 20× objective lens [numerical aperture (NA) 0.45]. During the time-lapse imaging, slices were kept in an acrylic chamber at 37°C in 5% CO_2. We captured time-lapse images with a CoolSNAP EZ camera (Roper Scientific) using NIS-Elements software (Nikon).

Statistical analysis.

Compiled data are expressed as mean ± SEM. We used the two-tailed Student's *t* test and one-way ANOVA, with posthoc Tukey or Dunnett tests, for statistical analyses. The *P* values in the Results are from *t* tests unless specified otherwise. $P<0.05$ was considered statistically significant.

1.1.4. Results and Discussion

Expression profile of TAOK2 in cultured cortical neurons and in the developing cerebral cortex.

To examine the subcellular expression profile of TAOK2, we analyzed TAOK2 immunoreactivity in cultured cortical mouse neurons dissociated at embryonic day 17 (E17).

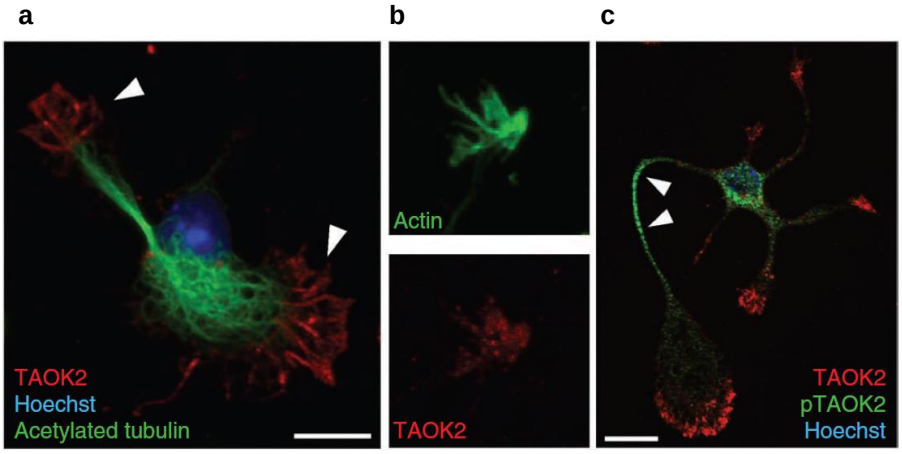

Figure 1.1.4.1. Distribution of TAOK2 and activated TAOK2 (pTAOK2) in cultured neurons.

(**a**) TAOK2 localizes to the growth cones (white arrowheads) of isolated cortical neurons. (**b**) TAOK2 (red) co-localizes with actin (green) in growth cones. (**c**) Activated TAOK2 (pTAOK2; green) localizes to the neurite shaft of isolated cortical neurons. Scale bar: 10 µm (a), 200 µm(c).

We found that TAOK2 preferentially localized to growth cones (Figure 1.1.4.1a, b). The growth cone is a region where actin, but not microtubules, accumulates (Figure 1.1.4.1b) and where the actin cytoskeleton is the most dynamic (Bradke and Dotti, 1999). In contrast, TAOK2 activated by phosphorylation on Ser 181 (pTAOK2) localizes to the neurite shaft, where microtubules also accumulate (Figure 1.1.4.1c). This pattern of TAOK2 expression suggests that TAOK2 may act as a coordinator of actin and microtubule dynamics (King et al., 2011).

In the mouse brain, TAOK2 and pTAOK2 are preferentially expressed in the intermediate zone (IZ) and the cortical plate (CP) of the developing cortex (E18), and their expression in the ventricular zone (VZ) is low (Figure 1.1.4.2).

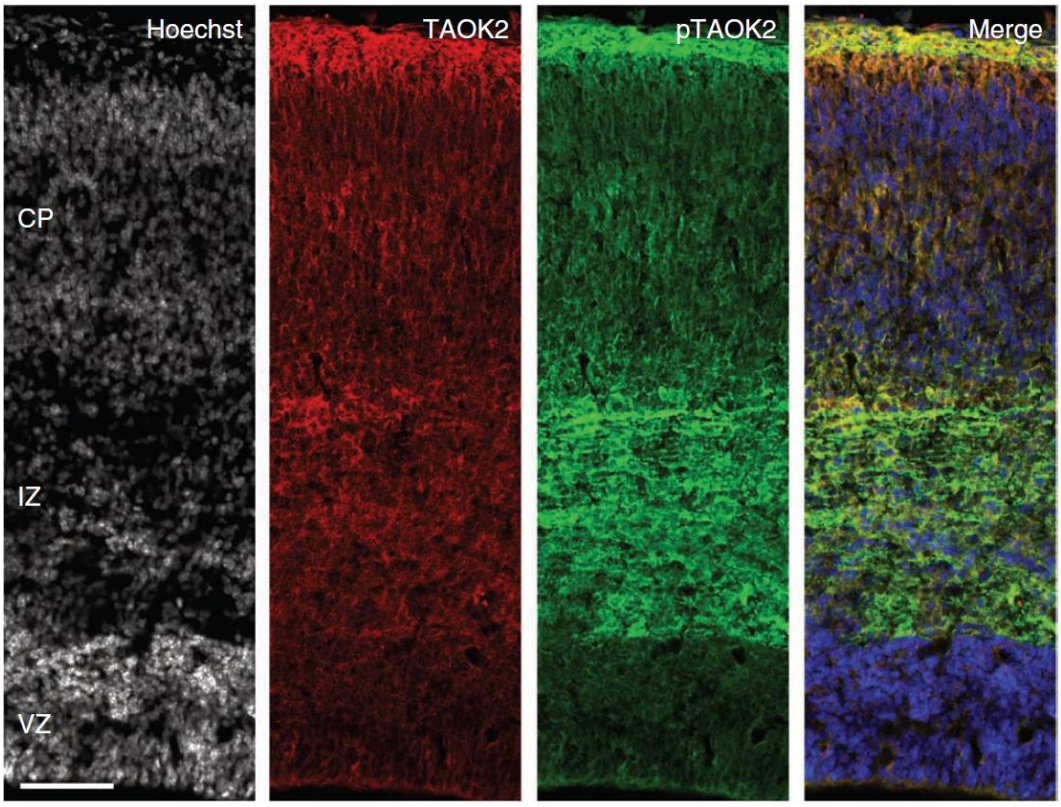

Figure 1.1.4.2. Distribution of TAOK2 and activated TAOK2 in the developing cerebral cortex.

TAOK2 and pTAOK2 are preferentially expressed in the IZ and CP of the developing cortex (E18). Scale bar: 200 µm.

Western blot analysis using whole-cell extracts from the cortices of mice at different embryonic and postnatal ages demonstrates that the long isoform of TAOK2 (TAOK2α; 140 KD) is expressed throughout the early cortical embryonic development. However, in perinatal (E19, P0) and adult mice, the TAOK2α isoform was considerably increased in expression. In contrast, the short isoform of TAOK2 (TAOK2β; 120KD) was only observed perinatally and in the adult brain (Figure 1.1.4.3).

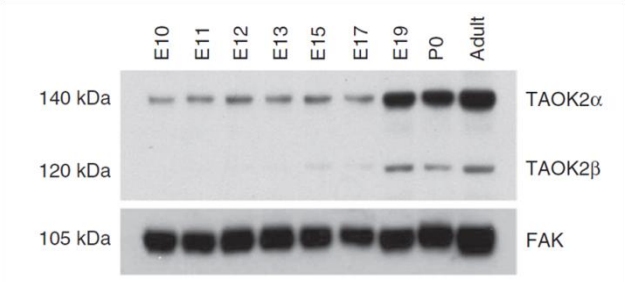

Figure 1.1.4.3. Distribution of TAOK2 in the early cortical embryonic mouse brain.

Western blotting reveals that TAOK2α expression levels are constant during early cortical embryonic development, but increase considerably at perinatal (E19, P0) and adult time points. The TAOK2β isoform is absent prior to E19.

In addition, in freshly cultured (DIV2) E17 cortical neurons, we detected expression of TAOK2α, but not TAOK2β, by immunoblot analysis (data not shown). These results suggest that TAOK2α is likely to be the TAOK2 isoform most important for neuronal differentiation. We therefore focused our subsequent studies on TAOK2α. Therefore, for the remaining of the chapter, TAOK2 will be referring to TAOK2α, unless is otherwise stated.

TAOK2 impacts neuronal differentiation in cultured cortical neurons.

The remodeling of the actin-based cytoskeleton is an important regulatory step in axon and dendrite formation (Arimura and Kaibuchi, 2007; Barnes et al., 2008; Witte and Bradke, 2008). Since it has been shown that TAOK2 modulates the organization of the actin cytoskeleton in non-neuronal cells (Chen et al., 1999), and we find that TAOK2 expression is concentrated in actin-rich structures, it was asked whether TAOK2 loss-of- and gain-of-function affects neuronal differentiation. To examine the role of TAOK2 in brain development, three specific short-hairpin (sh)RNAs were designed, targeting different coding sequences of TAOK2, to acutely knock down the expression of TAOK2. The specificity of our shRNA constructs with respect to their ability to down-regulate endogenous neuronal TAOK2 was confirmed by immunohistochemistry (Figure 1.1.4.4a-d, and data not shown for shRNA 3). To this end, isolated cortical neurons at E17 from embryos were transfected by *in utero* electroporation at E15 with constructs expressing *Taok2* shRNA- or control shRNA and membrane-bound GFP (F-GFP). Neurons were cultured for 48 hr before being processed for immunocytochemistry using antibodies against TAOK2 and acetylated tubulin (Figure 1.1.4.4a-d). Additionally, the specificity of our shRNA constructs was assessed for their ability to down-regulate endogenous TAOK2 by western blot analysis in Ht22 cells (Figure 1.1.4.4e, f, and data not shown for shRNA 3). These experiments show that *Taok2* shRNAs efficiently down-regulate TAOK2 expression. shRNAs 1 and 2 were used for all subsequent experiments.

At first, the impact of TAOK2 knockdown on the cytoskeleton and growth cone morphology was examined in primary neurons. The shRNA-mediated knockdown of TAOK2 decreased the F-actin content in the growth cones of cultured cortical neurons (Figure 1.1.4.5a, b; control, n=44 cells from three different cultures; *Taok2* shRNA 1: n=43 cells from three different cultures; *Taok2* shRNA2: n=36 cells from 2 different cultures; $P<0.0001$ by one-way ANOVA and posthoc Dunnett test $^{**}P<0.01$), and the number of intact (non-collapsed) growth cones per neuron, compared with control transfected neurons (Figure 1.1.4.5a, c; control: n=160 cells from three different cultures; *Taok2* shRNA 1: n=133 cells from three different cultures; *Taok2* shRNA 2: n=36 cells from two different cultures; $P<0.0001$ by one-way ANOVA and posthoc Dunnett test $^{**}P<0.01$).

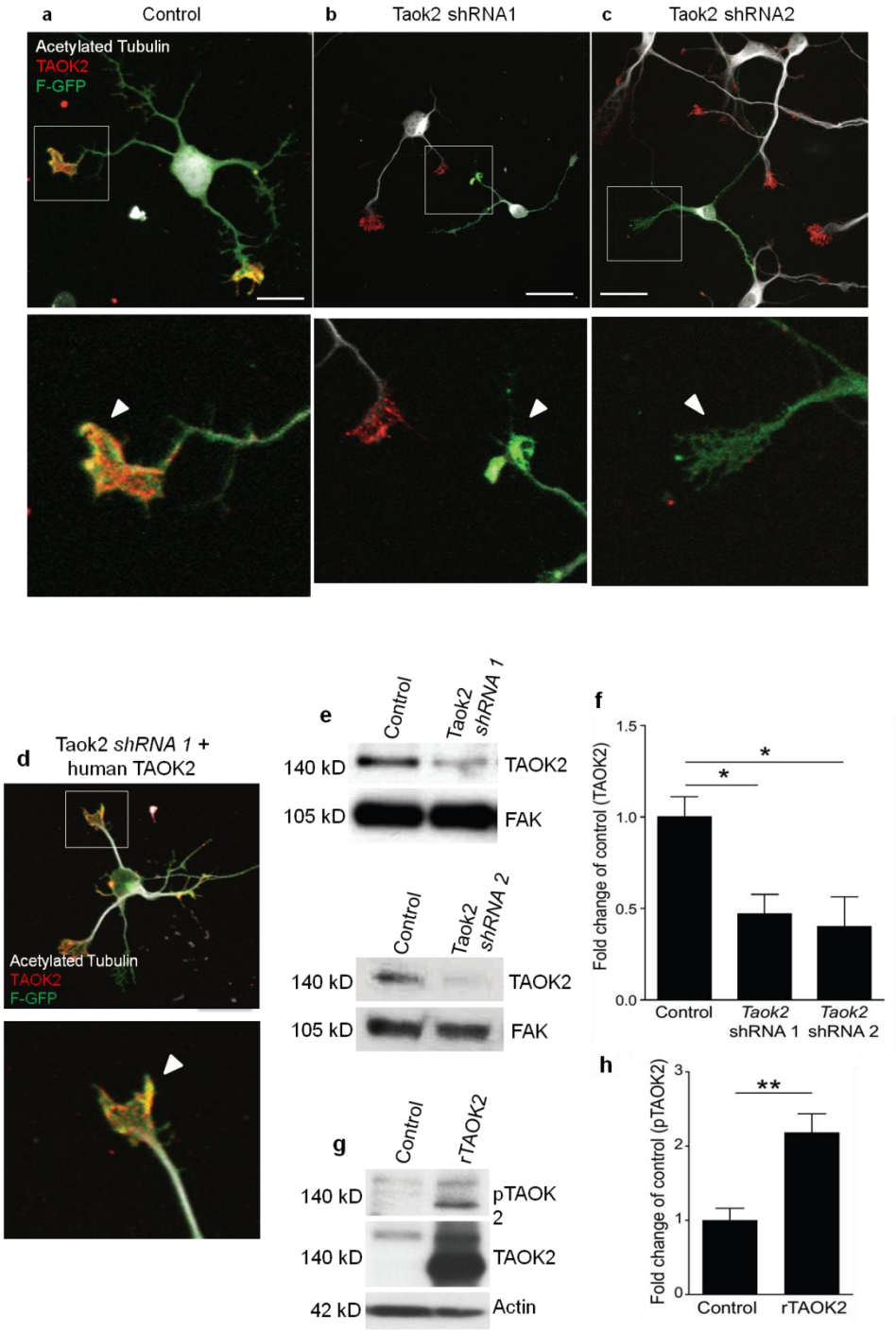

Figure 1.1.4.4. *Taok2* shRNA's specifically down-regulate TAOK2 expression in dissociated cortical neurons and Ht22 cells.

(a) Representative control transfected neuron. Inset: TAOK2 immunoreactivity is enriched in growth cones. (b-c) TAOK2 down-regulation with two different shRNAs reduces TAOK2 immunoreactivity in the growth cones of shRNA-transfected cells (inset, white arrowheads). (d) The expression of shRNA-resistant human TAOK2 cDNA is detected in growth cones by immunofluorescence in cultured neurons expressing *Taok2* shRNA1 (right panel, inset). (e) Western blot of extracts from Ht22 cells transfected with control plasmid and *Taok2* shRNA 1 and 2. Blots were probed with antibodies against TAOK2. (f) Quantification of the TAOK2 signal from lysates of Ht22 cells. *Taok2* shRNA 1 and 2 decreases endogenous TAOK2 immunoreactivity (*P=0.02 by one-way ANOVA, posthoc Dunnett test *P <0.05, n=3 experiments). (g, h) rTAOK2 overexpression in Ht22 cells increases levels of active TAOK2 (pTAOK2). (g) rTAOK2 overexpression produces doublets (Moore et al., 2000; Zihni et al., 2007) and increases levels of pTAOK2. (h) Quantification of the pTAOK2 upper band signal (~ 140 kDa; **P = 0.0084 by t test, n = 3). Mean ± s.e.m. Scale bar: 10 µm.

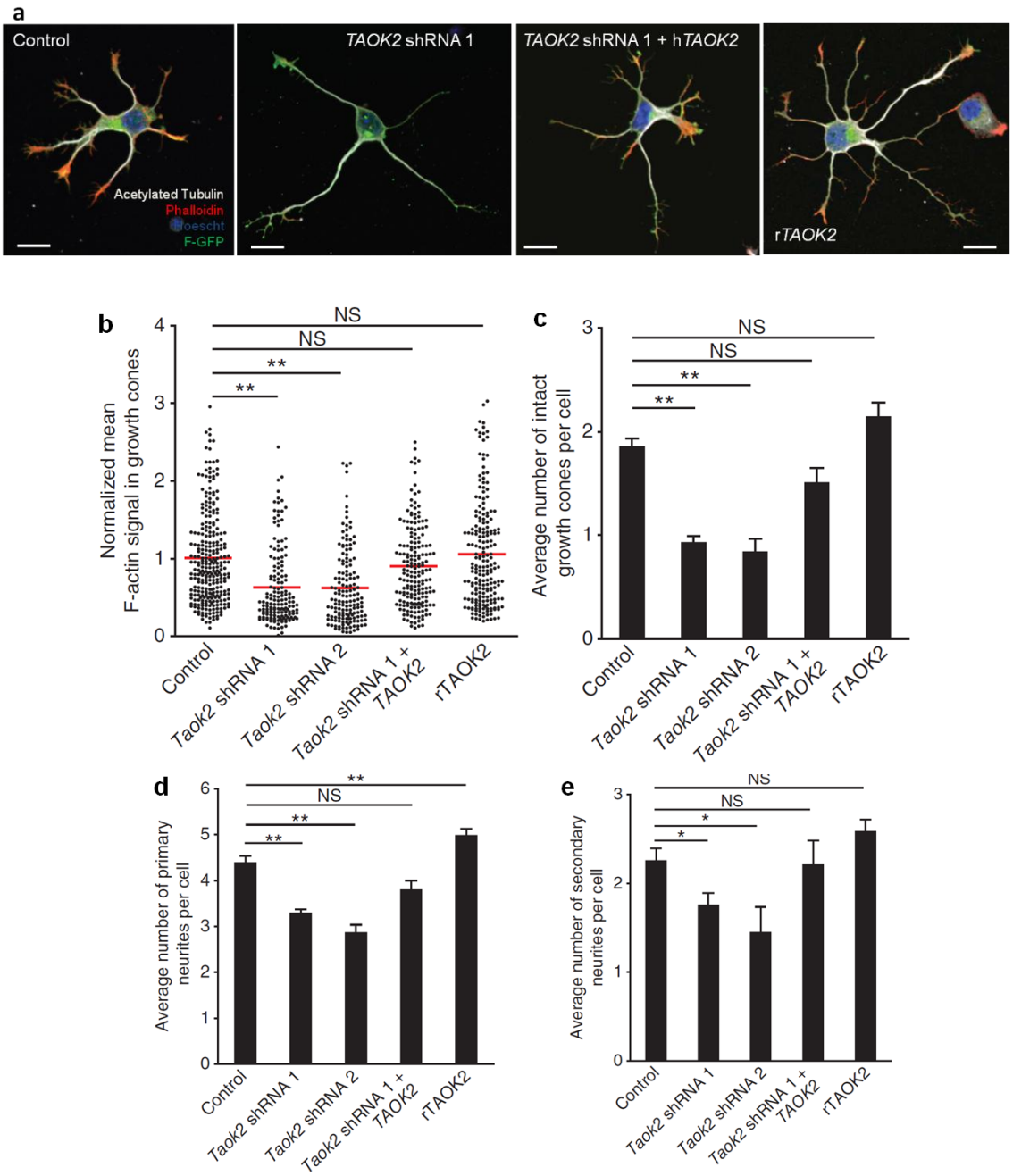

Figure 1.1.4.5. TAOK2 down-regulation or overexpression affects the differentiation of isolated cortical neurons.

(a) TAOK2 down-regulation and overexpression have opposite effects in the complexity of cortical neurons. Control neurons were transfected with F-GFP and labeled with phalloidin (actin), anti-acetylated tubulin, and Hoechst (DNA). *Taok2* shRNA-transfected neurons display fewer branched neurites, with collapsed growth cones. Expression of a shRNA-resistant human TAOK2 cDNA (hTAOK2) counteracts TAOK2 downregulation in dissociated cortical neurons. Rat (r)TAOK2 overexpression increases neuronal complexity with more primary neurites. (b) Quantification of F-actin content in growth cones of cultured neurons. TAOK2 silencing decreased the levels of F-actin in growth cones. (c) Quantification of the number of intact (noncollapsed) growth cones per transfected cell. TAOK2 silencing decreased the number of intact growth cones per cell. (d, e) TAOK2 down-regulation decreases the number of primary and secondary neurites per transfected cell. TAOK2 overexpression increases the number of primary neurites. Scale bar: 10 μm. *p < 0.05, **p < 0.01.

In addition, TAOK2 down-regulation decreased the number of neurites per neuron (Figure 1.1.4.5a, d; control: n=168 cells from three different cultures; *Taok2* shRNA 1: n=149 cells from three different cultures; *Taok2* shRNA 2: n=36 cells from two different cultures; $P<0.0001$ by one-way ANOVA and posthoc Dunnett test $^{**}P<0.01$) and the number of secondary branches per cell, compared with control transfected neurons (Figure 1.1.4.5a, e; $P=0.0102$ by one-way ANOVA and posthoc Dunnett test $^{*}P<0.05$).

TAOK2 autophosphorylation is known to play a role in TAOK2 activation (Chen et al., 1999; Zihni et al., 2007), thus the overexpression of TAOK2 increases levels of phosphorylated, active TAOK2 (Figure 1.1.4.4g, h). TAOK2 overexpression in cultured cortical neurons increased the number of primary, but not secondary, neuritis compared with control neurons (Figure 1.1.4.5a, d; rTAOK2: n=119 cells from three different cultures; $P<0.0001$ by one-way ANOVA and posthoc Dunnett test $^{**}P<0.01$).

In addition, it was analyzed whether TAOK2 down-regulation or overexpression affects polarization in cultured neurons. TAOK2 downregulation impaired axon formation (Figure 1.1.4.6a; control: 57.57 ± 7.68% of neurons with a neurite longer than 40 µm, n=168 cells from three different cultures; *Taok2* shRNA 1: 29.69 ± 4.3% of neurons with a neurite longer than 40 µm, n=149 cells from three different cultures; $P=0.0044$ by one-way ANOVA and posthoc Dunnett test $^{*}P<0.05$). Interestingly, TAOK2 overexpression did not affect the number of polarized (axon-bearing) neurons (Figure 1.1.4.6a), but did increase the proportion of neurons that elaborated multiple axons (Figure 1.1.4.6b, c; control: 2.22 ± 1.42% of neurons with multiple neurites longer than 40 µm, n=168 cells from three different cultures; rTAOK2: 15.84 ± 3.79 % of neurons with multiple neurites longer than 40 µm, n=119 cells from three different cultures; $^{*}P=0.0386$ by *t* test).

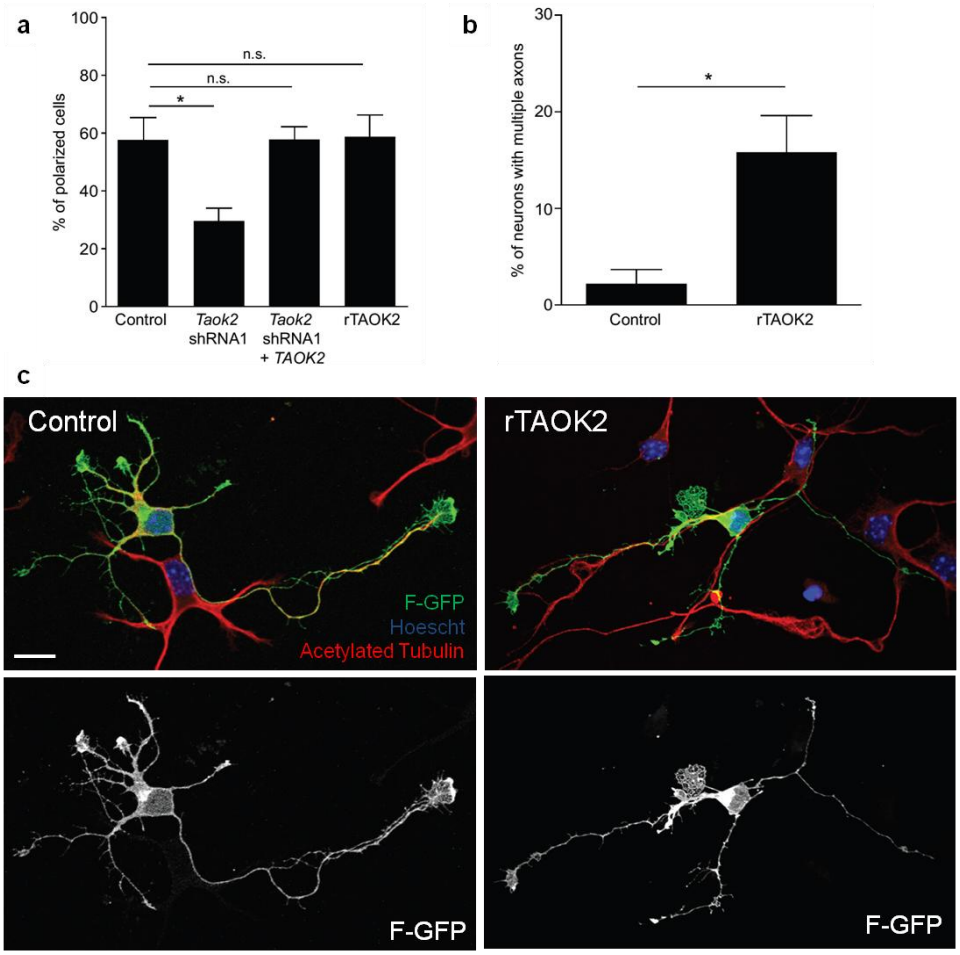

Figure 1.1.4.6. TAOK2 down-regulation or overexpression affects axon elongation of isolated cortical neurons.

(a) TAOK2 down-regulation decreases the number of neurons that elongate an axon (control: 57.57 ± 7.68% of neurons with a neurite longer than 40 µm, n=168 cells from three different cultures; *Taok2* shRNA 1: 29.69 ± 4.3% of neurons with a neurite longer than 40 µm, n=149 cells from three different cultures; *Taok2* shRNA 1 + *TAOK2*: n=48 cells from three different cultures; P=0.0044 by one-way ANOVA and posthoc Dunnett test *P <0.05). (b, c) rTAOK2 overexpression increases the number of neurons with multiple axons (control: 2.22 ± 1.42% of neurons with multiple neurites longer than 40 µm, n=168 cells from three different cultures; rTAOK2: 15.84 ± 3.79 % of neurons with multiple neurites longer than 40 µm, n=119 cells from three different cultures; *P=0.0386 by t test). Mean ± s.e.m. Scale bar: 10 µm.

To determine if these phenotypes resulted specifically from the down-regulation of TAOK2, *Taok2* shRNA1 was co-expressed with a shRNA resistant version of TAOK2 cDNA (*h*TAOK2), which rescued the *Taok2* shRNA1 phenotypes. This molecular replacement experiment further demonstrates the specificity of *Taok2* shRNA1 treatment (Figure 1.1.4.5a-e and Figure 1.1.4.6a; n=48 cells from three different cultures). Together, these data demonstrate that TAOK2 is critical for the morphological differentiation of cultured cortical neurons.

TAOK2 affects basal dendrite formation and axon elongation in vivo.

The previous results (Figure 1.1.4.5 and Figure 1.1.4.6) demonstrate the impact of TAOK2 upon the differentiation of cultured primary cortical neurons. We then sought to determine the effect of TAOK2 in the post-migratory differentiation of cortical neurons *in vivo*. E15 mouse embryos were *in utero* electroporated with *Taok2* shRNA, control shRNA, or rTAOK2 (rat *TAOK2* cDNA) plasmids together with F-GFP. Mice were sacrificed at postnatal day 7 (P7), and the dendritic morphology of control, *Taok2* shRNA, and rTAOK2-expressing neurons was evaluated. It was found that both the knockdown and overexpression of TAOK2 disrupted cortical neuronal differentiation *in vivo*. In layer II-III of the *in utero* electroporated brains, the *Taok2* shRNA-transfected neurons had significantly fewer primary dendrites compared to controls (Figure 1.1.4.7a, b; control: n=19 cells from three brains; *Taok2* shRNA 1: n=23 cells from three brains; *Taok2* shRNA 2: n=20 cells from two brains; $P<0.0001$ by one-way ANOVA and posthoc Dunnett test $^{**}P<0.01$). TAOK2 overexpression, on the other hand, increased the number of primary dendrites (Figure 1.1.4.7a, b; rTAOK2: n=31 cell from three brains).

Sholl analysis of the dendritic arbors from shRNA-transfected neurons revealed that TAOK2 down-regulation produced less complex basal dendritic arbors than control shRNA transfection. *Taok2* shRNA-transfected neurons had significantly fewer dendritic processes with intersections at a distance between 15 µm and 55 µm from the cell soma (Figure 1.1.4.7c; $P<0.0001$ by one-way ANOVA and posthoc Dunnett test $^{**}P<0.01$). In contrast, TAOK2 overexpression increased the complexity of the basal dendritic arbor compared to control-transfected neurons (Figure 1.1.4.7c; $P<0.0001$ by one-way ANOVA and posthoc Dunnett test $^{*}P<0.05$). Importantly, Sholl analysis demonstrated that TAOK2 down-regulation or TAOK2 overexpression did not affect the apical dendrites of transfected neurons (Figure 1.1.4.7d; Figure 1.1.4.8a).

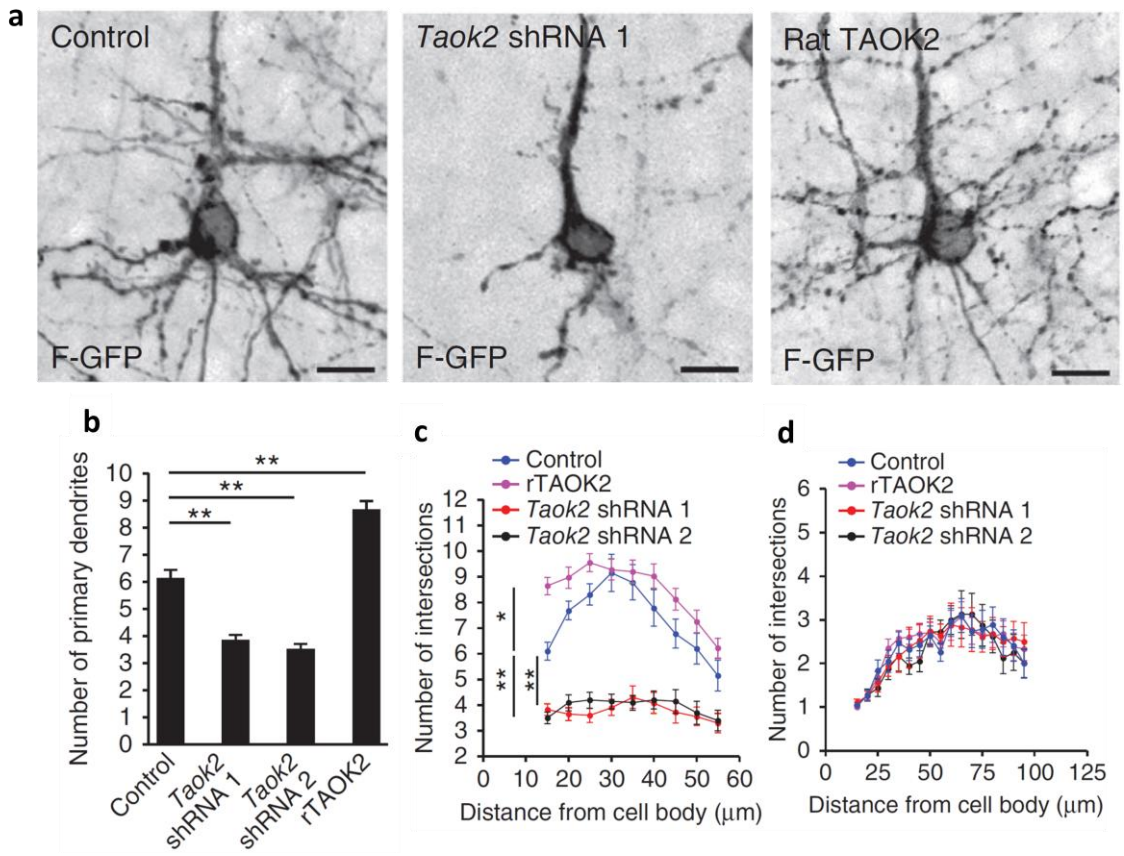

Figure 1.1.4.7. TAOK2 down-regulation or overexpression affects basal dendrite arborization in layer V neurons in the developing cortex.

(a) TAOK2 knockdown or up-regulation have opposite effects in basal dendrite development *in vivo*. (b) The number of primary dendrites decreases following TAOK2 knockdown and increases following rTAOK2 overexpression. (c) Sholl analysis of the dendritic arbor from upper cortical layer transfected neurons reveals significantly fewer and more dendritic process intersections at a distance between 15 µm and 55 µm from the cell soma in the TAOK2-silenced neurons or rTAOK2-overexpressed neurons, respectively, compared with control transfected neurons. (d) Sholl analysis of the apical dendrite does not show any differences between *Taok2* shRNA-mediated down-regulation, rTAOK2 overexpression, and control conditions. Scale bar: 10 µm (a). *P < 0.05, **P < 0.01.

To determine if the basal dendrite phenotype was exclusive to upper-layer neurons, or was a more general feature of pyramidal neurons in the different cortical layers, TAOK2 expression was knocked-down in deeper layer neurons (layer V) by *in utero* electroporating E13 embryos with *Taok2* shRNA or control shRNA plasmids together with F-GFP. Animals were harvested at P4 to evaluate the dendritic morphology of transfected neurons in layer V. TAOK2 downregulation using either shRNA 1 or 2 also impaired the basal dendrite complexity of layer V pyramidal neurons (Figure 1.1.4.8b, c; control: n=32 cells from three brains; *Taok2* shRNA 1: n=37 cells from three brains; *Taok2* shRNA 2: n=20 cells from two brains; *P*<0.0001 by one-way ANOVA and posthoc Dunnett test ***P* <0.01), without affecting apical dendrite complexity (Figure 1.1.4.8d). These findings demonstrate that TAOK2 loss-of- or gain-of-function impairs pyramidal neuron basal dendrite formation in the developing neocortex.

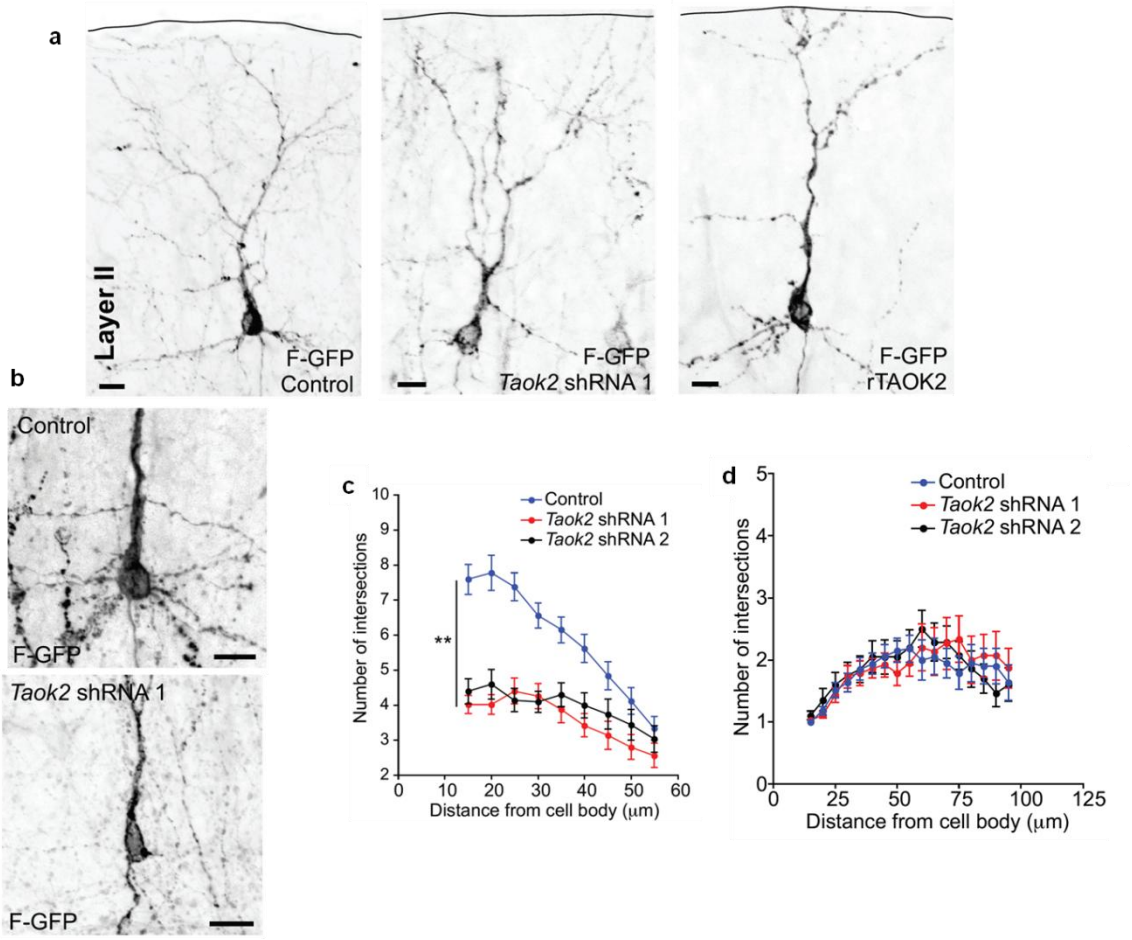

Figure 1.1.4.8. TAOK2 down-regulation or overexpression affects basal dendrite arborization in layer II-III neurons in the developing cortex.

(a) Neurons with TAOK2 down-regulation or overexpression in the upper cortical layers (layers II-III) develop apical dendrites that are similar to those from controltransfected neurons. (b) Lower cortical layer (layer V)-transfected neurons show underdeveloped basal dendrites following the shRNA-mediated knockdown of TAOK2 expression compared to control-transfected neurons. (c) Sholl analysis of the dendritic arbors of layer V neurons show significant differences between *Taok2* shRNA expressing neurons and control neurons at a distance between 15 µm and 55 µm from the cell soma (control: n=32 cells from three brains; *Taok2* shRNA 1: n=37 cells from three brains; *Taok2* shRNA 2: n=20 cells from two brains; P<0.0001 by one-way ANOVA, posthoc Dunnett test **P <0.01). (d) Apical dendrites from layer V transfected neurons are not affected following TAOK2 down-regulation. Scale bar: 10 µm (a, b).

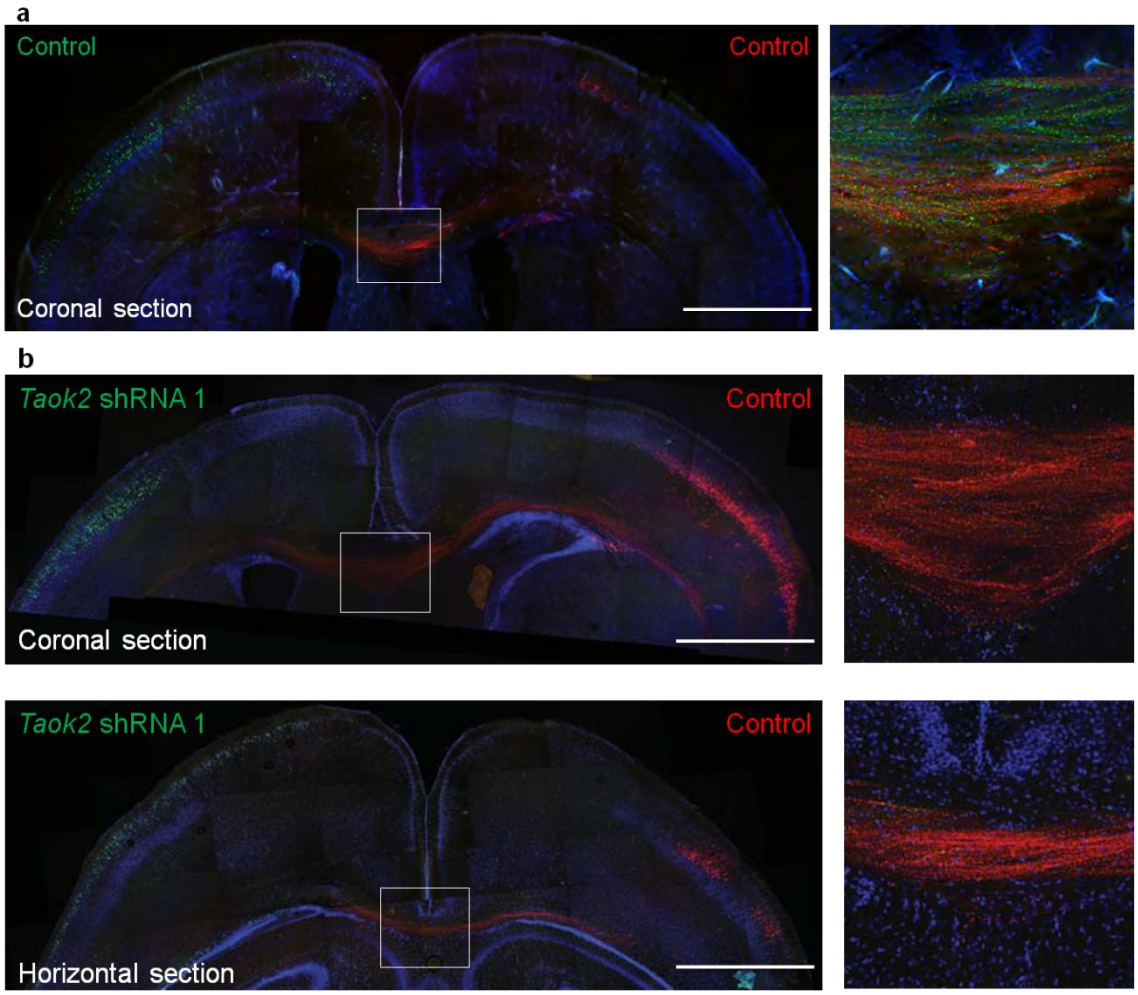

Figure 1.1.4.9. TAOK2 down-regulation affects callosal axon projection in the developing cortex.

(a, b) *Taok2* shRNA-mediated down-regulation diminishes the number of callosal axons traversing the midline. (a) Control transfected neurons in both hemispheres (Venus: left hemisphere; mCherry: right hemisphere) project callosal axons that crossed the midline. Right panel: inset of the corpus callosum. (b) *Taok2* shRNA-mediated knock-down in Venus-positive neurons prevents axons from these cells from crossing the midline, However, control transfected neurons positive for mCherry, from the contralateral hemisphere, project axons that cross the midline. Upper panel: coronal brain section. Lower panel: horizontal brain section. Right panels: inset of the corpus callosum from the coronal (upper panel) and horizontal section (lower panel). Scale bar: 500 μm (a, b).

We also estimated the contribution of TAOK2 to axon elongation during brain development. A sequential *in utero* transfection was performed, as previously reported (de Anda et al., 2010). mCherry expression and control shRNA constructs were introduced into E15 mouse cortex, followed by the introduction of a *Taok2* shRNA and a Venus-expressing constructs into the contra-lateral hemisphere. Callosal axons from transfected neurons crossing into the midline were examined at P7. TAOK2 down-regulation impaired axon elongation and axons were absent in the midline (Figure 1.1.4.9a, b; n=3 brains analyzed, per condition). On the other hand, TAOK2 overexpression caused some transfected axons to deviate from the axonal tract (Figure 1.1.4.10, black arrowheads). These results strongly support the role of TAOK2 in axon elongation in the mouse *in vivo*, as was previously reported in *Drosophila* (King et al., 2011).

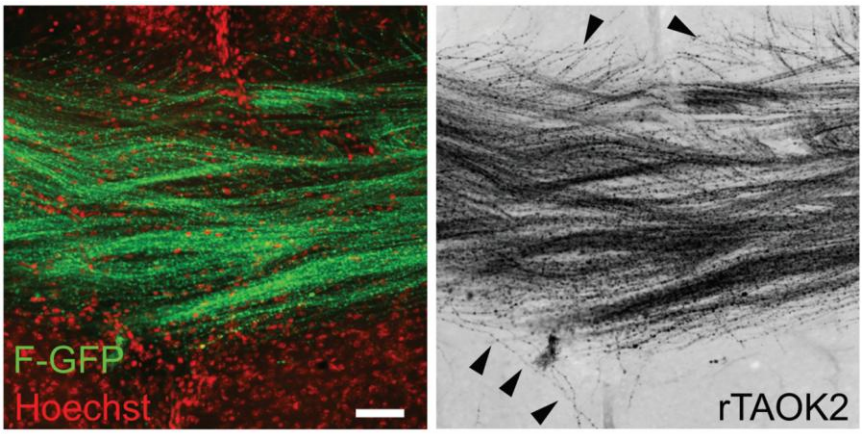

Figure 1.1.4.10. TAOK2 overexpression affects axonal projection at the corpus callosum in the developing cortex.

rTAOK2 overexpression produces minor defects in axons crossing the corpus callosum. Some transfected axons deviate from the axonal tract (arrowheads). Mean ± s.e.m. Scale bar: 100 µm.

TAOK2 interacts with the Neuropilin 1 receptor to modulate neuronal differentiation.

Previous studies have shown that the Sema3A – Nrp1/PlexinA4 signaling cascade controls basal dendritic arborization (Chen et al., 2008; Gu et al., 2003; Tran et al., 2009). *Nrp1*$^{Sema-}$ mice also develop axonal projection defects in the corpus callosum and the hippocampus (Gu et al., 2003). These defects vary from mild, in which some axons deviate from the axonal tract, to more severe phenotypes, where callosal axons defasciculate and do not cross the midline (Gu et al., 2003). We hypothesized that TAOK2 may collaborate with this pathway to modulate neuronal differentiation. To test this idea, coimmunoprecipitation experiments were performed to probe for an interaction between TAOK2 and Nrp1. TAOK2 and Nrp1-mCherry were co-expressed in HEK293 cells and it was found that TAOK2 interacts with Nrp1-mCherry (Figure 1.1.4.11a).

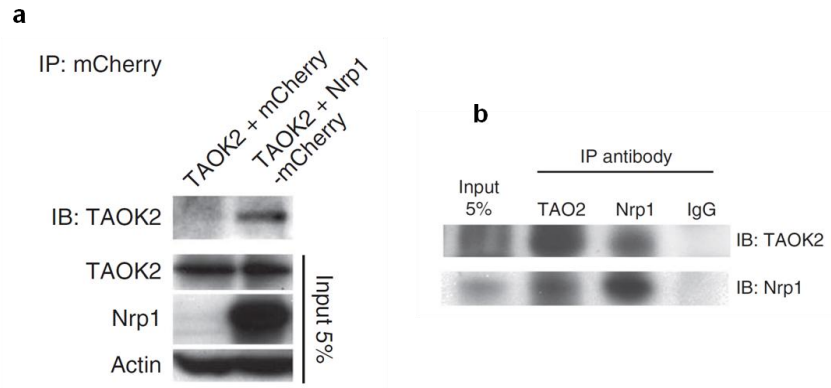

Figure 1.1.4.11. TAOK2 interacts with Nrp1.

(a) Immunoprecipitation with anti-mCherry antibodies demonstrates the interaction of Nrp1 and TAOK2. HEK293T cells were transfected with Nrp1- mCherry and Myc-TAOK2. The input lane represents 5% of the total protein quantity used for immunoprecipitation. (b) TAOK2 co-immunoprecipitates with Nrp1 in the developing cortex. P0 mouse cortical lysates were subjected to immunoprecipitation with anti-Nrp1 or anti-TAOK2 antibodies, and membranes were immunoblotted with anti-TAOK2 and anti-Nrp1 antibodies. The input lane represents 5% of the total protein quantity used for immunoprecipitation.

To investigate whether this complex also forms *in vivo*, cortices from P0 mice were homogenized and subjected to co-immunoprecipitation using antibodies against Nrp1 and TAOK2. Nrp1 was found to associate with TAOK2 in lysates from P0 mouse cortices (Figure 1.1.4.11b). TAOK2 is activated by phosphorylation on Ser 181, which resides in the activation loop of the kinase (Zhou et al., 2004). To determine whether Sema3A/Nrp1 activates TAOK2, we examined whether active TAOK2 (pTAOK2) co-localizes with Nrp1. In the mouse E19 cerebral wall, we found that pTAOK2 and Nrp1 co-localized preferentially in the IZ and lower CP, where axons elongate and deeper layer neurons begin to form dendrites (Romand et al., 2011) (Figure 1.1.4.12a, b).

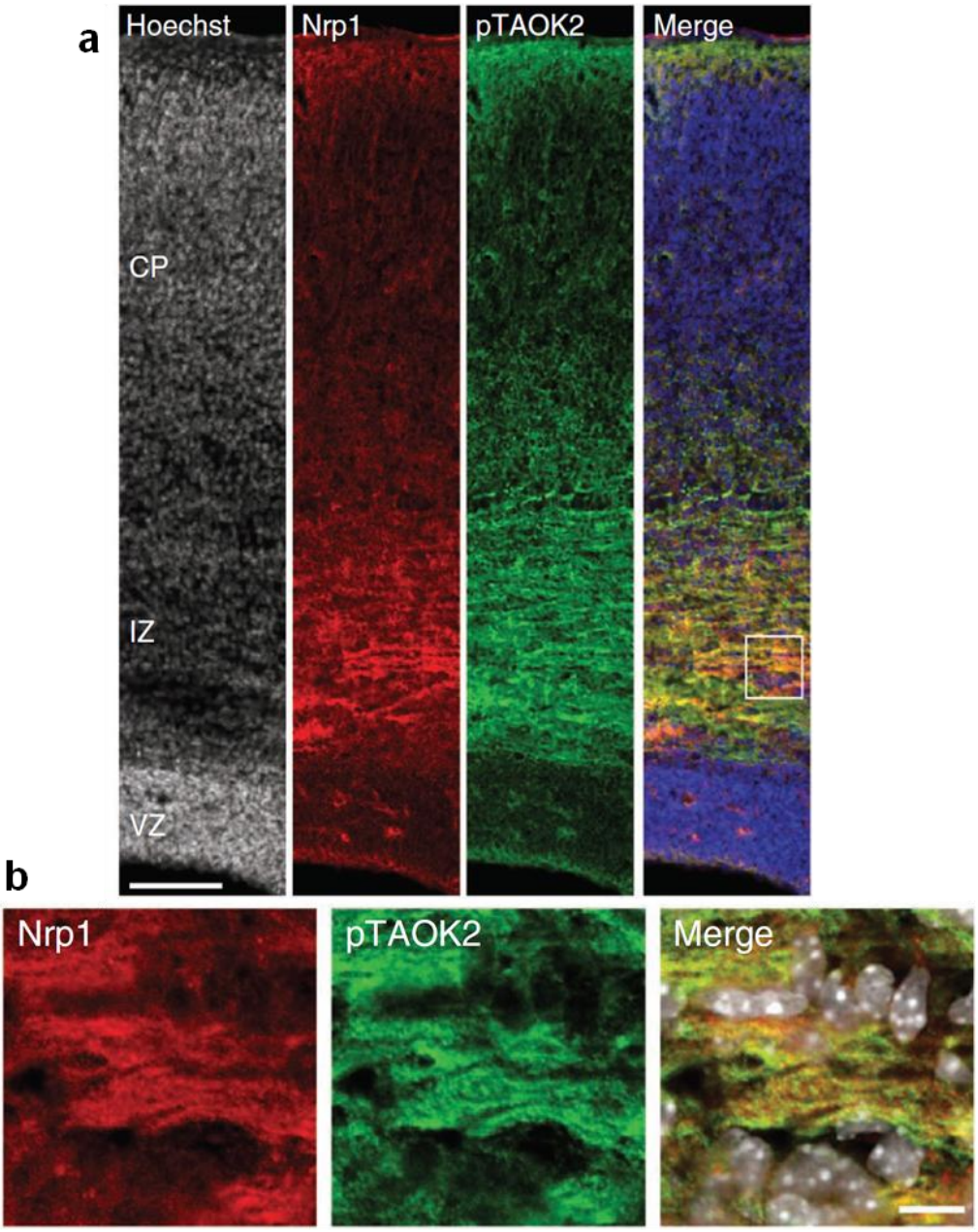

Figure 1.1.4.12. TAOK2 interacts with Nrp1 at the intermediate zone and cortical plate in the developing cortex.

(**a**) Nrp1 and pTAOK2 are preferentially expressed in the IZ and CP of the developing cortex. (**b**) Inset from (**a**), white box: Nrp1 and pTAOK2 co-localize in the developing cortex. Scale bar: 500 µm (a), 10 µm (b).

Next, we examined whether the Nrp1 ligand Sema3A modulates TAOK2 phosphorylation in cultured primary neurons. Cortical neurons dissociated from E17 mouse embryos and cultured for 48 hr were treated with Sema3A (2 µg/ml) for 30 min, 1 hr, 2 hr, or 6 hr. pTAOK2 immunoreactivity was significantly increased between 1 and 6 hr following Sema3A treatment in the longest neurite analyzed (the putative axon) compared to that of non-treated control cells (Figure 1.1.4.13a, b; 40 µm < neurite length < 150 µm; control: n=77 cells from three different cultures, Sema3A 30 min: n=25 cells from two different cultures, Sema3A 1 hr: n=32 cells from three different cultures, Sema3A 2 hr: n=99 cells from three different cultures, Sema3A 6 hr: n= 25 cells from three different cultures; $P<0.0001$ by one-way ANOVA and posthoc Dunnett test $^{**}P<0.01$).

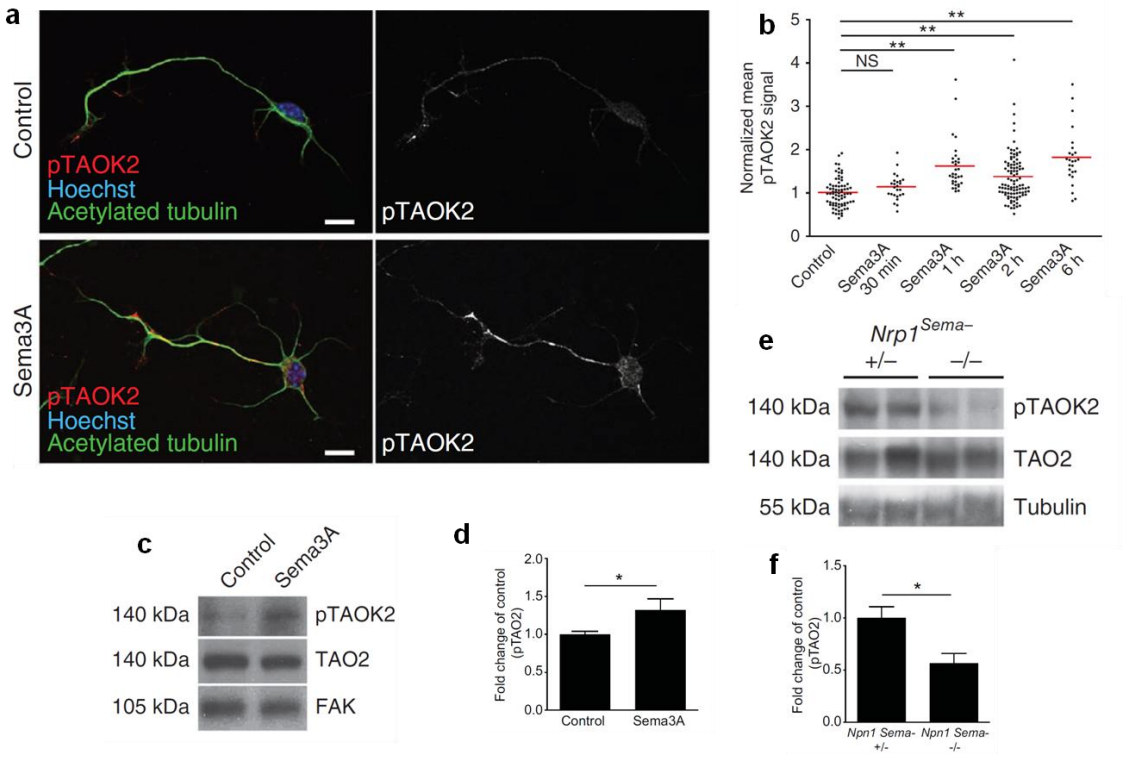

Figure 1.1.4.13. TAOK2 interacts with Nrp1 to modulate TAOK2 phosphorylation.

Sema3A treatment (2 µg/ml) increases pTAOK2 immunoreactivity in cultured cortical neurons. (a) Representative control neuron (upper panel) and a neuron treated with Sema3A for 2 hr (lower panel) (b) Quantification of pTAOK2 immunoreactivity from the longest neurite (40 µm < neurite length < 150 µm) of control and Sema3A-treated cultured cortical neurons. Following 1-6 hr of Sema3A stimulation, immunoreactivity for pTAOK2 significantly increases compared to control. (c) Immunoblot of cultured cortical neuron lysates shows that the 2 hr Sema3A treatment increases pTAOK2 immunoreactivity. (d) Quantification of (c), pTAOK2 immunoreactivity in lysates of cultured cortical neurons that were treated for 2 hr with Sema3A. Sema3A treatment increases pTAOK2 immunoreactivity. (e) Immunoblot of cortical lysates from *Nrp1*$^{Sema-}$ heterozygous (+/-) and *Nrp1*$^{Sema-}$ homozygous (-/-) P7 mice littermates shows a decrease in pTAOK2 immunoreactivity in the (-/-) mouse compared with the (+/-) littermate. (f) Quantification of (e), pTAOK2 immunoreactivity in lysates of cortices from *Nrp1*$^{Sema-}$ (+/-) and (-/-) mice. FAK and tubulin are used as the loading controls. Scale bar: 10 µm (a). *P < 0.05, **P < 0.01.

Western blot analysis of lysates harvested from neurons following 2 hr of Sema3A treatment revealed that endogenous TAOK2 phosphorylation was also induced following Sema3A treatment (Figure 1.1.4.13c, d; n=3 experiments per duplicate; *P=0.0401 by t test). Finally, we examined the levels of pTAOK2 in cortical extracts from mice homozygous for a knock-in mutation that renders the endogenous Nrp1 receptor incapable of binding Sema3A (*Nrp1*$^{Sema-}$). In agreement with the *in vitro* experiments, pTAOK2 levels are reduced in the cortical neurons of homozygous *Nrp1*$^{Sema-}$ mice compared with heterozygous littermates (Figure 1.1.4.13e, f; n(+/-) = 9 brains, n(-/-) = 4 brains; *P=0.0310 by t test). These results suggest that Sema3A signaling activates TAOK2 kinase activity.

TAOK2 and Sema3A modulate the activity of JNK in cortical neurons.

We next sought to elucidate the downstream effectors by which the interaction of TAOK2 with the Sema3A-Nrp1 signaling pathway modulates neuronal differentiation in cortical pyramidal neurons. The c-Jun amino-terminal kinases (JNK) have been shown to be important for many aspects of neuronal differentiation (Polleux and Snider, 2010). It was shown that TAOK2α, unlike TAOK2β, stimulates the JNK pathway in cell lines (Zihni et al., 2007). TAOK2 overexpression indirectly activates endogenous JNK1 in HEK293 cells via the preferential phosphorylation of MEK3 and MEK6 (Chen and Cobb, 2001). In addition, TAOK2 was shown to modulate the dual phosphorylation of JNK1 at Thr183/Tyr1855 (Chen and Cobb, 2001; Huangfu et al., 2006). Sema3A has also been shown to activate the JNK1/c-Jun signaling pathway in cultured dorsal root ganglion neurons (Ben-Zvi et al., 2006). Phosphorylated JNK1/2 can modulate neurite initiation, axon formation, and dendritic architecture in cultured (Barnat et al., 2010; Bjorkblom, 2005; Oliva et al., 2006; Rosso et al., 2005; Tararuk et al., 2006) and is required for the maintenance of neuronal microtubules in axons and dendrites *in vivo* (Chang et al., 2003). The deactivation of JNK1 by BDNF treatment destabilizes microtubules and induces axonal branching (Jeanneteau et al., 2010). Based on these findings, we hypothesized that JNK1 may mediate the effect of TAOK2 and Sema3A on neuronal differentiation.

To determine whether TAOK2 modulates JNK1 in cortical neurons, *Taok2* shRNA 1 or control plasmids together with F-GFP were introduced into E15 mouse embryos via *in utero* electroporation and isolated cortical neurons at E17. These neurons were cultured for 48 hr before being subjected to immunocytochemistry using antibodies against phosphorylated JNK1 (pJNK; Thr- 183/Tyr-185), which represents the active form of JNK1.

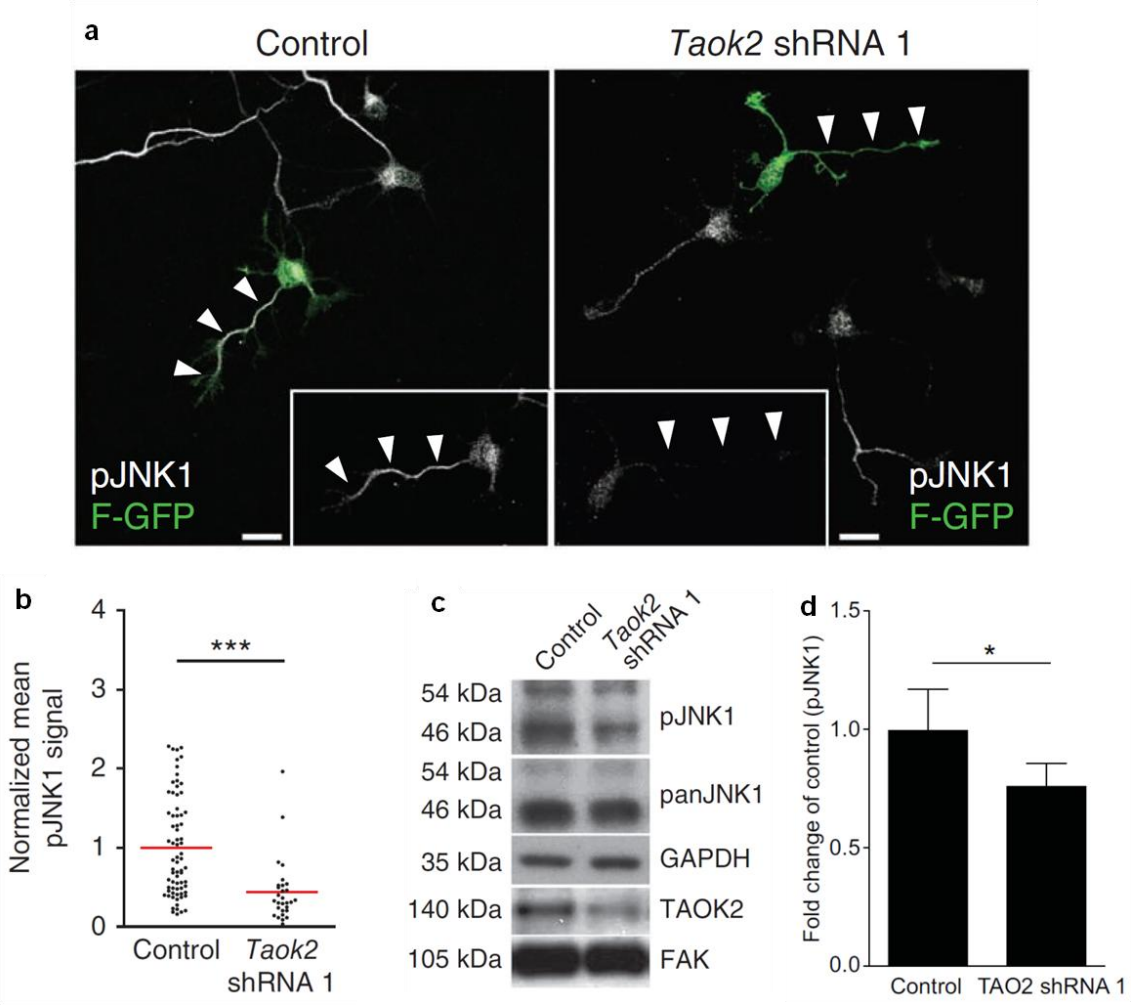

Figure 1.1.4.14. TAOK2 and Sema3A modulate the activity of JNK1: TAOK2 down-regulation descreases JNK1 signal in isolated neurons.

(a) shRNA mediated TAOK2 down-regulation decreases pJNK1 immunoreactivity in the longest neurite (40 µm < neurite length < 150 µm) of cultured cortical neurons.Control-transfected cells display an increasing proximal to distal gradient of pJNK1 signal in the longest neurite (left panel, white arrowheads). *Taok2* shRNAtransfected neurons have a decreased pJNK1 signal in the longest neurite (right panel, white arrowheads and inset). (b) Quantification of pJNK1 immunoreactivity in the longest neurite (40 µm < neurite length < 150 µm) of cultured control and TAOK2 down-regulated cortical neurons. shRNA-mediated knock-down of TAOK2 decreases the levels of pJNK1. (c, d) Western blotting with Ht22 cell lysates shows that TAOK2 down-regulation decreases JNK1 phosphorylation. (d) Quantification of pJNK1 immunoreactivity from Ht22 lysates. TAOK2 down regulation decreases JNK1 phosphorylation (pJNK1 in c, top panel, 46 kD) compared to control. Scale bar: 10 µm. *P < 0.05, ****P*<0.0001.

TAOK2 down-regulation decreased pJNK1 immunoreactivity in the longest neurite analyzed from shRNA transfected neurons, compared to that from control-transfected neurons (Figure 1.1.4.14a, b; 40 µm<neurite length<150 µm; control: n=72 cells from two different cultures; *Taok2* shRNA 1: n=29 cells from two different cultures; ****P*<0.0001 by *t* test). Additionally, in Ht22 cells transfected with *Taok2* shRNA 1, endogenous pJNK1 (top panel, lower band, 46 kD) was significantly reduced (Figure 1.1.4.14c, d; n=3 experiments per duplicate; **P*=0.02 by *t* test).

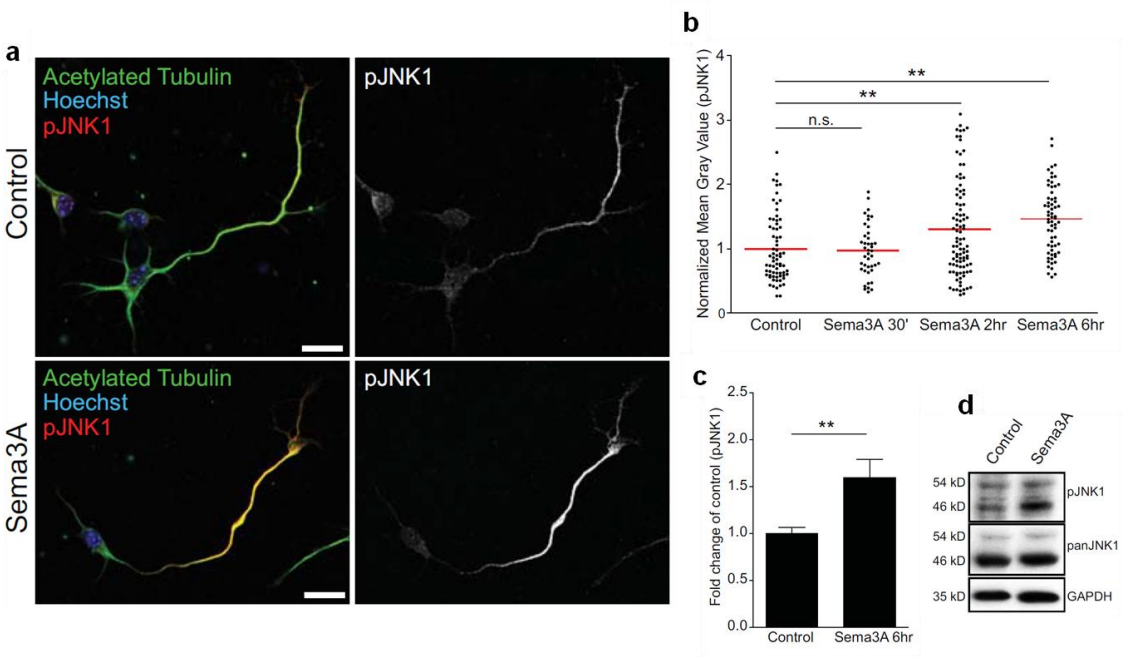

Figure 1.1.4.15. TAOK2 and Sema3A modulate the activity of JNK1: Sema3A treatment of isolated neurons increases JNK1 signal.

(a-b) Sema3A treatment (2 µg/ml) increases pJNK1 immunoreactivity in cultured cortical neurons. (a) Representative control neuron (upper panel) and a neuron treated with Sema3A for 2 hr (lower panel). (b) Quantification of pJNK1 immunoreactivity from the longest neurite (40 µm < neurite length < 150 µm) of control and Sema3A-treated cultured cortical neurons. Following 2 hr and 6 hr of Sema3A stimulation, immunoreactivity for pJNK1 significantly increases compared to control. (d) Immunoblot of cultured cortical neuron lysates shows that the 6 hr Sema3A treatment increases pJNK1 immunoreactivity. (c) Quantification of pJNK1 (in d, top panel, 46 kD) immunoreactivity in lysates of cultured cortical neurons that were treated for 6 hr with Sema3A. Sema3A treatment increases pJNK1 immunoreactivity. Scale bar: 10 µm. *P < 0.05, **P < 0.01.

As TAOK2 interacts with Nrp1, we asked whether treatment with the Nrp1 ligand Sema3A modulates JNK1 phosphorylation in cultured primary neurons. Since JNK1 phosphorylation is enriched in developed axons (Oliva et al., 2006), we used cultured neurons during the initiation of polarization to avoid endogenous JNK1 phosphorylation that could mask that induced by our Sema3A treatment. Cortical neurons dissociated from E17 mouse embryos and cultured for 48 hr were treated with Sema3A (2 µg/ml) for 30 min, 2 hr, or 6 hr. The levels of pJNK1 were measured using immunocytochemistry and western blot analysis. pJNK1 immunoreactivity was significantly increased at 2 and 6 hr following Sema3A treatment in the longest neurite analyzed (the putative axon) compared to that in non-treated control cells (Figure 1.1.4.15a, b; 40 µm<neurite length<150 µm; control: n=71 cells from three different cultures, Sema3A 30 min: n=42 cells from two different cultures, Sema3A 2 hr: n=97 cells from three different cultures, Sema3A 6 hr: n= 64 cells from three different cultures; $P<0.0001$ by one-way ANOVA and posthoc Dunnett test $^{**}P<0.01$). Western blot analysis of lysates harvested from neurons following 6 hr of Sema3A treatment revealed that endogenous JNK1 phosphorylation (pJNK, top panel, lower band, 46 kD) was also induced following Sema3A treatment (Figure 1.1.4.15c, d; n=3 experiments per duplicate; $^{**}P=0.0014$ by *t* test).

We also examined the levels of pJNK1 in cortical extracts from *Nrp1*$^{Sema-}$ mice. In agreement with our *in vitro* experiments, the pJNK1 levels were reduced in the cortical neurons of homozygous *Nrp1*$^{Sema-}$ mice compared with heterozygous littermates (Figure 1.1.4.16a, b; n(+/-) = 9 brains, n(-/-) = 4 brains; **P*=0.029 by *t* test). Sema3A and TAOK2 may modulate JNK1 via a common mechanism; alternatively, they may regulate JNK1 via distinct pathways. To differentiate between these possibilities, JNK1 activation was evaluated following Sema3A treatment in the absence or presence of TAOK2. Primary neurons were infected with recombinant lentivirus carrying control or *Taok2* shRNA 1 soon after plating. Three days later, we assessed levels of pJNK1 following the addition of exogenous Sema3A (2 µg/ml). Sema3A increased levels of pJNK1 in control shRNA-treated neurons by about 30% - 40% (Figure 1.1.4.16a, b; n=2 experiments per triplicate; *P*<0.0001 by one-way ANOVA and posthoc Dunnett test ***P*<0.01, **P*<0.05). Importantly, Sema3A failed to elevate pJNK1 when TAOK2 was knocked-down (Figure 1.1.4.16c, d). These results indicate that TAOK2 is required for Sema3A to induce pJNK1. Together, these data suggest that the interaction of TAOK2 with the Sema3A-Nrp1 signaling complex activated JNK1 phosphorylation to mediate neuronal differentiation in cortical pyramidal neurons.

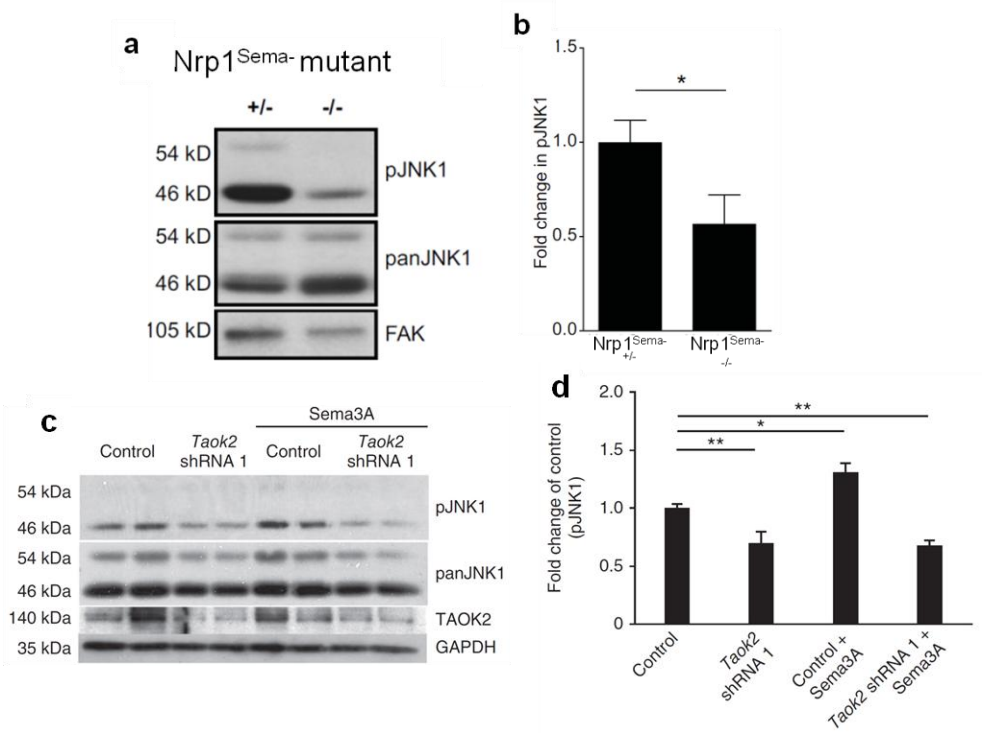

Figure 1.1.4.16. TAOK2 and Sema3A modulate the activity of JNK1: Nrp1 knock-out mouse has decreased activity of JNK1.

(a) Immunoblot of cortex lysates from *Nrp1*$^{Sema-}$ (+/-) and (-/-) P7 littermate mice shows a decrease in pJNK1 immunoreactivity in the (-/-) mouse compared with the (+/-) littermate. (b) Quantification of pJNK1 (in a, top panel, 46 kD) immunoreactivity in lysates of cortices from *Nrp1*$^{Sema-}$ (+/-) and (-/-) mice. (c, d) TAOK2 is necessary for Sema3A to exert an effect in JNK activation. Isolated cortical neurons infected with *Taok2* shRNA 1 lentivirus failed to increase levels of pJNK1 in the presence of Sema3A. (d) Quantification of pJNK1 (in c, top panel, 46 kD) immunoreactivity in lysates of cultured cortical neurons infected with *Taok2* shRNA 1 lentivirus and treated for 6 hr with Sema3A. Sema3A treatment does not increases pJNK1 immunoreactivity in TAOK2 down-regulated neurons. FAK and GADPH are used as the loading controls. *P < 0.05, **P < 0.01.

TAOK2 modulates basal dendrite formation downstream of Sema3A-Nrp1.

Little is known about the molecular pathways that determine the formation of basal dendrites in pyramidal neurons. Therefore, we decided to analyze whether TAOK2 modulates basal dendrite formation downstream of Sema3A-Nrp1. To this end, we examined whether TAOK2 overexpression is sufficient to restore the defect in dendrite arborization observed in neurons from *Nrp1*$^{Sema-}$ mice (Gu et al., 2003; Tran et al., 2009). These mice exhibit markedly reduced branching and growth of basal dendrites in layer V cortical neurons (Gu et al., 2003; Tran et al., 2009). In contrast, wild-type neurons *in situ* treated with Sema3A increase their dendritic complexity (Fenstermaker et al., 2004). We overexpressed TAOK2 in neurons dissociated from the E13.5 cortex of *Nrp1*$^{Sema-}$ and wild-type mice. At 7 days in vitro (DIV7), Sema3A treatment of *Nrp1*$^{Sema-}$ neurons did not restore the reduced dendritic arborization complexity to wild-type levels, confirming the inability of the *Nrp1*$^{Sema-}$ receptor to bind Sema3A (Figure 1.1.4.17a, b). However, TAOK2 overexpression ameliorated the defective dendritic arborization in *Nrp1*$^{Sema-}$ neurons (Figure 1.1.4.17a, b). Sholl analysis of the dendritic arbors located between 10 µm and 100 µm from the cell soma reveals that dendritic arborization is restored to wildtype levels in the *Nrp1*$^{Sema-}$/TAOK2 overexpressing neurons, compared to either neurons from *Nrp1*$^{Sema-}$ mice or *Nrp1*$^{Sema-}$ neurons treated with Sema3A (Figure 1.1.4.17b, n=20 cells per condition from two different cultures, ****P*<0.001 by *t* test).

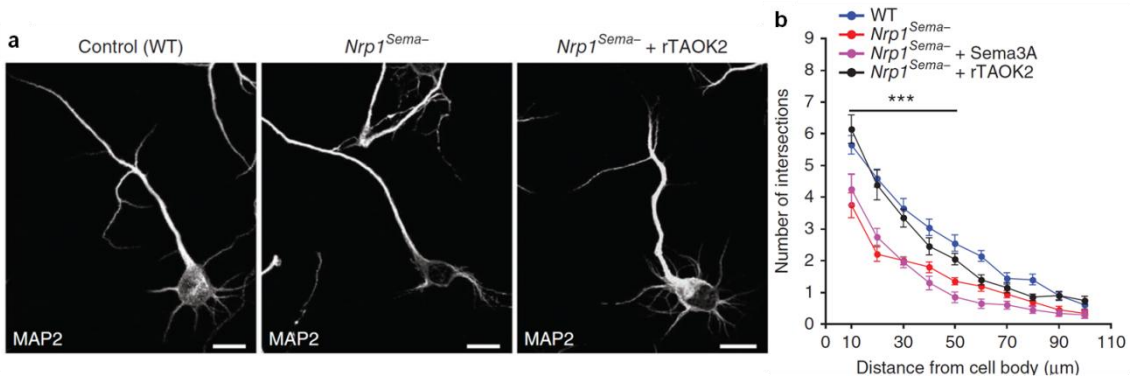

Figure 1.1.4.17. TAOK2 counteracts the dendritic arborization deficit in neurons expressing a deficient Nrp1 receptor.

(**a**) rTAOK2 overexpression ameliorates the dendritic arborization deficit in primary cortical *Nrp1*$^{Sema-}$ neurons. (**b**) Sholl analysis of the dendritic arbors reveals no statistical differences between wildtype (WT) and *Nrp1*$^{Sema-}$ + rTAOK2 overexpressing cultured neurons at a distance between 10 µm and 100 µm from the cell soma. Scale bar: 10 µm. **P < 0.01, ***P < 0.001.

To further confirm the functional interaction of TAOK2 and Nrp1 *in vivo*, we acutely knocked down the expression of Nrp1 using a shRNA construct, while simultaneously overexpressing TAOK2, in layer II-III cortical neurons by *in utero* electroporation. The Nrp1 shRNA sequence was previously reported to down regulate Nrp1 expression in the cortex (Chen et al., 2008), and we confirmed that it efficiently knocks down the expression of Nrp1-mCherry in HEK293 cells (Figure 1.1.4.18a, b).

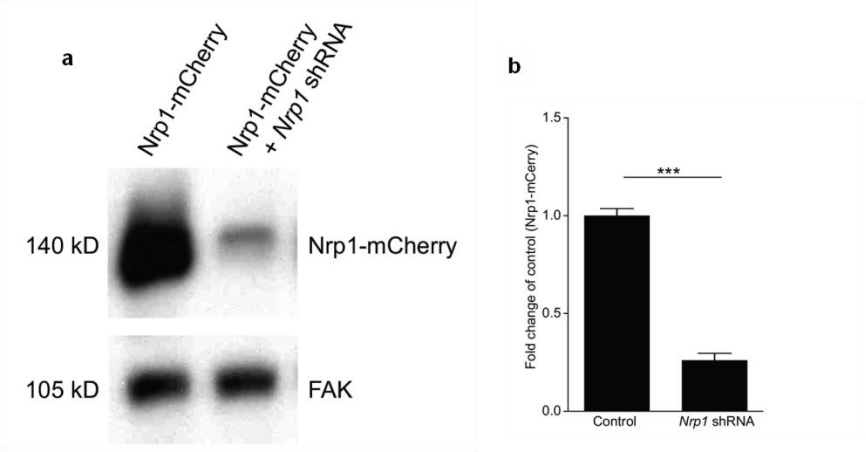

Figure 1.1.4.18. Nrp1 shRNA specifically down-regulates Nrp1-mCherry expression in HEK293Tcells.

(a) Western blot of extracts from HEK293Tcells transfected with control plasmid and Nrp1-mCherry cDNA, and HEK293Tcells transfected with Nrp1-mCherry cDNA and the Nrp1 shRNA construct. Blots were probed with antibodies against mCherry. (b) Quantification of the Nrp1-mCherry signal from lysates of HEK293Tcells. Nrp1 shRNA considerably decreases Nrp1-mCherry immunoreactivity (n=3 experiments per duplicate; ***P<0.0001 by t test; Mean ± s.e.m.).

E15 embryos were *in utero* electroporated with the Nrp1 shRNA plasmid, or a control shRNA plasmid, together with F-GFP and rTAOK2 cDNA, and sacrificed at P7. The dendritic morphology in neurons of the layer II-III cortex from control and Nrp1 shRNA-expressing brains was evaluated. The knockdown of Nrp1 impaired the formation of basal dendrites in the upper cortical layers (II-III; Figure 1.1.4.19a), as has been previously reported (Chen et al., 2008). Strikingly, TAOK2 overexpression ameliorated the basal dendrite arborization deficit in Nrp1 shRNA-expressing neurons (Figure 1.1.4.19c). TAOK2-overexpressing neurons show a significantly increased primary basal dendrite number in neurons with Nrp1 knockdown that is not significantly different from controls (Figure 1.1.4.19b; control: n=16 cells from two brains; Nrp1 shRNA: n=47 cells from three brains; Nrp1 shRNA + rTAOK2: n=35 cells from three brains; $P<0.0001$, by one-way ANOVA and posthoc Dunnett test $^{**}P<0.01$). However, using Sholl analysis, we found that the basal dendritic branching (secondary branching) is not restored to control levels (Figure 1.1.4.19c; $P<0.0001$ by one-way ANOVA and posthoc Dunnett test $^{**}P<0.01$). Importantly, Sholl analysis also demonstrated that Nrp1 down-regulation did not affect the apical dendrite of transfected neurons (Figure 1.1.4.19d). These results reflect a partial restoration of the formation of basal dendrites following TAOK2 expression in Nrp1-deficient neurons.

Our results provide evidence that Nrp1 and TAOK2 constitute a pathway that regulates basal dendrite development in pyramidal neurons of the developing cortex.

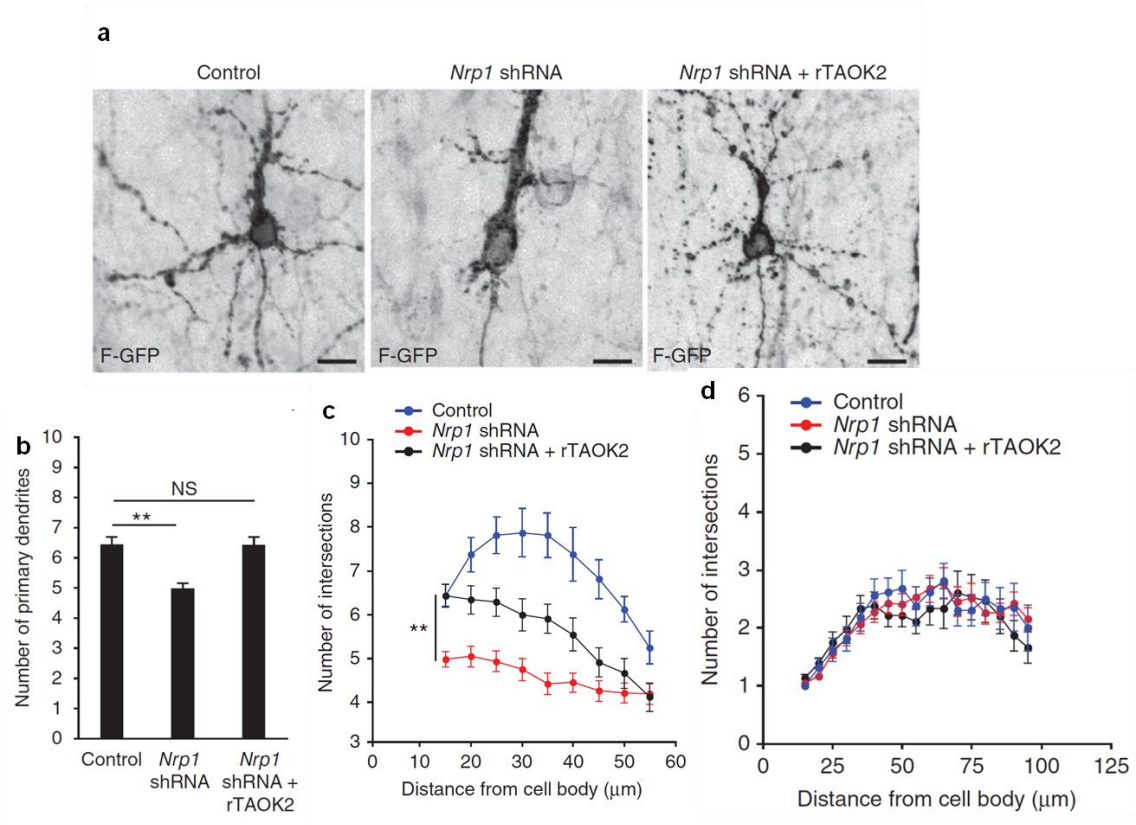

Figure 1.1.4.19. TAOK2 counteracts the dendritic arborization deficit in neurons with Nrp1 down-regulation.

(a) rTAOK2 overexpression reverses the basal dendritic arborization deficit in Nrp1 shRNA-transfected neurons from II-III layer cortex. (b) rTAOK2 overexpression restores the number of primary dendrites in Nrp1 downregulated neurons. (c) Sholl analysis of the dendritic arbors shows significant differences between Nrp1 shRNA-expressing neurons and Nrp1 shRNA + rTAOK2-expressing neurons. (d) Sholl analysis of the apical dendrite does not show any differences between Nrp1 down-regulation, Nrp1 shRNA + rTAOK2 overexpression, and control conditions. Scale bar: 10 µm. **P < 0.01, ***P < 0.001.

Activated JNK modulates basal dendrite formation downstream of TAOK2.

Activated JNK1 has been shown to preferentially localize to the longest neurite, presumably the axon, of cultured hippocampal neurons (Oliva et al., 2006). However, pJNK1 has also been reported to be involved in the regulation of microtubule dynamics in axons, as well as dendrites, in both hippocampus and cortex (Chang et al., 2003). Furthermore, JNK1-deficient mice exhibit a progressive loss of microtubules within both axons and dendrites (Chang et al., 2003). Previous to the current report, it has remained unclear whether pJNK1 modulates microtubules in basal or apical dendrites.

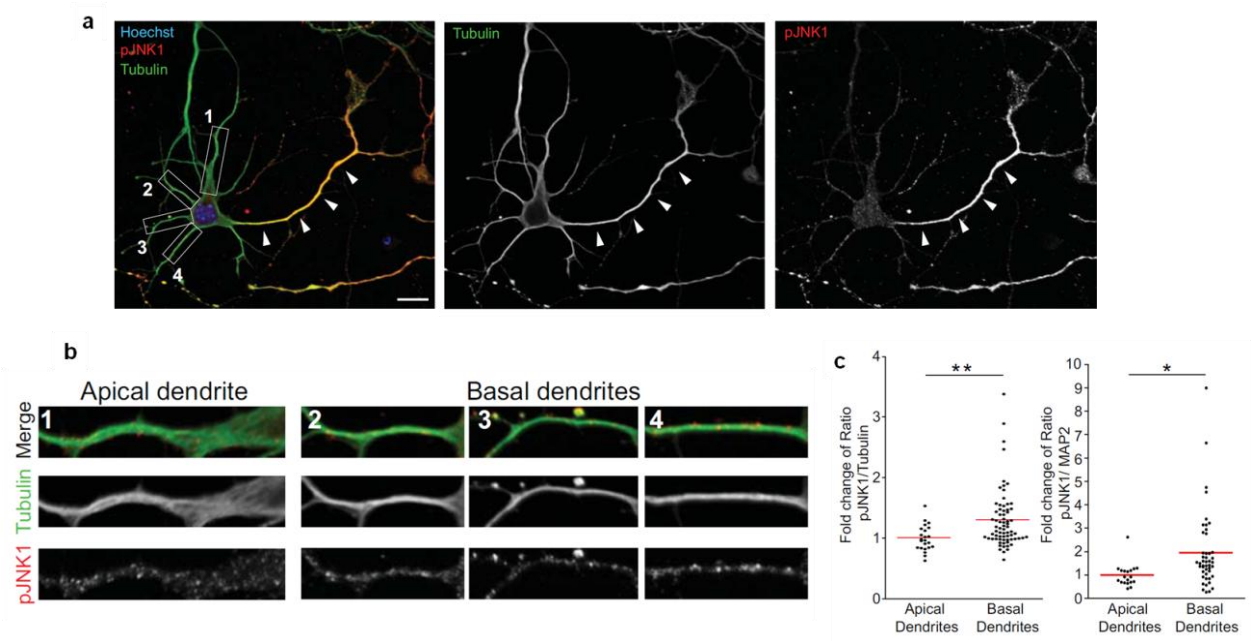

Figure 1.1.4.20. Activated JNK1 predominates in basal dendrites.

(a) Representative cortical pyramidal neurons in primary culture. Cortical neurons were dissociated at E17 and cultured for 7 days. Activated JNK1 is enriched in the axon (white arrowheads). (b) The insets show the apical dendrite (1) and basal dendrites (2, 3, 4) from the cell in (a) immunolabeled for tubulin (green) and pJNK1 (red). (c) The quantification of the ratio of pJNK1 and tubulin or MAP2 fluorescence intensities shows a higher ratio of pJNK1/tubulin and pJNK1/MAP2 in basal dendrites compared with apical dendrites. Values are normalized to the mean of apical dendrites. Scale bar: 10 μm. *P < 0.05, **P < 0.01.

To assess the localization of pJNK1 in cortical pyramidal neurons, we examined its subcellular localization in DIV7 mouse cortical neurons dissociated at E17. We analyzed cells that displayed a pyramidal morphology bearing a thick “apical” dendrite and several thin “basal” dendrites. We observed that pJNK1 is enriched in developed axons (Figure 1.1.4.20a, arrowheads) as previously reported (Oliva et al., 2006). Interestingly, the basal dendrites showed a significant increase in the intensity of pJNK1 immunoreactivity, normalized to tubulin or MAP2 immunoreactivity, compared with the apical dendrite (Figure 1.4.20a-c; tubulin: 1.3 ± 0.05-fold ratio increase, ***P*=0.0051 by *t* test; n=23 cells from three different cultures; MAP2: 1.95 ± 0.24-fold ratio increase, **P*=0.0154 by *t* test; n=20 cells from three different cultures). Thus, the compartmentalization of pJNK1 might play a role in the preferential elongation of basal versus apical dendrites.

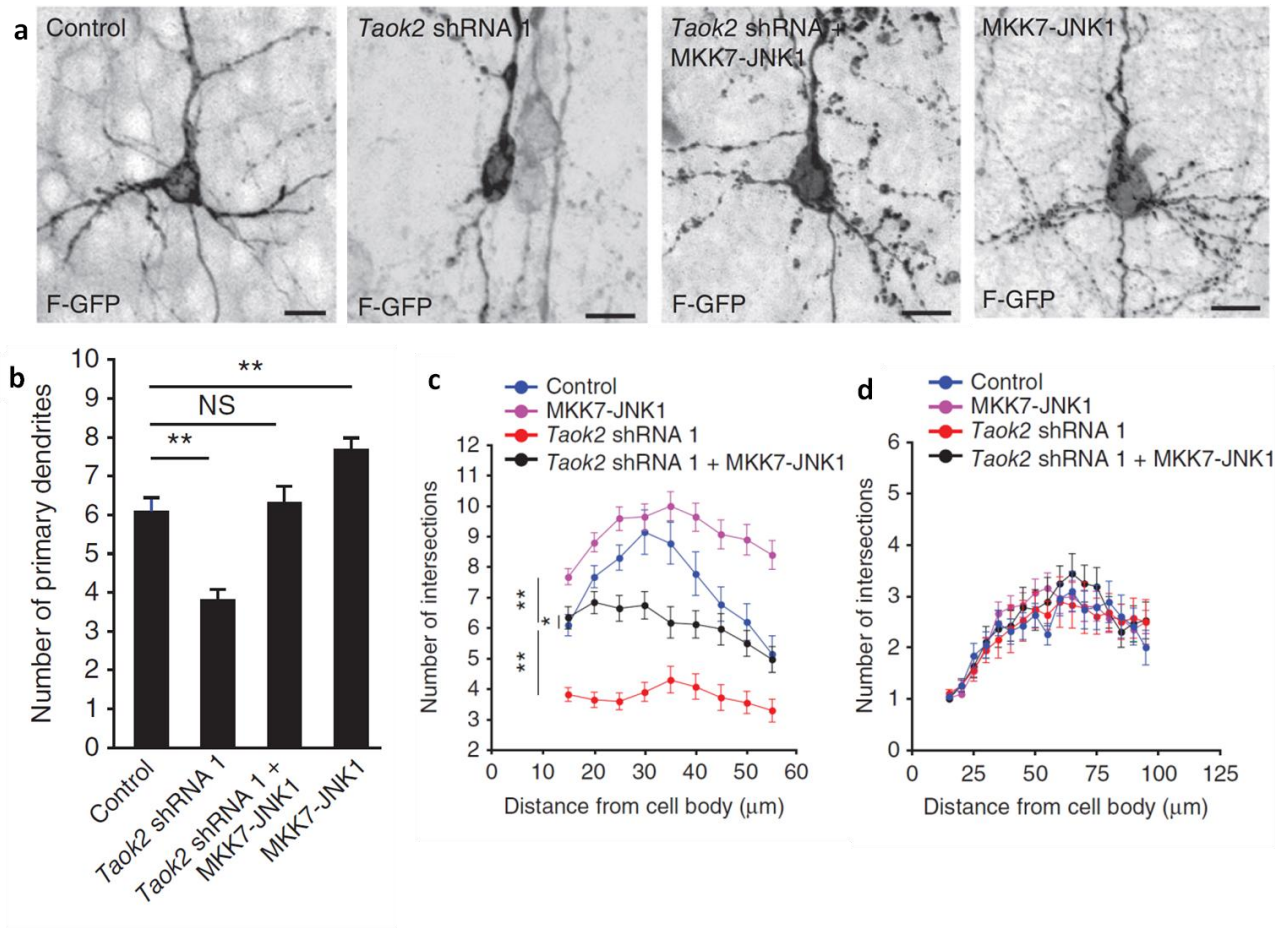

Figure 1.1.4.21. Activated JNK1 ameliorates deficient basal dendrite formation following TAOK2 down-regulation.

(a) Upper cortical layer (II-III) transfected neurons show underdeveloped basal dendrites following shRNA-mediated knockdown of TAOK2 compared with control-transfected neurons. MKK7-JNK1 overexpression ameliorates the basal dendrite deficit following *Taok2* shRNA-mediated downregulation. MKK7-JNK1 overexpression alone *increases* the number of basal dendrites compare with control-transfected cells. (b) The number of primary dendrites increases following MKK7-JNK1 overexpression. (c) Sholl analysis of the dendritic arbors demonstrates significant differences between *Taok2* shRNA expressing neurons and *Taok2* shRNA + MKK7-JNK1 or MKK-JNK1-expressing neurons at a distance between 15 μm and 55 μm from the cell soma. (d) The apical dendrite of transfected neurons is not affected by MKK7-JNK1 overexpression. Quantifications for control and *Taok2* shRNA 1-transfected cells are the same as in Figure 3b-d. Scale bar: 10 μm. *P < 0.05, **P < 0.01.

To further investigate the relationship between TAOK2 and JNK1 in basal dendritic arborization, we determined whether the addition of pJNK1 is able to abrogate the basal dendrite phenotypes caused by TAOK2 loss-of-function. It was previously shown that fusing MKK7 to JNK1 (MKK7-JNK1) renders JNK1 constitutively active, thus mimicking the activity of pJNK1 (Lei et al., 2002; Yamasaki et al., 2011). E15 mouse embryos were electroporated *in utero* with *Taok2* shRNA 1 or control shRNA together with F-GFP and MKK7-JNK1 cDNA, and sacrificed at P7. TAOK2 down-regulation impaired the formation of primary dendrites in layer II-III neurons (Figure 1.1.4.21a, b; control: n=19 cells from three brains; *Taok2* shRNA 1: n=23 cells from three brains; *Taok2* shRNA 1 + MKK7-JNK1: n=32 cells from three brains; MKK7- JNK1: n=42 cells from three brains; ***P<0.0001 by one-way ANOVA and posthoc Dunnett test **P<0.01).

Interestingly, the number of primary dendrites of transfected neurons was markedly increased when MKK7-JNK1 was expressed alone or co-expressed with *Taok2* shRNA1 (Figure 1.1.4.21a, b). Sholl analysis demonstrated significant differences in the dendritic arborization between *Taok2* shRNA 1-expressing neurons, *Taok2* shRNA 1 + MKK7-JNK1-expressing neurons, and MKK7-JNK1-expressing neurons at a distance between 15 µm and 55 µm from the cell soma. (Figure 1.1.4.21c; ***P<0.0001 by one-way ANOVA and posthoc Dunnett test **P<0.01, *P<0.05). However, neurons co-expressing *Taok2* shRNA and MKK7-JNK1 produced basal dendrites that were not as elaborated as those produced from control shRNA-transfected neurons (Figure 1.1.4.21c). This result reflects a partial restoration of the branching of basal dendrites in *Taok2* shRNA-transfected neurons following the expression of MKK7-JNK1. Importantly, MKK7-JNK1 overexpression with or without TAOK2 down-regulation did not affect apical dendrite morphology compared with control-transfected neurons (Figure 1.1.4.21d), further supporting a preferential basal dendrite compartmentalization of pJNK. The active JNK1 also rescued the callosal axon deficit in the midline following TAOK2 down-regulation (Figure 1.1.4.22). Together, these experiments provide evidence that TAOK2 and JNK1 modulate neuronal differentiation in cortical pyramidal neurons.

Collectively, these results delineate a molecular pathway whereby TAOK2 plays a key role in governing the morphogenesis of pyramidal neurons in the developing cortex.

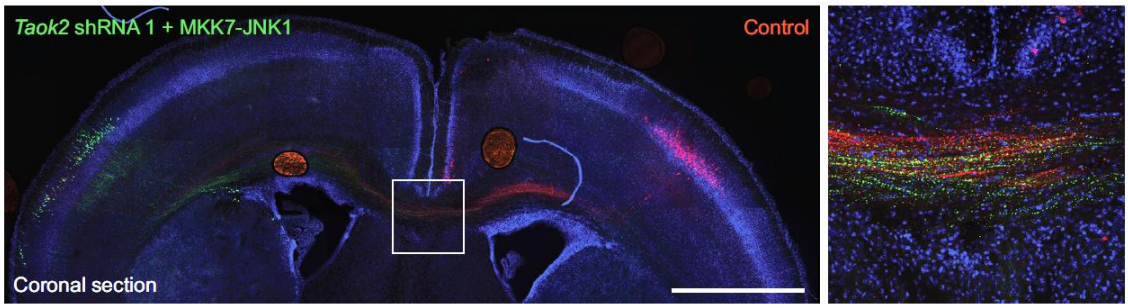

Figure 1.1.4.22. Activated JNK1 ameliorates axonal projection deficits following TAOK2 down-regulation.

MKK7-JNK1 overexpression rescues the deficit of callosal axons in the corpus callosum from cells transfected with Venus and *TaoK2* shRNA. Right panel: inset of the corpus callosum. Scale bar: 500 µm.

TAOK2 down regulation affects cortical neuronal migration, JNK1 rescues the phenotype

The migratory process requires major alterations in the cellular cytoskeleton, both in actin and microtubules, and action of very specialized molecules. The leading process is composed of several organelles and usually terminates in several protrusions oriented toward the cortical plate that by sensing the extracellular environment will determine the migratory pathway. Alteration to this dynamics usually is impairment for migration in cortical development studies.

TAOK2 was first described by Moore and colleagues under the name of PSK. In their study the authors describe how PSK selectively activates the JNK MAPK pathway through the activation of MKK4 and MKK7, and also, they show the relevance of the unknown c-terminal domain to the regulatory pathway and function of TAOK2 in the cells (Moore et al., 2000). Several other studies reveal the involvement of TAOK2 in regulating cytoskeleton properties during stress-like conditions and demonstrate that TAOK2 colocalizes with microtubules for their stabilization in a kinase independent fashion (Chen and Cobb, 2001; Mitsopoulos et al., 2003). So it is possible that TAOK2 is responsible for the stability of actin, having a major effect in the dynamics of microtubules present in the neurites and axons of pyramidal neurons.

To see if TAOK2 down-regulation had an effect in the migratory pathway, E15 mouse embryos were electroporated *in utero* with *Taok2* shRNA 1 or control shRNA together with F-GFP and MKK7-JNK1 cDNA. Mice were sacrificed at E17 and the pattern of neuronal migration was evaluated. We found that the knockdown of TAOK2 was responsible for a significant arrest of pyramidal neurons in the intermediate zone when compared to control neurons where the higher percentage of cells were already present in the upper cortical plate. TAOK2 down-regulation impaired the proper migration of neurons, with an increased accumulation of cells in the IZ when compared with the control brain, although when overexpressing MKK7-JNK1 there is a partially rescue of the migratory phenotype (Figure 1.1.4.23a, b; control: n=2 brains; *Taok2* shRNA 1: n=2 brains; *Taok2* shRNA 1 + MKK7-JNK1: n=2 brains; ***P<0.0001 by one-way ANOVA and posthoc Dunnett test **P<0.01).

The latter results suggest that TAOK2 has a role in the regulatory mechanism of neuronal migration trough the activation of JNK1.

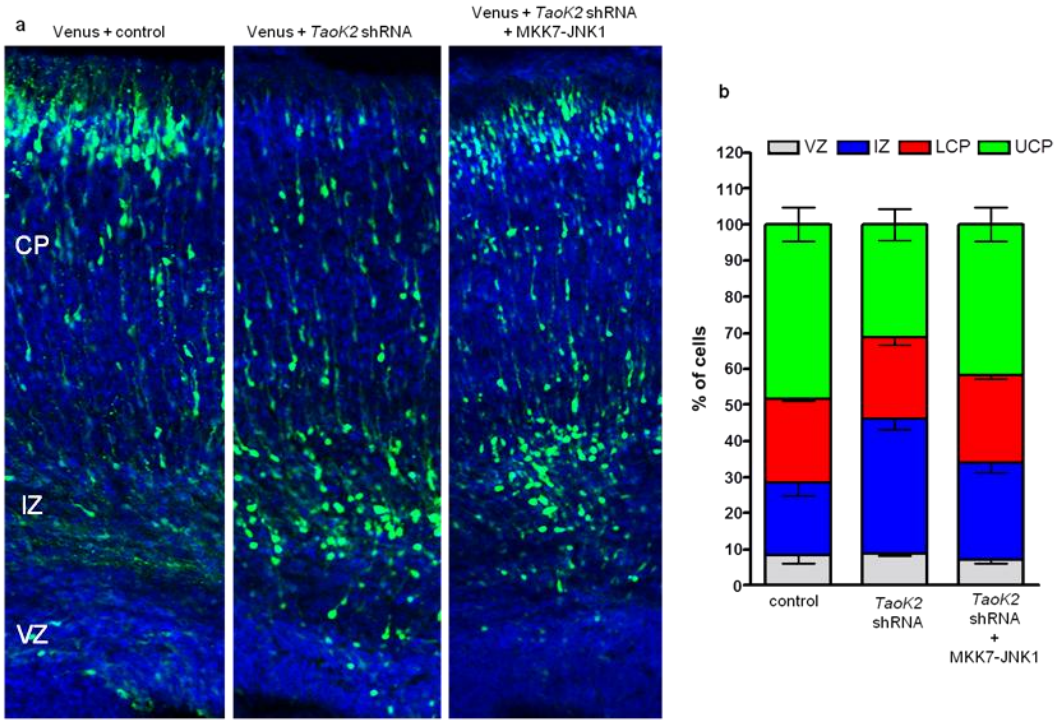

Figure 1.1.4.23. TAOK2 down-regulation affects neuronal migration in the developing cortex, while the overexpression of MKK7-JNK1 partially rescues the phenotype .

(a) Cortical mouse embrios were electroporated at E17 with F-GFP together with control shRNA (left panel), *Taok2* shRNA (central panel) and *Taok2* shRNA + MKK7-JNK1 cDNA (right panel). The knockdown of TAOK2 leads to a clear defect in neuronal migration, where the migration on pyramidal neurons is arrested in the intermediate zone. However, the defect in neuronal migration is not so clear when together with the knockdown of TAOK2 we overexpress a constitutively active form of MKK7-JNK1, having no absolute statistical difference from the control brains. (b) The quantification of migratory defect and partially rescue was done by quantifiyng the number of cells arrested in the Ventricular Zone (VZ), Intermediate Zone (IZ), Low-Cortical Plate (LCP) and Upper-Cortical Plate (UCP).

It is prooved that JNK1 is involved in axon formation, elongation and maintenace *in vivo* through the phosphorylation of diverse cytoeskeleton proteins and, also, that JNK1 modulates axon transport (Björkblom et al., 2005; Chang et al., 2003; Stagi et al., 2006; Tararuk et al., 2006; Yamauchi et al., 2006). We know that TAOK2 activates the JNK1 pathway. In our experiments we observed a partial rescue of the migration defect, when overexpressing an active form of JNK1 (MKK7-JNK1). The inactivation of JNK1 together with absence of TAOK2 may explain the migration defect observed, since the inability of the growth cone to expand and explore the environment will inhibit the detachment of the axon and consequently, inhibit the motility of the cell toward the CP. Also, the JNK1 molecule as been studied in neurons for its direct binding to motor molecules, kinesins (Stagi et al., 2006). The transport of molecules in the neurons between axon and nucleus will be impaired by the inactivation of JNK1. JNK1 is concluded to be a major player in neuronal development and migration.

We next sought to elucidate the effect of the *in vivo* TAOK2 down-regulation in the cortical layering in the post-migratory brain. Mouse embryos were electroporated bilaterally, the left hemisphere was electroporated with *Taok2* shRNA together with Venus, while the right

hemisphere was electroporated with control shRNA together with mCherry. The mice were sacrificed at posnatal day 7 (P7). A quantification of the distance from the most rostral labeled positive neuronal cell to the marginal zone was measured and a highly significant difference in average distance was observed in the brain between left hemisphere (TAO shRNA + Venus, Figure 1.1.4.24) and the right hemisphere (control shRNA + mCherry, Figure 1.1.2.24). Neuronal cells, where TAOK2 was down-regulated, ended in a higher layer of the cortex, i.e. in a most dorsal position, when compared to the control neurons, suggesting a delay in migration but not a complete arrest of the migratory mechanism. TAOK2 down-regulation affects the end fate of the pyramidal neurons and so they surpass the correct layer position, ending in a most upper layer of the cortex.

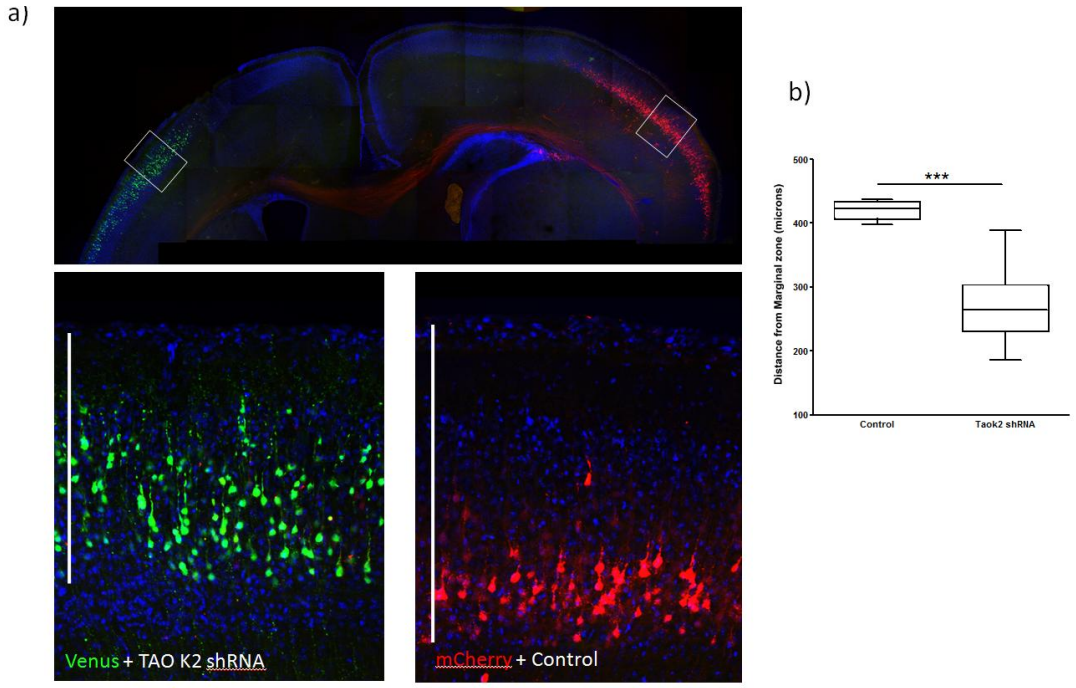

Figure 1.1.4.24. TAOK2 downregulation affects cortex layering.

(a) Brain coronal section showing that *Taok2* shRNA-mediated knock-down in Venus-positive neurons (bottom inset - left panel) appear in upper cortical layers when compared with control transfected neurons, at the contralateral hemisphere, positive for mCherry (bottom inset - right panel). (b) Quantification of distance (microns) from marginal zone to the base of transfected cells. shRNA-mediated knock-down of TAOK2 decreases the distance to marginal zone. ***P < 0.001.

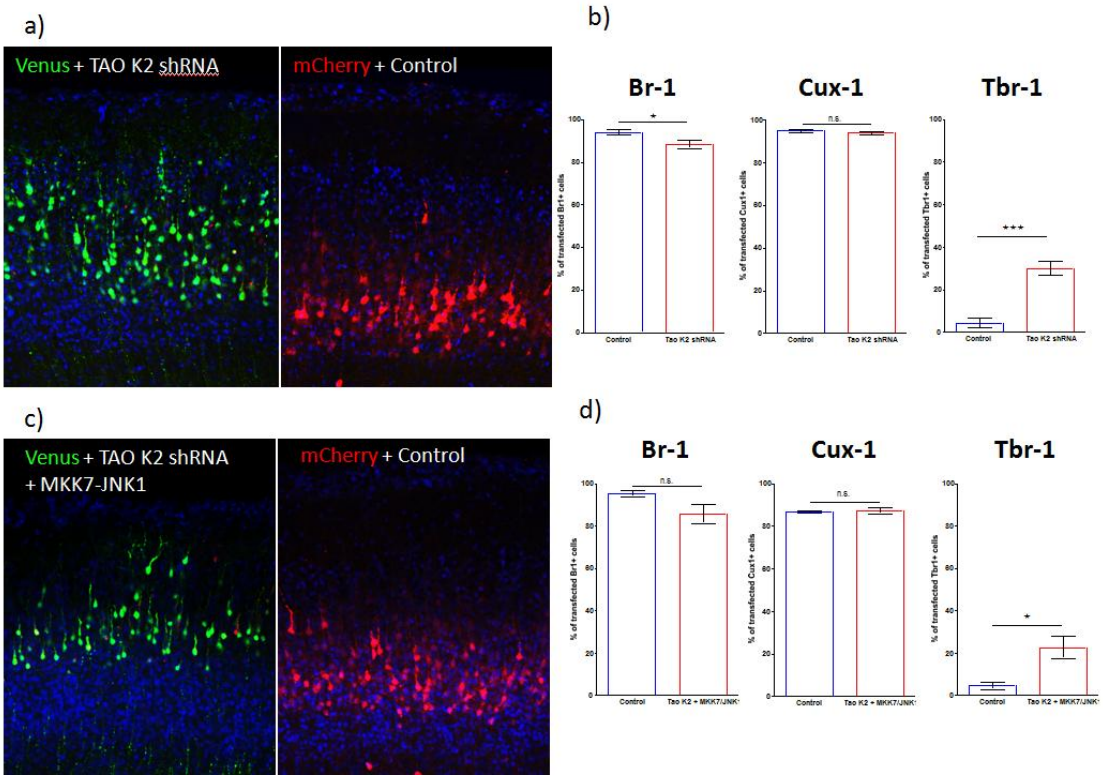

Figure 1.1.4.25. The overexpression of the constituve active form MKK7-JNK1 rescues the cortial layering defect.

(a) Layering markers are compared between *Taok2* shRNA-mediated knock-down in Venus-positive neurons and control transfected neurons positive for mCherry present in the contralateral hemisphere of the same mouse brain. (b) Immunoprecipitation with antibodies for the different six cortical layers: layer VI (anti-TBR1), layers II-IV (anti-CUX1) and layer (anti-BR1). TAOK2 down-regulation afects layering of upper cortical neurons. (c) Layering markers are compared between *Taok2* shRNA-mediated knock-down rescued with MKK7-JNK1 overexpression in Venus-positive neurons and control transfected neurons positive for mCherry present in the contralateral hemisphere of the same mouse brain. (d) Quantification of immunoreactivity to cortical layer markers as in (b). A significant rescue of neuronal position in the cortex is evident for markers Br-1 and Tbr-1.

Knowing that the *in vivo* knock-down of TAOK2 leads to defects in neuronal migration and cell positioning, we proceed to study TAOK2 influence in the neuronal fate of the cells. On that purpose, bilateral *in utero* electroporation to the mouse embryo at E15 was performed. The left hemisphere was electroporated with TAOK2 shRNA and Venus, while the right hemisphere was electroporated with control shRNA and mCherry. The mice were sacrificed at P7 for the analysis of the immunoreactivity of the cells with antibodies against cortical layer markers Br-1, Tbr-1 and Cux-1 (Figure 1.1.4.25a,b). We observed a highly significant difference in the Tbr-1 marker when compared to the control hemisphere. To assert if the overexpression of active JNK1 would rescue this phenotype, bilateral electroporation of the mouse embryo was performed as previously, however, the left hemisphere was electroporated with TAOK2 shRNA together with MKK7-JNK1 cDNA and Venus for labeling and the right hemisphere was electroporated with control shRNA and mCherry (Figure 1.1.4.25c,d). The quantification of the immunoreactivity against the refered (as in Figure 1.1.4.25a,b) markers for cortical layering show a decrease difference between Tbr-1 positive cells in the rescued hemisphere when compared to control. However, the rescue is not complete (Figure 1.1.4.25d).

TAOK2 is here proven to have a role in the proper organization of the neocortex. TAOK2 down regulation leads to a clear slow movement of the neuron towards the cortical plate which accounts for layer surpassing. Neurons end in an upper layer when compared to the ones that express TAOK2, having a mild different in cortical layering markers, suggesting that the TAOK2 mechanism might influence cell fate.

It is known that MyosinIIA and MyosinIIB are the most prominently expressed type II Myosins in projection neurons during migration. Schaar and McConnel have found that Myosin II activity is correlated with nuclear movement, being specifically activated in the leading and trailing domains at the time of translocation (Schaar and McConnell, 2005). Several Myosin were shown to be concentrated in the growth cones of neurons at the time of migration, as it is actin, which is responsible for the motility of the growth cone (Vallee et al., 2009). We have previously shown that disruption of TAOK2 expression leads to the collapsment of growth cones *in vitro.* It is plausible to accept that TAOK2 may interfere with Myosins motor molecules machinery, through the increased destabilization of actin. However, neurons with impaired actin dynamics can still migrate and their axons can move forward but the abnormal morphology of the growth cone confounds its selectivity (Marsh and Letourneau, 1984).

TAOK2 down-regulation affects *in vivo* leading process displacement and speed of migration

We next sought to understand the behavior of the neuronal cells after TAOK2 down-regulation. We have *in utero* electroporated mouse embryos at E15 with F-GFP for cell labeling and control shRNA or TAOK2 shRNA. Mice were sacrificed at E17 and we have captured images of the transfected cells migration behavior every 10 minutes at the inverted fluorescence microscope. The comparison between control cells and TAOK2 downregulated cells (Figure 1.1.4.26a, b) showed a significant decrease in the speed of migration. TAOK2 downregulation leads to slower speed of migration (Figure 1.1.4.26b). Also, we observed a significant difference in the displacement (microns) of the neuronal leading process between control neurons and shRNA-TAOK2 transfected neurons. Displacement of the leading process was much reduced in the TAOK2 knock-down neuron when compared to a control cell (Figure 1.1.4.26c). However, this phenotype was not so evident in the displacement of the neuronal cell body. So, depleting TAOK2 causes a major disability in the cells cytoskeleton inhibiting their proper migration since the leading and trailing process are unable to protrude and retreat, losing the capability to sense the extracellular environment and establish a migratory path.

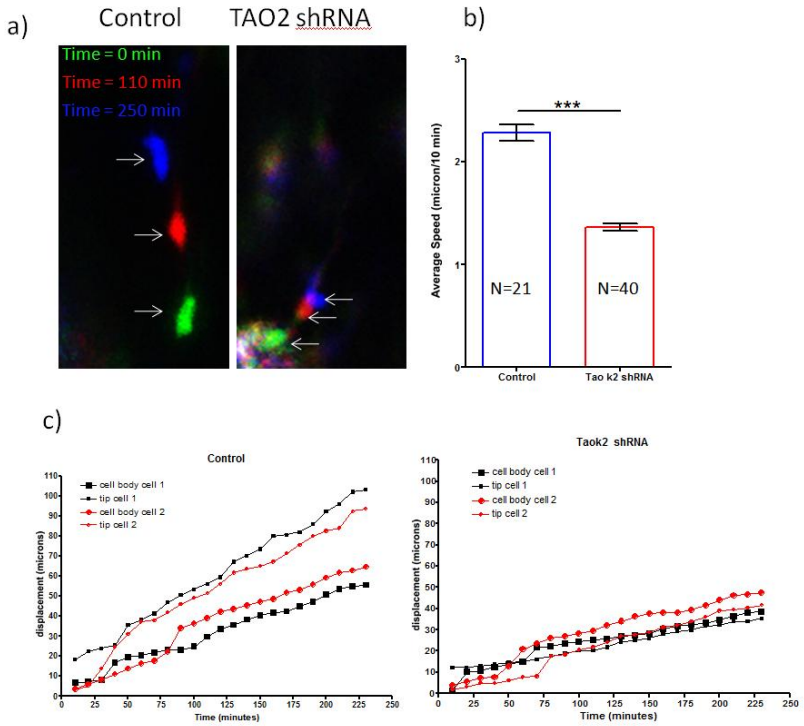

Figure 1.1.4.26. TAOK2 down-regulation affects *in vivo* cell body movement speed and displacement.

(a) Time-lapse fluorescent microscopy of pyramidal neuron transfected with EGFP and control shRNA (left panel) and of pyramidal neurons transfected with EGFP and shRNA-TAOK2. Over a period of 250 minutes is visible a slower migratory path for the knock-down neuron. (Green: time = o min; Red: time = 110 min; Blue: time = 250 min). (b) Quantification of average speed of cell body movement every 10 minutes. TAOK2 knock-down affects cell body movement in the mouse cortex. (c) Analysis of cell displacement over time. Down-regulation of TAOK2 impairs the movement of the neuronal tip during pyramidal neurons interkinetic nuclear migration.

1.1.5. Conclusion

In the current report, we describe a novel molecular pathway that preferentially modulates the formation of basal dendrites in cortical pyramidal neurons, and which also plays a role in axonal projection. Extensive work has addressed the roles of several molecules in dendrite arborization (for review, Jan and Jan, 2010). However, little is known about the molecular differences that may direct the formation of different domains within the same dendritic tree. This work represents the first approach aimed at understanding the mechanisms responsible for the delineation of basal and apical dendrites during pyramidal neuron development in the embryonic cortex.

Over a decade ago, electron microscopy studies in cultured neurons indicated that axons contain microtubules of uniform polarity, while dendrites contain microtubules of mixed polarity (Baas et al., 1989). These data support the concept of the molecular homogeneity of the dendritic tree. However, it was recently found that apical dendrites from hippocampal CA1 and cortical layer V pyramidal neurons ubiquitously have polarized microtubule arrays (Kwan et al., 2008), suggesting that the morphogenesis of dendritic subtypes (i.e. basal versus apical dendrites) may rely upon distinct cellular and molecular pathways. Accordingly, it was shown that post-Golgi membrane trafficking is polarized toward the apical dendrites of pyramidal neurons, and that the disruption of Golgi polarity produces neurons with symmetric dendritic arbors, which lack a single longest principal, or apical, dendrite (Horton et al., 2005).

The Sema3A-Nrp1 signaling cascade is coupled to TAOK2-JNK1 to modulate differentiation of cortical pyramidal neurons.

In previous reports, activation of the Nrp1 receptor by Sema3A appeared to orient the apical dendrites of cortical pyramidal neurons towards the marginal zone (MZ) of the developing cortex and to regulate neuronal polarization (Nishiyama et al., 2011; Shelly et al., 2011). It was also shown that Sema3A – Nrp1 signaling via PlexinA4 controls the basal dendritic arborization of cortical neurons (Chen et al., 2008; Gu et al., 2003; Tran et al., 2009). Since the Nrp1 receptor is likely to be uniformly distributed on all dendritic processes (Tran et al., 2009), as well as the axon (Polleux et al., 2000), one question that arises is how this ubiquitous receptor specifically controls the formation of basal dendrites. The asymmetric localization of soluble guanylate cyclase to apical dendrites has been suggested to mediate the distinct Sema3A responses of axons and dendrites, allowing for the orientation of the apical dendrite towards the MZ (Polleux et al., 2000). However, the downstream effectors by which Sema3A and its receptor regulate basal dendrite morphogenesis have remained obscure.

We now show that TAOK2 down-regulation specifically impairs the formation of basal dendrites, without affecting apical dendrites. These data strongly suggest that TAOK2 acts in concert with the Sema3A-Nrp1 pathway to sustain basal dendrite formation. Our biochemical analyses demonstrate that TAOK2 and Nrp1 form a complex, and that acute Nrp1 down-regulation specifically impairs the formation of the basal dendrite. Importantly, we report that the deficit in basal dendrite formation following Nrp1 down-regulation can be counteracted by TAOK2 overexpression.

Our data also show that TAOK2 appears to be uniformly distributed in the growth cones of cultured developing cortical neurons, without any preference for dendritic or axonal neurites. It is possible that our methods could not detect a differential subcellular distribution of TAOK2. Alternatively, the subcellular compartmentalization of molecules that sustain basal dendrite formation may occur downstream of TAOK2.

The current work implicates activated JNK1 (pJNK1) as an effector of TAOK2 that modulates basal dendrite morphogenesis. It has been shown that pJNK1 is enriched in axons of hippocampal neurons in culture (Oliva et al., 2006). We also found that pJNK1 was preferentially localized to the longest neurite, presumably the axon, of DIV2 cultured cortical neurons. It has also been reported that pJNK1 is involved in the regulation of microtubule dynamics in both axons and dendrites of the hippocampus and cortex (Chang et al., 2003), and that JNK1(-/-) mice exhibit a progressive loss of microtubules within both axons and dendrites (Chang et al., 2003). However, the role of pJNK within the different domains of the dendritic tree has not been clear. In vivo experiments examining the loss-of-function of the MAP kinase phosphatase 1 (MKP-1), which deactivates JNK1, show reduced dendritic arborization of the basal dendrites of cortical pyramidal neurons, as well as impaired axonal branching (Jeanneteau et al., 2010). In agreement with these findings, we found that pJNK1 is preferentially enriched in the basal dendrites and the axons of cortical pyramidal neurons. Moreover, the overexpression of the constitutively active JNK1 counteracted defects in basal dendrite formation and axonal projection following TAOK2 down-regulation.

Therefore, it is plausible that the subcellular compartmentalization of pJNK1 may explain, at least in part, the specific role of TAOK2 in basal dendrite formation and axonal projection (see model in Figure 1.1.4.27). Our results demonstrate that Sema3A/Nrp1-mediated activation of pJNK1 requires TAOK2 (Figure 1.1.4.16c, d), which indicates that the three proteins act in the same pathway. Although additional independent pathways could activate JNK, the existence of such pathways does not preclude the importance of the observed TAOK2-mediated activation of JNK1 in regulating dendrite morphogenesis.

We have concluded previously that TAOK2 down-regulation affects the capability by the neuron to properly guide the cell toward the cortical plate. Depletion of TAOK2 expression leads to actin destabilization and, ultimately, to an improper migration mechanism. However, the neuron keeps the ability to migrate, but it’s much slower in movement. This phenotype may be due to

the cell inability to properly stabilize actin, which would impair substratum selectivity of the growth cone. Since the cortex substratum confers information to the neurons, the slow migration creates a delay causing neurons to surpass their true final destination (they miss the information to stop migration), by adjustment they end more superficially than expected. When they are signaled by molecules for migratory arrest, they are already in a more superficial layer. Also, the down-regulation of TAOK2 affects axon formation, most likely by inactivation of JNK1, a known player in axon formation. The delay in the axon development and the difficulties for its maintenance will have an effect in the establishment of a connection between the axon and another target neuron, an encounter that dictates the end of migration to that specific neuron (Baird et al., 1992). More experiments are needed to understand in deep this phenotype, because we know that the activity of TAOK2 is through actin stabilization but we do not know exactly the mechanism involved. Also, overexpression of the constitutively active form of JNK1 (MKK7-JNK1) did not rescue entirely the migration defect, not only because TAOK2 directly interacts with microtubules, but because other signaling molecules might be involved.

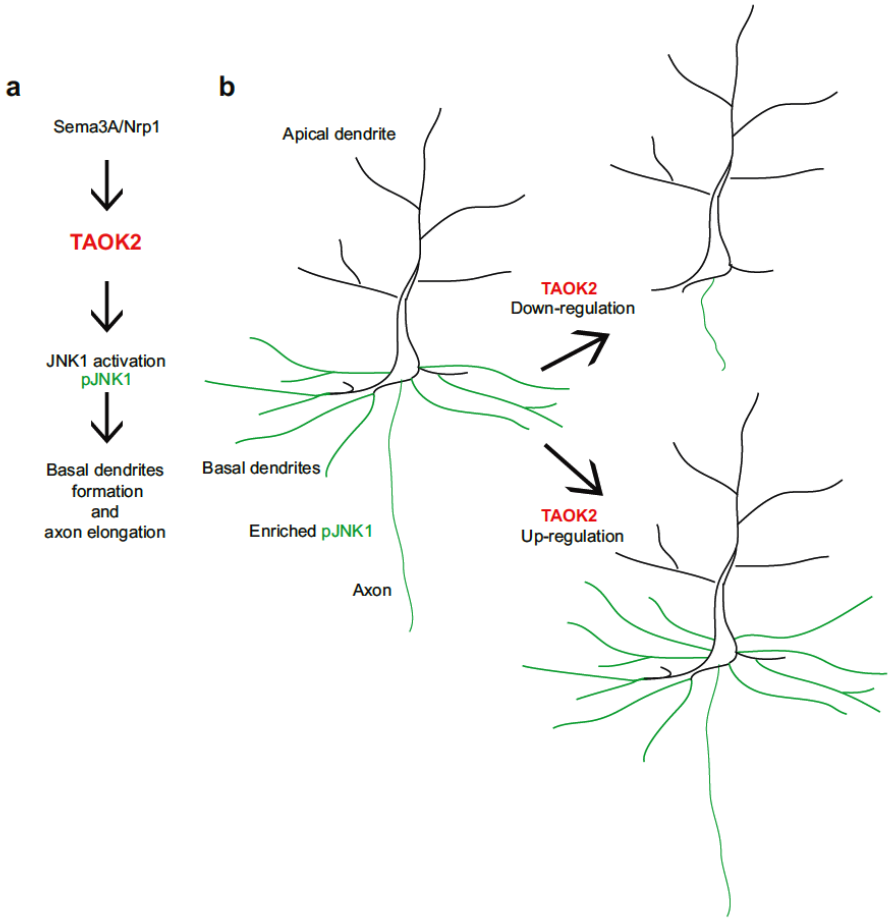

Figure 1.1.4.27. TAOK2 modulates the formation of basal dendrites and axonal elongation in pyramidal neurons.

(a) Flowchart of the key signaling pathway involved in TAOK2-induced formation of basal dendrites. (b) Model: Basal dendrites and axon have enriched activated JNK1 (green, pJNK1) compared with the levels of activated JNK1 in the apical dendrite. If TAOK2 is down regulated, then JNK1 is not active in the basal dendrites and the axon, thus precluding their proper elongation. TAOK2 overexpression increases number of basal dendrites.

TAOK2 and Autism Spectrum Disorders.

Autism spectrum disorder (ASD) is a heterogeneous neurodevelopmental syndrome for which there is not a clear neurobiological etiology. Although the genetic underpinnings of ASD remain elusive in most cases, a unifying model for ASD has recently been suggested (Geschwind and Levitt, 2007). This model proposes that ASD results from a developmental disconnection of brain regions that are involved in higher-order associations. Emerging literature, which shows functional and anatomical cortical under-connectivity in autistic patients, supports this model (Geschwind and Levitt, 2007; Just et al., 2007). The cellular basis for dysfunctional circuits, however, remains poorly understood. Several genes have been described as contributing to ASD (Pinto et al., 2010; Walsh et al., 2008; Weiss et al., 2009), and it has been proposed that aberrant synaptic protein synthesis may represent one pathway leading to an autistic phenotype (Kelleher and Bear, 2008). Recently, a novel, recurrent microdeletion, and a reciprocal microduplication, of chromosome 16p11.2 has been identified that carries substantial susceptibility to autism and appears to account for approximately 1% of cases (Weiss et al., 2008). One of the genes from the affected region encodes for TAOK2.

Therefore, our findings of immature basal dendrite development and axonal projections deficits following TAOK2 down-regulation support the hypothesis that underdeveloped neuron morphology contributes to the disconnection of brain regions that may underlie the autistic phenotype.

It is unknown how depletion of TAOK2 influences the specificity and connectivity between projection neurons, but TAOK2 absence leads to improper migration and basal dendrite formation with a marked diminution of colossal axon development with a pronounced disability to cross the midline. If inhibiting the expression of TAOK2 described in our studies leads to such marked phenotypes, it is most plausible that it will have an effect in the patophysiology of an individual where the TAOK2 gene happens to be misregulated or absent, most likely, leading to a psychiatric disorder associated with neocortical disconnection, the accepted model mechanism for Autism Spectrum Disorders (ASD). Recently, several studies suggest the involvement of TAOK2 in other brain disorders such as Fragile X syndrome (Darnell et al., 2011), schizophrenia (McCarthy et al., 2009), depressive disorders (Degenhardt et al., 2012) and Alzheimer disease (AD) (Tavares et al., 2013), suggesting not only a role in the considered brain developmental disorders with a pronounced pathology since infancy, but expanding to a relevance in brain disorders with onset in adult life. This may suggest that the disorders which happen in adults may have an underlying developmental defect. Further work is necessary to understand how the TAOK2 biological role and activity affects the human brain and how much contribution is given in the complexity of molecules where regulation fails, resulting in a neurological disorder.

1.1.6. References

Adams, P.D., Grosse-Kunstleve, R.W., Hung, L.W., Ioerger, T.R., McCoy, A.J., Moriarty, N.W., Read, R.J., Sacchettini, J.C., Sauter, N.K., and Terwilliger, T.C. (2002). PHENIX: building new software for automated crystallographic structure determination. Acta Crystallogr. D Biol. Crystallogr. *58*, 1948–1954.

Alberts, B. (2009). Essential cell biology (New York: Garland Science).

Alberts, B., Johnson, A., Lewis, J., Raff, M., Roberts, K., and Walter, P. (2002a). Neural Development.

Alberts, B., Johnson, A., Lewis, J., Raff, M., Roberts, K., and Walter, P. (2002b). From DNA to RNA.

Alfano, C., and Studer, M. (2013). Neocortical arealization: Evolution, mechanisms, and open questions. Dev. Neurobiol. *73*, 411–447.

De Anda, F.C., Meletis, K., Ge, X., Rei, D., and Tsai, L.-H. (2010). Centrosome motility is essential for initial axon formation in the neocortex. J. Neurosci. Off. J. Soc. Neurosci. *30*, 10391–10406.

Angevine, J.B., Jr, and Sidman, R.L. (1961). Autoradiographic study of cell migration during histogenesis of cerebral cortex in the mouse. Nature *192*, 766–768.

Arimura, N., and Kaibuchi, K. (2007). Neuronal polarity: from extracellular signals to intracellular mechanisms. Nat. Rev. Neurosci. *8*, 194–205.

Baas, P.W., Black, M.M., and Banker, G.A. (1989). Changes in microtubule polarity orientation during the development of hippocampal neurons in culture. J. Cell Biol. *109*, 3085–3094.

Baird, D.H., Hatten, M.E., and Mason, C.A. (1992). Cerebellar target neurons provide a stop signal for afferent neurite extension in vitro. J. Neurosci. Off. J. Soc. Neurosci. *12*, 619–634.

Balaz, M., Li, B.C., Steinkruger, J.D., Ellestad, G.A., Nakanishi, K., and Berova, N. (2006). Porphyrins conjugated to DNA as CD reporters of the salt-induced B to Z-DNA transition,. Org. Biomol. Chem. *4*, 1865–1867.

Barnat, M., Enslen, H., Propst, F., Davis, R.J., Soares, S., and Nothias, F. (2010). Distinct roles of c-Jun N-terminal kinase isoforms in neurite initiation and elongation during axonal regeneration. J. Neurosci. Off. J. Soc. Neurosci. *30*, 7804–7816.

Barnes, A.P., Solecki, D., and Polleux, F. (2008). New insights into the molecular mechanisms specifying neuronal polarity in vivo. Curr. Opin. Neurobiol. *18*, 44–52.

Bass, R.B., Strop, P., Barclay, M., and Rees, D.C. (2002). Crystal structure of Escherichia coli MscS, a voltage-modulated and mechanosensitive channel. Science *298*, 1582–1587.

Bastmeyer, M., and O'Leary, D.D. (1996). Dynamics of target recognition by interstitial axon branching along developing cortical axons. J. Neurosci. Off. J. Soc. Neurosci. *16*, 1450–1459.

Battaglia, A., Novelli, A., Bernardini, L., Igliozzi, R., and Parrini, B. (2009). Further characterization of the new microdeletion syndrome of 16p11.2-p12.2. Am. J. Med. Genet. A. *149A*, 1200–1204.

Behar, O., Golden, J.A., Mashimo, H., Schoen, F.J., and Fishman, M.C. (1996). Semaphorin III is needed for normal patterning and growth of nerves, bones and heart. Nature *383*, 525–528.

Behe, M., and Felsenfeld, G. (1981). Effects of methylation on a synthetic polynucleotide: the B--Z transition in poly(dG-m5dC).poly(dG-m5dC). Proc. Natl. Acad. Sci. U. S. A. *78*, 1619–1623.

Bellion, A., Baudoin, J.-P., Alvarez, C., Bornens, M., and Métin, C. (2005). Nucleokinesis in Tangentially Migrating Neurons Comprises Two Alternating Phases: Forward Migration of the Golgi/Centrosome Associated with Centrosome Splitting and Myosin Contraction at the Rear. J. Neurosci. *25*, 5691–5699.

Berger, I., Winston, W., Manoharan, R., Schwartz, T., Alfken, J., Kim, Y.G., Lowenhaupt, K., Herbert, A., and Rich, A. (1998). Spectroscopic characterization of a DNA-binding domain, Z alpha, from the editing enzyme, dsRNA adenosine deaminase: evidence for left-handed Z-DNA in the Z alpha-DNA complex. Biochemistry (Mosc.) *37*, 13313–13321.

Berry, M., and Rogers, A.W. (1965). The migration of neuroblasts in the developing cerebral cortex. J. Anat. *99*, 691–709.

Bill, R.M., Henderson, P.J.F., Iwata, S., Kunji, E.R.S., Michel, H., Neutze, R., Newstead, S., Poolman, B., Tate, C.G., and Vogel, H. (2011). Overcoming barriers to membrane protein structure determination. Nat. Biotechnol. *29*, 335–340.

Binda, C., Newton-Vinson, P., Hubálek, F., Edmondson, D.E., and Mattevi, A. (2002). Structure of human monoamine oxidase B, a drug target for the treatment of neurological disorders. Nat. Struct. Biol. *9*, 22–26.

Bjorkblom, B. (2005). Constitutively Active Cytoplasmic c-Jun N-Terminal Kinase 1 Is a Dominant Regulator of Dendritic Architecture: Role of Microtubule-Associated Protein 2 as an Effector. J. Neurosci. *25*, 6350–6361.

Björkblom, B., Ostman, N., Hongisto, V., Komarovski, V., Filén, J.-J., Nyman, T.A., Kallunki, T., Courtney, M.J., and Coffey, E.T. (2005). Constitutively active cytoplasmic c-Jun N-terminal kinase 1 is a dominant regulator of dendritic architecture: role of microtubule-associated protein 2 as an effector. J. Neurosci. Off. J. Soc. Neurosci. *25*, 6350–6361.

Bolla, J.R., Su, C.-C., and Yu, E.W. (2012). Biomolecular membrane protein crystallization. Philos. Mag. Abingdon Engl. *92*, 2648–2661.

Boulder Committee (1970). Embryonic vertebrate central nervous system: revised terminology. The Boulder Committee. Anat. Rec. *166*, 257–261.

Bowie, J.U. (2001). Stabilizing membrane proteins. Curr. Opin. Struct. Biol. *11*, 397–402.

Boyd, D., Schierle, C., and Beckwith, J. (1998). How many membrane proteins are there? Protein Sci. Publ. Protein Soc. *7*, 201–205.

Bracey, M.H., Hanson, M.A., Masuda, K.R., Stevens, R.C., and Cravatt, B.F. (2002). Structural adaptations in a membrane enzyme that terminates endocannabinoid signaling. Science *298*, 1793–1796.

Bradke, F., and Dotti, C.G. (1999). The role of local actin instability in axon formation. Science *283*, 1931–1934.

Brandt, T.A., and Jacobs, B.L. (2001). Both carboxy- and amino-terminal domains of the vaccinia virus interferon resistance gene, E3L, are required for pathogenesis in a mouse model. J. Virol. *75*, 850–856.

Brown, B.A., 2nd, and Rich, A. (2001). The left-handed double helical nucleic acids. Acta Biochim. Pol. *48*, 295–312.

Brown, B.A., Lowenhaupt, K., Wilbert, C.M., Hanlon, E.B., and Rich, A. (2000). The Zα domain of the editing enzyme dsRNA adenosine deaminase binds left-handed Z-RNA as well as Z-DNA. Proc. Natl. Acad. Sci. *97*, 13532–13536.

Brunger, A.T. (2007). Version 1.2 of the Crystallography and NMR system. Nat. Protoc. *2*, 2728–2733.

Brünger, A.T., Adams, P.D., Clore, G.M., DeLano, W.L., Gros, P., Grosse-Kunstleve, R.W., Jiang, J.S., Kuszewski, J., Nilges, M., Pannu, N.S., et al. (1998). Crystallography & NMR system: A new software suite for macromolecular structure determination. Acta Crystallogr. D Biol. Crystallogr. *54*, 905–921.

Buchanan, S.K. (1999). β-Barrel proteins from bacterial outer membranes: structure, function and refolding. Curr. Opin. Struct. Biol. *9*, 455–461.

Burbelo, P.D., Drechsel, D., and Hall, A. (1995). A conserved binding motif defines numerous candidate target proteins for both Cdc42 and Rac GTPases. J. Biol. Chem. *270*, 29071–29074.
Caffrey, M. (2003). Membrane protein crystallization. J. Struct. Biol. *142*, 108–132.
Caffrey, M. (2011). Crystallizing membrane proteins for structure-function studies using lipidic mesophases. Biochem. Soc. Trans. *39*, 725–732.
Caffrey, M., and Cherezov, V. (2009). Crystallizing membrane proteins using lipidic mesophases. Nat. Protoc. *4*, 706–731.
Campbell, K., and Götz, M. (2002). Radial glia: multi-purpose cells for vertebrate brain development. Trends Neurosci. *25*, 235–238.
Carmi, S., Borukhov, I., and Levanon, E.Y. (2011). Identification of widespread ultra-edited human RNAs. PLoS Genet. *7*, e1002317.
CCP4 (1994). The CCP4 suite: programs for protein crystallography. Acta Crystallogr. D Biol. Crystallogr. *50*, 760–763.
Chang, L., Jones, Y., Ellisman, M.H., Goldstein, L.S.B., and Karin, M. (2003). JNK1 is required for maintenance of neuronal microtubules and controls phosphorylation of microtubule-associated proteins. Dev. Cell *4*, 521–533.
Chen, Z., and Cobb, M.H. (2001). Regulation of stress-responsive mitogen-activated protein (MAP) kinase pathways by TAO2. J. Biol. Chem. *276*, 16070–16075.
Chen, C.X., Cho, D.S., Wang, Q., Lai, F., Carter, K.C., and Nishikura, K. (2000). A third member of the RNA-specific adenosine deaminase gene family, ADAR3, contains both single- and double-stranded RNA binding domains. RNA N. Y. N *6*, 755–767.
Chen, G., Sima, J., Jin, M., Wang, K.-Y., Xue, X.-J., Zheng, W., Ding, Y.-Q., and Yuan, X.-B. (2008). Semaphorin-3A guides radial migration of cortical neurons during development. Nat. Neurosci. *11*, 36–44.
Chen, Z., Hutchison, M., and Cobb, M.H. (1999). Isolation of the protein kinase TAO2 and identification of its mitogen-activated protein kinase/extracellular signal-regulated kinase kinase binding domain. J. Biol. Chem. *274*, 28803–28807.
Chen, Z., Raman, M., Chen, L., Lee, S.F., Gilman, A.G., and Cobb, M.H. (2003). TAO (thousand-and-one amino acid) protein kinases mediate signaling from carbachol to p38 mitogen-activated protein kinase and ternary complex factors. J. Biol. Chem. *278*, 22278–22283.
Chenn, A., and McConnell, S.K. (1995). Cleavage orientation and the asymmetric inheritance of Notch1 immunoreactivity in mammalian neurogenesis. Cell *82*, 631–641.
Chilton, J.K. (2006). Molecular mechanisms of axon guidance. Dev. Biol. *292*, 13–24.
Choi, Y.I., Duke-Cohan, J.S., Ahmed, W.B., Handley, M.A., Mann, F., Epstein, J.A., Clayton, L.K., and Reinherz, E.L. (2008). PlexinD1 glycoprotein controls migration of positively selected thymocytes into the medulla. Immunity *29*, 888–898.
Cohen, S.L., and Chait, B.T. (2001). Mass spectrometry as a tool for protein crystallography. Annu. Rev. Biophys. Biomol. Struct. *30*, 67–85.
Corty, M.M., Matthews, B.J., and Grueber, W.B. (2009). Molecules and mechanisms of dendrite development in Drosophila. Development *136*, 1049–1061.
Craig, A.M., and Banker, G. (1994). Neuronal polarity. Annu. Rev. Neurosci. *17*, 267–310.
Dahm, R. (2008). Discovering DNA: Friedrich Miescher and the early years of nucleic acid research. Hum. Genet. *122*, 565–581.
Darnell, J.C., Van Driesche, S.J., Zhang, C., Hung, K.Y.S., Mele, A., Fraser, C.E., Stone, E.F., Chen, C., Fak, J.J., Chi, S.W., et al. (2011). FMRP Stalls Ribosomal Translocation on mRNAs Linked to Synaptic Function and Autism. Cell *146*, 247–261.
Degenhardt, F., Priebe, L., Herms, S., Mattheisen, M., Mühleisen, T.W., Meier, S., Moebus, S., Strohmaier, J., Groß, M., Breuer, R., et al. (2012). Association between copy number variants in 16p11.2 and major depressive disorder in a German case-control sample. Am. J. Med. Genet. Part B Neuropsychiatr. Genet. Off. Publ. Int. Soc. Psychiatr. Genet. *159B*, 263–273.
Deisenhofer, J., Epp, O., Miki, K., Huber, R., and Michel, H. (1985). Structure of the protein subunits in the photosynthetic reaction centre of Rhodopseudomonas viridis at 3|[angst]| resolution. Nature *318*, 618–624.
Desterro, J.M.P., Keegan, L.P., Lafarga, M., Berciano, M.T., O'Connell, M., and Carmo-Fonseca, M. (2003). Dynamic association of RNA-editing enzymes with the nucleolus. J. Cell Sci. *116*, 1805–1818.
Diefenderfer, C., Lee, J., Mlyanarski, S., Guo, Y., and Glover, K.J. (2009). Reliable expression and purification of highly insoluble transmembrane domains. Anal. Biochem. *384*, 274–278.
Dobyns, W.B., and Truwit, C.L. (1995). Lissencephaly and other malformations of cortical development: 1995 update. Neuropediatrics *26*, 132–147.
Dotti, C.G., Sullivan, C.A., and Banker, G.A. (1988). The establishment of polarity by hippocampal neurons in culture. J. Neurosci. *8*, 1454–1468.
Drew, D., Slotboom, D.-J., Friso, G., Reda, T., Genevaux, P., Rapp, M., Meindl-Beinker, N.M., Lambert, W., Lerch, M., Daley, D.O., et al. (2005). A scalable, GFP-based pipeline for membrane protein overexpression screening and purification. Protein Sci. Publ. Protein Soc. *14*, 2011–2017.
Drew, D., Lerch, M., Kunji, E., Slotboom, D.-J., and de Gier, J.-W. (2006). Optimization of membrane protein overexpression and purification using GFP fusions. Nat. Methods *3*, 303–313.
Drew, D., Newstead, S., Sonoda, Y., Kim, H., von Heijne, G., and Iwata, S. (2008). GFP-based optimization scheme for the overexpression and purification of eukaryotic membrane proteins in Saccharomyces cerevisiae. Nat. Protoc. *3*, 784–798.
Drew, D.E., von Heijne, G., Nordlund, P., and de Gier, J.-W.L. (2001). Green fluorescent protein as an indicator to monitor membrane protein overexpression in Escherichia coli. FEBS Lett. *507*, 220–224.
Drew, H.R., Wing, R.M., Takano, T., Broka, C., Tanaka, S., Itakura, K., and Dickerson, R.E. (1981). Structure of a B-DNA dodecamer: conformation and dynamics. Proc. Natl. Acad. Sci. U. S. A. *78*, 2179–2183.
Du, Y., and Zhou, X. (2013). Targeting Non-B-Form DNA in Living Cells. Chem. Rec. *13*, 371–384.
Emsley, P., and Cowtan, K. (2004). Coot: model-building tools for molecular graphics. Acta Crystallogr. D Biol. Crystallogr. *60*, 2126–2132.
Etienne-Manneville, S., and Hall, A. (2002). Rho GTPases in cell biology. Nature *420*, 629–635.
Farkas, L.M., and Huttner, W.B. (2008). The cell biology of neural stem and progenitor cells and its significance for their proliferation versus differentiation during mammalian brain development. Curr. Opin. Cell Biol. *20*, 707–715.
Fenstermaker, V., Chen, Y., Ghosh, A., and Yuste, R. (2004). Regulation of dendritic length and branching by semaphorin 3A. J. Neurobiol. *58*, 403–412.

Ferguson, A.D., McKeever, B.M., Xu, S., Wisniewski, D., Miller, D.K., Yamin, T.-T., Spencer, R.H., Chu, L., Ujjainwalla, F., Cunningham, B.R., et al. (2007). Crystal structure of inhibitor-bound human 5-lipoxygenase-activating protein. Science *317*, 510–512.

Filimonova, M., Gubskaya, V., Davidov, R., Garusov, A., and Nuretdinov, I. (2008). Metal binding induces conversion of B- to the hybrid B-Z-form in natural DNA. Int. J. Biol. Macromol. *43*, 289–294.

Finlay, B.L., and Slattery, M. (1983). Local differences in the amount of early cell death in neocortex predict adult local specializations. Science *219*, 1349–1351.

Forscher, P., and Smith, S.J. (1988). Actions of cytochalasins on the organization of actin filaments and microtubules in a neuronal growth cone. J. Cell Biol. *107*, 1505–1516.

Fu, Y., Comella, N., Tognazzi, K., Brown, L.F., Dvorak, H.F., and Kocher, O. (1999). Cloning of DLM-1, a novel gene that is up-regulated in activated macrophages, using RNA differential display. Gene *240*, 157–163.

Fujii, T., Nakao, F., Shibata, Y., Shioi, G., Kodama, E., Fujisawa, H., and Takagi, S. (2002). Caenorhabditis elegans PlexinA, PLX-1, interacts with transmembrane semaphorins and regulates epidermal morphogenesis. Dev. Camb. Engl. *129*, 2053–2063.

Fukata, M., Nakagawa, M., and Kaibuchi, K. (2003). Roles of Rho-family GTPases in cell polarisation and directional migration. Curr. Opin. Cell Biol. *15*, 590–597.

Geschwind, D.H., and Levitt, P. (2007). Autism spectrum disorders: developmental disconnection syndromes. Curr. Opin. Neurobiol. *17*, 103–111.

Goshima, Y., Ito, T., Sasaki, Y., and Nakamura, F. (2002). Semaphorins as signals for cell repulsion and invasion. J. Clin. Invest. *109*, 993–998.

Götz, M., and Huttner, W.B. (2005). The cell biology of neurogenesis. Nat. Rev. Mol. Cell Biol. *6*, 777–788.

Govek, E.-E., Newey, S.E., and Van Aelst, L. (2005). The role of the Rho GTPases in neuronal development. Genes Dev. *19*, 1–49.

Gregory, W.A., Edmondson, J.C., Hatten, M.E., and Mason, C.A. (1988). Cytology and neuron-glial apposition of migrating cerebellar granule cells in vitro. J. Neurosci. *8*, 1728–1738.

Griffiths, A.J., Miller, J.H., Suzuki, D.T., Lewontin, R.C., and Gelbart, W.M. (2000a). Making recombinant DNA (W. H. Freeman and Company.).

Griffiths, A.J., Miller, J.H., Suzuki, D.T., Lewontin, R.C., and Gelbart, W.M. (2000b). Structure of DNA (W. H. Freeman and Company.).

Gu, C., Rodriguez, E.R., Reimert, D.V., Shu, T., Fritzsch, B., Richards, L.J., Kolodkin, A.L., and Ginty, D.D. (2003). Neuropilin-1 conveys semaphorin and VEGF signaling during neural and cardiovascular development. Dev. Cell *5*, 45–57.

Ha, S.C., Lokanath, N.K., Van Quyen, D., Wu, C.A., Lowenhaupt, K., Rich, A., Kim, Y.-G., and Kim, K.K. (2004). A poxvirus protein forms a complex with left-handed Z-DNA: crystal structure of a Yatapoxvirus Zalpha bound to DNA. Proc. Natl. Acad. Sci. U. S. A. *101*, 14367–14372.

Ha, S.C., Lowenhaupt, K., Rich, A., Kim, Y.-G., and Kim, K.K. (2005). Crystal structure of a junction between B-DNA and Z-DNA reveals two extruded bases. Nature *437*, 1183–1186.

Hall, K., Cruz, P., Tinoco, I., Jr, Jovin, T.M., and van de Sande, J.H. (1984). "Z-RNA"--a left-handed RNA double helix. Nature *311*, 584–586.

Halloran, M.C., and Kalil, K. (1994). Dynamic behaviors of growth cones extending in the corpus callosum of living cortical brain slices observed with video microscopy. J. Neurosci. Off. J. Soc. Neurosci. *14*, 2161–2177.

Hatten, M.E. (2002). New directions in neuronal migration. Science *297*, 1660–1663.

Hays, F.A., Teegarden, A., Jones, Z.J.R., Harms, M., Raup, D., Watson, J., Cavaliere, E., and Ho, P.S. (2005). How sequence defines structure: a crystallographic map of DNA structure and conformation. Proc. Natl. Acad. Sci. U. S. A. *102*, 7157–7162.

Herbert, A., and Rich, A. (1999a). Left-handed Z-DNA: structure and function. Genetica *106*, 37–47.

Herbert, A., and Rich, A. (1999b). Left-Handed Z-DNA: Structure and Function. In Structural Biology and Functional Genomics, E.M. Bradbury, and S. Pongor, eds. (Springer Netherlands), pp. 53–72.

Herbert, A.G., and Rich, A. (1993). A method to identify and characterize Z-DNA binding proteins using a linear oligodeoxynucleotide. Nucleic Acids Res. *21*, 2669–2672.

Herbert, A., Lowenhaupt, K., Spitzner, J., and Rich, A. (1995). Chicken double-stranded RNA adenosine deaminase has apparent specificity for Z-DNA. Proc. Natl. Acad. Sci. U. S. A. *92*, 7550–7554.

Hirokawa, T., Boon-Chieng, S., and Mitaku, S. (1998). SOSUI: classification and secondary structure prediction system for membrane proteins. Bioinformatics *14*, 378–379.

Hopkins, A.L., and Groom, C.R. (2002). The druggable genome. Nat. Rev. Drug Discov. *1*, 727–730.

Horton, A.C., Rácz, B., Monson, E.E., Lin, A.L., Weinberg, R.J., and Ehlers, M.D. (2005). Polarized secretory trafficking directs cargo for asymmetric dendrite growth and morphogenesis. Neuron *48*, 757–771.

Hota, P.K., and Buck, M. (2012). Plexin structures are coming: opportunities for multilevel investigations of semaphorin guidance receptors, their cell signaling mechanisms, and functions. Cell. Mol. Life Sci. CMLS *69*, 3765–3805.

Huangfu, W.-C., Omori, E., Akira, S., Matsumoto, K., and Ninomiya-Tsuji, J. (2006). Osmotic stress activates the TAK1-JNK pathway while blocking TAK1-mediated NF-kappaB activation: TAO2 regulates TAK1 pathways. J. Biol. Chem. *281*, 28802–28810.

Huber, A.B., Kolodkin, A.L., Ginty, D.D., and Cloutier, J.-F. (2003). SIGNALING AT THE GROWTH CONE: Ligand-Receptor Complexes and the Control of Axon Growth and Guidance. Annu. Rev. Neurosci. *26*, 509–563.

Huber, A.B., Kania, A., Tran, T.S., Gu, C., De Marco Garcia, N., Lieberam, I., Johnson, D., Jessell, T.M., Ginty, D.D., and Kolodkin, A.L. (2005). Distinct roles for secreted semaphorin signaling in spinal motor axon guidance. Neuron *48*, 949–964.

Iwata, S., and Chayen NE. Crystallization of Membrane Proteins in Oils. (2003). Methods and Results in Crystallization of Membrane Proteins (Internat'l University Line).

Jabr, F. (2012). Know Your Neurons: The Discovery and Naming of the Neuron.

Jan, Y.-N., and Jan, L.Y. (2010). Branching out: mechanisms of dendritic arborization. Nat. Rev. Neurosci. *11*, 316–328.

Jeanneteau, F., Deinhardt, K., Miyoshi, G., Bennett, A.M., and Chao, M.V. (2010). The MAP kinase phosphatase MKP-1 regulates BDNF-induced axon branching. Nat. Neurosci. *13*, 1373–1379.

Johnston, B.H., Quigley, G.J., Ellison, M.J., and Rich, A. (1991). The Z-Z junction: the boundary between two out-of-phase Z-DNA regions. Biochemistry (Mosc.) *30*, 5257–5263.

Jones, E.G. (1986). Neurotransmitters in the cerebral cortex. J. Neurosurg. *65*, 135–153.

Junge, F., Schneider, B., Reckel, S., Schwarz, D., Dötsch, V., and Bernhard, F. (2008). Large-scale production of functional membrane proteins. Cell. Mol. Life Sci. CMLS *65*, 1729–1755.

Just, M.A., Cherkassky, V.L., Keller, T.A., Kana, R.K., and Minshew, N.J. (2007). Functional and anatomical cortical underconnectivity in autism: evidence from an FMRI study of an executive function task and corpus callosum morphometry. Cereb. Cortex N. Y. N 1991 *17*, 951–961.

Kalil, K., Szebenyi, G., and Dent, E.W. (2000). Common mechanisms underlying growth cone guidance and axon branching. J. Neurobiol. *44*, 145–158.

Kawate, T., and Gouaux, E. (2006). Fluorescence-Detection Size-Exclusion Chromatography for Precrystallization Screening of Integral Membrane Proteins. Structure *14*, 673–681.

Kelleher, R.J., 3rd, and Bear, M.F. (2008). The autistic neuron: troubled translation? Cell *135*, 401–406.

Kelsch, W., Mosley, C.P., Lin, C.-W., and Lois, C. (2007). Distinct mammalian precursors are committed to generate neurons with defined dendritic projection patterns. PLoS Biol. *5*, e300.

Kim, D., Reddy, S., Kim, D.Y., Rich, A., Lee, S., Kim, K.K., and Kim, Y.-G. (2009). Base extrusion is found at helical junctions between right- and left-handed forms of DNA and RNA. Nucleic Acids Res. *37*, 4353–4359.

Kim, U., Wang, Y., Sanford, T., Zeng, Y., and Nishikura, K. (1994). Molecular cloning of cDNA for double-stranded RNA adenosine deaminase, a candidate enzyme for nuclear RNA editing. Proc. Natl. Acad. Sci. U. S. A. *91*, 11457–11461.

Kim, Y.-G., Lowenhaupt, K., Maas, S., Herbert, A., Schwartz, T., and Rich, A. (2000). The Zab Domain of the Human RNA Editing Enzyme ADAR1 Recognizes Z-DNA When Surrounded by B-DNA. J. Biol. Chem. *275*, 26828–26833.

Kim, Y.-G., Muralinath, M., Brandt, T., Pearcy, M., Hauns, K., Lowenhaupt, K., Jacobs, B.L., and Rich, A. (2003). A role for Z-DNA binding in vaccinia virus pathogenesis. Proc. Natl. Acad. Sci. U. S. A. *100*, 6974–6979.

King, I., Tsai, L.T.-Y., Pflanz, R., Voigt, A., Lee, S., Jäckle, H., Lu, B., and Heberlein, U. (2011). Drosophila tao Controls Mushroom Body Development and Ethanol-Stimulated Behavior through par-1. J. Neurosci. Off. J. Soc. Neurosci. *31*, 1139–1148.

Kitsukawa, T., Shimizu, M., Sanbo, M., Hirata, T., Taniguchi, M., Bekku, Y., Yagi, T., and Fujisawa, H. (1997). Neuropilin-semaphorin III/D-mediated chemorepulsive signals play a crucial role in peripheral nerve projection in mice. Neuron *19*, 995–1005.

Kolodkin, A.L., Matthes, D.J., O'Connor, T.P., Patel, N.H., Admon, A., Bentley, D., and Goodman, C.S. (1992). Fasciclin IV: sequence, expression, and function during growth cone guidance in the grasshopper embryo. Neuron *9*, 831–845.

Komiyama, T., and Luo, L. (2007). Intrinsic control of precise dendritic targeting by an ensemble of transcription factors. Curr. Biol. CB *17*, 278–285.

Konur, S., and Ghosh, A. (2005). Calcium signaling and the control of dendritic development. Neuron *46*, 401–405.

Kowalczyk, T., Pontious, A., Englund, C., Daza, R.A.M., Bedogni, F., Hodge, R., Attardo, A., Bell, C., Huttner, W.B., and Hevner, R.F. (2009). Intermediate neuronal progenitors (basal progenitors) produce pyramidal-projection neurons for all layers of cerebral cortex. Cereb. Cortex N. Y. N 1991 *19*, 2439–2450.

Kriegstein, A.R., and Götz, M. (2003). Radial glia diversity: a matter of cell fate. Glia *43*, 37–43.

Kumanogoh, A., and Takamatsu, H. (2012). Regulation of immune cell responses by semaphorins and their receptors. Arthritis Res. Ther. *14*, O45.

Kwan, A.C., Dombeck, D.A., and Webb, W.W. (2008). Polarized microtubule arrays in apical dendrites and axons. Proc. Natl. Acad. Sci. U. S. A. *105*, 11370–11375.

Lee, A.C., and Suter, D.M. (2008). Quantitative analysis of microtubule dynamics during adhesion-mediated growth cone guidance. Dev. Neurobiol. *68*, 1363–1377.

Lehninger, A.L., Nelson, D.L., and Cox, M.M. (2000). Lehninger principles of biochemistry. (New York: Worth Publishers).

Lei, K., Nimnual, A., Zong, W.-X., Kennedy, N.J., Flavell, R.A., Thompson, C.B., Bar-Sagi, D., and Davis, R.J. (2002). The Bax subfamily of Bcl2-related proteins is essential for apoptotic signal transduction by c-Jun NH(2)-terminal kinase. Mol. Cell. Biol. *22*, 4929–4942.

Leng, J., and Salmon, J.-B. (2009). Microfluidic crystallization. Lab. Chip *9*, 24–34.

Leslie, A.G.W. (2006). The integration of macromolecular diffraction data. Acta Crystallogr. D Biol. Crystallogr. *62*, 48–57.

Levanon, E.Y., Eisenberg, E., Yelin, R., Nemzer, S., Hallegger, M., Shemesh, R., Fligelman, Z.Y., Shoshan, A., Pollock, S.R., Sztybel, D., et al. (2004). Systematic identification of abundant A-to-I editing sites in the human transcriptome. Nat. Biotechnol. *22*, 1001–1005.

Liu, J.S. (2011). Molecular genetics of neuronal migration disorders. Curr. Neurol. Neurosci. Rep. *11*, 171–178.

Liu, T., Rohn, J.L., Picone, R., Kunda, P., and Baum, B. (2010). Tao-1 is a negative regulator of microtubule plus-end growth. J. Cell Sci. *123*, 2708–2716.

Liu, Y., Wolff, K.C., Jacobs, B.L., and Samuel, C.E. (2001). Vaccinia virus E3L interferon resistance protein inhibits the interferon-induced adenosine deaminase A-to-I editing activity. Virology *289*, 378–387.

Loll, P.J., Tretiakova, A., and Soderblom, E. (2003). Compatibility of detergents with the microbatch-under-oil crystallization method. Acta Crystallogr. D Biol. Crystallogr. *59*, 1114–1116.

London, M., and Häusser, M. (2005). Dendritic Computation. Annu. Rev. Neurosci. *28*, 503–532.

Long, S.B., Campbell, E.B., and Mackinnon, R. (2005). Crystal structure of a mammalian voltage-dependent Shaker family K+ channel. Science *309*, 897–903.

Lowery, L.A., and Van Vactor, D. (2009). The trip of the tip: understanding the growth cone machinery. Nat. Rev. Mol. Cell Biol. *10*, 332–343.

Lu, X.-J., and Olson, W.K. (2003). 3DNA: a software package for the analysis, rebuilding and visualization of three-dimensional nucleic acid structures. Nucleic Acids Res. *31*, 5108–5121.

Maas, S., Rich, A., and Nishikura, K. (2003). A-to-I RNA editing: recent news and residual mysteries. J. Biol. Chem. *278*, 1391–1394.

Mancia, F., and Hendrickson, W.A. (2007). Expression of recombinant G-protein coupled receptors for structural biology. Mol. Biosyst. *3*, 723–734.

Mao, Y., Ge, X., Frank, C.L., Madison, J.M., Koehler, A.N., Doud, M.K., Tassa, C., Berry, E.M., Soda, T., Singh, K.K., et al. (2009). Disrupted in schizophrenia 1 regulates neuronal progenitor proliferation via modulation of GSK3beta/beta-catenin signaling. Cell *136*, 1017–1031.

Marsh, L., and Letourneau, P.C. (1984). Growth of neurites without filopodial or lamellipodial activity in the presence of cytochalasin B. J. Cell Biol. *99*, 2041–2047.

Martinez Molina, D., Wetterholm, A., Kohl, A., McCarthy, A.A., Niegowski, D., Ohlson, E., Hammarberg, T., Eshaghi, S., Haeggström, J.Z., and Nordlund, P. (2007). Structural basis for synthesis of inflammatory mediators by human leukotriene C4 synthase. Nature *448*, 613–616.

McCarthy, S.E., Makarov, V., Kirov, G., Addington, A.M., McClellan, J., Yoon, S., Perkins, D.O., Dickel, D.E., Kusenda, M., Krastoshevsky, O., et al. (2009). Microduplications of 16p11.2 are associated with schizophrenia. Nat. Genet. *41*, 1223–1227.

McCormick, A.M., and Leipzig, N.D. (2012). Neural regenerative strategies incorporating biomolecular axon guidance signals. Ann. Biomed. Eng. *40*, 578–597.

McCoy, A.J., Grosse-Kunstleve, R.W., Adams, P.D., Winn, M.D., Storoni, L.C., and Read, R.J. (2007). Phaser crystallographic software. J. Appl. Crystallogr. *40*, 658–674.

McManus, M.F., and Golden, J.A. (2005). Neuronal migration in developmental disorders. J. Child Neurol. *20*, 280–286.

Medeiros, N.A., Burnette, D.T., and Forscher, P. (2006). Myosin II functions in actin-bundle turnover in neuronal growth cones. Nat. Cell Biol. *8*, 215–226.

Miao, H.Q., Soker, S., Feiner, L., Alonso, J.L., Raper, J.A., and Klagsbrun, M. (1999). Neuropilin-1 mediates collapsin-1/semaphorin III inhibition of endothelial cell motility: functional competition of collapsin-1 and vascular endothelial growth factor-165. J. Cell Biol. *146*, 233–242.

Micucci, C., Orciari, S., and Catalano, A. (2010). Semaphorins and their receptors in stem and cancer cells. Curr. Med. Chem. *17*, 3462–3475.

Mitsopoulos, C., Zihni, C., Garg, R., Ridley, A.J., and Morris, J.D.H. (2003). The prostate-derived sterile 20-like kinase (PSK) regulates microtubule organization and stability. J. Biol. Chem. *278*, 18085–18091.

Moore, T.M., Garg, R., Johnson, C., Coptcoat, M.J., Ridley, A.J., and Morris, J.D. (2000). PSK, a novel STE20-like kinase derived from prostatic carcinoma that activates the c-Jun N-terminal kinase mitogen-activated protein kinase pathway and regulates actin cytoskeletal organization. J. Biol. Chem. *275*, 4311–4322.

Murray, R.M., Jones, P., and O'Callaghan, E. (1991). Fetal brain development and later schizophrenia. Ciba Found. Symp. *156*, 155–163; discussion 163–170.

Neukirchen, D., and Bradke, F. (2011). Neuronal polarization and the cytoskeleton. Semin. Cell Dev. Biol. *22*, 825–833.

Newstead, S., Ferrandon, S., and Iwata, S. (2008). Rationalizing alpha-helical membrane protein crystallization. Protein Sci. Publ. Protein Soc. *17*, 466–472.

Ng, J.D., Gavira, J.A., and García-Ruíz, J.M. (2003). Protein crystallization by capillary counterdiffusion for applied crystallographic structure determination. J. Struct. Biol. *142*, 218–231.

Ng, J.D., Stevens, R.C., and Kuhn, P. (2008). Protein crystallization in restricted geometry: advancing old ideas for modern times in structural proteomics. Methods Mol. Biol. Clifton NJ *426*, 363–376.

Nishiyama, M., Togashi, K., von Schimmelmann, M.J., Lim, C.-S., Maeda, S., Yamashita, N., Goshima, Y., Ishii, S., and Hong, K. (2011). Semaphorin 3A induces CaV2.3 channel-dependent conversion of axons to dendrites. Nat. Cell Biol. *13*, 676–685.

Noctor, S.C., Flint, A.C., Weissman, T.A., Dammerman, R.S., and Kriegstein, A.R. (2001). Neurons derived from radial glial cells establish radial units in neocortex. Nature *409*, 714–720.

Noctor, S.C., Martínez-Cerdeño, V., Ivic, L., and Kriegstein, A.R. (2004). Cortical neurons arise in symmetric and asymmetric division zones and migrate through specific phases. Nat. Neurosci. *7*, 136–144.

Noctor, S.C., Martínez-Cerdeño, V., and Kriegstein, A.R. (2008). Distinct behaviors of neural stem and progenitor cells underlie cortical neurogenesis. J. Comp. Neurol. *508*, 28–44.

Nordheim, A., and Rich, A. (1983). The sequence (dC-dA)n X (dG-dT)n forms left-handed Z-DNA in negatively supercoiled plasmids. Proc. Natl. Acad. Sci. U. S. A. *80*, 1821–1825.

O'Leary, D.D., Bicknese, A.R., De Carlos, J.A., Heffner, C.D., Koester, S.E., Kutka, L.J., and Terashima, T. (1990). Target selection by cortical axons: alternative mechanisms to establish axonal connections in the developing brain. Cold Spring Harb. Symp. Quant. Biol. *55*, 453–468.

Oliva, A.A., Jr, Atkins, C.M., Copenagle, L., and Banker, G.A. (2006). Activated c-Jun N-terminal kinase is required for axon formation. J. Neurosci. Off. J. Soc. Neurosci. *26*, 9462–9470.

Opekarová, M., and Tanner, W. (2003). Specific lipid requirements of membrane proteins--a putative bottleneck in heterologous expression. Biochim. Biophys. Acta *1610*, 11–22.

Patterson, J.B., and Samuel, C.E. (1995). Expression and regulation by interferon of a double-stranded-RNA-specific adenosine deaminase from human cells: evidence for two forms of the deaminase. Mol. Cell. Biol. *15*, 5376–5388.

Pearlman, A.L., Faust, P.L., Hatten, M.E., and Brunstrom, J.E. (1998). New directions for neuronal migration. Curr. Opin. Neurobiol. *8*, 45–54.

Peck, L.J., Nordheim, A., Rich, A., and Wang, J.C. (1982). Flipping of cloned d(pCpG)n.d(pCpG)n DNA sequences from right- to left-handed helical structure by salt, Co(III), or negative supercoiling. Proc. Natl. Acad. Sci. U. S. A. *79*, 4560–4564.

Perälä, N., Sariola, H., and Immonen, T. (2012). More than nervous: the emerging roles of plexins. Differ. Res. Biol. Divers. *83*, 77–91.

Pinto, D., Pagnamenta, A.T., Klei, L., Anney, R., Merico, D., Regan, R., Conroy, J., Magalhaes, T.R., Correia, C., Abrahams, B.S., et al. (2010). Functional impact of global rare copy number variation in autism spectrum disorders. Nature *466*, 368–372.

Placido, D., Brown, B.A., 2nd, Lowenhaupt, K., Rich, A., and Athanasiadis, A. (2007). A left-handed RNA double helix bound by the Z alpha domain of the RNA-editing enzyme ADAR1. Struct. Lond. Engl. 1993 *15*, 395–404.

Pohl, F.M., and Jovin, T.M. (1972). Salt-induced co-operative conformational change of a synthetic DNA: equilibrium and kinetic studies with poly (dG-dC). J. Mol. Biol. *67*, 375–396.

Poliakov, G.I. (1961). Some results of research into the development of the neuronal structure of the cortical ends of the analyzers in man. J. Comp. Neurol. *117*, 197–212.

Polleux, F., and Snider, W. (2010). Initiating and growing an axon. Cold Spring Harb. Perspect. Biol. *2*, a001925.

Polleux, F., Morrow, T., and Ghosh, A. (2000). Semaphorin 3A is a chemoattractant for cortical apical dendrites. Nature *404*, 567–573.

Popenda, M., Milecki, J., and Adamiak, R.W. (2004). High salt solution structure of a left-handed RNA double helix. Nucleic Acids Res. *32*, 4044–4054.

Potiron, V.A., Roche, J., and Drabkin, H.A. (2009). Semaphorins and their receptors in lung cancer. Cancer Lett. *273*, 1–14.

Poulsen, H., Nilsson, J., Damgaard, C.K., Egebjerg, J., and Kjems, J. (2001). CRM1 Mediates the Export of ADAR1 through a Nuclear Export Signal within the Z-DNA Binding Domain. Mol. Cell. Biol. *21*, 7862–7871.

Powell, H.R. (1999). The Rossmann Fourier autoindexing algorithm in MOSFLM. Acta Crystallogr. D Biol. Crystallogr. *55*, 1690–1695.

Privé, G.G. (2007). Detergents for the stabilization and crystallization of membrane proteins. Methods San Diego Calif *41*, 388–397.

Privé, G.G., Yanagi, K., and Dickerson, R.E. (1991). Structure of the B-DNA decamer C-C-A-A-C-G-T-T-G-G and comparison with isomorphous decamers C-C-A-A-G-A-T-T-G-G and C-C-A-G-G-C-C-T-G-G. J. Mol. Biol. *217*, 177–199.
Rakic, P. (1972). Mode of cell migration to the superficial layers of fetal monkey neocortex. J. Comp. Neurol. *145*, 61–83.
Rakic, P. (1974). Neurons in rhesus monkey visual cortex: systematic relation between time of origin and eventual disposition. Science *183*, 425–427.
Rakic, P. (1990). Principles of neural cell migration. Experientia *46*, 882–891.
Ramón y Cajal, S. (1952). Structure and connections of neurons. Bull. Los Angel. Neurol. Soc. *17*, 5–46.
Ramón y Cajal, S. (1995). Histology of the nervous system of man and vertebrates (New York: Oxford University Press).
Rasmussen, S.G.F., Choi, H.-J., Rosenbaum, D.M., Kobilka, T.S., Thian, F.S., Edwards, P.C., Burghammer, M., Ratnala, V.R.P., Sanishvili, R., Fischetti, R.F., et al. (2007). Crystal structure of the human beta2 adrenergic G-protein-coupled receptor. Nature *450*, 383–387.
Rich, A., and Davies, D.R. (1956). A new two stranded helical structure: polyadenylic acid and polyuridylic acid. J. Am. Chem. Soc. *78*, 3548–3549.
Rich, A., and Zhang, S. (2003a). Z-DNA: the long road to biological function. Nat. Rev. Genet. *4*, 566–572.
Rich, A., and Zhang, S. (2003b). Timeline: Z-DNA: the long road to biological function. Nat. Rev. Genet. *4*, 566–572.
Robert C. Hockney (1994). Recent developments in heterologous protein production in Escherichia coli. Trends Biotechnol. *12*, 456–463.
Rockel, A.J., Hiorns, R.W., and Powell, T.P. (1980). The basic uniformity in structure of the neocortex. Brain J. Neurol. *103*, 221–244.
Romand, S., Wang, Y., Toledo-Rodriguez, M., and Markram, H. (2011). Morphological development of thick-tufted layer v pyramidal cells in the rat somatosensory cortex. Front. Neuroanat. *5*, 5.
Rosário, M., Schuster, S., Jüttner, R., Parthasarathy, S., Tarabykin, V., and Birchmeier, W. (2012). Neocortical dendritic complexity is controlled during development by NOMA-GAP-dependent inhibition of Cdc42 and activation of cofilin. Genes Dev. *26*, 1743–1757.
Rosso, S.B., Sussman, D., Wynshaw-Boris, A., and Salinas, P.C. (2005). Wnt signaling through Dishevelled, Rac and JNK regulates dendritic development. Nat. Neurosci. *8*, 34–42.
Rothenburg, S., Deigendesch, N., Dittmar, K., Koch-Nolte, F., Haag, F., Lowenhaupt, K., and Rich, A. (2005). A PKR-like eukaryotic initiation factor 2alpha kinase from zebrafish contains Z-DNA binding domains instead of dsRNA binding domains. Proc. Natl. Acad. Sci. U. S. A. *102*, 1602–1607.
Sansam, C.L., Wells, K.S., and Emeson, R.B. (2003). Modulation of RNA editing by functional nucleolar sequestration of ADAR2. Proc. Natl. Acad. Sci. U. S. A. *100*, 14018–14023.
Savva, Y.A., Rieder, L.E., and Reenan, R.A. (2012). The ADAR protein family. Genome Biol. *13*, 252.
Schaar, B.T., and McConnell, S.K. (2005). Cytoskeletal coordination during neuronal migration. Proc. Natl. Acad. Sci. U. S. A. *102*, 13652–13657.
Schade, M., Turner, C.J., Kühne, R., Schmieder, P., Lowenhaupt, K., Herbert, A., Rich, A., and Oschkinat, H. (1999). The solution structure of the Zα domain of the human RNA editing enzyme ADAR1 reveals a prepositioned binding surface for Z-DNA. Proc. Natl. Acad. Sci. *96*, 12465–12470.
Schaefer, A.W., Schoonderwoert, V.T.G., Ji, L., Mederios, N., Danuser, G., and Forscher, P. (2008). Coordination of actin filament and microtubule dynamics during neurite outgrowth. Dev. Cell *15*, 146–162.
Schultz, J., Milpetz, F., Bork, P., and Ponting, C.P. (1998). SMART, a simple modular architecture research tool: identification of signaling domains. Proc. Natl. Acad. Sci. U. S. A. *95*, 5857–5864.
Schüz, A., and Palm, G. (1989). Density of neurons and synapses in the cerebral cortex of the mouse. J. Comp. Neurol. *286*, 442–455.
Schwartz, T., Rould, M.A., Lowenhaupt, K., Herbert, A., and Rich, A. (1999). Crystal structure of the Zalpha domain of the human editing enzyme ADAR1 bound to left-handed Z-DNA. Science *284*, 1841–1845.
Schwartz, T., Behlke, J., Lowenhaupt, K., Heinemann, U., and Rich, A. (2001). Structure of the DLM-1-Z-DNA complex reveals a conserved family of Z-DNA-binding proteins. Nat. Struct. Biol. *8*, 761–765.
Serini, G., Maione, F., Giraudo, E., and Bussolino, F. (2009). Semaphorins and tumor angiogenesis. Angiogenesis *12*, 187–193.
Severs, V.-N., and Whiting, J. (2002). Oswald Avery and the story of DNA (Bear, Del.: Mitchell Lane).
Shelly, M., Cancedda, L., Lim, B.K., Popescu, A.T., Cheng, P., Gao, H., and Poo, M. (2011). Semaphorin3A regulates neuronal polarization by suppressing axon formation and promoting dendrite growth. Neuron *71*, 433–446.
Shing, P., and Carter, M. (2011). DNA Structure: Alphabet Soup for the Cellular Soul. In DNA Replication-Current Advances, H. Seligmann, ed. (InTech),.
Sidman, R.L., and Rakic, P. (1973). Neuronal migration, with special reference to developing human brain: a review. Brain Res. *62*, 1–35.
SIDMAN, R.L., MIALE, I.L., and FEDER, N. (1959). Cell proliferation and migration in the primitive ependymal zone: an autoradiographic study of histogenesis in the nervous system. Exp. Neurol. *1*, 322–333.
Simó, S., and Cooper, J.A. (2012). Regulation of dendritic branching by Cdc42 GAPs. Genes Dev. *26*, 1653–1658.
Singer, S.J., and Nicolson, G.L. (1972). The Fluid Mosaic Model of the Structure of Cell Membranes. Science *175*, 720–731.
Smith, H.C., Gott, J.M., and Hanson, M.R. (1997). A guide to RNA editing. RNA *3*, 1105–1123.
Stagi, M., Gorlovoy, P., Larionov, S., Takahashi, K., and Neumann, H. (2006). Unloading kinesin transported cargoes from the tubulin track via the inflammatory c-Jun N-terminal kinase pathway. FASEB J. Off. Publ. Fed. Am. Soc. Exp. Biol. *20*, 2573–2575.
Stevens, T.J., and Arkin, I.T. (2000). Do more complex organisms have a greater proportion of membrane proteins in their genomes? Proteins Struct. Funct. Bioinforma. *39*, 417–420.
Sutton, B.J., and Sohi, M.K. (1994). Crystallization of membrane proteins for X-ray analysis. Methods Mol. Biol. Clifton NJ *27*, 1–18.
Tabet, A.-C., Pilorge, M., Delorme, R., Amsellem, F., Pinard, J.-M., Leboyer, M., Verloes, A., Benzacken, B., and Betancur, C. (2012). Autism multiplex family with 16p11.2p12.2 microduplication syndrome in monozygotic twins and distal 16p11.2 deletion in their brother. Eur. J. Hum. Genet. EJHG *20*, 540–546.
Takahashi, T., Nowakowski, R.S., and Caviness, V.S., Jr (1996). The leaving or Q fraction of the murine cerebral proliferative epithelium: a general model of neocortical neuronogenesis. J. Neurosci. Off. J. Soc. Neurosci. *16*, 6183–6196.
Takahashi, T., Fournier, A., Nakamura, F., Wang, L.H., Murakami, Y., Kalb, R.G., Fujisawa, H., and Strittmatter, S.M. (1999). Plexin-neuropilin-1 complexes form functional semaphorin-3A receptors. Cell *99*, 59–69.

Takamatsu, H., Takegahara, N., Nakagawa, Y., Tomura, M., Taniguchi, M., Friedel, R.H., Rayburn, H., Tessier-Lavigne, M., Yoshida, Y., Okuno, T., et al. (2010). Semaphorins guide the entry of dendritic cells into the lymphatics by activating myosin II. Nat. Immunol. *11*, 594–600.

Tamagnone, L., Artigiani, S., Chen, H., He, Z., Ming, G.I., Song, H., Chedotal, A., Winberg, M.L., Goodman, C.S., Poo, M., et al. (1999). Plexins are a large family of receptors for transmembrane, secreted, and GPI-anchored semaphorins in vertebrates. Cell *99*, 71–80.

Taniguchi, M., Yuasa, S., Fujisawa, H., Naruse, I., Saga, S., Mishina, M., and Yagi, T. (1997). Disruption of semaphorin III/D gene causes severe abnormality in peripheral nerve projection. Neuron *19*, 519–530.

Tararuk, T., Ostman, N., Li, W., Björkblom, B., Padzik, A., Zdrojewska, J., Hongisto, V., Herdegen, T., Konopka, W., Courtney, M.J., et al. (2006). JNK1 phosphorylation of SCG10 determines microtubule dynamics and axodendritic length. J. Cell Biol. *173*, 265–277.

Tavares, I.A., Touma, D., Lynham, S., Troakes, C., Schober, M., Causevic, M., Garg, R., Noble, W., Killick, R., Bodi, I., et al. (2013). Prostate-derived Sterile 20-like Kinases (PSKs/TAOKs) Phosphorylate Tau Protein and Are Activated in Tangle-bearing Neurons in Alzheimer Disease. J. Biol. Chem. *288*, 15418–15429.

Tillo, M., Ruhrberg, C., and Mackenzie, F. (2012). Emerging roles for semaphorins and VEGFs in synaptogenesis and synaptic plasticity. Cell Adhes. Migr. *6*, 541–546.

Tobin, M.J. (2003). April 25, 1953: Three Papers, Three Lessons. Am. J. Respir. Crit. Care Med. *167*, 1047–1049.

Tran, T.S., Rubio, M.E., Clem, R.L., Johnson, D., Case, L., Tessier-Lavigne, M., Huganir, R.L., Ginty, D.D., and Kolodkin, A.L. (2009). Secreted semaphorins control spine distribution and morphogenesis in the postnatal CNS. Nature *462*, 1065–1069.

Trulson, M.O., Cruz, P., Puglisi, J.D., Tinoco, I., Jr, and Mathies, R.A. (1987). Raman spectroscopic study of left-handed Z-RNA. Biochemistry (Mosc.) *26*, 8624–8630.

Tsai, L.-H., and Gleeson, J.G. (2005). Nucleokinesis in Neuronal Migration. Neuron *46*, 383–388.

Vagin, A., and Teplyakov, A. (2010). Molecular replacement with MOLREP. Acta Crystallogr. D Biol. Crystallogr. *66*, 22–25.

Vallee, R.B., Seale, G.E., and Tsai, J.-W. (2009). Emerging roles for myosin II and cytoplasmic dynein in migrating neurons and growth cones. Trends Cell Biol. *19*, 347–355.

Wallin, E., and von Heijne, G. (1998). Genome-wide analysis of integral membrane proteins from eubacterial, archaean, and eukaryotic organisms. Protein Sci. Publ. Protein Soc. *7*, 1029–1038.

Walsh, C.A., Morrow, E.M., and Rubenstein, J.L.R. (2008). Autism and brain development. Cell *135*, 396–400.

Wang, A.H.-J., Quigley, G.J., Kolpak, F.J., Crawford, J.L., van Boom, J.H., van der Marel, G., and Rich, A. (1979). Molecular structure of a left-handed double helical DNA fragment at atomic resolution. Nature *282*, 680–686.

Wang, A.J., Quigley, G.J., Kolpak, F.J., van der Marel, G., van Boom, J.H., and Rich, A. (1981). Left-handed double helical DNA: variations in the backbone conformation. Science *211*, 171–176.

Wang, G., Christensen, L.A., and Vasquez, K.M. (2006). Z-DNA-forming sequences generate large-scale deletions in mammalian cells. Proc. Natl. Acad. Sci. U. S. A. *103*, 2677–2682.

WATSON, J.D., and CRICK, F.H. (1953). Molecular structure of nucleic acids; a structure for deoxyribose nucleic acid. Nature *171*, 737–738.

Weiner, S.J., Kollman, P.A., Case, D.A., Singh, U.C., Ghio, C., Alagona, G., Profeta, S., and Weiner, P. (1984). A new force field for molecular mechanical simulation of nucleic acids and proteins. J. Am. Chem. Soc. *106*, 765–784.

Weiss, L.A., Shen, Y., Korn, J.M., Arking, D.E., Miller, D.T., Fossdal, R., Saemundsen, E., Stefansson, H., Ferreira, M.A.R., Green, T., et al. (2008). Association between microdeletion and microduplication at 16p11.2 and autism. N. Engl. J. Med. *358*, 667–675.

Weiss, L.A., Arking, D.E., Gene Discovery Project of Johns Hopkins & the Autism Consortium, Daly, M.J., and Chakravarti, A. (2009). A genome-wide linkage and association scan reveals novel loci for autism. Nature *461*, 802–808.

Witte, H., and Bradke, F. (2008). The role of the cytoskeleton during neuronal polarization. Curr. Opin. Neurobiol. *18*, 479–487.

Woisard, A., Fazakerley, G.V., and Guschlbauer, W. (1985). Z-DNA is formed by poly (dC-dG) and poly (dm5C-dG) at micro or nanomolar concentrations of some zinc(II) and copper(II) complexes. J. Biomol. Struct. Dyn. *2*, 1205–1220.

Yamasaki, T., Kawasaki, H., Arakawa, S., Shimizu, K., Shimizu, S., Reiner, O., Okano, H., Nishina, S., Azuma, N., Penninger, J.M., et al. (2011). Stress-activated protein kinase MKK7 regulates axon elongation in the developing cerebral cortex. J. Neurosci. Off. J. Soc. Neurosci. *31*, 16872–16883.

Yamauchi, J., Miyamoto, Y., Sanbe, A., and Tanoue, A. (2006). JNK phosphorylation of paxillin, acting through the Rac1 and Cdc42 signaling cascade, mediates neurite extension in N1E-115 cells. Exp. Cell Res. *312*, 2954–2961.

Yang, X.L., and Wang, A.H. (1997). Structural analysis of Z-Z DNA junctions with A:A and T:T mismatched base pairs by NMR. Biochemistry (Mosc.) *36*, 4258–4267.

Yasuda, S., Tanaka, H., Sugiura, H., Okamura, K., Sakaguchi, T., Tran, U., Takemiya, T., Mizoguchi, A., Yagita, Y., Sakurai, T., et al. (2007). Activity-induced protocadherin arcadlin regulates dendritic spine number by triggering N-cadherin endocytosis via TAO2beta and p38 MAP kinases. Neuron *56*, 456–471.

Yoshida, Y. (2012). Semaphorin signaling in vertebrate neural circuit assembly. Front. Mol. Neurosci. *5*, 71.

Zarling, D.A., Calhoun, C.J., Feuerstein, B.G., and Sena, E.P. (1990). Cytoplasmic microinjection of immunoglobulin Gs recognizing RNA helices inhibits human cell growth. J. Mol. Biol. *211*, 147–160.

Zhou, T., Raman, M., Gao, Y., Earnest, S., Chen, Z., Machius, M., Cobb, M.H., and Goldsmith, E.J. (2004). Crystal structure of the TAO2 kinase domain: activation and specificity of a Ste20p MAP3K. Struct. Lond. Engl. 1993 *12*, 1891–1900.

Zihni, C., Mitsopoulos, C., Tavares, I.A., Baum, B., Ridley, A.J., and Morris, J.D.H. (2007). Prostate-derived sterile 20-like kinase 1-alpha induces apoptosis. JNK- and caspase-dependent nuclear localization is a requirement for membrane blebbing. J. Biol. Chem. *282*, 6484–6493.

Ben-Zvi, A., Yagil, Z., Hagalili, Y., Klein, H., Lerman, O., and Behar, O. (2006). Semaphorin 3A and neurotrophins: a balance between apoptosis and survival signaling in embryonic DRG neurons. J. Neurochem. *96*, 585–597.

Chapter 1 - Section 2

Deciphering *human* TAOK2α structure – an unfinished business

"There is no perfect method, but if there were, it would be crystallography."

Martin Caffrey

Part of the work presented in this chapter will be published in:

Ana Lúcia Rosário, Marco Patrone, Margarida Archer, Paula M. Alves and Gonçalo Real. An Integrated Platform for Challenging Membrane Proteins: The TAOK2 Approach. (*in preparation).*

Author contributions: ALR, MP, GR and MA designed and conceived experiments. GR performed mammalian cells experiments, MP performed insect cells experiments, ALR and GR performed bacterial experiments and purification experiments, ALR carried out solubilization tests, ALR, MP, MA, PA and GR discussed the results and wrote the manuscript.

1.2.1. Abstract 70
1.2.2. Introduction 71
The biological membrane 71
From Gene to Protein – recombinant DNA 72
Studying Membrane Proteins 73
Overexpression of membrane proteins 75
Detergent-based crystallization of membrane proteins 77
TAOK2 secondary structure predictions 79
1.2.3. Materials and Methods 82
High-throughput small scale overexpressing tests in *Escherichia coli* strains – Pcube – OPPF platform 82
Construction of the pOPIN-*h*TAOK2-GFP-His vector for Expression in *E. coli* and HEK293T cells 83
Plasmid construction for initial Baculovirus expression screening 84
Cell cultures, generation of recombinant Baculovirus derivatives and infections 85
Expression in *E. coli* and protein purification 85
Expression and purification from HEK 293T cells 86
Solubilization screen of *h*TAOK2 expressed in HEK293T and insect cells 87
Antibodies and Immunoblots 87
Fluorescence microscopy 87
1.2.4. Results and Discussion 88
Expression tests of 47 *h*TAOK2 constructs 88
In-house expression tests with OPPF constructs 92
Testing *in-house* full-length constructs of *h*TAOK2 94
High-throughput solubilization tests 101
1.2.5. Conclusions 109
1.2.6. References 111

1.2.1. Abstract

In order to determine the structure of a protein by X-ray crystallography, well ordered three-dimensional crystals are required. At present, despite the wealth of experience accumulated in the course of crystallization and structural analysis of several hundred soluble globular proteins and their complexes, the process of crystallization still remains something of an art, and is often one of the rate limiting step for any crystallographer. Particularly for membrane proteins this represents an additional challenge by virtue of their amphipathic nature, and so their production and purification is troublesome. As a result, to date fewer than 400 structures of membrane proteins are known, less than 0.5% of all the known structures deposited in the Protein Data Bank (PDB). For higher eukaryotes the story is even starker, with less than 50 mammalian integral membrane proteins (IMPs) solved.

Membrane protein production and purification is therefore one of the most important remaining frontiers for structural biology research. One way to improve the throughput of eukaryotic membrane protein structures is to develop methods that reliably facilitate the identification of well expressing IMPs that are stable and functional. In this work, we used the multi-spanning human membrane MAP3K kinase TAOK2 isoform 1 (further referred as *h*TAOK2) as a model to setup a GFP-based approach, for the fast and cost effective multi-host expression screening towards the purification of eukaryotic IMPs.

The *hTaok2* gene was cloned fused to GFP with either a polyhistine or Strep-tag into pOPIN-F, a vector designed to enable high-level target gene expression in multiple systems. A GFP-based expression screening and optimization was carried out using different *E. coli* strains, mammalian and insect cells to determine the host best suited for *h*TAOK2 production. GFP fluorescence was further used to facilitate detergent screening and downstream processing. The measurement of GFP fluorescence intensity was found to be a fast measure of expression and localization, and with higher accuracy when comparing to the in-gel fluorescence.

Accordingly, by monitoring expression through GFP fluorescence, we show that *h*TAOK2 fusion protein only localizes correctly throughout the cell membrane when expressed in mammalian cells and only when GFP is present at the N-terminus. We show the practical steps that constitute our GFP-based pipeline for evaluation of expression, as well as to speed up membrane extraction detergent screening up to protein purification. Therefore, GFP-tag is very useful to facilitate the production process that all IMPs are required to go through on the way to obtain stable and homogeneous material for functional and structural studies, although the functionality of the IMP still has to be checked/confirmed at the end of the purification.

1.2.2. Introduction

The biological membrane

The first cell had origin when a membrane was formed, inclosing a watery solution and separating it from the rest of the universe. In 1972, Singer and Nicolson presented to the scientific community a model for biological membranes, the fluid mosaic model (Figure 1.2.2.1). This model introduces an organized bilayer of phospholipids, creating an amphipathic structure, which provide an hydrophobic interior environment - with nonpolar groups buried, facing each other, at the bilayer core, whereas ionic and highly polar groups protrude outward from the membrane into the aqueous phase (Singer and Nicolson, 1972). Embedded in the membrane are proteins, held by hydrophobic interactions between the lipids and hydrophobic domains in the protein. Because most of the interactions between the membrane components are noncovalent, the proteins are free to move laterally within the lipid bilayer by membrane diffusion, reason why it is named fluid mosaic model of the cell membrane.

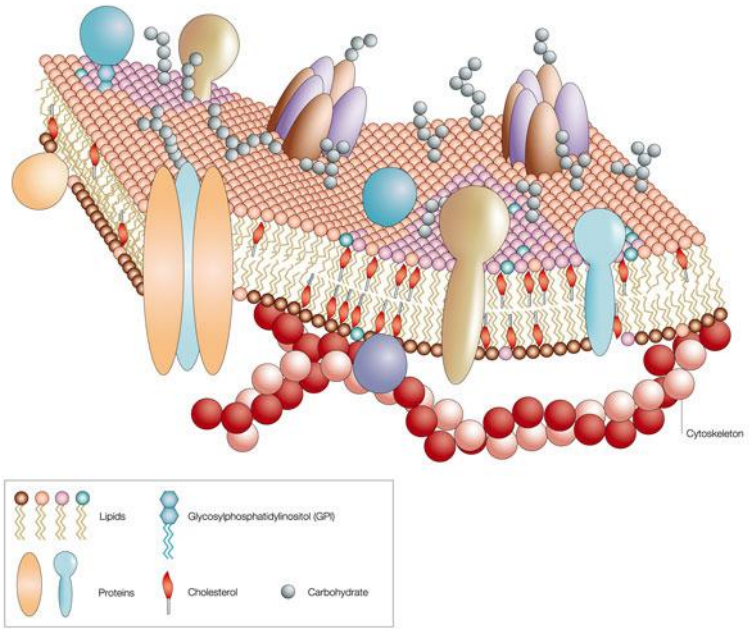

Figure 1.2.2.1. Model of fluid mosaic membrane first described by Singer and Nicolson.

Like a mosaic, the cell membrane is a complex structure composed mainly of phospholipids, proteins and cholesterol. Biological membrane components are diversified, depending on the type of lipid constituting the membrane and its function (Alberts, 2009).

Biological membranes share fundamental properties: all are impermeable to most polar groups or charged solutes but permeable to nonpolar compounds; they are 5 to 8 nm (50 to 80 Å) thick and

appear trilaminar at the electron microscope (Lehninger et al., 2000). The relative proportion of proteins and lipids varies with the type of membrane.

From Gene to Protein – recombinant DNA

In 1868, a Swiss physician, Friedrich Miescher, isolated a total new compound from the nucleus. That thing no one has ever seen before was named nuclein at the time, but it is now best known as DNA, the deoxyribonucleic acid (Dahm, 2008). The connection between DNA and genes wasn't made until 1944 by Oswald Avery, in his study about bacterial transformation (Severs and Whiting, 2002):

"*If we are right, and of course that is not yet proven, then it means that nucleic acids are not merely structurally important but functionally active substances in determining the biochemical activities and specific characteristics of cells and that by means of a known chemical substance it is possible to induce predictable and hereditary changes in cells. This is something that has long been the dreams of geneticists."*

Oswald T. Avery, 1943

From this point, scientists started to unravel more details about DNA, its constitution and biochemical properties, even the pairing of bases was known, however the models of how its constituents assembled to form a molecule were highly controversial. The big breakthrough happened in 1953 when Watson and Crick (1962 Nobel prize of medicine) revealed the first true model of DNA (Watson and Crick, 1953). This model aroused because it was finally possible to analyze the X-ray crystallographic data of a DNA fiber produced by Rosalind Franklin´s work.

The knowledge on how genetic material is stored and copied allowed an advance to a new era of bioprocess manipulation. New techniques were developed to understand the specific role of different genes. Within the first lights of molecular biology, molecules of DNA stretches were cut-out and inserted in a different place – the birth of recombinant DNA technology.

In recombinant DNA, the donor organism DNA (or GOI, gene of interest) in study is extracted by specific enzymes, cut in fragments and inserted individually into bacterial plasmids. The bacterial plasmids act as carriers, or vectors. The vector plus its DNA insert consists of the recombinant DNA, a novel combination of DNA from completely different sources (Figure 1.2.2.2). The technology of recombinant DNA allowed to transform bacterial cells with those vectors and cultured them in plates, where a single transformed cell will form a colony by sequential divisions, carrying the same recombinant DNA – a clone (Griffiths et al., 2000a). In recent years, advancements in technology permitted the transfer of DNA from any origin, not only to bacteria, as to eukaryotic cells, virus, and highly complex organism, *e.g.* mouse, flies, worms and others.

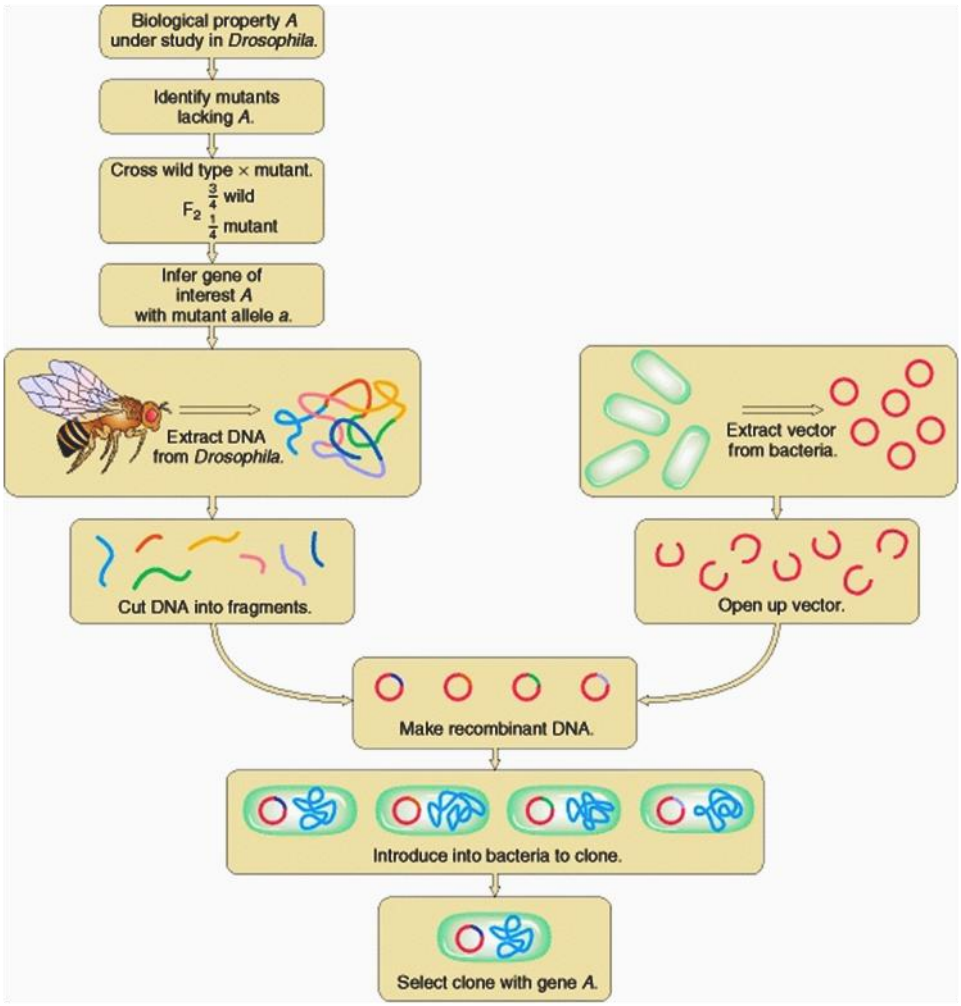

Figure 1.2.2.2. Recombinant DNA technology.

Individual fragments of DNA from any genome are inserted into a vector, e.g. plasmid. The vector-DNA combination is amplified by a single bacterial cell originating a DNA clone (Griffiths et al., 2000a).

In the last century, basic science has evolved to a complex system of genomics and proteomics of entire organisms as the human body, hoping that in a near future, it will contribute to a better understanding of the mechanisms of biological processes.

Studying Membrane Proteins

Membrane proteins (MPs) are a class of proteins that play specific roles in the communication between biological compartments allowing these to take on specialized functions. Integral membrane proteins (IMPs) can act as receptors, channels, transporters, and are also involved in cell adhesion and signaling, whereas peripheral membrane proteins are primarily implicated in cell signaling (Stevens and Arkin, 2000; Wallin and von Heijne, 1998).

About 20 to 35% of open reading frames from the currently known genomes encode for MPs (Boyd et al., 1998). Moreover, 70% of the current pharmaceutical targets are MPs, leaving no doubt to their extreme importance in medicine, and creating an immediate need for high resolution structural to functional information (Hopkins and Groom, 2002). Protein structures provide relevant insights into their reaction mechanisms. The most reliable method to acquire high resolution structures of proteins is X-ray crystallography. The first membrane protein crystal structure, the bacterial photosynthetic reaction center complex, was solved by Johann Deisenhofer, Robert Huber and Hartmut Michel in 1985 (Deisenhofer et al., 1985). Since then, increasing numbers of membrane protein structures have been reported (Figure 1.2.2.3), to an actual number of 427 unique membrane protein structures present at the 'Membrane protein of known 3D structure' database (http://blanco.biomol.uci.edu/mpstruc/). However, despite the increased advances in the field, less than 0.5% of unique structures in PDB belong to MPs (PDB: http://www.rcsb.org/pdb), largely because of difficulties inherent to membrane proteins. Eukaryotic membrane proteins are particularly difficult and underrepresented, with less than 50 unique known 3D structures.

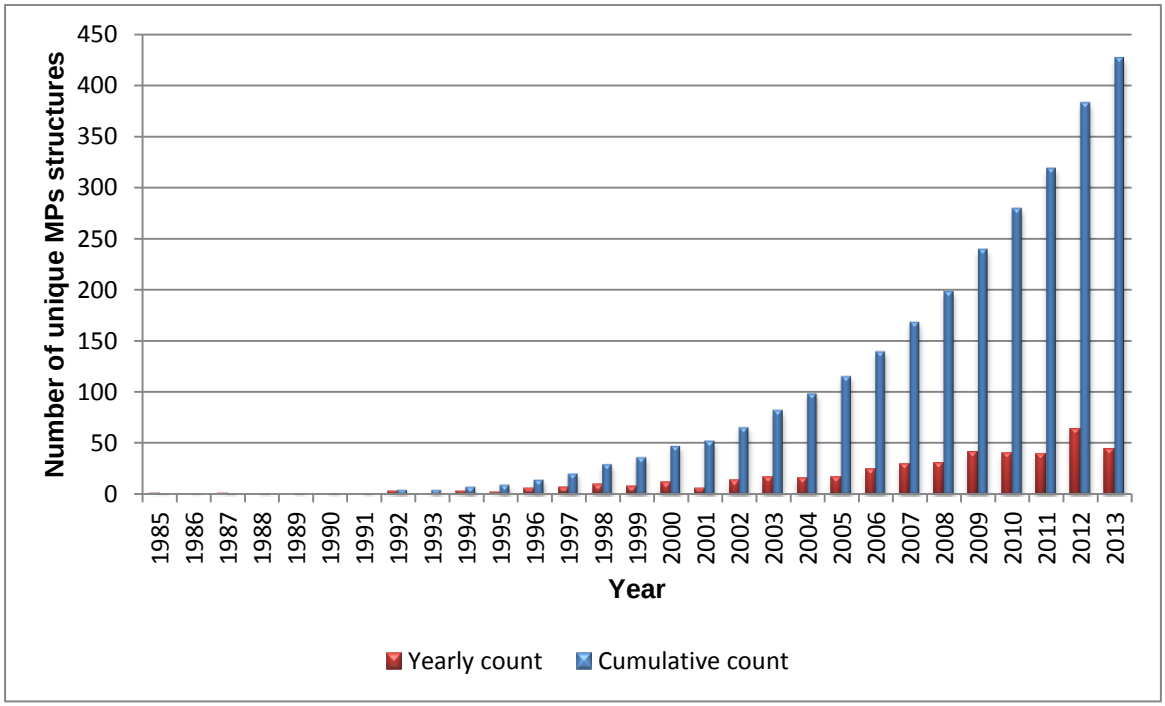

Figure 1.2.2.3. Number of unique membrane protein structures. Currently, 427 unique membrane protein structures are present at the 'Membrane protein of known 3D structure' database (http://blanco.biomol.uci.edu/mpstruc/).

MPs represent a challenging class of proteins for structural biochemistry due to the difficulties associated with their expressing and handling, as they are often flexible and unstable, and only available when extracted from the membrane by the use of detergents. The hydrophobic nature of MPs makes them unsoluble in a simpler aqueous solution or in organic solvents of low dielectric constant. An increased difficulty comes from their usual low expression levels when compared to

soluble proteins. Those low yields can be associated with toxicity to the host cell, due to the overload of membrane translocation machinery or to the potential accumulation of protein molecules incorrectly incorporated into the membranes. For high resolution structure determination, a protein must be soluble at high concentrations and remain intact and stable for a period of time that allow crystals to form (Bowie, 2001). The most common problem is poor stability, leading to inactivation of the protein, which becomes biochemically intractable. Usually, obtaining membrane proteins in sufficient quantity and quality for structural and biochemical/biophysical analysis can be a challenging and time consuming task.

Because of the obstacles related to stability and solubility of membrane proteins, it is often difficult to study these proteins using common biophysical techniques such as x-ray scattering, magnetic and optical spectroscopy. Despite the advance those methodologies have taken recently, X-ray crystallography remains the top choice technique for structure-to-function analysis (Bolla et al., 2012).

Overexpression of membrane proteins

Suitable starting material is often in short supply. Membrane proteins can be obtained directly from the source organism, as by enriching a membrane preparation that will naturally be enriched in the target protein. However, the amount of a membrane protein purified and present in nature is, quite usually, very low. Over time, scientists have developed strategies for the overexpression of proteins in order to increase its yield. **The challenge then, is to find a suitable temporary hosting environment for the excised protein and a means for ratcheting it into crystal lattice in native conformation** (Caffrey, 2003).

Following the discovery of the tools allowing DNA manipulations in vitro, *Escherichia coli* became the most widely used expression host of recombinant proteins. It provided a source for producing proteins in high quantity and quality, which were previously difficult or impossible to achieve from their natural source. *E. coli* can be grown to high cell density, having a duplication time of only 20 minutes, the fastest and inexpensive techniques applied in a fermentation process and consequently, very high yields are to be expected. Biotherapeutics and proteins associated with industrial scale are thoroughly expressed in this system (Robert C. Hockney, 1994).

Having cloning as an option for our gene of interest, leads to the advantage taken at the ability to engineer the sequence for overexpression resulting in modifications at the N- and/or C-terminal, as well at the internal sequence, for the removal of troublesome co- and post-translational modification sites. The wide use of affinity tags, fusion proteins and amino acid analogs, for phasing purposes, facilitates purification and structure determination. Protein sequences are many times engineered (mutations) to improve stability or to enable determination of different functional states, which are usually transient in nature and difficult to capture in X-ray

crystallography (Caffrey, 2003). Exploring the crystallizability of homologues of the target protein in other organisms is a strategy that has proved successful (Bass et al., 2002).

Apparently, *E. coli* was a good starting point for the herelogous expression of relatively small proteins or proteins with simple structural properties. However, the isolation of complex proteins, particularly those requiring post-translational modifications for their biological activity, i.e. the eukaryotic proteins, is limited in such a system. Many overexpressed proteins can cause toxicity to the host and kill it; or it may happen that the target ends accumulating in inclusion bodies (IBs). Overexpression of proteins is not a trivial subject and many developments and reports on the subject highlight the necessity of a cautious high-throughput approach of host strains. Meanwhile, vectors availability have increased enormously, and also protein tagging have been extensively studied, becoming important parameters to be taken in consideration when experimenting the overexpression of a protein, even more, if it is an eukaryotic protein (due to their higher structural complexity). To overcome the difficulties of finding satisfactory expression condition when using *Escherichia coli* strains as host, C-terminal tagging of MPs with green fluorescent protein (GFP) has been tested as an expression/folding marker. Correctly folded GFP is fluorescent, as opposed to overexpressed GFP in inclusion bodies which does not fluoresce, allowing to discriminate between correctly membrane insertion and folding versus inclusion bodies and aggregates formation (Drew et al., 2001).

Some proteins, when overexpressed, may accumulate in an insoluble and inactive form, and agglomerate forming an inclusion body. To retrieve the protein from IBs, it is necessary to use strong denaturating agents and refolding processes. Even if refolding has proved to be capable of producing authentic protein in a biological active form, it most often fails. In addition, the complexity of experiments totally abolish the simplicity expected when using *E. coli* (Bolla et al., 2012). Also, the fact that such proteins never encounter a natural membrane raises questions regarding the fidelity of the structure determined (Caffrey, 2003). On the other hand, membrane proteins are extremely hard to work with and when present in IBs, especially those less complex or with lower size, but that are prone to cause cell death, are many times powerful candidates for IBs and successfully refolded to soluble ones (Buchanan, 1999; Caffrey, 2003). Overexpression in inclusion bodies became a powerful strategy followed by many lead researchers (Diefenderfer et al., 2009).

Other bacteria like *Lactococcus lactis,* or yeast cells as *Pichia Pastoris* and *Saccharomices cerevisae* are being increasingly used for overexpression of MPs. With increased knowledge on cell culture techniques, insect and mammalian cell lines also became widely used, especially for complex eukaryotic proteins (Junge et al., 2008). It is necessary to adequate the target protein to the expression system to use. As an example, mammalian membrane proteins are most commonly purified from native sources. The nature of the lipid usually affects the stability of the protein and its insertion within the membrane, as different systems have different lipid compositions, nature sources are more suitable for isolation of a target protein (Opekarová and Tanner, 2003). Also, bacteria are unable to perform post-translational modifications due to the

absence of the required enzyme systems, demanding for alternative expressing systems (Junge et al., 2008; Mancia and Hendrickson, 2007). However, some mammalian MPs have been successfully produced in yeast systems (Binda et al., 2002; Long et al., 2005; Martinez Molina et al., 2007), insect cells (Rasmussen et al., 2007) and also *E. coli* (Bracey et al., 2002; Ferguson et al., 2007).

It is often necessary to explore a variety of expression systems for a single protein target (Bill et al., 2011). Another relevant approach is the use of small fraction of a complex protein (by genomic truncation, limited proteolysis) and use it in crystallization trials, enhancing the probability of structure determination when compared to a multidomain membrane protein. However, functional insights so derived must be taken cautiously, as those structures can be misleading to some degree.

Detergent-based crystallization of membrane proteins

Generating stable conditions for membrane proteins after extraction from their lipid bilayer environment is essential for subsequent characterization. The use of detergents is required for extraction from the cellular membrane and for solubilization in solution. Detergents are widely used to obtain this stable environment; however, different types of membrane proteins have been found to require detergents with varying properties for optimal extraction efficiency and stability after extraction (Caffrey, 2003). Mild detergents are used in handling membrane proteins, however, many MPs tend to aggregate or denature when subjected to solubilization by these amphiphilic chemicals. Researchers usually test a diverse range of detergents with the purpose of increasing extraction while conferring stability to the MP, so that the optimal conditions for solubilization of MPs must be found before proceeding to protein purification and crystallization. Also, purification of IMPs requires in-depth screening to identify the proper physicochemical features that confer stability to the MP of interest. Ionic strength along with suitable blends of lipids, detergents and other factors are all involved in supporting the active conformation of IMPs. This is particular acute in IMPs from higher eukaryotes, which are often post-translational modified.

Tagging of membrane proteins with GFP facilitates the monitorization of protein expression, but also allows the development of a good purification scheme for the target protein (Drew et al., 2005, 2008, 2001). GFP fluorescence from whole-cell culture and from SDS-polyacrylamide gel electrophoresis provides a direct measurement for the quantity of the membrane protein integrated at the membrane when overexpressed (Drew et al., 2006). When successfully overexpressed, a target protein fused with GFP can be further screened for detergent extraction using fluorescence-detection size-exclusion chromatography (FSEC) by accessing “monodispersity” of the sample at the crude detergent solubilized extract prior to purification. Setting the best candidate for extraction can shed light on the most suitable detergent for further

purification, enabling a fast optimization for the condition that render the highest stability (Drew et al., 2008; Kawate and Gouaux, 2006).

As it happens with soluble proteins, membrane proteins used in crystallization must be as pure and homogeneous as possible. Different techniques can be used for their assessment, as gel electrophoresis, circular dichroism spectroscopy, dynamic light scattering and mass spectrometry. The latter, has recently emerged as a very powerful tool routinely used as alternative to the other methods, given that, it offers picomole sensitivity, high-mass accuracy, high-throughput capability, in a fast and cost effective way easily accessibility at every research institution (Cohen and Chait, 2001).

In protein crystallization a large variety of crystallization reagents are tested. The first experiments are usually done at 96 well plates making use of robotic instruments. Advances in technology allowed successive reduction in the volumes required for initial experiments, with most of the robotic equipment performing drops as small as 100 nl. There are several commercial screens that were specifically designed for membrane proteins, such as MemStart, MemGold and MemSys (Newstead et al., 2008). Moreover, testing the detergent used in the crystallization process has proven to be extremely important (Privé, 2007). Vapor-diffusion (Sutton and Sohi, 1994); micro-batch (Iwata and Chayen NE., 2003; Loll et al., 2003), dialysis (Fromme, 2003), counter-diffusion (Ng et al., 2003, 2008) and micro-fluidics (Leng and Salmon, 2009) are methods applied to crystallize proteins embedded in detergent micelles (Figure 1.2.2.4).

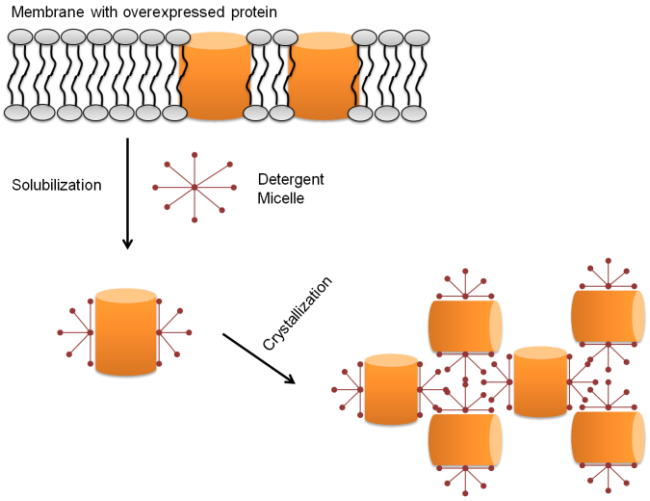

Figure 1.2.2.4. Schematic diagram of detergent-based crystallization of membrane proteins.

The membrane protein is removed from native cell membrane using detergent micelle. The purified protein is then crystallized in detergent micelles. The membrane protein molecule is in orange color, detergent micelle are colored red, and the cell membrane is gray (adapted from Bolla et al., 2012).

Crystallization of membrane proteins can also be achieved recurring to lipidic cube or sponge phases. Detergent bicelles have also been used instead of the detergent micelles, however those will develop a 2D crystal packing type, which may not be the most suitable for achieving a good

diffracting crystal and permit structure resolution (Caffrey, 2003, 2011; Caffrey and Cherezov, 2009).

TAOK2 secondary structure predictions

First described by Moore and colleagues with the name PSK (Prostate-derived STE20-like kinase 1), TAOK2 is a member of the mitogen-activated protein kinase kinase kinase (MAP3K) family of signaling modules, ubiquitous to eukaryotic cell regulation. TAOK2 selectively activates the JNK-MAPK pathway through the phosphorylation of MKK4 and MKK7, and it is regulated by a still undefined mechanism via its C-terminal domain (Moore et al., 2000). TAOK2 was later shown to activate other signaling pathways, i.e. p38 and ERK family members (Chen et al., 1999, 2003). Several other studies revealed the involvement of TAOK2 in regulating cytoskeleton dynamics during stress-like conditions and demonstrated that TAOK2 co-localizes with microtubules for their stabilization in a kinase independent fashion (Chen and Cobb, 2001; Mitsopoulos et al., 2003). So it is possible that TAOK2 would be responsible for the stability of tubulin, playing a major role in the organization of the microtubules network.

Thousand-and-one-aminoacids kinase 2 isoform 1 (TAOK2α) is a large (1235 aa) integral polytopic type II membrane Ser/Thr protein kinase, with a 963 aa-long N-terminal cytosolic portion (containing the kinase domain located in the first 320 aa) followed by 4 predicted transmembrane helices (Table 1.2.2.1) and a C-terminal domain of uncertain topology (Figure 1.2.2.5a, b).

Table 1.2.2.1. Predicted transmembrane helices (TMs) for *human*TAOK2α.

TMs structure prediction using SOSUI engine ver. 1.11: (http://bp.nuap.nagoya-u.ac.jp/sosui/) (Hirokawa et al., 1998) predicted 4 TMs, in accordance to other engines for TMs predictors.

N terminal	transmembrane region	C terminal
952	LAGLSFAVGSSSLLGLLPLLLLLL	974
985	LQAALLALEVGLVGLGASYLLLC	1007
1012	LPSSLFLLLAQGTALGAVLGLSW	1034
1043	LGLGAAWLLAWPGLALPLVAMMA	1065

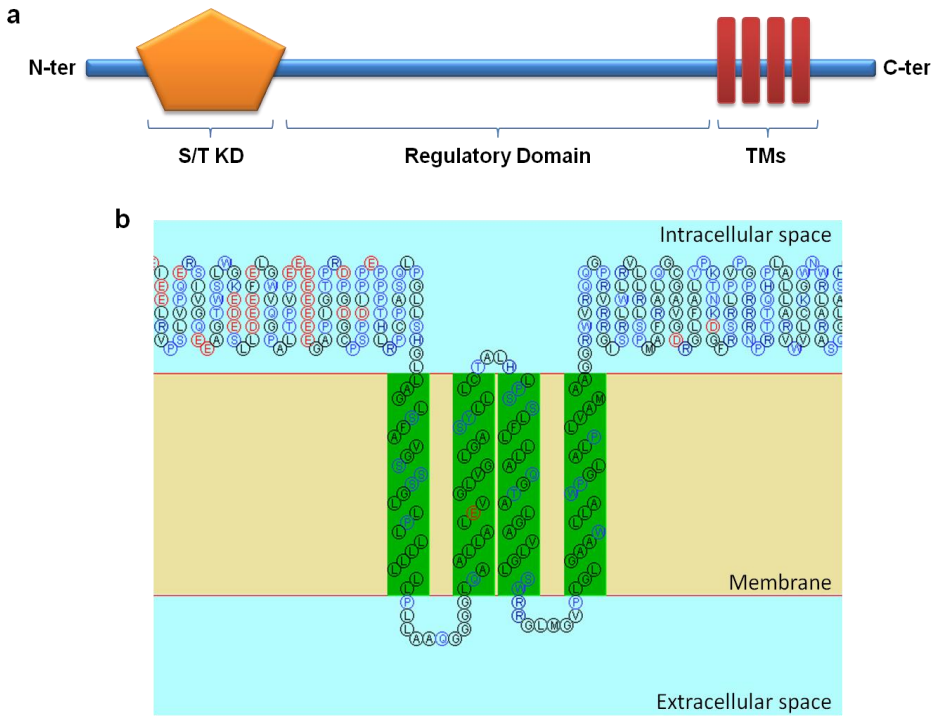

Figure 1.2.2.5. Schematic diagram of secondary structure predictions for *human*TAOK2.

(a) Topology of the different domains identifiable at hTAOK2 using SMART (Schultz et al., 1998). (b) Transmembrane helices (as in Table 2.2.1) scheme created by SOSUI (Hirokawa et al., 1998). Abbreviations: N-ter: N-terminal Domain, C-ter: C-terminal Domain, S/T KD: Serine/Threonine Kinase Domain, TMs: Transmembrane Helices.

A typical protein kinase two-domain architecture was revealed by x-ray crystallography when the kinase domain structure of *h*TAOK2 was solved in its phosphorylated active conformation (Figure 1.2.2.6) (Zhou et al., 2004). In the same paper, the authors evaluate the kinase activity of the truncated form of the kinase domain versus the full-length construct and conclude that the full-length enzyme exhibits a decreased activity, suggesting that TAOK2 self-inhibits/activates by a segment located downstream of the kinase domain. Despite all the work in understanding TAOK2α signaling pathway, further experiments are necessary to understand the structural roles of the noncatalytic domain, which is most likely involved in the functional regulation of TAOK2.

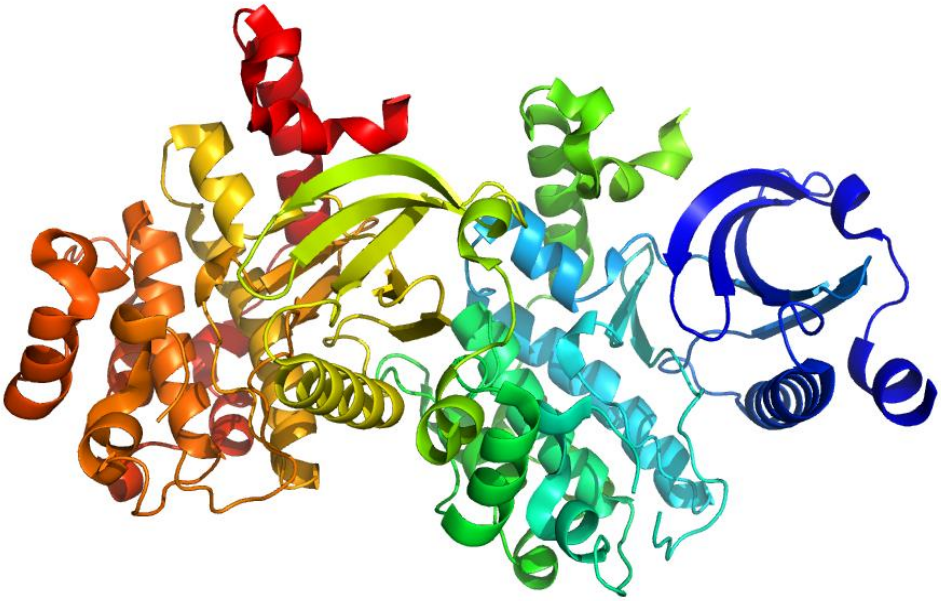

Figure 1.2.2.6. Crystal structure of the TAOK2 kinase domain.

Cartoon representation (colored spectra) of the crystal structure of TAOK2 kinase domain (PDB ID 1U5Q) showing the interaction between 2 polipetide chains in the asymmetric unit. Structure solved at 2.1 Å resolution (Zhou et al., 2004).

1.2.3. Materials and Methods

High-throughput small scale overexpressing tests in *Escherichia coli* strains – Pcube – OPPF platform

The OPPF platform offered a cloning and expression screening of 48 contructs, where 47 belonged to the *h*TAOK2 gene and 1 of GFP alone (control). The procedures are standardized by the host laboratory. Briefly, the primers are designed for In-Fusion™ (Clontech Laboratories, Inc.) cloning. The vector to use depended on the fusion tag required for the resulting protein construct. Polimerase chain reaction (PCR) for clone amplification was done using KOD Xtreme™ Hot Star DNA Polymerase (Novagen). The thermal cycling was performed using the following parameters: 94ºC - 2 minutes; 98ºC – 10 seconds; 60ºC – 30 seconds; 68ºC – 4 minutes (1 min/kbp); repeat from step 2 29 times; 68ºC – 2 minutes; 4ºC – hold. If another round of PCR was needed then we would use Phusion Flash Mastermix (NEB). 98ºC – 10 seconds; 98ºC – 1 second; 60ºC – 5 seconds; 72ºC – 1 minute (15 sec/kbp); repeat from step 2 29 times; 72ºC – 2 minutes; 4ºC – hold. PCR products were analyzed on a 1.25% TBE agarose gel with 4 µl of Hyperladder I (BioLine) as reference. PCR products of good quality (i.e. few multiple bands and "smeared" products) across the plate were purified using the AMPure XP (Agencourt/Beckman) magnetic-bead purification step. If a significant number of the PCR products showed multiple bands or were smeared,then gel purification and extraction were performed. Cloning to the appropriate and previously linearised pOPIN vector was done by In-Fusion reaction, followed by immediate HTP transformation into OmniMaxII competentes *E. coli* cells (Invitrogen) in a 96 deep-well plate (Matrix). The transformation reaction was plated onto LB agar supplemented with the appropriate antibiotic, X-Gal and IPTG. Two white colonies per construct were selected (blue colonies are derived from inefficiently linearised parental plasmid and are non-"recombinant") and added to Deep-well blocks (BD Falcon) containing Power Broth supplemented with antibiotic and cultured over-night (37ºC, 220 rpm). A glycerol stock was prepared by transferring 100 µl from each well to a microplate MTP (Greiner V-bottom) containing 100 µl/well of filter-sterilized Luria-Bertani Broth with 30% v/v glycerol followed by storage at -80ºC. Cells from the remaining culture were harvested by centrifugation at 5,000 *g* for 15 minutes (Beckman JS5.3 rotor). HTP mini plasmid preparation using wizard SV96 purification plates was performed in the Bio-Robot 8000 (Qiagen) and constructs verified by setting an HTP PCR reaction with KOD Polymerase Master. *E. coli* expression strains B834(DE3) and Rosetta(DE3)pRARELysS (plasmid retained by the addition of chloramphenicol to the culture media, 34 µg/mL) were aliquotted in loose tubes racked in 96-well (Matrix) format and stored at -80ºC. Both *E. coli* strains were transformed, by heating-shock the cells for 30 seconds at 42ºC and immediately returning to ice for 2 minutes. HTP small scale expression screenings were done as following: deep-well blocks (BD Falcon), containing 0.5 mL of Power Broth supplemented with 1% glucose and 50 µg/mL of the appropriate antibiotic, were

inoculated with the strain/construct to culture a pre-inoculum overnight at 37ºC. IPTG induction was done by diluting the overnight culture in 2.5 mL Power Broth, supplement with 1% glucose and appropriate antibiotic, and incubated at 37ºC until $O.D._{(595\ nm)}$ reached ≈ 0.5 (3-5 hours). At this point the temperature was lowered to 20ºC and IPTG was added to a final concentration of 0.5 mM, and expression carried overnight (≈18 hours). Auto-induction screening was done by diluting 62.5 µl of the pre-inoculum cultured overnight in 2.5 mL of OvernightExpress™Instant TB Medium (TBONEX) supplemented with appropriate antibiotic. After 3-5 hours at 37ºC, plates were transferred to an incubator at 25ºC and left for 24 hours. Cells were harvested by centrifugation at 5,000 *g* and subjected to a Nickel-nitrilotriacetic acid (Ni-NTA) miniature expression screen purification using a standard protocol available for the Qiagen BioRobot 8000 by lysing the cells and using Ni-NTA magnetic beads to isolate the His-Tagged expressed protein from the remaining extract. Insoluble fraction was collected and subjected to an HTP denaturing purification protocol using Ni-sepharose and a vacuum manifold as purification system. Expression was evaluated by analyzing purified proteins on SDS-PAGE.

Construction of the pOPIN-*h*TAOK2-GFP-His vector for Expression in *E. coli* and HEK293T cells

pOPINF was obtained from Oxford Module Consortium (OMC), OPPF, Wellcome Trust Centre for Human Genetics, Roosevelt Drive, Headington, Oxford, OX3 7BN. UK. The *h*TAOK2 sequence was amplified from I.M.A.G.E. clone 40148752 (Open Biosystems) with primers TEV-TAOK2_D (5'-GAAAACCTGTATTTTCAGTCTCCAGCTGGGGGCCGGGCCGGGAGCC-3') and TAOK2 (HindIII)_R (5'-CGTGTCAAGCTTCTACTACCTCCAGGGGGGCAGGGCCCGGG-3'). The 8xHis-GFP encoding sequence was amplified from pTarget-OpIE2eGFP (Fernandes et al., 2012) with primers 8xHis-GFP (EcoRI BspHI)_D (5'-GGATGAATTCTCATGAACCATGGCACATCACCATCACCATCACCATCACAGATCTGTGAGCA AGGGCGAGGAGCTG-3') and TEV-GFP_R (5-CTGAAAATACAGGTTTTCAGATCTCTTGTACAGCTCGTCCATGCCGAGAGTGATCCCG G-3'). All polymerase chain reactions were carried out using Phusion High-Fidelity DNA Polymerase (Thermo Scientific). The two products were joined together using the splicing by overlay extension (SOE) technique (Horton et al., 1989) and primers 8xHis-GFP (EcoRI BspHI)_D and *h*TAOK2 (HindIII)_R. The resulting amplicon was digested with BspHI and HindIII and cloned into NcoI/HindII digested pOPINF rendering pOPINE-*h*TAOK2-GFP-His.

Plasmid construction for initial Baculovirus expression screening

Plasmids were constructed by using Phusion High-Fidelity DNA Polymerase (Thermo Scientific) for PCR with primers listed in Table 1.2.3.1, and In-Fusion® HD (Clontech) for ligase independent cloning (LIC). I.M.A.G.E. clone 40148752 was obtained from Open Biosystems and used as a source for *h*TAOK2 open reading frame (ORF). GFP ORF was amplified from pTarget-OpIE2eGFP (Fernandes et al., 2012) with either primers setA or setB and G RV.1, to generate N-terminal His-tag or Twin-Strep-tag® GFP coding DNA respectively by 5' extension PCR. *h*TAOK2 ORF was amplified with primers Fw.1 and Rv.1. The resulting tagged GFP variants and TAOK2 amplimer had overlapping sequences at 3' and 5' respectively, each encompassing a TEV site coding region. Each GFP amplimer was then cloned along with *h*TAOK2 by LIC into flashBAC pOET1 transfer vector (Oxford Expression Technologies) digested with BamHI and XhoI, obtaining pOET-His-GFP-*h*TAOK2 and pOET-strep-GFP-*h*TAOK2, respectively.

Table 1.2.3.1. PCR primers list for In-Fusion protocol to obtain the His-GFP-*h*TAOK2 and the strep-GFP-*h*TAOK2 constructs for Baculovirus expression.

setA Fw.1	5'-CCATCACCATCACCATCACAGATCTGTGAGCAAGGGCGAGGAGCTGT-3'
setA Fw.2	5'-TATAAATATAGGATCCCGCCACCATGGCACATCACCATCACCATCACCATCACAGATC-3
setB Fw.1	5'-TATAAATATAGGATCCCGCCACCATGTCGGCCTGGAGCCACCCGCAA-3'
setB Fw.2	5'-TCGGCCTGGAGCCACCCGCAATTTGAAAAAGGCGGTGGCTCGGG-3'
setB Fw.3	5'-TTTGAAAAAGGCGGTGGCTCGGGTGGAGGCTCGGGAGGCTCTGC-3'
setB Fw.4	5'-TGGAGGCTCGGGAGGCTCTGCGTGGTCGCATCCGCAATTCGAAAA-3'
setB Fw.5	5'- TGGTCGCATCCGCAATTCGAAAAGAGATCTGTGAGCAAGGGCGAGGA-3'
G Rv.1	5'-CCAGCAGACTGAAAATACAGGTTTTCAGATCTCTTGTACAGCTCGTCCATGCCGA-3'
Pr Fw.1	5'-GAAAACCTGTATTTTCAGTCTGCTGGGGGCCGGGCCGGGA-3'
Pr Rv.1	5'-GCCGCGGTACCTCGAGCTACCTCCAGGGGGG-3'

Cell cultures, generation of recombinant Baculovirus derivatives and infections

S. frugiperda Sf9 and *T. ni* HighFive™ (the latter abbreviated Hi5 hereafter) were maintained as suspension cultures in Sf-900™ II SFM (Life Technologies) and Insect-XPRESS™ (Lonza) culture media, respectively. Cell density and viability were routinely assessed with Trypan Blue test. Recombinant Baculoviruses expressing either hGhTAOK2 (His-GFP-*h*TAOK2) or stGhTAOK2 (strep-GFP-*h*TAOK2) were generated in Sf9 with flashBAC methodology according to manufacturer's guidelines and lipofection with Cellfectin® II. Viral stocks were titrated by GFP flow cytometry with *CyFlow® space (Partec*). For expression tests, both Sf9 and Hi5 cells were infected at 2.5x 10^6 cell/mL with a multiplicity of infection (m.o.i.) of 5. At the indicated time points, aliquots of infected cell cultures were sampled for immunoblot analysis. Total protein extracts from infected insect cells were prepared at a ratio of 10^7 total cells/mL in 25 mM Tris-HCl, 0.15 M NaCl, 0.5% N-Lauroylsarcosine, 20% Glycerol, 1 mM DTT, 1.25 U/mL Benzonase® (Merck Millipore), cOmplete EDTA-free protease inhibitor cocktail (Roche), pH 8.0. Insoluble material was sedimented by 13,000 *g* centrifugation at 4°C for 10 min and the supernatant from 10^5 cell equivalents loaded onto 4-12% Novex® NuPAGE® Bis-Tris pre-cast gel (Life Technologies) followed by blotting to nitrocellulose membrane.

Expression in *E. coli* and protein purification

pOPINE-His-GFP-*h*TAOK2 was transformed into *E. coli* BL21(DE3) (Novagen) or C43(DE3), an *Escherichia coli* mutant host that allows synthesis and over-production of some membrane proteins and globular proteins at high levels (Miroux and Walker, 1996). Plates were incubated for 18 h at 37°C before individual colonies were used to inoculate 10 mL LB medium supplemented with 1% w/v glucose and 100 µg/mL ampicilin and shaken at 225 rpm. at 37°C for 18 h. For IPTG induction, 500 µl of each overnight culture was used to inoculate in duplicate, 30 mL of LB supplemented with 100 µg/mL ampicilin. The diluted cultures were grown at 37°C with shaking at 225 rpm for 3 h, afterwards the temperature was reduced/set to 20°C, ITPG added to a final concentration of 0.5 mM to one of the duplicates and shaked for further 4h at 20°C. Expression of His-GFP-*h*TAOK2 in induced and uninduced cultures was monitored on hourly intervals by fluorescence microscopy and fluorimetry. At the end of the induction period, cells were collected by centrifugation, ressuspended in 10 mL of 100 mM Tris-HCl pH 8.0, 500 mM NaCl, 15% Glycerol, 10 mM $MgCl_2$, 1 mM ATP, containing 1000 KUnits/ml DNAse I (Sigma, Poole Dorset, UK) and Complete EDTA-Free Protease inhibitors (Roche), and disrupted by 2-fold passages through a One Shot (Constant Cell Disruption Systems, Northants, UK) at 17,000 psi. Whole cell extracts were centrifuged at 10,000 *g* for 10 min, at 4°C (J2-MI, Beckman Coulter, Inc.), and the supernatant transferred into Ti70 (Beckman Coulter, Inc.) tubes for further ultracentrifugation at 100,000x *g* for 1 h, at 4°C (XL-100, Beckman Coulter, Inc.). Membrane proteins present in the pellets were resuspended in 6 mL of 100 mM Tris-HCl pH 8.0, 500 mM NaCl, 15% Glycerol, 10

mM MgCl2, 1 mM ATP, 1% DDM, pH 8.0 and incubated with gentle stiring at 4ºC for 12 h. After an additional centrifugation at 100,000 *g* for 30 min at 4°C (Optima™ TLX, Beckman Coulter, Inc.), solubilized membrane proteins were applied to Ni-NTA spin columns (Qiagen). Protein purification was performed according to the manufacturer's instructions (Ni-NTA spin kit; Qiagen) under native conditions (without using denaturating reagents). All solutions included 1% DDM and 10% glycerol. Proteins purified by elution from the Ni-NTA spin columns were analyzed by SDS-PAGE and Western blot.

Expression and purification from HEK 293T cells

HEK293-EBNA cells were routinely maintained in Freestyle medium (InVitrogen) supplemented with 1% FBS (InVitrogen). For expression screening, fresh cells were seeded onto a 6-well plate at a concentration of $1x10^6$ cells/mL and in a final volume of 1,5 mL. Transfection with pOPIN-*h*TAOK2-GFP-His was performed using polyethylenimine (PEI). In brief and per well, 2 µg of plasmid DNA and 4 µL of PEI (1 mg/mL) were diluted separately in 250 µL Freestyle medium. The PEI/Freestyle mix was added dropwise to the DNA/Freestyle medium while gently shaking. The DNA/PEI complex was incubated for 15 min at room-temperature after which it was added to the cells. Transfected cells were incubated at 37°C/5% CO_2/95% air environment and at an agitation of 120 rpm. *h*TAOK2-GFP-His expression in mammalian cells was monitored by fluorescence microscopy, fluorimetry, SDS-PAGE and Western blot.

Scale-up and purification of *h*TAOK2-GFP-His from HEK293T cells was carried out as follows. Cells were grown in 5 L flasks and transfected with plasmid DNA using PEI, as previously described. 48 h post-transfection cells were collected by centrifugation, ressuspended to a final concentration $1x10^7$ cells/mL with 25 mM Tris-HCl pH 8.0 and 150 mM NaCl containing 1 Unit/mL OmniCleave™ Endonuclease (Epicentre, Germany) and Complete EDTA-Free Protease inhibitors (Roche), and disrupted by 2-fold passages through a One Shot (Constant Cell Disruption Systems, Northants, UK) at 8,000 psi. Membrane protein was solubilized as previously described (solubilization buffer: 100 mM Tris-HCl pH 8.0, 500 mM NaCl, 15% Glycerol, 10 mM $MgCl_2$, 1 mM ATP, 1% DDM). *h*TAOK2-GFP-His was purified on an ÄKTA Xpress instrument (GE Healthcare, Uppsala, Sweden) at 4ºC. The solubilized fraction was applied to a HiTrap TALON superflow column (GE Healthcare, Uppsala, Sweden), previously equilibrated with binding buffer (composition of solubilization buffer, but with 0.1% DDM), at 0.6 mL/min constant flow. The column was washed with binding buffer until UV cell reached the baseline. The protein was eluted using a gradient of the binding buffer supplemented with 500 mM of imidazole (Sigma-Aldrich).

Solubilization screen of *h*TAOK2 expressed in HEK293T and insect cells

All manipulations were done at 4ºC. Membranes were resuspended to a final concentration of 4-5 mg/mL in 20 mM KH_2PO_4, 500 mM NaCl, 20% glycerol, 0.1 mM DTT, 10 mM $MgCl_2$, 2.5 mM ATP, pH 7.6; using a glass tissue homogenizer. The total volume of homogenized membranes was divided equally in a black bottom 96 well plate (Greiner). To each well was added a specific detergent (supplementary information Table 1). The plate was covered with aluminum foil and left overnight under mild shaking. GFP intensity signal was quantified on the total solubilized fraction using a FLUOstar OPTIMA microplate reader (BMG labtech). To a sample of 15 µl was added 5 µl of 4X Laemmli buffer (0.25 M Tris base, 15% SDS, 10% β-mercaptoethanol, 30% glycerol, 0.02% bromophenol blue, pH 6.8). The mixture was stored at 37ºC for 30 minutes and applied to a pre-cast 4-14% acrylamide gel (Biorad) and ran at constant 150 V for 50 minutes. The remaining of the fractions was ultracentrifuged at 100,000 g for 30 minutes (Optima^{TM} TLX, Beckman Coulter, Inc.). Supernatant was collected to a 96 well plate and GFP signal was quantified. A SDS-PAGE was done as described before but samples were applied to a home-made 6% polyacrylamide gel. All gels were in bidistilled water for 30 minutes, scanned for detection of GFP labeled protein using a 430-nm laser (Fuji TLA-5100) and stained with coomassie (Fazekas de St Groth et al., 1963).

Antibodies and Immunoblots

Total protein extracts from infected insect cells were prepared at a ratio of 10^7 total cells/mL in 25 mM Tris-HCl, 0.15 M NaCl, 0.5% N-Lauroylsarcosine, 20% Glycerol, 1 mM DTT, 1.25 U/mL Benzonase® (Merck Millipore), complete EDTA-free protease inhibitor cocktail (Roche), pH 8.0. Insoluble material was sedimented by 13,000x *g* centrifugation at 4°C for 10 min and the supernatant from 10^5 cell equivalents loaded onto 4-12% Novex® NuPAGE® Bis-Tris pre-cast gel (Life Technologies) followed by blotting to nitrocellulose membrane. Goat polyclonal anti-TAOK2 (αTAOK2) and mouse monoclonal anti-GFP (αGFP) clone GFP-20 antibodies (from Santa Cruz Biotechnology and Sigma-Aldrich, respectively) were used to assess expression levels and ECL signal recorded by ChemiDoc XRS+ (Bio-Rad).

Fluorescence microscopy

Insect cells infected in suspension were briefly left to adhere in 6 multiwell plates and observed under a Leica DM IRB inverted fluorescence microscope, images were acquired at a 20x magnification.

1.2.4. Results and Discussion

Expression tests of 47 *h*TAOK2 constructs

To facilitate a high-throughput screening, of a multiple number of constructs from the human gene encoding for the TAOK2 protein, we had access though the Protein Production Platform (P^3) to the Oxford Protein Production Facility (OPPF-UK) located in the Research Complex at Harwell. Primers were designed by Dr. Louise Bird (OPPF-UK) for insertion into the pOPIN vector by In-Fusion™ cloning (Figure 1.2.4.1). A variety of pOPIN derived vectors had been constructed in order to test protein expression in multiple tags (6xHis; Maltose Binding Protein, MBP; Small Ubiquitin-like Modifier, SUMO; and Green Fluorescent Protein, GFP) and using different segments of the *hTaok2* gene (Table 1.1.4.1). The majority of the pOPIN vectors allow the expression of proteins within multiple hosts, i.e. a single vector is capable of expression in *E. coli*, mammalian cell lines (e.g. HEK293T cells) and insect cells (e.g. *Sf*9 cells) enabling to screen for target expression in multiple hosts in parallel.

SUMO, MBP and GFP are widely used for the overexpression of eukaryotic proteins with increasing success (Arnau et al., 2006; Kiedzierska et al., 2008). However, GFP is mostly used to evaluate solubilization conditions of the expressed membrane protein, as it facilitates the application of a simpler technique, FSEC, to establish the target solubilization and stability in different detergents. As it happens with most affinity tags, GFP, MBP and SUMO may hinder the crystallization process. To overcome that problem a 3C cleavage site for the protease activity is available.

From each construct 2 clones were selected and a PCR reaction was done to evaluate the insertion of the correct DNA insert size on an agarose gel. Due to time constraints in this platform (2 week experimental trials at OPPF-UK), it was not possible to wait for results concerning the sequencing of the different constructs (confirmed latter on). For the same reason, the platform was only considered for overexpression trials in *Escherichia coli.* A clone of each construct was selected for overexpression trials in *E. coli* Rosetta and *E. coli* B834, under induction with IPTG or auto-induction. Together with the 47 constructs, a control vector containing only GFP (target H06, Table 1.1.4.1) was used in parallel with the expression of our target protein.

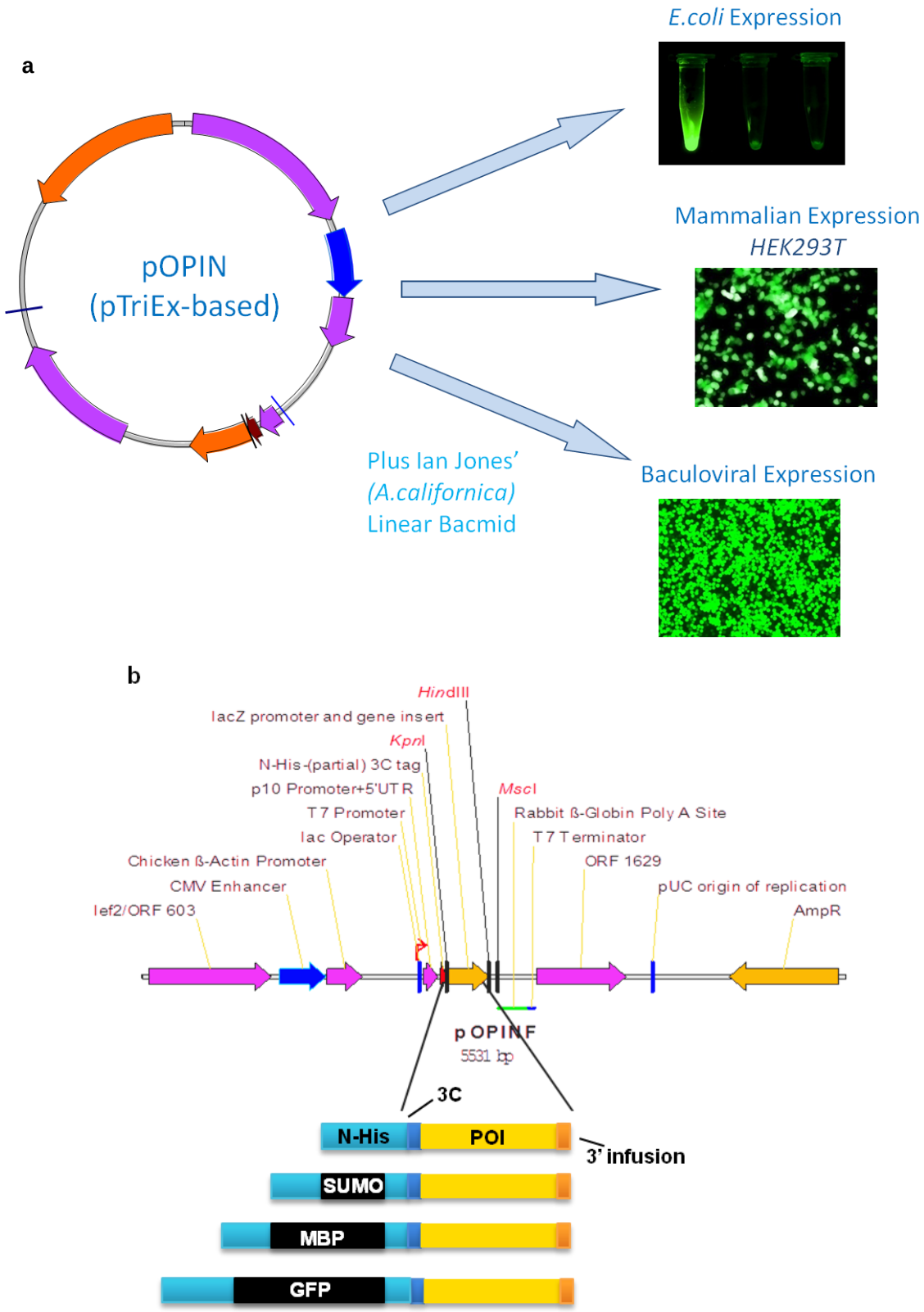

Figure 1.2.4.1. pOPIN vector used at the OPPF laboratory for high-throughput screening of *h*TAOK2 in *Escherichia coli* strains.

OPPF based constructs (a) pTriEx based vector pOPIN designed to overexpress genes of interest at multiple host systems. (b) Schematic diagram of pOPIN vectors fused with multiple tags (credits to OPPF-UK laboratory).

After a small scale overexpression test, affinity chromatography was performed on the soluble fraction and the overexpression was evaluated through presence/absence of bands on SDS-PAGE (see Appendix A1). Purification from the inclusion bodies was also evaluated. Table 1.2.4.1 shows the detailed information of the different constructs and the observed results concerning the overexpression and purification of the different 47 constructs of *h*TAOK2. In green are the constructs showing a band in the SDS-PAGE gel, at the expected molecular weight (MW) size, in soluble (S) or insoluble (I) fractions.

Most of the constructs were overexpressed only in inclusion bodies at the *E. coli* Rosetta strain when using the auto-induction protocol. Also, most of the expressed constructs were the ones without the transmembrane helices domain, and those concerning the constructs with fusion tags of MBP and SUMO (which may help stabilizing the protein). *h*TAOK2, as referred earlier in the introduction, is a large eukaryotic protein, with 135 kDa. The high molecular weight of the protein, together with its complexity, is likely to have a negative effect on its stability, hindering the expressing capacity of the *E. coli* machinery to properly fold and insert in the membrane such a complex protein. Also, it was visible, during the expression tests, a low optical density of the bacterial culture, even at pre-induction, present at some of the constructs. The observed results lead to the conclusion that the target protein seems to exert a toxic effect when expressed, provoking death to the bacterial host. Even when there is expression (observed in the SDS-PAGE gels) no construct provides a good expressing yield. For structural studies, a reasonable yield is obtained when a liter of culture renders ≥ 1 mg of protein target, which appears at the SDS-PAGE gel as a thick band upon coomassie staining. Accordingly to the expression results of the constructs presented above, the yields obtained should not have been higher than 0.1 mg per liter of culture.

Table 1.2.4.1. List of the 47 *h*TAOK2 constructs tested at OPPF-UK.

Well	aa_N	aa_C	Vector	MW isrt	pI	ε	MW TAG	Final MW	S	I
A01	2	1235	pOPINE3CeGFP	138	6,88	1,080	27	165		
B01	321	1235	pOPINE3CeGFP	101	6,84	1,031	27	128		
C01	370	1235	pOPINE3CeGFP	96	8,42	1,062	27	123		
D01	460	1235	pOPINE3CeGFP	86	9,78	1,140	27	114		
E01	590	1235	pOPINE3CeGFP	71	9,55	1,339	27	98		
F01	2	900	F (N-HIS-3C)	102	5,58	0,833	2	104		
G01	321	900	F (N-HIS-3C)	66	5,25	0,623	2	68		
H01	370	900	F (N-HIS-3C)	61	5,41	0,646	2	63		
A02	460	900	F (N-HIS-3C)	51	7,32	0,690	2	53		
B02	595	900	F (N-HIS-3C)	35	5,32	0,917	2	37		
C02	2	750	F (N-HIS-3C)	86	6,42	0,735	2	88		
D02	321	750	F (N-HIS-3C)	50	6,19	0,384	2	52		
E02	370	750	F (N-HIS-3C)	44	7,23	0,394	2	47		
F02	460	750	F (N-HIS-3C)	34	10,05	0,379	2	37		
G02	590	750	F (N-HIS-3C)	19	9,87	0,515	2	21		
H02	2	370	F (N-HIS-3C)	41	5,94	1,103	2	43		
A03	2	460	F (N-HIS-3C)	51	4,99	0,975	2	53		
B03	2	590	F (N-HIS-3C)	66	5,73	0,796	2	68		
C03	321	370	F (N-HIS-3C)	5	4,26	0,289	2	7		
D03	321	595	F (N-HIS-3C)	31	5,25	0,288	2	33		
E03	370	595	F (N-HIS-3C)	26	5,51	0,285	2	28		
F03	2	900	S3C(N-HIS-SUMO3C)	102	5,58	0,833	13	115		
G03	321	900	S3C(N-HIS-SUMO3C)	66	5,25	0,623	13	79		
H03	370	900	S3C(N-HIS-SUMO3C)	61	5,41	0,646	13	74		
A04	460	900	S3C(N-HIS-SUMO3C)	51	7,32	0,690	13	64		
B04	595	900	S3C(N-HIS-SUMO3C)	35	5,32	0,917	13	48		
C04	2	750	S3C(N-HIS-SUMO3C)	86	6,42	0,735	13	99		
D04	321	750	S3C(N-HIS-SUMO3C)	50	6,19	0,384	13	63		
E04	370	750	S3C(N-HIS-SUMO3C)	45	7,23	0,394	13	58		
F04	460	750	S3C(N-HIS-SUMO3C)	35	10,05	0,379	13	48		
G04	595	750	S3C(N-HIS-SUMO3C)	19	9,87	0,515	13	32		
H04	2	370	S3C(N-HIS-SUMO3C)	41	5,94	1,103	13	54		
A05	2	460	S3C(N-HIS-SUMO3C)	51	4,99	0,975	13	64		
B05	2	595	S3C(N-HIS-SUMO3C)	67	5,78	0,789	13	80		
C05	321	370	S3C(N-HIS-SUMO3C)	5	4,26	0,289	13	18		
D05	321	595	S3C(N-HIS-SUMO3C)	31	5,25	0,288	13	44		
E05	370	595	S3C(N-HIS-SUMO3C)	26	5,51	0,285	13	39		
F05	2	750	M(N-HIS-MBP)	86	6,42	0,735	43	129		
G05	321	750	M(N-HIS-MBP)	50	6,19	0,384	43	93		
H05	370	750	M(N-HIS-MBP)	45	7,23	0,394	43	88		
A06	460	750	M(N-HIS-MBP)	35	10,05	0,379	43	78		
B06	595	750	M(N-HIS-MBP)	18	9,81	0,539	43	62		
C06	2	370	M(N-HIS-MBP)	41	5,94	1,103	43	85		
D06	2	460	M(N-HIS-MBP)	51	4,99	0,975	43	95		
E06	2	595	M(N-HIS-MBP)	67	5,78	0,789	43	110		
F06	321	370	M(N-HIS-MBP)	5	4,26	0,289	43	48		
G06	321	595	M(N-HIS-MBP)	31	5,25	0,288	43	74		
H06	-	-	GFP positive control	27				27		

Abbreviations: aa-N: aminoacid at N-terminal, aa-C: aminoacid at C-terminal, MW: molecular weight, isrt: insert, KDa: kiloDalton, pI: isolectric point, ε: molar extinction coefficient, S: protein expressed in soluble fraction, I: protein expressed in insoluble fraction.

In-house expression tests with OPPF constructs

Despite the low expression yields observed for the high-throughput expression tests executed in OPPF-UK, some of the constructs were further experimented under different conditions and expression hosts, taking advantage of the multiple host system of the pOPIN vectors.

The first approach was to try the constructs with GFP in the mammalian HEK293T cells system for overexpression of eukaryotic membrane proteins.

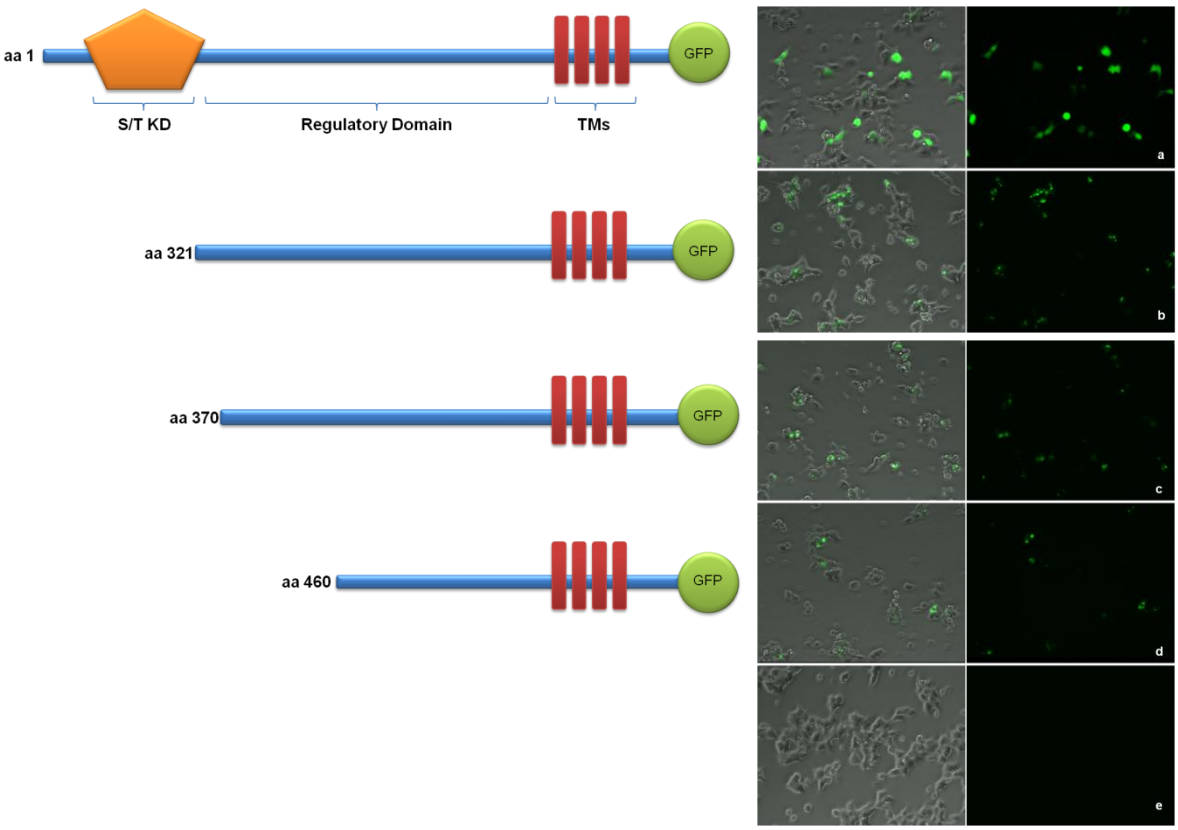

Figure 1.2.4.2. OPPF constructs of *h*TAOK2-GFP tested in HEK293T cells.

Four of the constructs done at OPPF were selected for overexpression experiments using the mammalian system HEK293T cells. The constructs were specifically selected because all contained GFP and the TMs. In the left panel there is a schematic representation of the constructs. On the right panels a fluorescent microscopical photograph of the cellular culture after transfection. (a) Full-length *h*TAOK2-GFP (OPPF A1), (b) aa 321-1235-*h*TAOK2-GFP (OPPF B1), (c) aa 370-1235-*h*TAOK2-GFP (OPPF C1), (d) aa 460-1235-*h*TAOK2-GFP (OPPF D1), (e) negative control.

To detect GFP, on the different constructs, after overexpression in HEK293T cells (Figure 1.2.4.2), a picture was taken at a fluorescence microscope. A positive indication that *h*TAOK2 is being overexpressed is the presence of a fluorescence peak in the area determined as the membrane, which was only observed for the A01 construct (representing the full-length protein) (Figure 1.2.4.2a). The A01 construct was then tested in *E. coli* strains BL21, C43 and Rosetta (Figure 1.2.4.3) with C43 strain showing the best results for this construct. C43 is a strain

specifically designed for the overexpression of membrane proteins, with specific properties to diminish the toxic effects of the incorporation of proteins in the bacterial membrane.

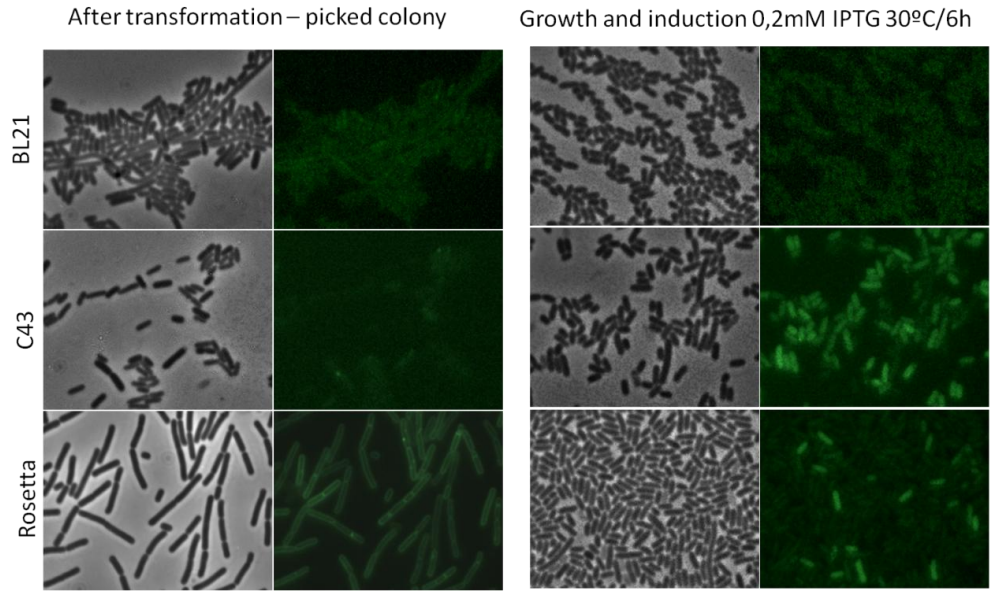

Figure 1.2.4.3. OPPF construct, full length *h*TAOK2-GFP, tested in different *Escherichia coli* strains.

Overexpression tests were done with other constructs. However, A01 and F02 were the only expressed in higher yields (see Appendix A2) and selected for small scale purification experiments (Figure 1.2.4.4). Urea was used during purification in order to maintain a denaturating environment, and so overcoming the need of solubilizing membranes with detergents, and assuring no occlusion of the tag by embedment with the lipid/detergent layer or due to aggregation of the target protein.

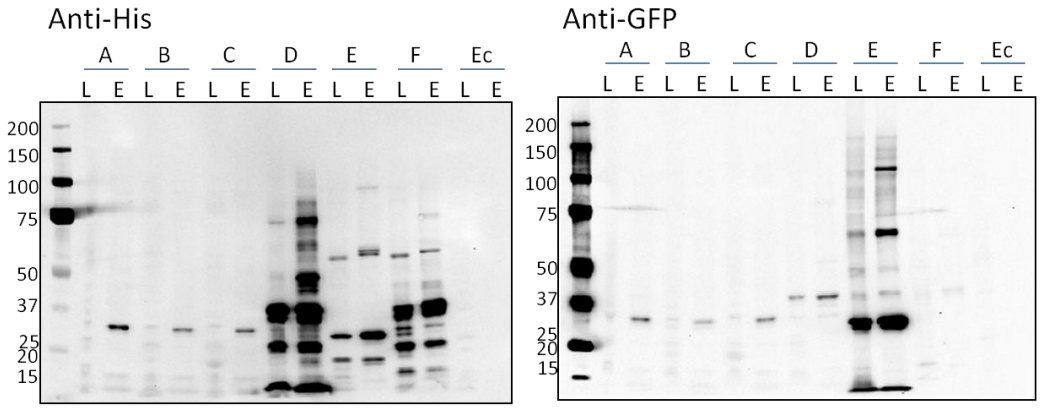

Figure 1.2.4.4. Small scale expression and purification of *h*TAOK2 constructs.

Different constructs were expressed in different conditions and purified by using a Ni-NTA Qiagen spin column under denaturating conditions (8 M Ureia). Loading and elution fractions were probed by immunohistochemistry with specific antibodies (left, anti-His tag; right, anti-GFP) for evaluation. Letter code, top: A, *E. coli* C43 construct A01; B, *E. coli* Rosetta construct A01; C, *E. coli* Rosetta construct A01; D, *E. coli* Rosetta construct F02; E, HEK293T cells construct A01; F, HEK293T cells construct F02; Ec, expression control; bottom: L, loading fraction; and E, elution fraction

Testing *in-house* full-length constructs of *h*TAOK2

The pOPIN expressing vector has already been validated for high-throughput screening of soluble proteins, using different expression hosts, besides *Escherichia coli* (Bird, 2011). For further testing the expression of full-length *h*TAOK2 in different host systems (mammalian cells, insect cells and bacteria), with various C- and N-terminal tagging, together with the possibility of monitorization by GFP fluorescence, primers were designed and three constructs were prepared (Figure 1.2.4.5) for *in-house h*TAOK2 overexpression, as described.

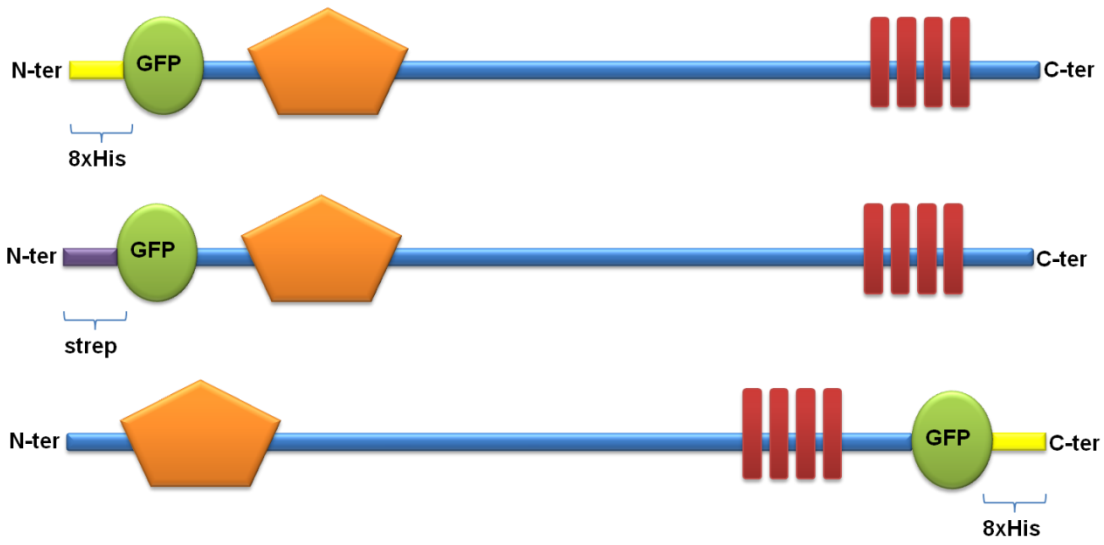

Figure 1.2.4.5. Schematic diagram of full-length constructs designed *in house.*

Three constructs were designed, two having tag (histidine tail or strep) together with GFP upstream of *h*TAOK2, Hist-GFP-*h*TAOK2 and strep-GFP-*h*TAOK2, respectively; and one construct with C-terminal tag (histidine tail) together with GFP downstream of *h*TAOK2, *h*TAOK2-GFP-His.

The three different constructs were tested in HEK293T cells. At different time points (48, 72 and 96 hours post induction), the GFP signal was observed under the fluorescent microscope. At mid-time point (48 hours) it was possible to observe differences in overexpression of the different constructs (Figure 1.2.4.6). While the strep-GFP-*h*TAOK2 constructs showed less green fluorescence than the constructs with histidine tags, the GFP seemed to colocalize with the membrane. However, the C-terminal His-GFP tagged construct showed that the overexpressed protein was not correctly inserted in the membrane. The best construct, showing membrane colocalization and substancial GFP signal, was the His-GFP-*h*TAOK2.

The overexpression of *h*TAOK2 was evaluated by Western blot using the αTAOK2 antibody (Figure 1.2.4.7).

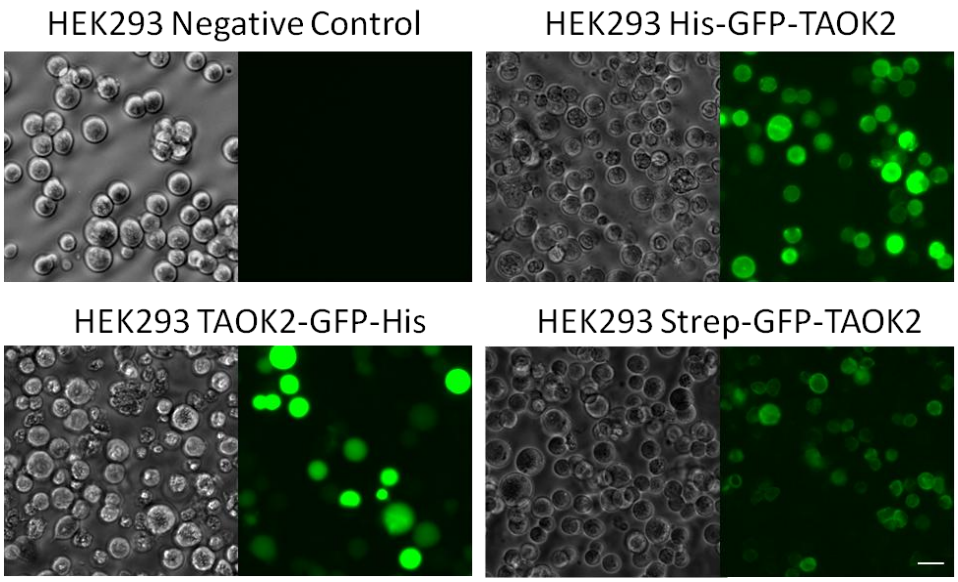

Figure 1.2.4.6. HEK293T cells 48 hours after transfection with the different constructs.

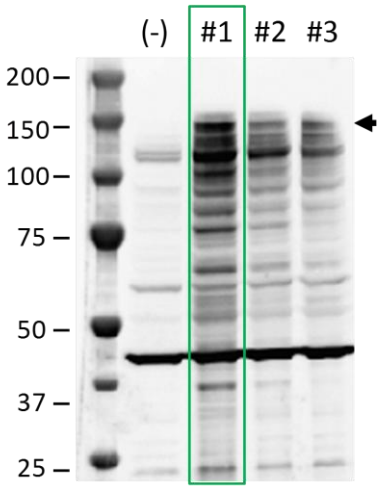

Figure 1.2.4.7. His-GFP-*h*TAOK2 overexpression evaluated by western blot.

Anti-TAOK2 antibody was used to probe the membrane. (-) control expression vector, #1, cells collected at 48 h post-transfection; #2, cells collected at 72 h post-transfection; #3, cells collected at 96 h post-transfection.

The Western blot shows a specific band at ≈150 kDa, stronger at 48 hours post-transfection. However, the strongest band exists at ≈ 120 kDa, 48 hours post-transfection, and gets weaker over the time of expression. There is also a very strong band at ≈ 45 kDa, present in all samples that could result from: recognition of an unspecific protein by the antibody; a proteolysis product resulting from cleaved TAOK2 polypeptide; or as a result of the endogenous expression of the *h*TAOK2 protein from the HEK293T cells intrinsic genome.

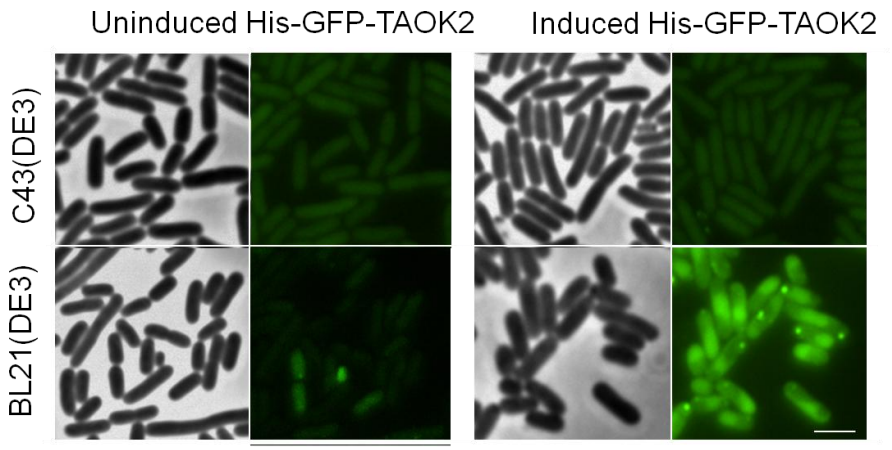

Figure 1.2.4.8. *E. coli* strains 48 hours after transfection with the different constructs.

This figure shows BL21(DE3) (lower panels) and C43(DE3) (upper panels) *E. coli* strains transfected with His-GFP-TAOK2 without induction (left) or after 48 hours of induction (right).

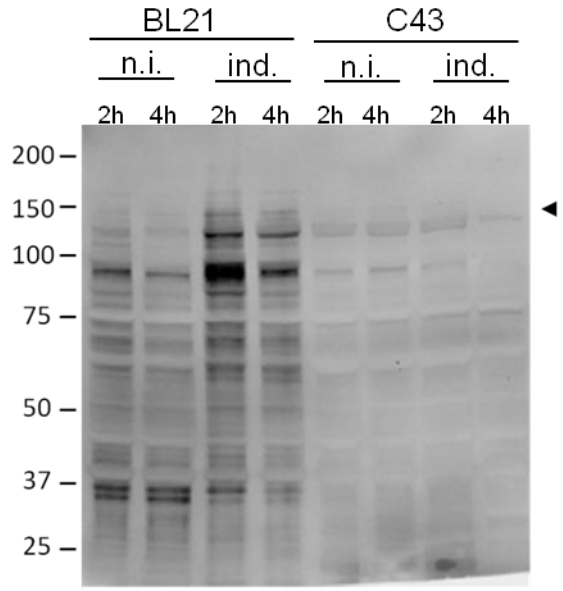

Figure 1.2.4.9. Western blot of BL21(DE3) and C43(DE3) probed for αTAOK2 polyclonal antibody.

Cells were transformed with the His-GFP-*h*TAOK2. Western blot with samples from non-induced (n.i.) BL21(DE3) cells or C43(DE3) cells (2 and 4 hours p.i.) and with induced cells (ind.). Arrowhead indicates expected molecular weight of protein construct.

The overexpression of His-GFP-*h*TAOK2 in the *E. coli* strains BL21(DE3) and C43(DE3) shows a specific overexpression in BL21(DE3) but none at the C43(DE3) strains (Figure 1.2.4.8). However, His-GFP-*h*TAOK2 does not localize to the cell membranes of *E. coli* cells and expression renders a protein with lower molecular weight, as observed by the Western blot probed with the anti-TAOK2 antibody (Figure 1.2.4.9, arrowhead). Only a very faint band with a high molecular weight, possibly the band of interest, was visible at ≈160 kDa (Figure 1.2.4.9). Moreover, it a highly degradation smear was visible at the induced BL21(DE3) with a large

accumulation of a product below 100 kDa at 2 hours post-induction (p.i.), most likely resulting from specific cleavage of *h*TAOK2 or due to extensive degradation by the bacterial proteolytic machinery.

Based on these results, an expression trial of His-GFP-*h*TAOK2 was performed in HEK293T cells, followed by a bench-top purification protocol using Ni-NTA spin columns. The cells were harvested and lysed chemically with Bugbuster, and solubilization done at pH 8.0 with 1% DDM. After applying the sample to the spin column, protein was eluted with a buffer containing an excess of imidazole (500 mM). Western-blot analysis on the fractions after purification revealed a specific band for *h*TAOK2 at ≈ 150 kDa (Figure 1.2.4.10a, arrowhead).

The total yield of each downstream step towards purification was calculated based on the GFP fluorescence, with a calibration curve measured at the time (Figure 1.2.4.10b) and using the following equation:

$$h\text{TAOK2 (µg/mL)} = \frac{\text{MW (}h\text{TAOK2}-128\text{ kDa)}}{\text{MW (GFP}-27\text{ kDa)}} \text{ x Amount of GFP (µg/mL).}$$

According to this equation, *h*TAOK2 purification had a recovery yield of around 26% (compared to the initial amount of overexpressed membrane protein) revealing a high lost of protein during the process (Figure 1.2.4.10c). However, due to the presence of diverse proteins in solution, besides our protein target, it is possible that the GFP intensity signal is extrapolated.

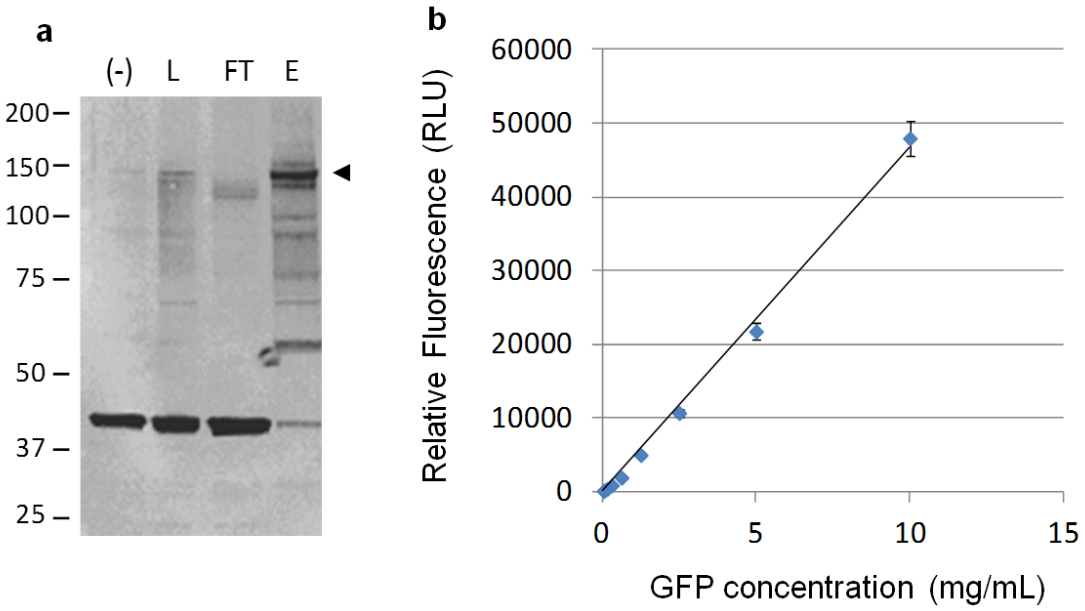

c

	Fluorescence (RLU)	GFP (µg/mL)	*h*TAOK2 (µg/mL)	*h*TAOK2 (mg)	Recovery (per step, %)
Membranes (40 mL)	624	32.2	152.9	6.2	-
Extraction (40 mL)	256	23.8	113.2	4.3	69
Purification (10 mL)	203	22.6	107.5	1.1	26

Figure 1.2.4.10. Affinity chromatography (Ni-NTA) for *h*TAOK2 overexpressed in HEK293T cells.

(a) Western blot of the samples from the purification trial: (-), lysed sample of HEK293T cells without expression of our construct; L, sample loaded in the column; FT, flow-through of loaded sample; E, eluted. (b) Calibration curve of GFP fluorescent signal used at the fluorimeter at the same time point of our purification samples, in order to establish a concentration of tagged *h*TAOK2 during purification. (c) Table demonstrating the final concentration at each step (membrane preparation, protein extraction and purification) and the recovery yield of the downstream process of overexpressed *h*TAOK2.

A time-course expression screening of His-GFP-*h*TAOK2 in Baculovirus-infected insect cell lines showed the substantial accumulation at mid-late time points of a ~70-75 kDa fragment and -to a lower extent of a ~120 kDa polypeptide (Figure 1.2.4.11a).

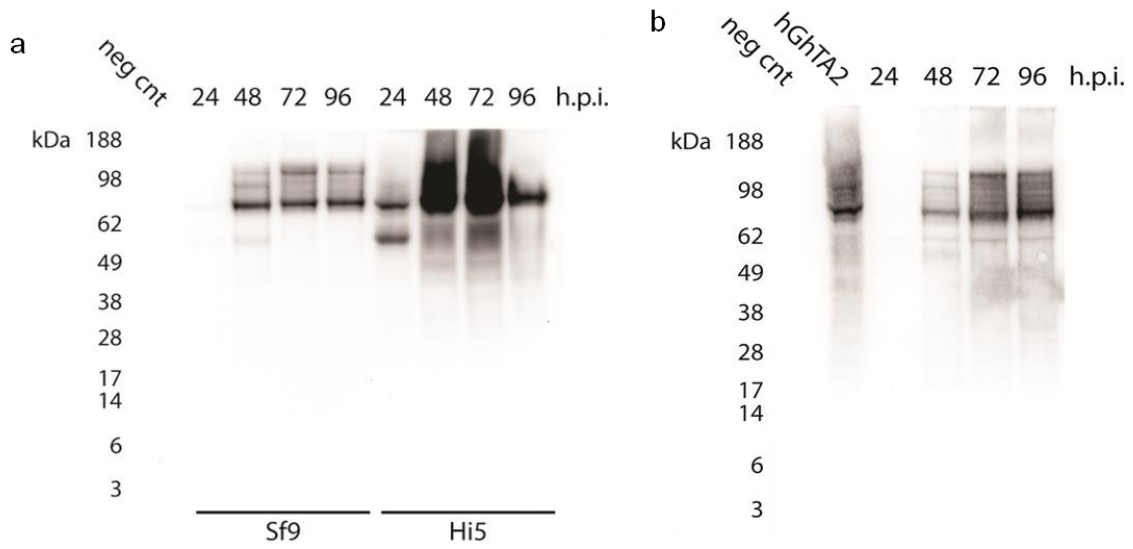

Figure 1.2.4.11. Time-course expression screening of His-GFP-*h*TAOK2 and strep-GFP-hTAOK2 in Baculovirus-infected insect cell lines

(a) Sf9 and Hi5 cells were infected and processed as stated in Material and Methods with His-GFP-*h*TAOK2 (hGhTAO2) expressing recombinant Baculovirus and harvested at the indicated hours post-infection (h.p.i.); (b) Hi5 cells infected with strep-GFP-*h*TAOK2 (stGhTAOK2) expressing Baculovirus were collected at the indicated h.p.i.; hGhTAO2: Hi5 cells expressing hGhTAO2 96 h.p.i.; neg cnt: negative control was by cells infected with a recombinant Baculovirus expressing an unrelated protein. Both immunoblots were probed with α-TAOK2 polyclonal antibody.

The major product is then reminiscent of the caspase-dependent p70 *h*TAOK2 fragment previously reported (Zihni et al., 2007). The full length chimeric protein, with an expected molecular weight of 168 kDa, remained undetectable. However, it was observed a time-dependent increase in the size of TAOK2 fragments: a 55 kDa fragment transiently visible early after Baculovirus infection. The latter behaviour is reminiscent of a progressively inhibited site-specific cleavage rather than a merely unspecific protein degradation (which is nevertheless present). Indeed, this up-shifting in the molecular weight occured earlier in Hi5 cells. His-GFP-*h*TAOK2 expression appeared stronger earlier in the cells, so it is temptative to speculate that the 75 kDa major fragment acts as an inhibitor of the 55 kDa form-releasing cleavage. On the other hand, using Strep-tag in place of the polyHis repeat resulted in very low expression (Figure 1.2.4.11b), showing this tag negatively affects the bioynthesis/accumulation of this chimeric protein. The expression resulted in a ladder of polypetides between 120 and 75 kDa. The difference in the expression levels between the two tagged variants was visible also at cellular level (Figure 1.2.4.12), with His-GFP-*h*TAOK2-expressing cells showing a brighter GFP fluorescence.

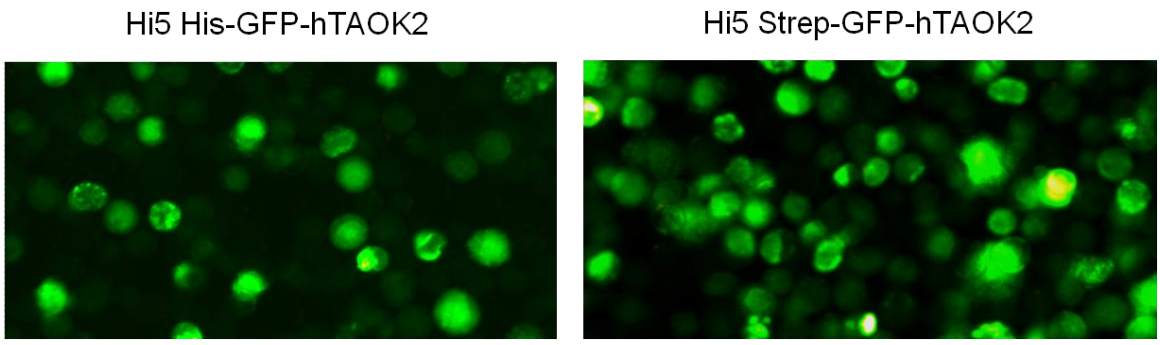

Figure 1.2.4.12. Hi5 cell cultures were infected with the indicated recombinant Baculoviruses.

At 72 h.p.i., each seeded into a well of a six multiwell plate for 30 min and the GFP fluorescence recorded supravitally under an inverted UV microscope.

Yet and independently of the affinity tag present, only few cells displayed an intracellular dotted pattern, anyway not suggestive of the described microtubule association via cytosolic vesicles (Mitsopoulos et al., 2003). Indeed, the most positive cells were characterized by a total cell GFP localization. Moreover, neither the stable 75 kDa nor the 120 kDa form detected in immunoblots with the α-TAOK2 polyclonal antibody in His-GFP-*h*TAOK2-expressing cells turned-out to contain the N-terminal recombinant HisGFP tag. When tested in IMAC, both *h*TAOK2 fragments were found to bind, though not tightly, the Ni-NTA resin independently of the polyHis-GFP (Figure 1.2.4.13). However, it was hardly detected a 38 kDa band, corresponding to the polyHis-GFP, in the eluted fractions by a α-GFP monoclonal antibody (MAb) upon digital intensification of the chemo-luminescent signal. The very low abundance of the His-GFP containing polypeptide found in the solubilized extracts suggested that the majority of GFP fluorescence observed at cellular level in infected insect cells was due to an insoluble His-GFP-*h*TAOK2 N-terminal portion comprising only the first - probably misfolded - 70-75 residues of TAOK2. The His-tag independent binding of the 75 and 120 kDa TAOK2 fragments was likely mediated by the polyGlu stretches present in this protein (aa 378-392 and aa 900-907 present in the wt *h*TAOK2 sequence). As a consequence, the larger 120 kDa accounts for almost the complete sequence of unfused TAOK2.

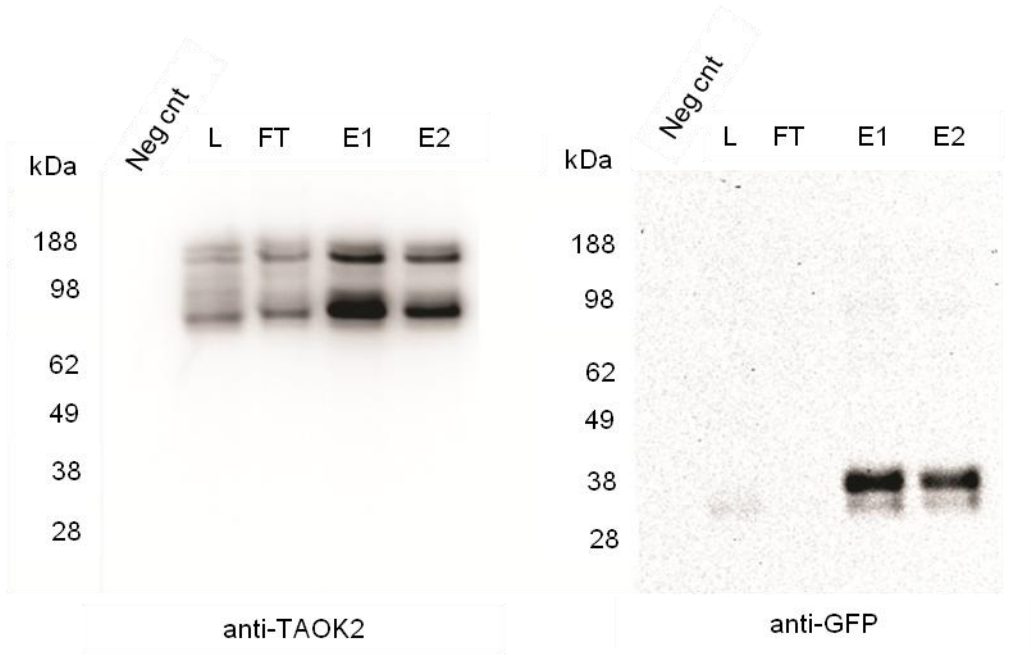

Figure 1.2.4.13. Microscale Ni-NTA from Hi5 cells infected with His-GFP-*h*TAOK2 expressing recombinant Baculovirus.

At 72 h.p.i. cells were harvested, extracted with 1% Triton and the extract clarified at 13000x *g* for 10 min at 4°C; the supernatant was then loaded onto Ni^{+2}-NTA spin columns from Quiagen and the affinity chromatography was performed according to the manifacturer's guidelines; L: loaded clarified extract; F.T.: column flow through; E1 - E2: two subsequent elutions performed with 500 mM imidazole; negative control was as in Figure 1. Aliquots from each sample were probed in immunoblot with either α-TAOK2 polyclonal (**a**) or α-GFP monoclonal antibody (**b**).

Actually, the polyclonal antibody α-TAOK2 used in this study recognizes several endogenous TAOK2 forms. In extracts from human neuron-like teratoma cells and total newborn rat brain (Figure 1.2.4.14), two 120 and 40 kDa most prominent bands and 90-95 and 55 kDa less abundant forms are present. It is then unlikely that the tendency to proteolytic cleavage displayed by this membrane-bound kinase is just the result of recombinant overexpression. Thus, the multi-platform approach reported here allowed uncovering a complex and possibly dynamic cleavage pattern of stable shorter fragments from *h*TAOK2. Further effort is warranted to map the observed cleavage sites, their possible role in regulating *h*TAOK2 cellular activities and the interplay with the multiple *h*TAOK2 phosporylation sites.

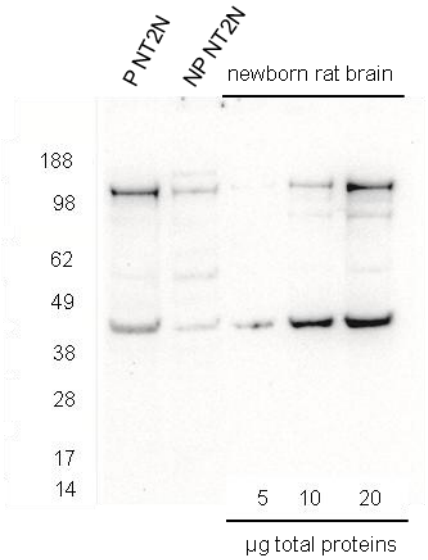

Figure 1.2.4.14. Immunoblot with α-TAOK2 polyclonal antibody.

Protein extracts from 10^5 proliferating (P NT2) or non proliferating (NP NT2) NTera2 cells, and from total 7 days old rat brain.

High-throughput solubilization tests

After expressing the full-length *h*TAOK2 protein in HEK293T cells and Hi5 insect cells, we proceeded with our experiments of solubilization and purification of *h*TAOK2 in higher quantities. The first approach consisted on overexpressing His-GFP-*h*TAOK2 in HEK293T cells and test different detergents for solubilization (Figure 1.2.4.15). Detergents were chosen based on their successfully use for the solubilization of eukaryotic membrane proteins. SDS being a potent denaturating reagent was used as a control. This way, it would be possible to understand if *h*TAOK2 is aggregated or, in contrary, is not even being extracted from the membrane. The results show that the protein is not solubilized (no band at soluble fraction), with exception for the sample extracted with SDS (Figure 1.2.4.15, left). When looking to the insoluble fraction (1.2.4.15, right) several fluorescent bands at ≈ 150 kDa are visible, leading us to conclude that extraction of *h*TAOK2 is taking place, however the protein is aggregating most probably because of His- tag.

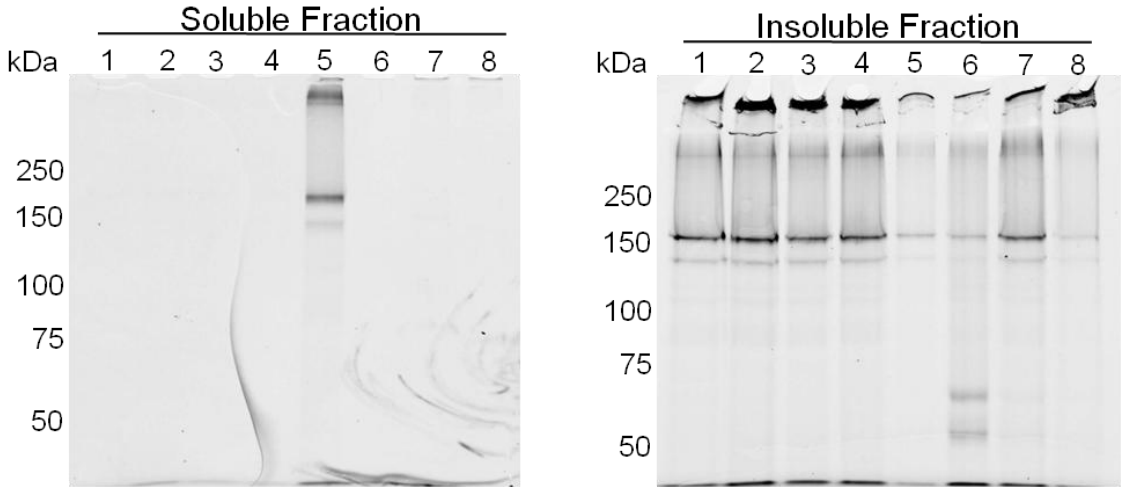

Figure 1.2.4.15. Initial solubilization tests performed on overexpressed His-GFP-*h*TAOK2 in HEK293T cells.

In-gel fluorescence. After overexpression of His-GFP-*h*TAOK2 at HEK293 cells, membranes were isolated and split in 8 parts, solubilization of the target was done overnight at 4ºC using 8 different detergents: 1, 2% DDM; 2, 2% Triton X-100; 3, 2% CYMAL-5; 4, 2% LDAO; 5, 2% SDS; 6, 9 mM CHAPS; 7, 142.5 mM Foscholine-8; 8, 1.2% ANAPOE-$C_{13}H_8$. After solubilization, the soluble fraction was separated from the insoluble fraction, ran on SDS-PAGE and scanned through a laser to detect GFP fluorescence.

To test for this hypothesis, the extraction of *h*TAOK2 overexpressed using the two different tags– His and Strep – under a high variety of detergents was performed.

Cultures from Baculovirus induced cells with the strep-GFP-*h*TAOK2 were used for a second trial with a 96 detergent screen (Table 1.2.4.2) for solubilization of the full-length construct from TAOK2. Cells were homogeneized and resuspended (in an appropriate buffer as described previously), distributed in a 96 well plate (Table 1.2.4.2) with a black-bottom (to allow detection of the GFP signal intensity) and measured at the fluorimeter for the total amount of protein and for the solubilized protein. Samples from insoluble and soluble fraction were subjected to SDS-PAGE and the GFP signal detected in a scanner (Appendix A3). The three best conditions identified on the SDS-PAGE (intensity of band in the gel) were selected for analysis on Western blot in order to verify if bands truly corresponded to the *h*TAOK2 protein (Figure 1.2.4.16).

Table 1.2.4.2. Detailed information of the 96 detergent screen.

W	Type	Detergent	CMC	[]	W	Type	Detergent	CMC	[]
A1	I	SDS	8.27	1%	E1	N	CYMAL-2	120	1 CMC
A2	N	Triton X-100	0.9	1%	E2	Z	ZWITTERGENT 3-08	330	1 CMC
A3	N	Pluronic F-68	17.9	1%	E3	N	CYMAL-1	340	1 CMC
A4	N	ANAPOE-35	0.091	1%	E4	Z	ZWITTERGENT 3-16	0.06	1 CMC
A5	N	2,6-dimethyl-4-heptyl-β-D-maltopyranoside	27.5	1 CMC	E5	N	C12E9	0.08	1 CMC
A6	N	ANAPOE-58	0.004	1%	E6	N	C12E8	0.11	1 CMC
A7	N	ANAPOE-X-114	0.2	1%	E7	L	Dodecyl-ββ-D-Glucoside	0.13	1 CMC
A8	N	ANAPOE-X-305	N/A	1%	E8	Z	SWITTERGENT 3-14	0.4	1 CMC
A9	N	ANAPOE-X-405	0.81	1%	E9	N	MEGA-10	7	1 CMC
A10	N	ANAPOE-20	0.059	1%	E10	N	C8E4	7	1 CMC
A11	N	ANAPOE-80	0.012	1%	E11	N	C10E5	0.81	1 CMC
A12	N	ANAPOE-C10E6	0.9	1%	E12	N	DDAO	10.4	1 CMC
B1	N	ANAPOE-C10E9	1.3	1%	F1	N	Octyl-β-D-Glucoside	25	1 CMC
B2	N	ANAPOE-C12E10	0.2	1%	F2	N	MEGA-8	79	1 CMC
B3	N	ANAPOE-C13E8	0.1	1%	F3	Z	SWITTERGENT 3-8	330	1 CMC
B4	N	IPTG	N/A	1%	F4	I	Na-cholate	0.5	0,01
B5	Z	n-dodecyl-N,N-dimethylglycine	1.5	1 CMC	F5	L	1,2-dioctanoyl-*sn*-glycero-3-phosphocholine	0.27	1%
B6	N	HEGA-10	7	1 CMC	F6	N	Cymal-5	2.4-5	1%
B7	N	C8E5 (Octylpentaglycol)	7.1	1 CMC	F7	L	DMPC (1,2-dimyristoyl-*sn*-glycero-3-phosphocholine)	0.006	1%
B8	Z	CHAPS	8	1 CMC	F8	N	DDM (n-dodecyl-β-D-maltopyranoside)	0.17	1%
B9	Z	CHAPSO	8	1 CMC	F9	N	LDAO	1-2	1%
B10	N	C-HEGA-11	11.5	1 CMC	F10	N	n-octyl-β-D-thioglucoside	9	1%
B11	N	HEGA-9	39	1 CMC	F11	N	DM (n-decyl-β-D-maltoside)	1.8	1%
B12	N	C-HEGA-9	108	1 CMC	F12	N	NG (n-nonyl-β-D-glucoside)	6.5	1%
C1	N	HEGA-8	109	1 CMC	G1	L	1,2-diheptanoyl-*sn*-glycero-3-phosphocholine	1.4	1%
C2	N	C-HEGA-8	277	1%	G2	N	n-nonyl-β-D-thioglucoside	2.9	1%
C3	N	Nonidet P-40	0.17	1%	G3	N	n-decyl-β-D-glucoside	2.2	1%
C4	I	BAM	N/A	1%	G4	Z	Fos-choline-14	0.12	1%
C5	N	n-hexadecyl-β-D-maltoside	0.0006	1 CMC	G5	Z	Fos-choline-16	0.013	1%
C6	N	n-tetradecyl-β-D-maltoside	0.01	1 CMC	G6	N	n-heptyl-β-D-thioglucoside	29	1%
C7	N	n-tridecyl-β-D-maltoside	0.033	1 CMC	G7	N	n-decyl-β-D-thioglucoside	0.9	1%
C8	N	Thesit	0.09	1 CMC	G8	N	Cymal-3	34.5	1%
C9	Z	SWITTERGENT 3-14	0.4	1 CMC	G9	N	CYGLU-3	28	1%
C10	N	n-undecyl-β-D-maltoside	0.59	1 CMC	G10	N	n-hexyl-β-D-glucoside	250	1%
C11	N	n-decyl-β-D-thiomaltoside	0.9	1 CMC	G11	N	n-heptyl-β-D-glucoside	70	1%
C12	Z	FOS-Choline-12	1.5	1 CMC	G12	N	n-decyl-N,N-dimethylglycine	19	1%
D1	N	n-decanoylsucrose	2.5	1 CMC	H1	N	n-hexyl-β-D-maltoside	210	1%
D2	N	1-s-nonyl-β-D-thioglucoside	2.9	1 CMC	H2	N	n-octyl-β-D-galactoside	29.5	1%
D3	N	n-nonyl-β-D-thiomaltoside	3.2	1 CMC	H3	N	n-dodecyl-β-D-glucoside	0.19	1%
D4	Z	DDMAB	4.3	1 CMC	H4	N	Dodecyl-ββ-D-glucopyranoside	0.13	1%
D5	N	n-nonyl-β-D-maltoside	6	1 CMC	H5	N	n-octyl-β-D-glucoside	18 - 20	1%
D6	N	CYMAL-4	7.6	1 CMC	H6	N	n-undecyl-β-D-thiomaltoside	0.21	1%
D7	N	n-octyl-β-D-thiomaltoside	8.5	1 CMC	H7	I	sodium-dodecanoyl-sarcosine	14.4	1%
D8	Z	Fos-choline-10	11	1 CMC	H8	N	Mega-8	79	1%
D9	Z	Fos-choline-9	39.5	1 CMC	H9	I	CTAB	1	1%
D10	N	MEGA-9	25	1 CMC	H10	N	TMAO	N/A	1%
D11	L	1,s-heptyl-β-D-thioglucoside	29	1 CMC	H11	N	Borane complex	N/A	1%
D12	Z	Fos-choline-8	114	1 CMC	H12	L	1,2-dihexanoyl-*sn*-glycero-3-phosphocholine	15	1%

Abbreviations: W, well position of the 96 conditions of detergents; Type, type of detergent (I) ionic, (N) non-ionic, (Z) zwitterionic, (L) lipid; Detergent, classification of the detergent same as for the Anatrace Detergent and Lipids (http://www.affymetrix.com); CMC, Critical micelar detergent concentration as in the Anatrace Detergent and Lipids; [], final concentration of the detergent in the screen (CMC or % W/V as in the Avanti® Polar Lipids, Inc). SDS – Sodium Dodecyl Sulphate, Pluronic F-68 - Polyoxyethylene-Polyoxypropylene Block Copolymer, ANAPOE-35 - a-Dodecyl-w-hydroxy-poly(oxy-1,2-ethanediyl), ANAPOE-58 - a-Hexadecyl-w-hydroxy-poly(oxy-1,2-ethanediyl), ANAPOE-X-114 - α-[(1,1,3,3-Tetramethylbutyl)phenyl]-w-Hydroxy-Poly(Oxy-1,2-Ethanediyl), ANAPOE-X-305 - α-[4-(1,1,3,3-Tetramethylbutyl)phenyl]-w-Hydroxy-Poly(Oxy-1,2-Ethanediyl), ANAPOE-X-405 - α-[4-(1,1,3,3-Tetramethyl-Butyl)Phenyl]-w-Hydroxy-Poly(Oxy-1,2-Ethanediyl), ANAPOE-20 - Polyoxyethylene(20)sorbitan Monolaurate, ANAPOE-80 - (Z)-Sorbitan Mono-9-octadecanoate, ANAPOE-C10E6 - Polyoxyethylene(6)decyl Ether, ANAPOE-C10E9 - Polyoxyethylene(9)decyl Ether, ANAPOE-C12E10 - Polyoxyethylene(10)dodecyl Ether, ANAPOE-C13E8 - Polyoxyethylene(8)tridecyl Ether, IPTG - Isopropyl β-D-thiogalactoside, HEGA-10 - Decanoyl-N-Hydroxyethylglucamide, C8E5 – Octylpentaglycol, CHAPS - 3-[(3-Cholamidopropyl)-Dimethylammonio]-1-Propane Sulfonate/N,N-Dimethyl-3-Sulfo-N-[3-[[3α,5β,7α,12α)-3,7,12-Trihydroxy-24-Oxocholan-24-yl]Amino]propyl]-1-Propanaminium Hydroxide, CHAPSO - 3-[(3-Cholamidopropyl)dimethylammonio]-2-Hydroxy-1-Propanesulfonate, C-HEGA-9 - Cyclohexylpropanoyl-N-Hydroxyethylglucamide, C-HEGA-11 - Undecanoyl-N-Hydroxyethylglucamide, HEGA-9 - Nonanoyl-N-Hydroxyethylglucamide, C-HEGA-9 - Cyclohexylpropanoyl-N-Hydroxyethylglucamide, HEGA-8 - Octanoyl-N-Hydroxyethylglucamide, C-HEGA-8 - Cyclohexylethanoyl-N-Hydroxyethylglucamide, Nonidet P 40 - octyl phenoxypolyethoxylethanol, BAM – Benzyldimethyldodecylammonium bromide, Thesit – ANAPOE-C12E9 [Polyoxyethylene(9)dodecyl Ether], SWITTERGENT 3-14 - n-Tetradecyl-N,N-dimethyl-3-ammonio-1-propanesulfonate, FOS-Choline-12 - n-Dodecylphosphocholine, DDMAB - N-Dodecyl-N,N-(dimethylammonio)butyrate, CYMAL-4 - 4-Cyclohexyl-1-Butyl-β-D-Maltoside, Fos-choline-10 - n-Decylphosphocholine, Fos-choline-9 - n-Nonylphosphocholine, MEGA-9 - Nonanoyl-N-Methylglucamide, CYMAL-2 - 2-Cyclohexyl-1-Ethyl-β-D-Maltoside, ZWITTERGENT 3-08 - 3-(N,N-Dimethyloctylammonio)propanesulfonate inner salt, CYMAL-1 - Cyclohexyl-Methyl-β-D-Maltoside, SWITTERGENT 3-16 - 3-(N,N-Dimethylpalmitylammonio)propanesulfonate, ANAPOE-C12E9 - α-

Dodecyl-w-Hydroxy-Poly(oxy-1,2-Ethanediyl), C12E8 - Dodecyl octaethylene glycol ether, ZWITTERGENT 3-14 - n-Tetradecyl-N,N-Dimethyl-3-Ammonio-1-Propanesulfonate, MEGA-10 - Decanoyl-N-Methylglucamide, C8E4 – Octyltetraglycol, C10E5 – Decylpentaglycol, DDAO - n-Dodecyl-N,N-Dimethylamine-N-Oxide, MEGA-8 - Octanoyl-N-Methylglucamide, ZWITTERGENT 3-8 - n-Octyl-N,N-Dimethyl-3-Ammonio-1-Propanesulfonate, Cymal-5 - 5-Cyclohexyl-1-Pentyl-β-D-Maltoside, DMPC - 1,2-dimyristoyl-sn-glycero-3-phosphocholine, DDM - n-dodecyl-β-D-maltopyranoside, LDAO - Lauryldimethylamine oxide, DM - n-decyl-β-D-maltoside, NG - n-nonyl-β-D-glucoside, Fos-choline-14 - n-Tetradecylphosphocholine, Fos-choline-16 - n-Hexadecylphosphocholine, Cymal-3 - 3-Cyclohexyl-1-Propyl-β-D-Maltoside, CYGLU-3 - 3-Cyclohexyl-1-Propyl-β-D-Glucoside, Mega-8 - Octanoyl-N-Methylglucamide, CTAB - Cetyl Trimethyl Ammonium Bromide, TMAO - Trimethylamine N-oxide.

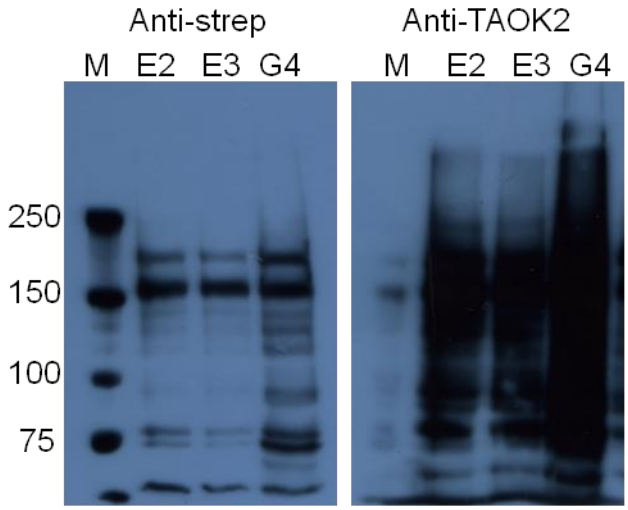

Figure 1.2.4.16. Western blot of soluble samples extracted from the membranes of Hi5 cells with higher yields.

Western blot with Anti-strep (left) and Anti-TAOK2 (right) showing the best extraction detergents. M, Marker; E2, Zwittergent-3-08; E3, CYMAL-1; and G4, Fos-choline-14.

A second solubilization screen was done using HEK293T cell overexpressing His-GFP-*h*TAOK2. Samples from insoluble and soluble fractions were subjected to SDS-PAGE and the GFP signal detected in a scanner as previously (Appendix A4), with the best conditions being selected for Western blot analysis (Figure 1.2.4.17).

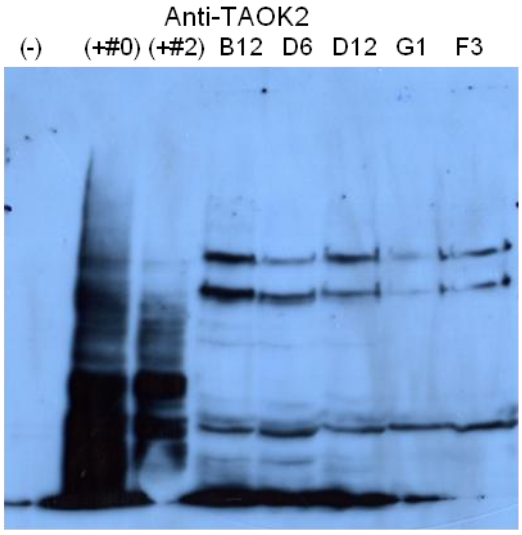

Figure 1.2.4.17. Western blot of soluble samples extracted from the membranes of HEK293T cells with higher yields.

Western blot probed for TAOK2 showing the best extraction detergents. (-) negative control; (+#0) and (+#2) positive controls; B12, C-HEGA-9; D6, CYMAL-4; D12, Fos-choline-8; G1, 1,2-diheptanoyl-sn-glycero-3-phosphocholine; F3, SWITTERGENT 3-8.

The detergent conditions were also evaluated by fluorimetry, measuring the GFP signal intensity (Figure 1.2.4.18). The % of solubilization was calculated, based on the ratio of the GFP signal obtained in the soluble fraction *versus* the total fraction after solubilization. From this experiment, the best detergents for extraction of *h*TAOK2α, seem to be n-decyl-β-D-thioglucoside (G7), Fos-choline 16 (G5), Fos-choline 14 (G4) and DDM (F8), with extractions from the membrane preparation fraction above 70%. This has led to the conclusion that theresults based on in-gel fluorescence can be misleading, and prone to consider a different detergent from the one best suited for our studies.

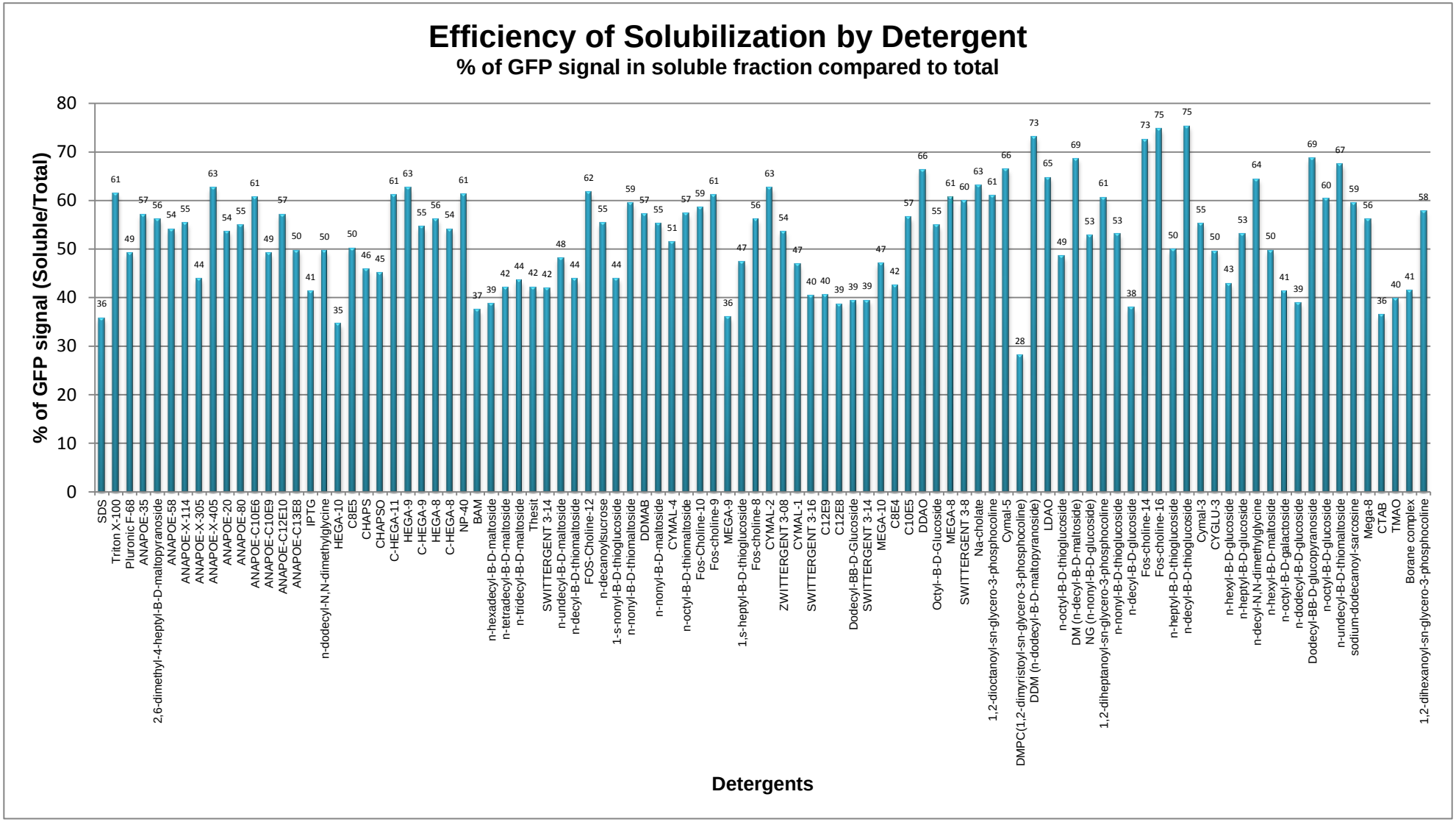

Figure 1.2.4.18. Graphical representation of detergent solubilization capacity of His-GFP-*h*TAOK2 construct when expressed in HEK293T cells.

The strep-GFP-*h*TAOK2 overexpressed at HEK293T cells was subjected to purification using a manual syringe column with streptactin resin (IBA) for affinity chromatography. After extraction from the membrane using Tris-HCl buffer supplemented with 1% DDM, the sample was applied to the 1 mL column and the purification ran at room temperatute under gravity flow. After several washes with the same buffer, the protein of interest was eluted with 5 mM desthibiotin and the aggregated protein was eluted with 0.5 M NaOH. The resulting fractions were evaluated by Western blot.

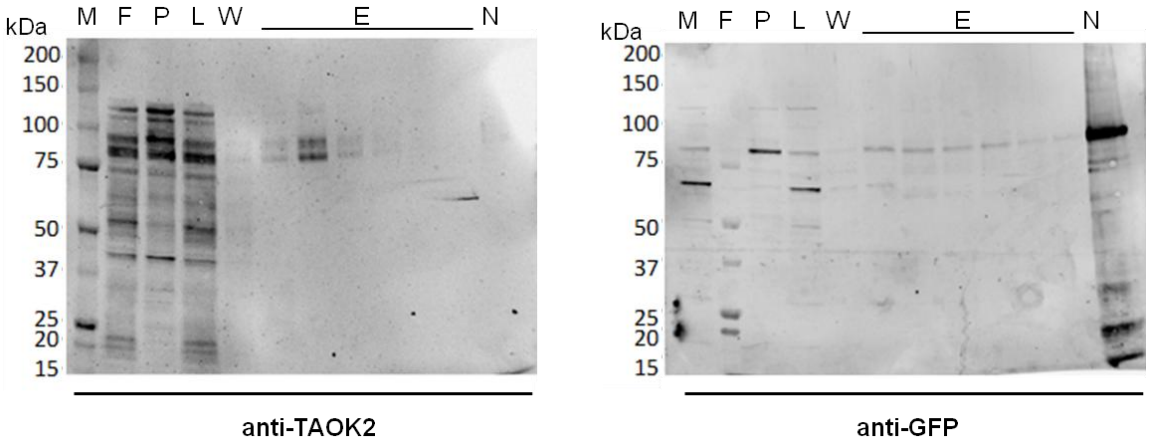

Figure 1.2.4.19. Western blot analysis after manual affinity chromatography of strep-GFP-*h*TAOK2.

The Western blot membrane was probed sequentially with anti-TAOK2 (left) and anti-GFP (right) antibodies. M, molecular weight marker (Bio-rad); F, flow-through, P, membrane pellet after extraction; L, sample loaded in column; W, washing step; E, eluted fraction; N, fraction eluted with 0.5 M NaOH.

The Western blot (Figure 1.2.4.19) shows only specific band for hTAOK2 at ≈90 kDa at the eluted fractions. Higher molecular weight bands were found at the flow-through and remaining membrane pellet after extraction. This indicates that the used purification column does not efficiently binds to the present protein, and also, that the protein was not efficiently extracted from the membrane. Moreover, the most intense band present at the eluted fraction, with 0.5 M NaOH, only reacts with anti-GFP and not with the TAOK2 antibody, a possible outcome of C-terminal degradation of the target protein. The eluted fractions were concentrated using a 100 kDa MWCO centricon (Millipore) to a final volume of 50 µl and applied to a qualitative SEC column (S200 5/150 GEHealthcare) for analysis (Figure 1.2.4.20).

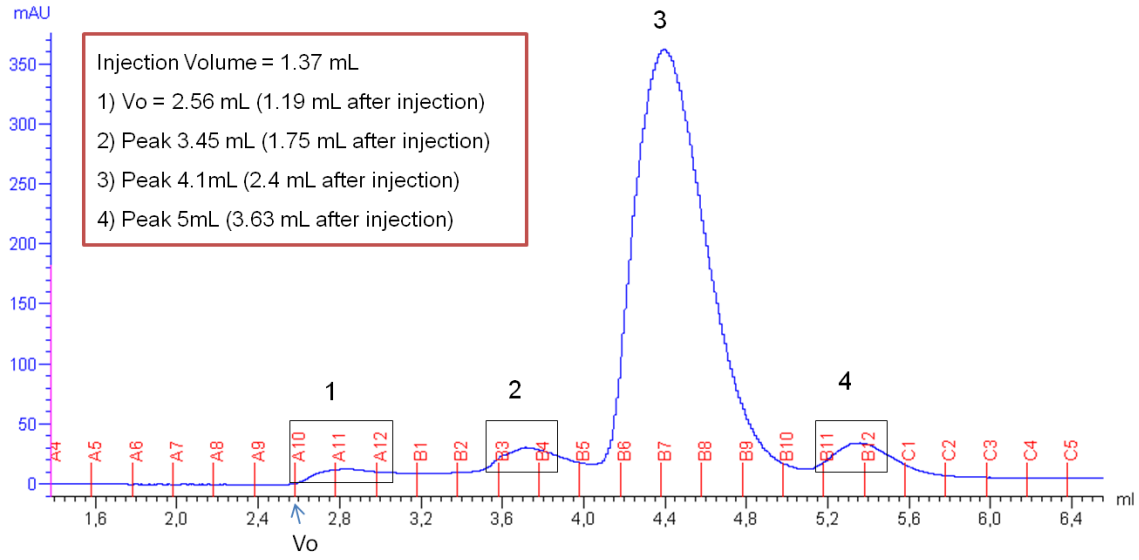

Figure 1.2.4.20. Analytical SEC of eluted fractions from affinity column Ni-NTA.

Analysis of peak fractions from SEC chromatogram (Figure 1.2.4.20) together with elution volumes of each fraction suggests that most protein was in the soluble fraction with only a minor peak seen at the void volume (peak 1). However, the major peak (3) eluted at a volume of 2.4 mL after injection, corresponding to a molecular weight around 50 kDa, indicates that most protein was degraded/fragmented. Peak 2 represents the higher molecular weight molecules present in sample (≈ 160 kDa), although it is expected a dimerization of our protein, these peak might correspond to the monomeric form of strep-GFP-*h*TAOK2, as it does corresponds to the total expected molecular weight of our constructed protein.

Some additional purification experiments in both strep-GFP-*h*TAOK2 and his-GFP-*h*TAOK2 overexpressed proteins were conducted. However, the binding efficiency of the affinity columns was quite lower than expected. This might have been due to the presence of detergent micelles, which may compromise the accessibility of the tag towards the column matrix. Another hypothesis is that the low expression yield of the protein - when the tagged protein is not in abundance compared to other polypeptides in the sample - may decrease the binding efficiency considerably.

Therefore, after extensively tests with different detergents, matrix columns and overexpression systems, the aim of purifying the *h*TAOK2 protein was not achieved.

1.2.5. Conclusion

Membrane proteins represent a challenging field of research. Their study, not only requests additional efforts in the laboratory as it consumes extra time when compared with soluble ones. Such efforts may not always pay-off the made investment. However, new techniques and knowledge of such systems are being developed in this area, so new strategies are being applied resulting in an increase number of known 3D structures of IMPs. Those strategies comprise new techniques in protein expression, the applied techniques in tagging and fusion proteins, the diversity of available detergents, novel methodologies for MPs crystallization (as meso- and sponge-phases) and new beamlines aimed for small and weak-diffraction crystals at synchrotron sources, crystallographic-related software developments and the increased power of computer calculations. All together with novel advances in high-throughput devices in many laboratories worldwide offer the scientists a multiple approach in structure determination of MPs.

The *h*TAOK2 protein is a complex eukaryotic membrane protein of 135 kDa. Its high complexity led us to find a high-throughput platform for cloning and expression a multiple set of constructs. The successful application to the P^3 OPPF expression platform was very exciting, having the possibility of expressing 47 different constructs of the selected target. However, the results were not satisfactory, since the successfully expressed constructs were only mildly expressed at inclusion bodies and lacking the TMs domain. These results indicate that *h*TAOK2 is a too complex protein for *Escherichia coli* overexpression, and that the use of other systems were essential to pursue our work. Because OPPF was using a derived pTriEx vector, the pOPIN, it was possible to select a set of clones for overexpression trials using mammalian and insect cells. The experimental trials done using the OPPF constructs, especially those with GFP at the C-terminal, showed that the localization of the expressed protein was not within the membrane. Moreover, the protein, even when expressed, was highly degraded upon processing, which might be addressed to the presence of the GFP at the protein C-terminus.

*h*TAOK2 was then cloned fused to GFP and with a polyhistine- or Strep-tag, at different protein terminus, into pOPIN-F (the same vector designed to enable high-level target gene expression in multiple systems). A GFP-based expression screening and optimization was carried out using different *E. coli* strains, mammalian and insect cells, in order to determine the host best suited for TAOK2 production. The GFP fluorescence allowed monitorization of the detergent screening and the choice of the best suited for protein extraction from membranes and solubilization. This method has proved to be a more reliable and faster technique for quantification of target protein. The GFP fluorescence would also be very helpful at the downstream processing of the target protein, *h*TAOK2, as it is widely used to assess the monodispersity and stability of the protein sample in different conditions by FSEC. GFP fluorescence was found to be a fast measure of expression and localization. Accordingly, by monitoring GFP expression, it is shown that the

TAOK2 fusion protein only localizes correctly throughout the cell membrane when expressed in mammalian cells and only when GFP is present at the N-terminus.

The practical steps that constitute this GFP-based pipeline approach to evaluate the expression and speed up the screening of detergents for membrane extraction up to protein purification are shown along the work presented. Thus, GFP-tag can facilitate the process to obtain stable and homogeneous samples of membrane proteins for functional and structural work.

1.2.6. References

Alberts, B. (2009). Essential cell biology (New York: Garland Science).

Arnau, J., Lauritzen, C., Petersen, G.E., and Pedersen, J. (2006). Current strategies for the use of affinity tags and tag removal for the purification of recombinant proteins. Protein Expr. Purif. *48*, 1–13.

Bass, R.B., Strop, P., Barclay, M., and Rees, D.C. (2002). Crystal structure of Escherichia coli MscS, a voltage-modulated and mechanosensitive channel. Science *298*, 1582–1587.

Bill, R.M., Henderson, P.J.F., Iwata, S., Kunji, E.R.S., Michel, H., Neutze, R., Newstead, S., Poolman, B., Tate, C.G., and Vogel, H. (2011). Overcoming barriers to membrane protein structure determination. Nat. Biotechnol. *29*, 335–340.

Binda, C., Newton-Vinson, P., Hubálek, F., Edmondson, D.E., and Mattevi, A. (2002). Structure of human monoamine oxidase B, a drug target for the treatment of neurological disorders. Nat. Struct. Biol. *9*, 22–26.

Bird, L.E. (2011). High throughput construction and small scale expression screening of multi-tag vectors in Escherichia coli. Methods *55*, 29–37.

Bolla, J.R., Su, C.-C., and Yu, E.W. (2012). Biomolecular membrane protein crystallization. Philos. Mag. Abingdon Engl. *92*, 2648–2661.

Bowie, J.U. (2001). Stabilizing membrane proteins. Curr. Opin. Struct. Biol. *11*, 397–402.

Boyd, D., Schierle, C., and Beckwith, J. (1998). How many membrane proteins are there? Protein Sci. Publ. Protein Soc. *7*, 201–205.

Bracey, M.H., Hanson, M.A., Masuda, K.R., Stevens, R.C., and Cravatt, B.F. (2002). Structural adaptations in a membrane enzyme that terminates endocannabinoid signaling. Science *298*, 1793–1796.

Buchanan, S.K. (1999). β-Barrel proteins from bacterial outer membranes: structure, function and refolding. Curr. Opin. Struct. Biol. *9*, 455–461.

Caffrey, M. (2003). Membrane protein crystallization. J. Struct. Biol. *142*, 108–132.

Caffrey, M. (2011). Crystallizing membrane proteins for structure-function studies using lipidic mesophases. Biochem. Soc. Trans. *39*, 725–732.

Caffrey, M., and Cherezov, V. (2009). Crystallizing membrane proteins using lipidic mesophases. Nat. Protoc. *4*, 706–731.

Chen, Z., and Cobb, M.H. (2001). Regulation of stress-responsive mitogen-activated protein (MAP) kinase pathways by TAO2. J. Biol. Chem. *276*, 16070–16075.

Chen, Z., Hutchison, M., and Cobb, M.H. (1999). Isolation of the protein kinase TAO2 and identification of its mitogen-activated protein kinase/extracellular signal-regulated kinase kinase binding domain. J. Biol. Chem. *274*, 28803–28807.

Chen, Z., Raman, M., Chen, L., Lee, S.F., Gilman, A.G., and Cobb, M.H. (2003). TAO (thousand-and-one amino acid) protein kinases mediate signaling from carbachol to p38 mitogen-activated protein kinase and ternary complex factors. J. Biol. Chem. *278*, 22278–22283.

Cohen, S.L., and Chait, B.T. (2001). Mass spectrometry as a tool for protein crystallography. Annu. Rev. Biophys. Biomol. Struct. *30*, 67–85.

Dahm, R. (2008). Discovering DNA: Friedrich Miescher and the early years of nucleic acid research. Hum. Genet. *122*, 565–581.

Deisenhofer, J., Epp, O., Miki, K., Huber, R., and Michel, H. (1985). Structure of the protein subunits in the photosynthetic reaction centre of Rhodopseudomonas viridis at 3|[angst]| resolution. Nature *318*, 618–624.

Diefenderfer, C., Lee, J., Mlyanarski, S., Guo, Y., and Glover, K.J. (2009). Reliable expression and purification of highly insoluble transmembrane domains. Anal. Biochem. *384*, 274–278.

Drew, D., Slotboom, D.-J., Friso, G., Reda, T., Genevaux, P., Rapp, M., Meindl-Beinker, N.M., Lambert, W., Lerch, M., Daley, D.O., et al. (2005). A scalable, GFP-based pipeline for membrane protein overexpression screening and purification. Protein Sci. Publ. Protein Soc. *14*, 2011–2017.

Drew, D., Lerch, M., Kunji, E., Slotboom, D.-J., and de Gier, J.-W. (2006). Optimization of membrane protein overexpression and purification using GFP fusions. Nat. Methods *3*, 303–313.

Drew, D., Newstead, S., Sonoda, Y., Kim, H., von Heijne, G., and Iwata, S. (2008). GFP-based optimization scheme for the overexpression and purification of eukaryotic membrane proteins in Saccharomyces cerevisiae. Nat. Protoc. *3*, 784–798.

Drew, D.E., von Heijne, G., Nordlund, P., and de Gier, J.-W.L. (2001). Green fluorescent protein as an indicator to monitor membrane protein overexpression in Escherichia coli. FEBS Lett. *507*, 220–224.

Fazekas de St Groth, S., Webster, R.G., and Datyner, A. (1963). Two new staining procedures for quantitative estimation of proteins on electrophoretic strips. Biochim. Biophys. Acta *71*, 377–391.

Ferguson, A.D., McKeever, B.M., Xu, S., Wisniewski, D., Miller, D.K., Yamin, T.-T., Spencer, R.H., Chu, L., Ujjainwalla, F., Cunningham, B.R., et al. (2007). Crystal structure of inhibitor-bound human 5-lipoxygenase-activating protein. Science *317*, 510–512.

Fernandes, F., Vidigal, J., Dias, M.M., Prather, K.L.J., Coroadinha, A.S., Teixeira, A.P., and Alves, P.M. (2012). Flipase-mediated cassette exchange in Sf9 insect cells for stable gene expression. Biotechnol. Bioeng. *109*, 2836–2844.

Griffiths, A.J., Miller, J.H., Suzuki, D.T., Lewontin, R.C., and Gelbart, W.M. (2000). Making recombinant DNA (W. H. Freeman and Company.).

Hirokawa, T., Boon-Chieng, S., and Mitaku, S. (1998). SOSUI: classification and secondary structure prediction system for membrane proteins. Bioinformatics *14*, 378–379.

Hopkins, A.L., and Groom, C.R. (2002). The druggable genome. Nat. Rev. Drug Discov. *1*, 727–730.

Horton, R.M., Hunt, H.D., Ho, S.N., Pullen, J.K., and Pease, L.R. (1989). Engineering hybrid genes without the use of restriction enzymes: gene splicing by overlap extension. Gene *77*, 61–68.

Iwata, S., and Chayen NE. Crystallization of Membrane Proteins in Oils. (2003). Methods and Results in Crystallization of Membrane Proteins (Internat'l University Line).

Junge, F., Schneider, B., Reckel, S., Schwarz, D., Dötsch, V., and Bernhard, F. (2008). Large-scale production of functional membrane proteins. Cell. Mol. Life Sci. CMLS *65*, 1729–1755.

Kawate, T., and Gouaux, E. (2006). Fluorescence-Detection Size-Exclusion Chromatography for Precrystallization Screening of Integral Membrane Proteins. Structure *14*, 673–681.

Kiedzierska, A., Czepczynska, H., Smietana, K., and Otlewski, J. (2008). Expression, purification and crystallization of cysteine-rich human protein muskelin in Escherichia coli. Protein Expr. Purif. *60*, 82–88.

Lehninger, A.L., Nelson, D.L., and Cox, M.M. (2000). Lehninger principles of biochemistry. (New York: Worth Publishers).

Leng, J., and Salmon, J.-B. (2009). Microfluidic crystallization. Lab. Chip *9*, 24–34.

Loll, P.J., Tretiakova, A., and Soderblom, E. (2003). Compatibility of detergents with the microbatch-under-oil crystallization method. Acta Crystallogr. D Biol. Crystallogr. *59*, 1114–1116.

Long, S.B., Campbell, E.B., and Mackinnon, R. (2005). Crystal structure of a mammalian voltage-dependent Shaker family K+ channel. Science *309*, 897–903.

Mancia, F., and Hendrickson, W.A. (2007). Expression of recombinant G-protein coupled receptors for structural biology. Mol. Biosyst. *3*, 723–734.

Martinez Molina, D., Wetterholm, A., Kohl, A., McCarthy, A.A., Niegowski, D., Ohlson, E., Hammarberg, T., Eshaghi, S., Haeggström, J.Z., and Nordlund, P. (2007). Structural basis for synthesis of inflammatory mediators by human leukotriene C4 synthase. Nature *448*, 613–616.

Miroux, B., and Walker, J.E. (1996). Over-production of proteins in Escherichia coli: mutant hosts that allow synthesis of some membrane proteins and globular proteins at high levels. J. Mol. Biol. *260*, 289–298.

Mitsopoulos, C., Zihni, C., Garg, R., Ridley, A.J., and Morris, J.D.H. (2003). The prostate-derived sterile 20-like kinase (PSK) regulates microtubule organization and stability. J. Biol. Chem. *278*, 18085–18091.

Moore, T.M., Garg, R., Johnson, C., Coptcoat, M.J., Ridley, A.J., and Morris, J.D. (2000). PSK, a novel STE20-like kinase derived from prostatic carcinoma that activates the c-Jun N-terminal kinase mitogen-activated protein kinase pathway and regulates actin cytoskeletal organization. J. Biol. Chem. *275*, 4311–4322.

Newstead, S., Ferrandon, S., and Iwata, S. (2008). Rationalizing alpha-helical membrane protein crystallization. Protein Sci. Publ. Protein Soc. *17*, 466–472.

Ng, J.D., Gavira, J.A., and García-Ruíz, J.M. (2003). Protein crystallization by capillary counterdiffusion for applied crystallographic structure determination. J. Struct. Biol. *142*, 218–231.

Ng, J.D., Stevens, R.C., and Kuhn, P. (2008). Protein crystallization in restricted geometry: advancing old ideas for modern times in structural proteomics. Methods Mol. Biol. Clifton NJ *426*, 363–376.

Opekarová, M., and Tanner, W. (2003). Specific lipid requirements of membrane proteins--a putative bottleneck in heterologous expression. Biochim. Biophys. Acta *1610*, 11–22.

Privé, G.G. (2007). Detergents for the stabilization and crystallization of membrane proteins. Methods San Diego Calif *41*, 388–397.

Rasmussen, S.G.F., Choi, H.-J., Rosenbaum, D.M., Kobilka, T.S., Thian, F.S., Edwards, P.C., Burghammer, M., Ratnala, V.R.P., Sanishvili, R., Fischetti, R.F., et al. (2007). Crystal structure of the human beta2 adrenergic G-protein-coupled receptor. Nature *450*, 383–387.

Robert C. Hockney (1994). Recent developments in heterologous protein production in Escherichia coli. Trends Biotechnol. *12*, 456–463.

Schultz, J., Milpetz, F., Bork, P., and Ponting, C.P. (1998). SMART, a simple modular architecture research tool: identification of signaling domains. Proc. Natl. Acad. Sci. U. S. A. *95*, 5857–5864.

Severs, V.-N., and Whiting, J. (2002). Oswald Avery and the story of DNA (Bear, Del.: Mitchell Lane).

Singer, S.J., and Nicolson, G.L. (1972). The Fluid Mosaic Model of the Structure of Cell Membranes. Science *175*, 720–731.

Stevens, T.J., and Arkin, I.T. (2000). Do more complex organisms have a greater proportion of membrane proteins in their genomes? Proteins Struct. Funct. Bioinforma. *39*, 417–420.

Sutton, B.J., and Sohi, M.K. (1994). Crystallization of membrane proteins for X-ray analysis. Methods Mol. Biol. Clifton NJ *27*, 1–18.

Wallin, E., and von Heijne, G. (1998). Genome-wide analysis of integral membrane proteins from eubacterial, archaean, and eukaryotic organisms. Protein Sci. Publ. Protein Soc. *7*, 1029–1038.

WATSON, J.D., and CRICK, F.H. (1953). Molecular structure of nucleic acids; a structure for deoxyribose nucleic acid. Nature *171*, 737–738.

Zhou, T., Raman, M., Gao, Y., Earnest, S., Chen, Z., Machius, M., Cobb, M.H., and Goldsmith, E.J. (2004). Crystal structure of the TAO2 kinase domain: activation and specificity of a Ste20p MAP3K. Struct. Lond. Engl. 1993 *12*, 1891–1900.

Zihni, C., Mitsopoulos, C., Tavares, I.A., Baum, B., Ridley, A.J., and Morris, J.D.H. (2007). Prostate-derived sterile 20-like kinase 1-alpha induces apoptosis. JNK- and caspase-dependent nuclear localization is a requirement for membrane blebbing. J. Biol. Chem. *282*, 6484–6493.

Chapter 2

Structural Studies on Z-RNA and Z-DNA Junctions

The work on Z-DNA presented in this chapter was published in:

Matteo de Rosa, Daniele de Sanctis, **Ana Lucia Rosario**, Margarida Archer, Alexander Rich, Alekos Athanasiadis, and Maria Armenia Carrondo, 2010**. Crystal structure of a junction between two Z-DNA helices.** *Proc. Natl. Acad. Sci*. 107, 9088–9092.

Author contributions: M.d.R., A.R., A.A., and M.A.C. designed research; M.d.R., D.d.S., A.L.R., and A.A. performed research; D.d.S. and M.A.C. contributed new reagents/analytic tools; M.d.R., D.d.S., M.A., A.R., A.A., and M.A.C. analyzed data; and M.d.R., M.A., A.R., A.A., and M.A.C. wrote the paper.

2.1. Abstract 118
2.2. Introduction 119
Nucleic Acids 119
DNA – *Deoxyribonucleic Acid* 119
The discovery of Z-DNA, the left-handed conformation of nucleic acids 121
RNA - ribonucleic acid 123
Proteins that bind Z-DNA/Z-RNA 127
ADAR1 127
ADAR1 Zalpha Domain 129
Other proteins that bind Z-DNA/Z-RNA 133
The biological role of Z-DNA 134
2.3. Materials and Methods 136
Protein Production 136
Oligonucleotides Preparation 137
Crystallization of $Z\alpha_{ADAR1}$ complexed with Z-Z RNA oligonucleotide 137
Crystallization of $Z\alpha_{ADAR1}$ complexed with A-Z RNA oligonucleotide 137
Crystallization, Data Collection, and Processing of $Z\alpha_{ADAR1}$:Z-Z-DNA 138
Structure Determination of $Z\alpha_{ADAR1}$:Z-Z-DNA 138
Circular Dichroism (CD) Spectroscopy 139
2.4. Results and Discussion 140
Protein Production 140
Crystallization of a Z-Z-RNA and a A-Z-RNA junction bound to $Z\alpha_{ADAR1}$ Domain 140
RNA conformational changes studied by CD spectroscopy 142
Toward the structure determination of A-Z-RNA and Z-Z-RNA bound to $Z\alpha_{ADAR1}$ 145
Structure Determination of a Z-Z DNA Junction Bound by the $Z\alpha_{ADAR1}$ Domain. 149
Overall Structure and Stoichiometry of the $Z\alpha_{ADAR1}/(CG)_3A(CG)_3$ Complex. 150
A Close View of the Z-Z DNA Junction. 154
Comparing the Z-Z junction with a B-Z junction 156
2.5. Conclusion 159
2.6. References: 160

2.1. Abstract

X-ray crystallography is a powerful technique to determine the three-dimensional structure of biomacromolecules and hence very relevant for structural biology studies.

With the discovery of Z-DNA, in 1979, questions about its biological role held the scientific public on to the subject until this moment, mostly due to the fact that a human protein, double-stranded RNA adenosine deaminase – ADAR1 – binds selectively to the Z-form of DNA and RNA at the moment of transcription, within its Zα domain.

Here, it is described the experimental work done with the $Z\alpha_{ADAR1}$ with specific oligonucleotides of RNA and DNA, with a nucleotide sequence with the properties to form the Z double helical structure, consisting of alternating cytidines and guanosines. For reasons not entirely understood, such dinucleotide repeats in genomic sequences have been associated with genomic instability leading to cancer.

Adoption of the left-handed conformation results in the formation of conformational junctions. In DNA a B-to-Z junction is formed at the boundaries of the helix, whereas a Z-to-Z junction is commonly formed in sequences where the dinucleotide repeat is interrupted by single base insertions or deletions that bring neighboring helices out of phase. B-Z junctions are shown to result in exposed nucleotides vulnerable to chemical or enzymatic modification. In RNA, no such junctions were described so far.

Two oligonucleotides sequences of Z-RNA were used and led to a collection of data sets at high resolution to determine the complex structure. However, and because RNA does not so easily shifts to the Z form, the complex was never crystallized, and we could only have a high-resolution structure of RNA double helix.

Here it is also described the three-dimensional structure of a Z-Z junction stabilized by $Z\alpha_{ADAR1}$. We show that the junction structure consists of a single base pair and leads to partial or full disruption of the helical stacking. The junction region allows intercalating agents to insert themselves into the left-handed helix, which is otherwise resistant to intercalation. However, unlike a B-Z junction, in this structure the bases are not fully extruded, and the stacking between the two left-handed helices is not continuous.

2.2. Introduction

Nucleic Acids

DNA – *Deoxyribonucleic Acid*

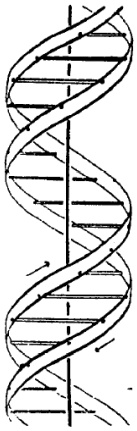

Figure 2.2.1: Diagram of DNA structure as proposed by Watson and Crick in 1953.

The ribbon symbolizes the sugar-phosphate chain, and the horizontal rods the pairs of bases holding two chains together. The vertical line marks the fiber axis. The arrows indicate that each chain runs at opposite directions (from Watson and Crick, 1953).

DNA, the deoxyribonucleic acid, is an important macromolecule found in all living cells and contains all the information necessary to their survival and expansion. It is formed by four different types of nucleotides, the building blocks, constituted by a sugar (2'-deoxyribose), one or more phosphate groups and one base of four possible heterocyclic bases (Griffiths et al., 2000b). The constituting bases are purines (adenine and guanine) or pyrimidines (thymine and cytosine) (Figure 2.2.1). Purines pair with pyrimidines, adenine with thymine and guanine with cytosine, respectively (Figure 2.2.2). This based model was held together in 1953 only with X-ray data from DNA fibers from Rosalind Franklin and Maurice Wilkins (Tobin, 2003). The real "proof" for the Watson-Crick model of DNA came in 1981 after the B-form of DNA was crystallized and the X-ray pattern was solved (Drew et al., 1981).

The DNA can be found in the A-, B- or Z-DNA form (Figure 2.2.3). The B-DNA is the right handed, anti-parallel form, and also, the most predominant conformation of DNA found in nature. It is considered the physiological form of DNA double helix and it was first described by

Watson and Crick in 1953. At the time, Watson and Crick have “put forward a radically different structure for the salt of deoxyribose nucleic acid”, not entirely accepted by the community.

The A-DNA form arises from a conformational change from the B-DNA, induced by a decrease in the relative humidity to 75% or below. A-DNA is a wider and flatter helix, closely resembling the A-RNA double helix (Shing and Carter, 2011).

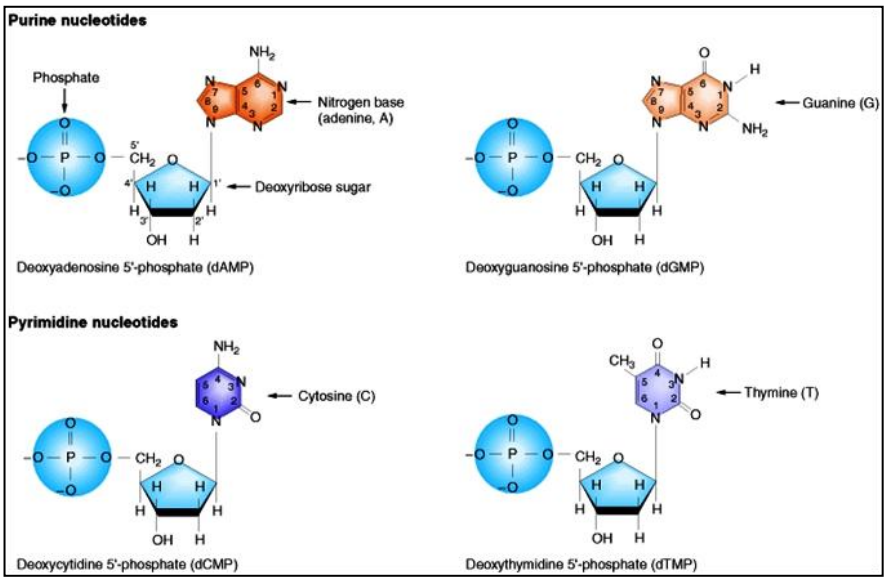

of

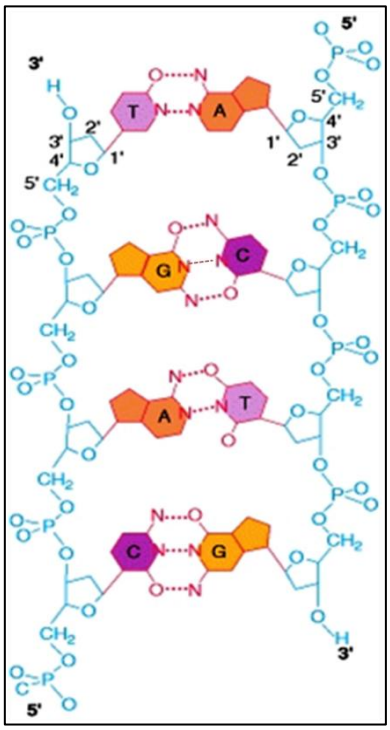

Figure 2.2.2. The chemical structure of DNA.

The four nucleotides are the fundamental building blocks of DNA. The sugar is called deoxyribose because it is a variation a common sugar, the ribose, but with an extra oxygen atom (upper panel). The DNA double helix, unrolled to show the sugar-phosphate backbones (blue) and base-pair rings (red) (left panel). The backbones run in opposite directions; the 5′ and 3′ ends are named for the orientation of the 5′ and 3′ carbon atoms of the sugar rings. Each base pair has one purine base, adenine (A) or guanine (G), and one pyrimidine base, thymine (T) or cytosine (C), connected by hydrogen bonds (dotted lines) (Griffiths et al., 2000b).

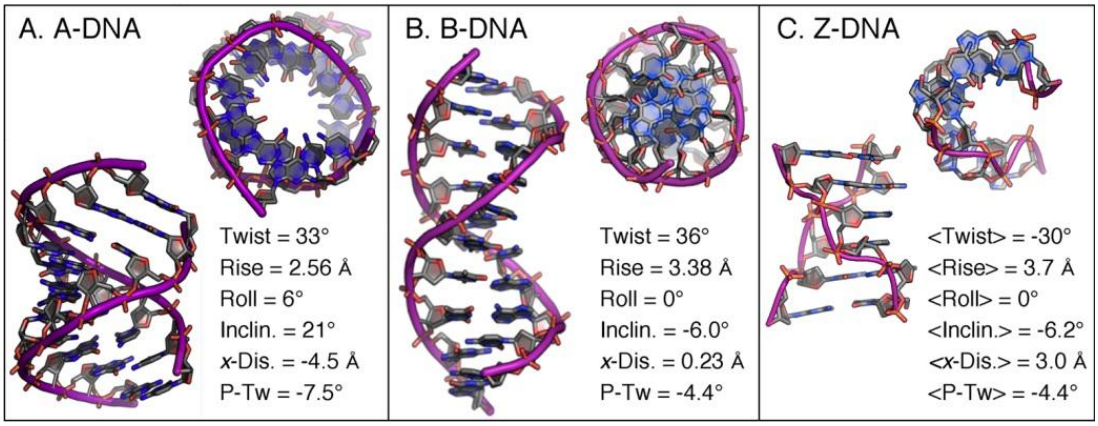

Figure 2.2.3. Representative double-helical structures of DNA.

Structures of A-DNA (Hays et al., 2005), B-DNA (Privé et al., 1991), and Z-DNA (Wang et al., 1979). Abbreviations: Incl. = inclination, *x*-Disp. = *x*-displacment, P-Tw = propeller twist. For Z-DNA, the helical parameters are given as averages of the alternating dinucleotide steps (from Shing and Carter, 2011).

The DNA, now so familiar to us, was an exciting discovery for the all scientific community at the time. Its implications and the way science evolved are at this point visible, so it's not so striking having DNA as one of the most important discoveries of all time. With the discovery of DNA structure, it was obvious that the molecule could be replicated, the essential property of a genetic molecule. The base pair sequence suggested an influence in the polypeptide chain of aminoacids forming a protein; this was the first notion of genetic code - one gene, one protein (Griffiths et al., 2000b).

The discovery of Z-DNA, the left-handed conformation of nucleic acids

In 1979, Alexander Rich and colleagues reported the discovery of an intriguing new acid nucleic conformation, the left-handed DNA, or as it is also known Z-DNA confirming the spectroscopic studies of Pohl and Jovin (Pohl and Jovin, 1972; Wang et al., 1979). At the time, that was also the first DNA molecule to be analyzed by X-ray crystallography. Z-DNA was so named because of its zigzag phosphodiester backbone, consisting of two anti-parallel chains, with bases that still form the Watson-Crick base pairs (Figure 2.2.4). It is usually found in DNA molecules with alternate GC sequences and is favored by specific conditions, such as high salt (Hall et al., 1984; Pohl and Jovin, 1972), low concentration of certain metal complexes (Behe and Felsenfeld, 1981; Woisard et al., 1985), and superhelical torsional stress (Peck et al., 1982). This DNA form is stabilized by the negative supercoiling generated upon transcription, indicating a transient, although, localized conformational change. This conformational transition between two different double helical forms is accompanied by changes of optical rotatory dispersion, circular dichroism and ultraviolet absorption, which are methodologies widely used for their characterization (Pohl and Jovin, 1972).

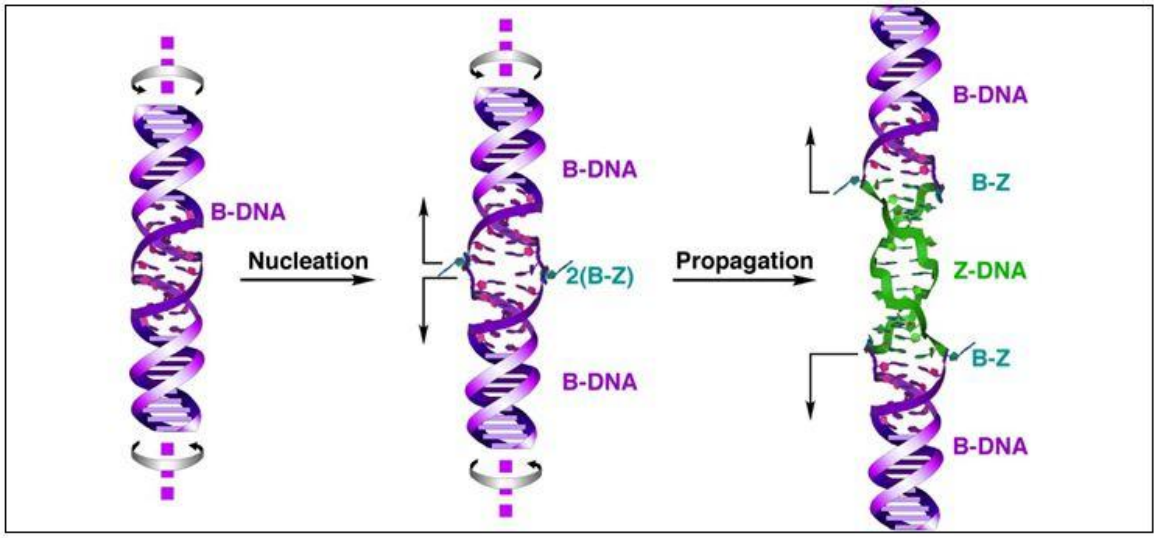

Figure 2.2.4. B to Z-DNA transition.

When unwound by negative supercoiling, DNA will first extrude two flipped out base pairs (serving as two B-Z junctions). Further unwinding results in the formation of left-handed Z-DNA between the two junctions as they migrate in opposite directions (from Shing and Carter, 2011).

Two different conformations were observed for the phosphates in the GpC sequences of DNA when adopting a Z conformation, as the phosphates are found either facing the helical groove or rotated away from it. The latter conformation is often found when hydrated magnesium ions are complexed to a phosphate oxygen atom (Wang et al., 1981).

Biologists were intrigued by Z-DNA because it seemed unnecessary. However, the discovery that certain classes of proteins bound to Z-DNA with high affinity and great specificity indicated a biological role. The new discovery led to a worldwide race to study the Z-DNA form, and once again Rich and his co-workers showed that Z-DNA is not only biologically relevant but also important (Rich and Zhang, 2003a).

RNA - ribonucleic acid

In living cells, DNA holds the genetic code, some regions are transcribed to RNA that, in its turn, will be translated to proteins. DNA is significantly long, mostly present in the nucleus, and much longer than RNA, which carries one gene at a time, and is also found in the cytoplasm (Alberts et al., 2002b).

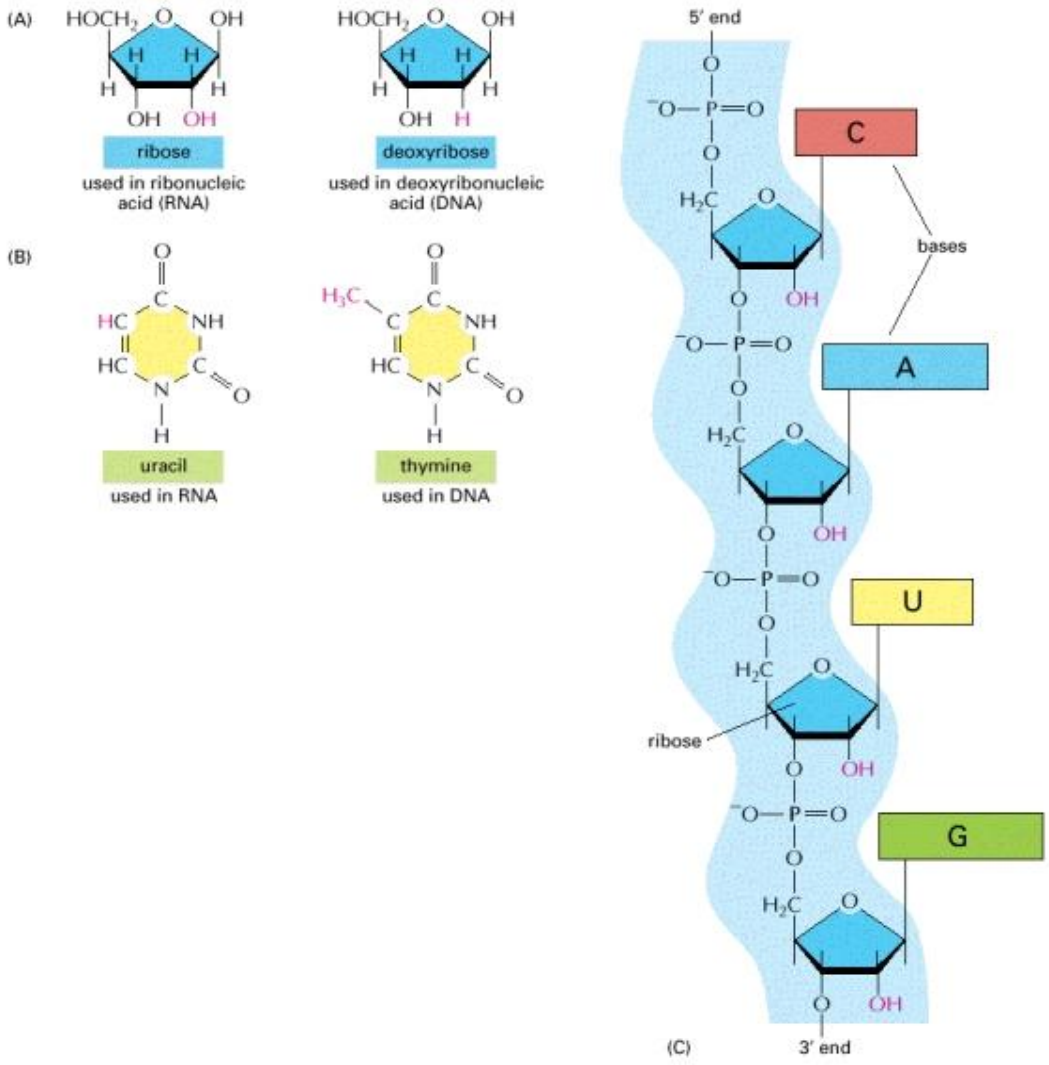

Figure 2.2.5. The chemical structure of RNA.

The (A) RNA contains the sugar ribose, which differs from deoxyribose, the sugar used in DNA, by the presence of an additional -OH group. (B) RNA contains the base uracil, which differs from thymine, the equivalent base in DNA, by the absence of a -CH3 group. (C) A short length of RNA. The phosphodiester chemical linkage between nucleotides in RNA is the same as that in DNA (Alberts et al., 2002b).

Despite its similarity to DNA, the RNA molecule comprises two chemical differences. RNA has a ribonucleic acid instead of a deoxyribonucleic acid, because of an extra hydroxyl group on the 2'

carbon sugar; also, it contains a uracil base (without methyl group) instead of the thymine base (Figure 2.2.5).

Because RNA contains a ribose instead of a deoxyribose, in the *Nature* report by Watson and Crick from 1953, the authors claim that "*It is probably impossible to build this structure with a ribose sugar in place of a deoxyribose, as an extra oxygen atom would make too close a van der Waals contact*", suggesting that it was unlikely for RNA to have the proposed double helical structure (Watson and Crick, 1953).

In fact, the ribose turns RNA more bulky than DNA, making it harder to form a stable double helix. A breakthrough came later in 1956, when it was discovered that double stranded RNA (dsRNA) indeed exists (Rich and Davies, 1956). It was then eventually observed that the double-stranded RNA molecule adopts a conformation similar to the A-form of DNA (Rich, 2003).

Both DNA and RNA form stable double helices, held together by Watson-Crick base pairs. However, the presence of an added oxygen atom in the backbone of RNA turns in a different geometry when compared to DNA. A-RNA and B-DNA are the most stable forms of these double-stranded molecules (Brown and Rich, 2001). With an input of energy, both these conformations can be transformed into left-handed double stranded conformations, the Z-DNA and Z-RNA.

As in DNA, the Z conformation of RNA is stabilized *in vitro* by very high concentrations of salt, higher temperatures and other agents that monitor repulsion between electronegative phosphate residues, which are closer together in the Z conformation (Hall et al., 1984; Trulson et al., 1987). The transition from the A-RNA right-handed duplex to the Z-form is less favorable then the B to Z-DNA transition. In fact, the energy for changing the sugar pucker of a ribonucleotide to the Z-form is considerably bigger that the energy required for a deoxyribonucleotide (Brown and Rich, 2001).

The A to Z conformational transition in RNA may be of relevance to the biological situations in which double-stranded RNA occurs, such as in ribosomes and in some viruses (Hall et al., 1984).

The first structure of Z-RNA was determined at very high salt concentration (6M $NaClO_4$) for the helix $(GCGCGC)_2$ by Nuclear Magnetic Resonance (NMR) (Figure 2.2.6). However, this Z-RNA helix structure shows several conformational features different from Z-DNA, e.g. a unique stracking, alternating, low positive and high negative helical twist angle values, a small helical rise and base pairs locations close to helix axis. Both helix grooves of Z-RNA are well defined. Cytidine 2 –OH groups, deeply buried in the narrow minor groove play a crucial role on the Z-RNA structure and A to Z helicity reversal (Popenda et al., 2004).

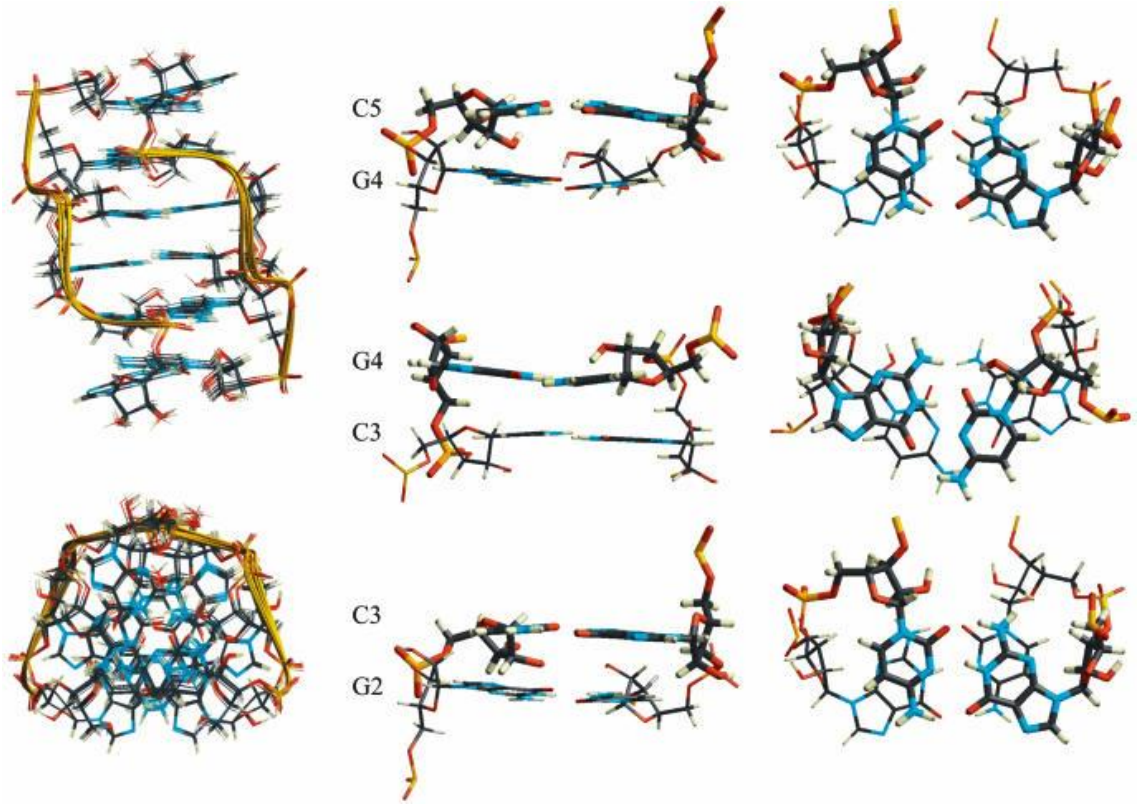

Figure 2.2.6. First structure of Z-RNA by NMR.

First column: superposition of 12 conformers representing the refined structure of $(CGCGCG)_2$ in the Z-RNA form as viewed from the minor groove and along the helix *z*-axis. Second and third column: stacking pattern within the CpG and GpC steps in Z-RNA as viewed from the minor groove and along the helix *z*-axis. For both steps only intra- but no inter-strand stacking is observed (from Popenda et al., 2004).

Most of the gross conformational features of Z-DNA are also present at the Z-RNA molecule in solution, including *syn* guanosines, *anti* cytidines, a zigzagged phosphodiester backbone, and alternating cytidine 2'-*endo* and guanosine 3'-*endo* sugar puckers, making them almost indistinguishable, contrary to the right-handed conformations (B-DNA and A-RNA) (Weiner et al., 1984). The only major difference would be the 2'-hydroxyl group in the Z-RNA, which is not exposed in the double-helice (Figure 2.2.7) (Popenda et al., 2004).

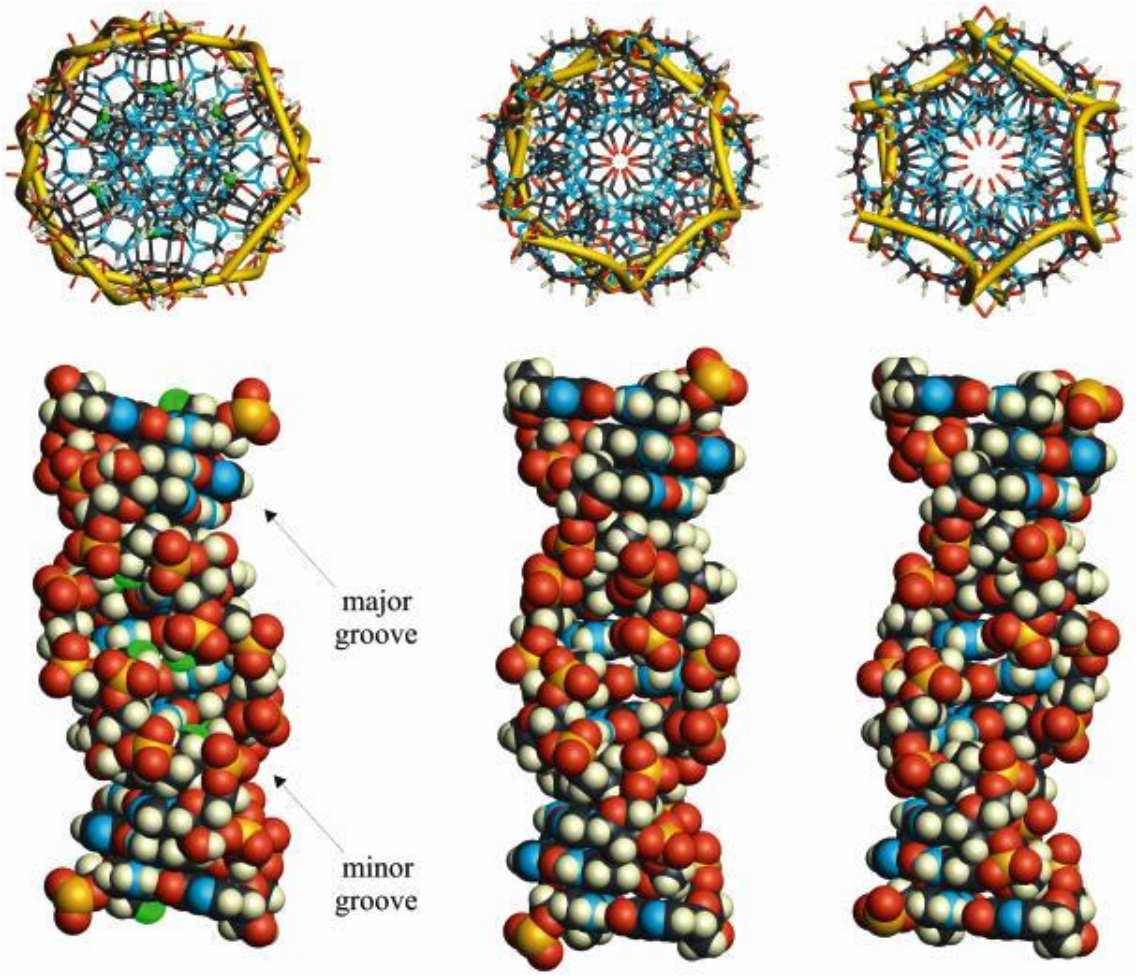

Figure 2.2.7. Full-turn model of the Z-RNA helix (12.4 bp per turn) (left) compared to the 12 bp per turn models of Z_I- (middle) and Z_{II}-DNA (right).

Models are presented in two different conventions, by the top (upper models) and laterally (bottom models) in order to show their base pair location and groove architecture. Atoms color code – carbon: black, hydrogen: white, nitrogen: blue, phosphorus: yellow, oxygen: red; cytidine 2′ oxygens: green (from Popenda et al., 2004). Models for the Z_I- (middle) and Z_{II}-DNA (right) were described by Wang et al., 1981.

As it was found for DNA, Z-RNA can also adopt two distinct conformations based on Raman spectroscopic studies, with differences both in the base stacking and in the backbone geometry. The Z form of poly[r(CG)] named Z_R-RNA forms in high salt concentrations of NaBr or $NaClO_4$ and exhibits a unique and distinct CD spectrum from the Z_D-RNA, which is found in concentrated $MgCl_2$, and has a CD signature similar to poly[d(GC)] (Trulson et al., 1987).

Staining with antibodies against Z-RNA suggests its presence in both the cytoplasm and the nucleus (Zarling et al., 1990).

Proteins that bind Z-DNA/Z-RNA

ADAR1

After its discovery, the nucleic acid Z-form started losing researchers interest, as it seemed not to have any biological function. If this particular form of nucleic acids was to have a biological role, it would be highly likely for it to bind specifically to a class of proteins. At the time, the problem was to find a method that would enable the isolation of proteins that would bound selectively to Z-DNA and simultaneously, exclude those that would bind to B form of DNA (Rich and Zhang, 2003a). The supposed method was only described in 1993 (Herbert and Rich, 1993) and consisted on the utilization of a radioactive labeled oligodeoxynucleotide stabilized in the Z conformation together with an excess of thousands fold of B-DNA and single-stranded DNA in a bandshift experiment. Also, because the Z-DNA used would contain bromine atoms, DNA-complexes would be easily identifiable by UV light crosslink. The technique allowed for the detection of proteins that would bind tightly to Z-DNA. One of the first proteins found was double-stranded RNA adenosine deaminase type I (ADAR1) (Herbert et al., 1995).

ADAR1 is an ubiquitous and highly conserved enzyme in metazoan (Figure 2.2.8), acts on double-stranded regions formed in precursor messenger RNA (pre-mRNA), selectively deaminating adenosine producing inosine (A to I) (Kim et al., 1994). The mammalian genome encodes for three ADARs. ADAR1 and ADAR2 are catalytically active (Savva et al., 2012). ADAR3 is not editing competent, only present in the postmitotic neurons, where it may play a role on the regulation of substrate-specific RNA editing in the brain (Chen et al., 2000).

RNA editing is essential for mammalian development. Mapping the A-to-I sites in humans showed that their primary targets are noncoding regions of the RNA, Alu repeats, and suggested a role of editing in controlling dsRNA stability (Carmi et al., 2011; Levanon et al., 2004). Inosine is later interpreted as guanine during translation, so ADARs will alter the amino acid sequence encoded in the gene. ADARs recognize short, imperfect RNA duplexes and their function is to deaminate selected adenosines (specific RNA editing). However, ADARs may act promiscuously by editing multiple adenosines (non-selected), this process is also known as 'hyper-editing', and usually occurs in long, perfectly paired RNA duplexes (Savva et al., 2012).

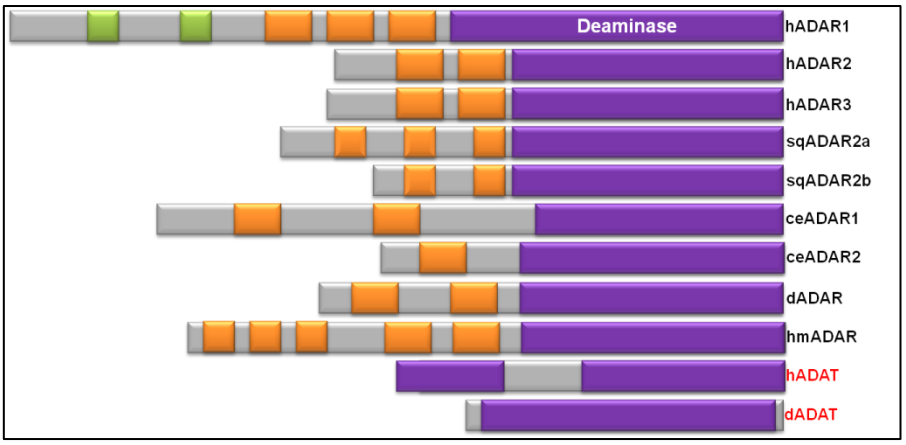

Figure 2.2.8. The ADAR family protein.

Metazoan ADARs share a common domain architecture, consisting of a variable number of amino-terminal dsRNA binding domains (dsRBDs, in orange) and a carboxyl-terminal catalytic deaminase (purple). Human ADAR1 have unique Z-DNA binding domains (green). The squid *Loligo pealeii* contains an ADAR2-like gene (sq*ADAR2*) that through alternative splicing produces 2 variants (a and b). *C. elegans* contains two genes (ce*ADAR1* and *2*), while the genome of *D. melanogaster* encodes only one (dADAR) homologous to hADAR2. Although the dsRBMs found in the *Hydra magnapapillata* genome are highly divergent, five such motifs are recognizable in hm*ADAR*, the only identified gene in this species. Human and *Drosophila* ADAT architectures are included (red), as these enzymes are believed to be ancestral to present-day ADARs (adapted from Savva et al., 2012).

ADAR1 gene has two transcription start sites and two promoters, giving rise to two variants: an interferon induced form ADAR1p150 (longer form, 150 kDa) and a constitutively induced form ADAR1p110 (shorter form, 110 kDa), differing in the length of their N-terminal sequence, as ADAR1p110 is amino-terminally truncated lacking the first 296 residues. Both contain dsRNA-binding domains and the demaniase domain, however, Z binding domains is restricted to ADAR1p150 (Patterson and Samuel, 1995). They also differ in their cellular distributions: ADAR1p110 is exclusive to the nucleus, while ADAR1p150 shuttles between nucleus and cytoplasm, suggesting a targeting for mature mRNAs present outside the nucleus (Desterro et al., 2003; Poulsen et al., 2001; Sansam et al., 2003).

ADAR1 Zalpha Domain

In ADAR1 editing, the substrate if formed by folding an intron back onto the exon that is targeted for modification (Figure 2.2.9.). Because it uses introns, editing must take place before splicing. It is thought that ADAR1 recognition of Z-DNA is essential for editing of nascent transcripts to begin immediately after transcription, ensuring that editing and splicing are performed in the correct sequence (Herbert and Rich, 1999a).

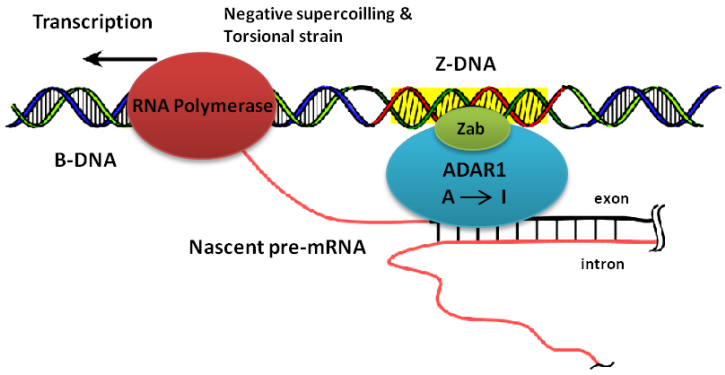

Figure 2.2.9. Model for regulation of ADAR1 activity by Z-DNA.

ADAR1 has been shown to bind Z-DNA and dsRNA with nanomolar affinity (Brown and Rich, 2001). Each nucleic acid is bound to a specific domain. Transcription gives rise to regions of dsRNA, when a nascent RNA transcript (pre-mRNA) folds back to itself. *In vivo*, Z-DNA can be stabilized by the negative supercoiling generated by an RNA polymerase moving through a gene. It is proposed that binding to Z-DNA allosterically activates editing by ADAR1, initiating modification of a transcript as it forms and before splicing has occurred. This enzyme causes the hydrolytic deamination of adenine within the dsRNA to form inosine, which is subsequently translated as guanine. Editing thus changes the read-out of a gene. Several editing sites may exist in a particular pre-mRNA. ADAR1 thus utilizes the structural information encoded in Z-DNA and dsRNA to alter the linear flow of information from DNA to RNA (adapted from Herbert and Rich, 1999b).

Several experiments were carried out to illustrate the interaction of the $Z\alpha_{ADAR1}$ domain with DNA in solution. The first prove of evidence for the existence of the left-handed Z-DNA conformation in a complex of poly(dGdC) with Zα was done by spectroscopic studies, which showed that the typical circular-dichroism spectrum of B-DNA was changed when Zα was added to the solution (Berger et al., 1998).

Typically, Zα domains are 66 amino acids long (Pfam 02295), with a fold constituted by 3 α-helices (α1 - α3) and 3 β-strands (β1 - β3) arranged with the following topology: α1β1α2α3β2β3 (Schwartz et al., 1999).

Further *in vitro* experiments showed that Zα was capable of stabilizing and maintaining the Z-form of long DNA molecules, independently of other factors, upon binding. The DNA in study was a segment of CG repeat flanked by other segments, which were without properties that would favor the alteration to the Z form. In such cases, Zα binds to the central region in the Z conformation, while the remaining DNA is in the B-form, forming two B-Z junctions. Not only has the binding energy enough to hold the small segment as Z-DNA, as it also stabilized the formed

junctions. Two models are proposed, (1) Zα binds to B-DNA and promotes the B to Z transition or (2) Zα captures transient Z-DNA segments formed in small amounts, due to Brownian motion, even in conditions that strongly favor B-DNA, thereby shifting the B-Z equilibrium (Kim et al., 2000).

The resolution by X-ray crystallography of the 3D structure of the Z-binding domain of ADAR1, Zα, with Z-DNA, made it possible to identify the aminoacid residues involved in the recognition of the Z-form (Figure 2.2.10). Intriguingly, the helix-turn-helix-β-sheet motif (α+βHTH), frequently used to recognize B-DNA in a variety of proteins, was the one bound to five successive sugar phosphate groups, including the *syn*-conformation of guanine, of the Z-DNA backbone (Schwartz et al., 1999). Those results suggest that ZαADAR1 domain, specifically helix 3 (α3) and the loop connecting β2 and β3 strands, recognizes the Z-form and not the nucleic acid sequence.

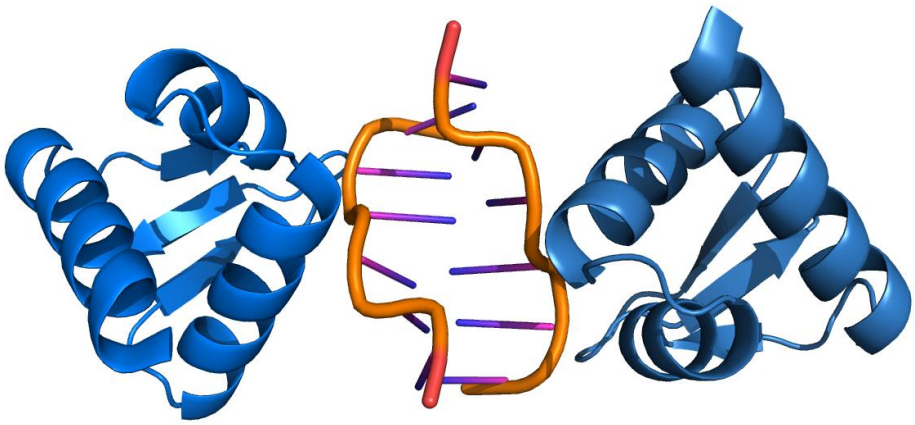

Figure 2.2.10. Crystal structure of $Z\alpha_{ADAR1}$:Z-DNA complex (PDB ID 1QBJ).

The structure evidenciates the need for a Zα dimer for the binding to the 6-bp DNA duplex (colored orange to purple). Protein chains are colored blue (from Schwartz et al., 1999).

The first high-resolution structure of Zα alone and in complex with Z-DNA led to the proposition that most likely, B-DNA binding is disfavored by steric hindrance, but Z-DNA binding to Zα is favored because seven out of the nine contacting residues are prepositioned to bind the distinct backbone of Z-DNA. These structural modifications of the α+βHTH fold may enable Zα to recognize Z-DNA in the presence of excess B-DNA in the nucleus of a living cell (Schade et al., 1999).

A crystal structure of a B-Z-DNA (Figure 2.2.11) junction formed upon binding of a 15-base-pair segment of DNA to Zα was determined, revealing a continuity in the base stacking between the B and the Z segments, and a break of one base pair at the junction, resulting into an extrusion of the adjacent base pair at each side (Ha et al., 2005). Every time a section of DNA forms a left-handed Z-DNA segment, two B–Z junctions are formed. Every time a dsDNA segment turns

into Z-DNA, such a junction is formed, which may facilitate the use of Z-DNA more widely in nature (Du and Zhou, 2013).

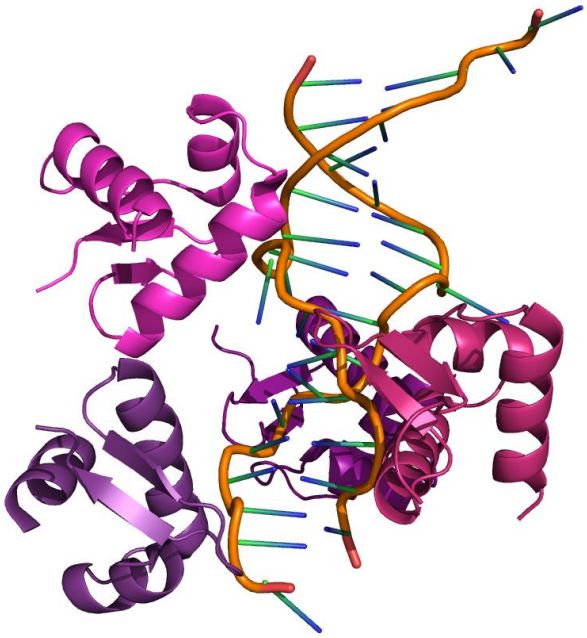

Figure 2.2.11. Crystal structure showing a B-Z-DNA junction (PDB ID: 2ACJ).

Proteins are colored in pink tones; RNA oligomer is colored orange (backbone) to blue (base pairs).

The significance of the observed junction is that it requires little structural disruption, preserves helix integrity and, through maximizing base pairing, it minimizes the energetic cost of the junction. This makes it possible to use the Z-DNA conformation more widely and may be related to the widespread occurrence of sequences favoring Z-DNA formation. B–Z junctions are easily formed in biological systems owing to the widespread occurrence of negative supercoiling. These can be further stabilized by Z-DNA binding proteins. The knowledge that these are associated with extrusion of bases at the junction is likely to open many new avenues of research as a lot more remains to be known.

It was later shown that $Z\alpha_{ADAR1}$ also binds Z-RNA and stabilizes the Z-conformation, as it was expected since left-handed conformations of the distinct nucleic acids are very similar (Brown et al., 2000).

The fist high-resolution structure displaying dsRNA in the left handed conformation bound to $Z\alpha_{ADAR1}$ (Figure 2.2.12) was later published by the group of Alexander Rich (Placido et al., 2007). It was for the first time demonstrated that Z-RNA structure would adopt such conformation at almost physiological environment (Figure 2.2.13), closely taking on the helical parameters observed for Z-DNA (Wang et al., 1979), adopting a different conformation from that described by NMR spectroscopy when induced by high ionic strength (Popenda et al., 2004).

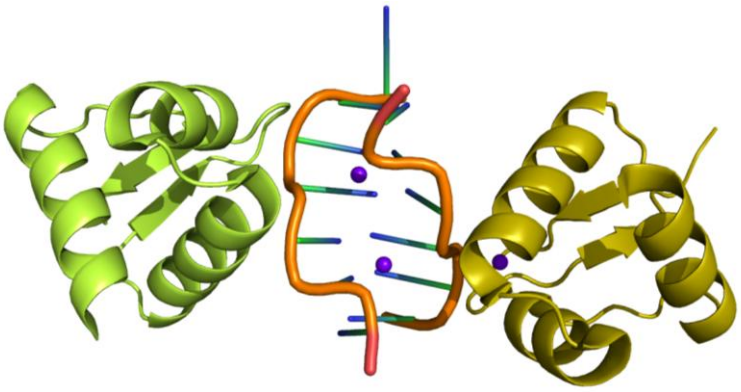

Figure 2.2.12. Crystal structure showing a $Z\alpha_{ADAR1}$:Z-RNA complex (PDB ID 2GXB).

Proteins are colored green and lemon, RNA oligomer is colored orange (backbone) to blue (base pairs), sodium atoms are colored purple.

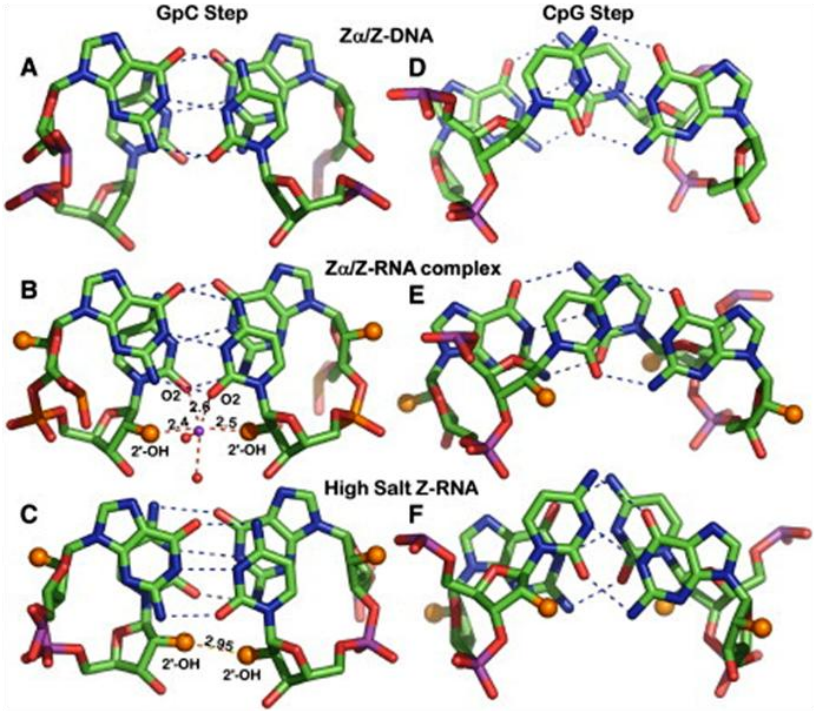

Figure 2.2.13. Base Stacking and Backbone Hydration of two Z-RNA Conformations one Z-DNA.

(A and D) Z-DNA (Schwartz et al., 1999), (B and E) Z-RNA cocrystal (Placido et al., 2007), and (C and F) NMR structure of Z-RNA in 6 M $NaClO_4$ (Popenda et al., 2004). Dashes show Watson-Crick hydrogen bonding (blue) and 2′-OH hydrogen bonds (red/orange). The 2′-OH groups are displayed as larger orange spheres. Distances are given in Angstroms. Note the overall similarity and the (D and E) interstrand base stacking of CpG steps in the Zα/Z-DNA and Zα/Z-RNA complexes, as opposed to (F) intrastrand stacking in high-salt RNA (from Placido et al., 2007).

Other proteins that bind Z-DNA/Z-RNA

The crystallographic structure of the $Z\alpha_{ADAR1}$:Z-DNA complex allowed the identification of the amino acids responsible for the nucleic acid binding (Schwartz et al., 1999). A computer based search for proteins with sequence motifs, similar to that of $Z\alpha_{ADAR1}$, identified interferon response related proteins such as DLM1 (Fu et al., 1999; Schwartz et al., 2001), E3L (Brandt and Jacobs, 2001; Liu et al., 2001) and PKZ (Rothenburg et al., 2005) has containing Zα domains (Figure 2.2.14).

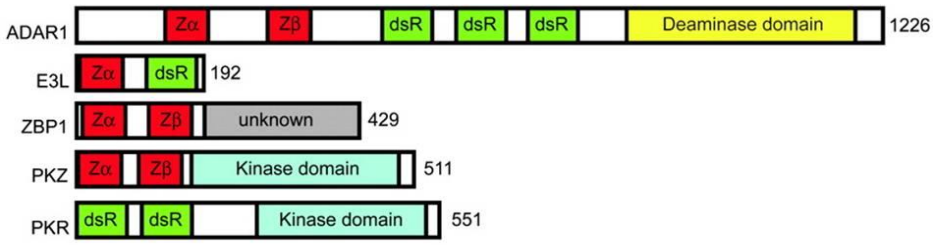

Figure 2.2.14. Proteins containing a Zα domain.

Domain organization is shown schematically. Numbers to the right indicate the number of residues in human ADAR1, vaccinia virus E3L, human ZBP-1 (also known as DLM1), zebrafish PKZ, and human PKR. Domains containing a Zα motif (Zα and Zβ) are shown in red. dsRNA binding domains are in green. The deaminase domain of ADAR1 (yellow) and the kinase domains of PKR and PKZ (light blue) are labeled. The function of the C-terminal region of ZBP-1 (gray) is unknown (from Rothenburg et al., 2005).

The high resolution (1.85 Ă) crystal structure of the Z-DNA binding domain in DLM1 – $Z\alpha_{DLM1}$ – in complex with $d(GC)_3$ showed that the recognition of the Z-DNA was similar to ADAR1, and that important residues – Asn, Tyr and Trp - responsible for fold maintenance, were conserved between the two otherwise unrelated proteins, whereas additional DNA interacting residues are conservatively replaced (Schwartz et al., 2001). This strongly indicates that the Zα family shares Z-DNA binding as a common function.

E3L was another protein identified as a potential Z-DNA binding protein, containing a characteristic sequence at the N-terminal domain ($Z\alpha_{E3L}$) and a dsRNA-binding motif at the C-terminal domain (Figure 2.2.14). The E3L gene is found in poxvirus, including the vaccinia virus, where E3L provides interferon (IFN) resistance and the capability for the virus to be cultured in a broad host range, due to its ability to inhibit the antiviral dsRNA-dependent protein kinase, PKR (Brandt and Jacobs, 2001). A virus that has mutated or missing E3L maintains the capability to reproduce in cell cultures, but is no longer pathogenic to a mouse, where a virus without any alteration would kill a mouse within a week post infection (Brandt and Jacobs, 2001), providing evidence that E3L is essential for viral pathogenesis. This is the first example

in which a Z-DNA binding protein is found to be involved in pathogenesis. If other viruses own a similar mechanism, Zα domains will be potential targets for anti-viral drugs (Rich and Zhang, 2003b). Cocrystallization of the Yatapoxvirus Zalpha ($Zα_{yabE3L}$) bound to Z-DNA show similarity with the previous structures, supporting a conformation specific manner for the interaction between Zα and DNA (Ha et al., 2004).

PKZ is the closest relative of PKR found in several fish species, it differs from PKR in having Zα domains replacing the normally found two dsRBD while maintaining an intact kinase domain. PKR is using its dsRNA binding domains for the detection of viral dsRNA which lead to its activation and subsequent shutdown of cellular translation (Rothenburg et al., 2005). Since dsRNA can also adopt the Z conformation, it is reasonable to assume a similar role for $Zα_{PKZ}$ although for a more specialized feature of viral RNAs, as part of the host antiviral response.

The biological role of Z-DNA

Since its discovery, biologists were puzzled by Z-DNA. It seemed unnecessary, but in fact some proteins contain specific domains that bind Z-DNA and Z-RNA with high affinity, the Zα domain.

RNA editing changes the sequence of mRNAs, which results in synthesis of proteins not encoded in the genes (Smith et al., 1997). It had been known for some time that certain RNA viruses, e.g. Measles virus, the causative agent of encephalitis that replicate in the cytoplasm, undergo considerable changes in sequence – adenines are replaced by guanines, uracyls by cytosines -, which were probably the consequence of hyper-editing by ADAR1 (double-stranded RNA adenosine deaminase) (Maas et al., 2003). The full length form of this enzyme, the form that contains the Z-DNA/Z-RNA binding domain, is upregulated by the interferon response of the cell, which is triggered by the measles virus. Furthermore, ADAR1 accumulates in the cytoplasm, where the measles virus replicates. So, it is possible that the Zα domain from ADAR1 binds to the negatively torsionally strained double-stranded RNA, which might form during viral replication, showing that the Z-DNA/Z-RNA binding domain might have a role in the attempts of cells to inactivate the invading virus.

Also, findings indicate a link between the structure of Z-DNA and vaccinia viral pathogenesis (Kim et al., 2003). One of the most striking biological effects of a Z-DNA binding protein is seen in the vaccinia poxvirus interferon resistance protein (E3L). This virus is lethal for mice, but if Z-DNA binding ability is diminished, pathogenicity decreases, and if the binding is lost, the virus is no longer lethal for the mouse (Brandt and Jacobs, 2001; Liu et al., 2001).These results raise the possibility that some diseases as smallpox could be treated by blocking Z-DNA binding in variola, which has a nearly identical domain to vaccinia viruses. The findings in the area indicate

a clear link between Z-DNA/Z-RNA, viral pathogenesis and cell protection against invading virus.

Because Z-DNA was detected only in negatively supercoiled plasmid, but not in a relaxed plasmid, it is suggested that this non-B DNA conformation could exist *in vivo* under physiological conditions as general chromosomal DNA is mostly negatively supercoiled (Nordheim and Rich, 1983). Also, methylation of DNA promotes the formation of the Z form of DNA, due to the slight modification of its backbone, it requires less energy to switch conformation (Behe and Felsenfeld, 1981). So, Z-DNA is thought to play a role in the regulation of gene expression; Z-DNA is also thought to be involved in DNA processing events and/or genetic instability. Z-DNA-forming sequences have the potential to enhance the frequencies of recombination, deletion, and translocation events in cellular systems (Wang et al., 2006).

Z-DNA is an active element in the genomes of prokaryotes and eukaryotes and its transient state and functional activities make it challenging to target and regulate. Although the biological function(s) is not fully understood, accumulating experimental and clinical evidence support the idea that this conformation is involved in several important biological processes and may provide a target for the prevention and treatment of some human diseases. Research on Z-DNA has expanded the current insight into its role and new progress should pave the way to further investigation on this unusual left-handed DNA double helix (Du and Zhou, 2013).

2.3. Materials and Methods

Protein Production

The Zα domain of human ADAR1 was expressed and purified as previously reported by Placido et al., 2007. Briefly, the bacteria growth medium was Luria-Bertuni (Sigma; 10 g/L tryptone, 5 g/L yeast extract, 10 g/L NaCl), supplemented with 50 µg/ml of kanamycin (Sigma). A glycerol stock of *Escherichia coli* BL21 cells was previously prepared. A previous culture of 100 mL was grown at 37ºC, 250 rpm, overnight and used as pre-inoculum. Next day, 2 L culture, divided within 4 Erlenmeyer's with 500 mL each, with a pre-inoculum of 15 ml each (1/30 of culture volume) were growth at 37ºC, 220 rpm until the optical density at 600 nm (OD_{600}) reached 0.2. At this point, expression was induced by adding 1 mM of Isopropyl β-D-1-thiogalactopyranoside (IPTG) to the culture. Growth was performed until OD_{600} reached 0.8-0.9. The culture was centrifuged at 7000 rpm, at 4ºC for 6 minutes. The pellet was resuspended in 10 mM HEPES pH 7.4 and 20 mM NaCl and centrifuged at 5000 rpm, 4ºC for 5 minutes. The pellet was stored at -20ºC until further use for purification. Bacterial cell pellet was resuspended in 1x BugBuster® Reagent (Novagen) diluted (in a concentration of 5 ml of BugBuster® Reagent per 5 g of cell pellet) in Buffer A (50 mM Tris-HCl pH 8.0; 500 mM NaCl; 5 mM Imidazole; 1 mM β-mercaptoethanol (βME)), for chemical cellular disruption. Per mL of this solution, 0.1 µl of Benzonase®Nuclease (Sigma-Aldrich) was added. The resuspension was left at room temperature for 1 hour and then centrifuged at 11000 rpm at 4ºC per 30 minutes. The supernatant was applied onto a nickel-nitrilotriacetic acid (Ni-NTA) agarose column (GE Healthcare) on the FPLC system (Amersham). After loading of sample, the column was washed with 20 times the colum volume (CV) of Buffer A. Sample elution was performed by passing 20 CV of Buffer B (50 mM Tris-HCl pH 8.0; 500 mM NaCl; 300 mM Imidazole; 1 mM βME). Protein sample was collected and immediately stored on ice and concentrated by centrifugation. Buffer was exchanged to 10 mM HEPES pH 7.4 and 20 mM NaCl using a desalting column on the FPLC system. Thrombin was added to the sample, for His-Tag cleavage overnight. On the day after, the sample was applied to a Mono-S HP 5/5 column (Amersham Biosciences) in the FPLC system for purification of the cleaved protein. 5 CV of buffer were passed through the column before elution. A gradient from 0% to 50% of the buffer constituted by 10 mM HEPES pH 7.4 and 1 M NaCl was used for protein elution. After elution, the buffer was exchanged to the final storage conditions of 10 mM HEPES pH 7.4 and 20 mM NaCl. Protein purity was accessed by loading the samples on a 10% Bis-acrylamide gel and running an SDS-PAGE. The protein was concentrated by using Centricon filtration devices (Millipore) to a final concentration of 10 mg/mL in 10 mM Hepes, pH 7.0, 20 mM NaCl. The Hepes-free protein sample was prepared by dialysis against a 10 mM Tris-HCl, pH 7.0, and 20 mM NaCl solution.

Oligonucleotides Preparation

DNA oligonucleotides: Z-Z DNA: $AC(CG)_3A(CG)_3$ and $GT(CG)_3T(CG)_3$.

RNA oligonucleotides: Z-Z RNA: $GU(CG)_3UA(CG)_3$ and $AC(CG)_3UA(CG)_3$; A-Z RNA: $GU(CG)_3CCAUAAACC$ and $ACGGUUUAUGG(CG)_3$.

The oligonucleotides were purchased from IDT (Coralville) and resuspended in 10 mM Hepes, pH 7.0, 20 mM NaCl or in 10 mM Tris-HCl, pH 7.0, 20 mM NaCl. The Hepes-free protein sample was prepared by dialysis against a 10 mM Tris-HCl, pH 7.0, and 20 mM NaCl solution. The duplex (Z-Z DNA; Z-Z RNA; A-Z RNA) oligonucleotides were prepared by heating a stoichiometric mixture of the two oligonucleotides to 80°C (10 minutes) and leaving the sample to slowly cool down (1ºC per minute) to 20ºC. In order to verify the success of annealing, and to assess the size and purity of the oligonucleotides mixture, a 3% agarose gel electrophoresis was done (Amersham).

Crystallization of $Z\alpha_{ADAR1}$ complexed with Z-Z RNA oligonucleotide

Initial crystallization screenings (Classical I and II, Qiagen) were done with the nanoliter crystallization robot (Cartesian mini-bee) using a mixture of protein:oligo with a ratio of 4, at 96 well plates using the sitting-drop vapour diffusion technique. Initial hits were found in drops containing ammonium sulphate as precipitant. Further optimization experiments were performed around the initial conditions, by varying the concentration of precipitant, testing various additives (e.g. polyethylene glycols - PEGs -, sugars, and alcohols), trying different drop size and protein:oligo ratios and by doing streak- and macro- seeding. The best crystallization condition consisted of 1.8 M Ammonium Sulphate and 100 mM Sodium Acetate pH 4.6 in a 1 + 1 µl drop size, with 1000 µl of reservoir solution and using the sitting-drop vapor diffusion technique at 20ºC. For X-ray diffraction data set collection, different cryopreservants were tested in-house. Best cryoprotectant was glycerol, which is supplemented to the crystallization solution to a final concentration of 10 to 15%. Two data sets were collected at ESRF, the European Synchrotron Radiation Facility in Grenoble, at 1.2 and 2 Å resolution, using 15% glycerol as a cryoprotectant.

Crystallization of $Z\alpha_{ADAR1}$ complexed with A-Z RNA oligonucleotide

A similar strategy was adopted to crystallize $Z\alpha_{ADAR1}$ in complex with A-Z RNA oligonucleotide. Classical screenings I and II (Qiagen) were done with the nanoliter crystallization robot using a ratio of protein: oligo of 4. From these initial screenings, further optimization was performed to a final optimal solution of 2.2 M Ammonium Sulphate and 100 mM Tris.HCl pH8.5. In addition, different cryoprotectants were tested, the best ones being glycerol (at 20% or 25% final

concentration) and ethylene glycol (20%) supplemented to the crystallization solution. Two X-ray diffraction data sets were collected at ESRF, the European Synchrotron Radiation Facility in Grenoble, at 1.4 and 2 Å resolution, both using 20% ethylene glycol as cryoprotectant.

Crystallization, Data Collection, and Processing of $Z\alpha_{ADAR1}$:Z-Z-DNA

The $Z\alpha_{ADAR1}$/Z-Z DNA complex was obtained by mixing 0.8 mM Zα with 0.2 mM DNA duplex. The mixture was incubated at room temperature for 1 h before crystallization trials. Best diffracting crystals were obtained, in two different conditions, by the hanging drop vapor diffusion method at 20 °C, using 1 µL of the mixture with 1 µL of the reservoir solution containing 16% PEG 2000 monomethyl ether), 0.1 M Hepes, pH 7.0, 0.2 M ammonium acetate or 17% PEG 2000, 0.1 M Tris-HCl, pH 7.0, 0.2 M ammonium acetate. Platelet-like crystals were grown in both conditions. Then 20% PEG 400 was added as cryoprotectant, and the crystals were flash-cooled in liquid nitrogen. X-ray diffraction data were measured at 100 K at the European Synchrotron Radiation Facility (Grenoble) on beam lines ID23EH2 or ID14EH4 and at Diamond Light Source. Two datasets were collected from single crystals, grown with either in Hepes or Tris as a buffer, to 2.65 and 2.8 Å resolution, respectively. Diffraction data was integrated and scaled using MOSFLM/SCALA (CCP4, 1994; Leslie, 2006) with final R_{merge} of 9.2 (Hepes) and 8.3 (Hepes-free). The crystals belong to the orthorhombic $P2_12_12_1$ space group with similar unit cell parameters of a = 30.67 *Å*, b =102.21 *Å*, c = 105.89 *Å*, $\alpha = \beta = \gamma = 90^o$ and a = 29.28 *Å*, b = 99.76 *Å*, c = 106.48 *Å*, $\alpha = \beta = \gamma = 90^o$ (for the Hepes and Tris crystals, respectively). See Table 2.4.2 for data collection and processing statistics.

Structure Determination of $Z\alpha_{ADAR1}$:Z-Z-DNA

$Z\alpha_{ADAR1}$/Z-Z DNA structure was solved by molecular replacement using a single Zα domain bound to a single strand $(CG)_3$ oligonucleotide (PDB ID code 1QBJ) as a search model making use of the program PHASER (McCoy et al., 2007). We were able to identify four molecules in the asymmetric unit. The structure was refined with PHENIX (Adams et al., 2002) and model building was carried out using COOT (Emsley and Cowtan, 2004). The structure from Hepes-crystal was refined to a final R_{factor} of 0.23 (R_{free} 0.28) at 2.65 Å resolution, whereas the structure from Tris-crystal was refined to a final R_{factor} of 0.23 (R_{free} 0.27) at 2.8 Å. Non-crystallographic symmetry was used throughout the refinement process relating portions of the four Zα monomers. The general quality of the electron density maps were very good for all protein residues, with exception of the C-terminal amino acid residues V199-Q202 (for all chains) and the solvent exposed side chains of Q141, K145, E152, K170, and K187; and the two DNA overhanging bases, which were not visible in the electron density maps. Both $Z\alpha_{ADAR1}$/Z-Z DNA structures show good geometry/stereochemistry, where 94.4% (for Hepes) and 91.8% (for Tris)

of the amino acid residues belong to the most favored regions of the Ramachandran plot, and all other residues are found within the allowed regions of the plot. Analysis of the Z-DNA helix parameters was performed with 3DNA (Lu and Olson, 2003). The two structures have been deposited at the Protein Data Bank (PDB) database with ID codes 3IRQ (Tris) and 3IRR (Hepes).

Circular Dichroism (CD) Spectroscopy

CD measurements were performed on several samples using a Jasco J-815 CD system in a 0.1-mm cuvette asdescribed:

Z-Z-DNA: A variable quantity (5–10 μM) of the Z-Z-DNA duplex was mixed with different concentrations of $Z\alpha_{ADR1}$ to final molar ratios of 1:0, 1:1, 1:2, 1:4, and 1:6. Kinetics characterization of the B → Z conversion was followed at single wavelength (254 nm) and CD spectra were collected in 1-nm steps from 230 to 330 nm after 10 min of incubation when absorbance changes reach a plateau. Experiments were performed at 25 °C in 10 mM Hepes, pH 7.0, 20 mM NaCl or 10 mM Tris-HCl, pH 7.0, 20 mM NaCl.

Z-Z-RNA and A-Z-RNA: 10 μM of RNA duplex is mixed with $Z\alpha_{ADAR1}$ to a final molar ratio 1:4. Experiments were performed at 45ºC or 37ºC in 10 mM Hepes, pH 7.0, 20 mM NaCl or 10 mM Tris-HCl, pH 7.0, 20 mM NaCl.

2.4. Results and Discussion

Protein Production

The gene coding for $Z\alpha_{ADAR1}$ was successfully expressed and the protein purified by immobilized metal ion *affinity chromatography* (IMAC). The His-tag was removed by thrombin cleavage and further purified with a Mono-S HP 5/5 column. The purity of the protein sample was confirmed by SDS-PAGE (Figure 2.4.1). The estimated yield of production was 16.5 mg/L of culture. After each protein purification batch, the protein was divided in small aliquots and stored at -20ºC for crystallization trials with the different oligonucleotides.

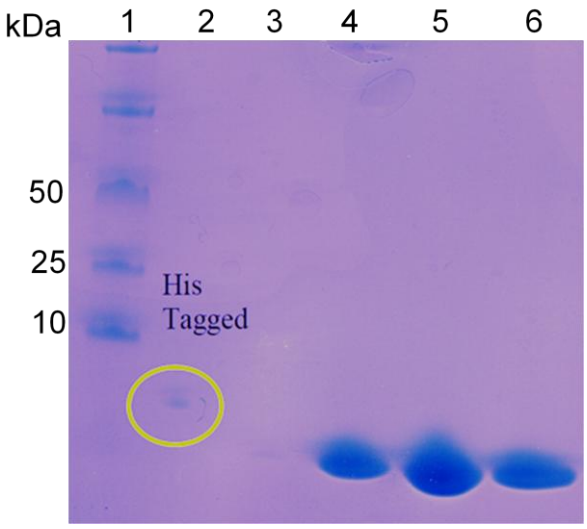

Figure 2.4.1. SDS-PAGE after His-tag cleavage and ion-exchange chromatography.

Layer 1: Protein Markers; 2: Sample after Ni-NTA column (His-Tagged protein); 3: flow-through of Ni-NTA column; 4 to 6: protein sample eluted after Mono-S HP 5/5 column.

Crystallization of a Z-Z-RNA and a A-Z-RNA junction bound to $Z\alpha_{ADAR1}$ Domain

The crystallization of Z-Z-RNA/A-Z-RNA junctions bound to $Z\alpha_{ADAR1}$ domain was successfully. After the first hints found in the crystallization screenings, a 5 week-period of optimization was necessary to obtain suitable diffraction crystals. In the best conditions described, crystals appear in just 2 to 3 days and grow for one week in both cases (Figure 2.4.2). With exception for the Z-Z RNA junction experiments (Figure 2.4.2a-f), where several trials were performed to improve crystal quality. Despite the well defined external shape, all the crystals were very small,

and did not diffract well. Both streak seeding and macroseeding fail to show good results. After 3 weeks of crystallization trials with additives, some nucleation and crystals were visible; those kept growing for more than 2 weeks, having a final size of 150 µm (Figure 2.4.4c).

Regarding the A-Z-RNA trials (Figure 2.4.2g-l), the additives trial did not show successful results. All crystals were transparent, had a rod shape, and most of them were very small (10 µm).

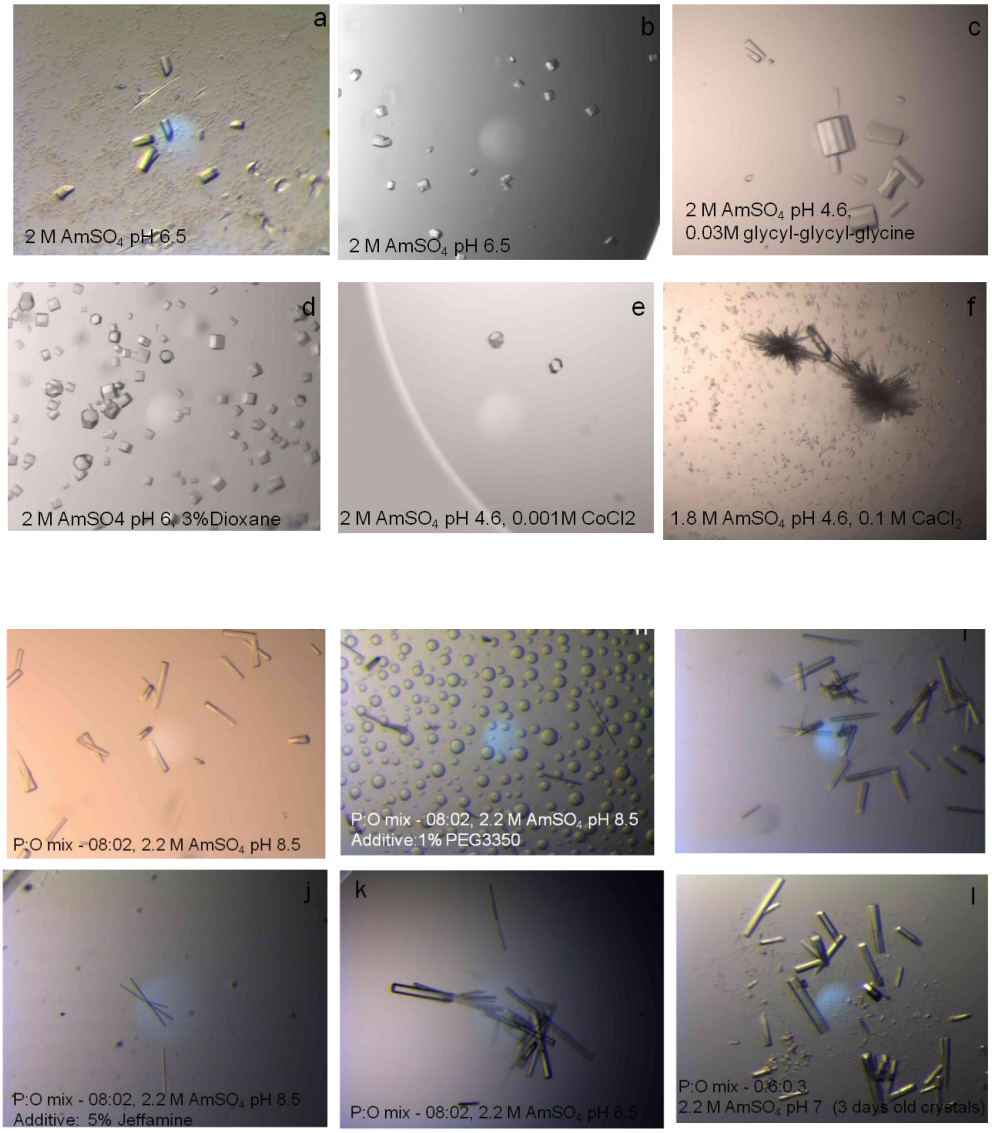

Figure 2.4.2. Crystals for $Z\alpha_{ADAR1}$:Z-Z-RNA (a-f) and for $Z\alpha_{ADAR1}$:A-Z-RNA (g-l).

RNA conformational changes studied by CD spectroscopy

Previous experiments showed that the A form of RNA [r(CG)6] is characterized by a positive band at 263 nm and a broad negative elipticity peak at 292 nm. The spectrum changes upon addition of sodium perchlorate (6.5 M) with the negative band becoming positive at 285 nm, and the band at 263 nm shifting to 258 nm, with reduced intensity (Brown and Rich, 2001).

Each experiment should be started by measuring a spectrum of 10 µM RNA only, protein only, and salt only. This way, the absorbing spectrum of each component is individually evaluated. RNA only is our control, having a CD spectrum characteristic of the A-RNA form, to check for conformational changes upon addition of highly concentrated salts or micromolar (µM) amounts of $Z\alpha_{ADAR1}$. Each solution should have a final volume of 250 µl, and for stability purposes, should be prepared on ice. Upon preparation, we immediately start following the CD spectra of the solution.

First experiments were conducted at 45ºC, since it was known that RNA requires higher energy for the conformational change from A- to Z- RNA. This would allow us to explore lower concentration of salts, and test for the successful ones at lower temperatures, as 37ºC. If in a specific condition, there is no change at 45ºC, it's improbable that any change would happen at a lower temperature.

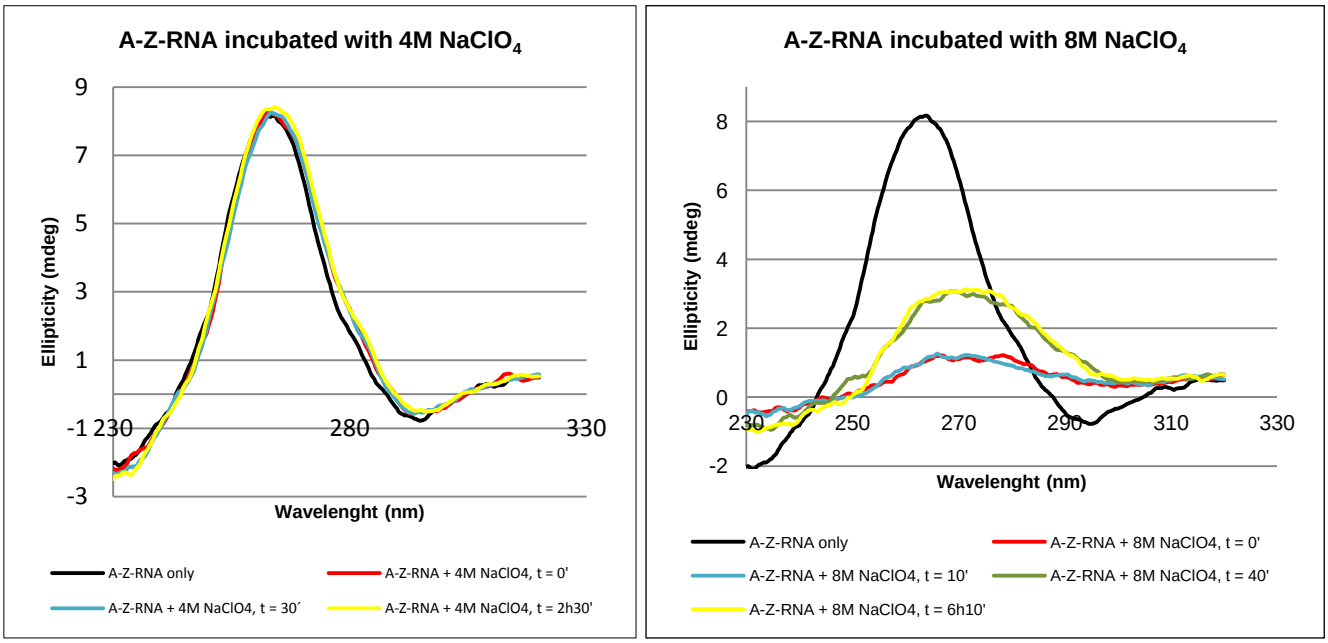

Figure 2.4.3. CD measurements on A-Z-RNA oligonucleotide incubated with different concentrations of $NaClO_4$.

Evaluation of conformational change of A to Z RNA by incubation of the AZ oligonucleotide with (left) 4M $NaClO_4$ and (right) 8M $NaClO_4$.

The first experiments with high salt concentration revealed that conformational changes are only visible with a high excess (8 M) of $NaClO_4$ (Figure 2.4.3), where the negative band at 292 nm becomes positive and shifts to 270 nm (Figure 2.4.3, right). These results agree with the reports that RNA needs high excess salt to change conformation to Z-RNA. It is visible a first change (red and blue line), within the first minutes of incubation, followed by a second alteration (green and yellow line), revealing a increased intensity of the positive 270 nm band, which is then maintained constant over time. We can think of plausible explanations for this change. One hypothesis is that there is a first transition to Z_D-RNA and then to Z_R-RNA (Trulson et al., 1987). Trulson described the Z_R-RNA as a structure prone to be formed in the presence of high concentrations of NaBr and $NaClO_4$, exhibiting a unique CD signature (Trulson et al., 1987). Moreover, Z_D-RNA is found in concentrated $MgCl_2$ solutions and has a similar CD signature as Z-DNA. Here, we see differences in intensity of the positive band, but not in the negative band, so the transition Z_R-RNA → Z_D-RNA is not likely, as both of these RNA forms have different base-stacking geometry. Another hypothesis is that the addition of salt destabilizes the RNA structure. Furthermore, some of the A-RNA is not in the right conformation (A conformation), which results in a weaker signal. In summary, most likely, the difference in intensity is caused by this destabilization effect at the initial incubation period with high salt concentration.

Subsequently, we tested the incubation of A-Z-RNA with 40 µM cobalt hexammine chloride $[Co(NH_3)_6Cl_3]$ at 45º C. Cobalt hexamine chloride has been described as an inducer of Z-DNA (Filimonova et al., 2008). In this experiment, there is no change conformational observed of the RNA, even in the presence of higher concentrations (2 mM) of $Co(NH_3)_6Cl_3$. We also did some studies with $NiCl_2$ (nickel chloride). According to previous studies, this salt can induce the conformational change from B to Z-DNA (Balaz et al., 2006), however there is no evidence or study supporting the same effect on the transition to Z-RNA. The experiment was performed by using 10 mM of $NiCl_2$ at 37ºC, and no changes were observed in the CD spectrum. Changes were only observed when using 30 mM $NiCl_2$ at 45ºC. Also, $MgCl_2$ was tested until a concentration of 3 M, without affecting the conformational stability of A-RNA.

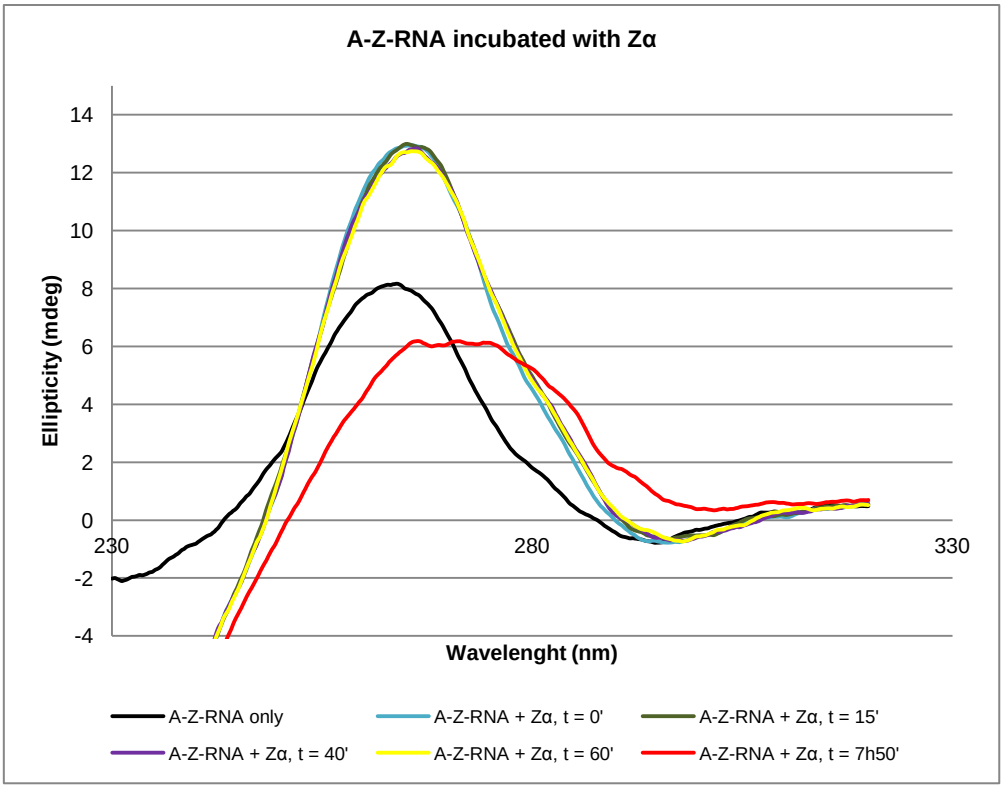

Figure 2.4.4. A-Z-RNA oligonucleotide incubated with $Z\alpha_{ADAR1}$.

Evaluation of conformational change of A to Z RNA by incubation of the AZ oligonucleotide with $Z\alpha_{ADAR1}$ at 45ºC.

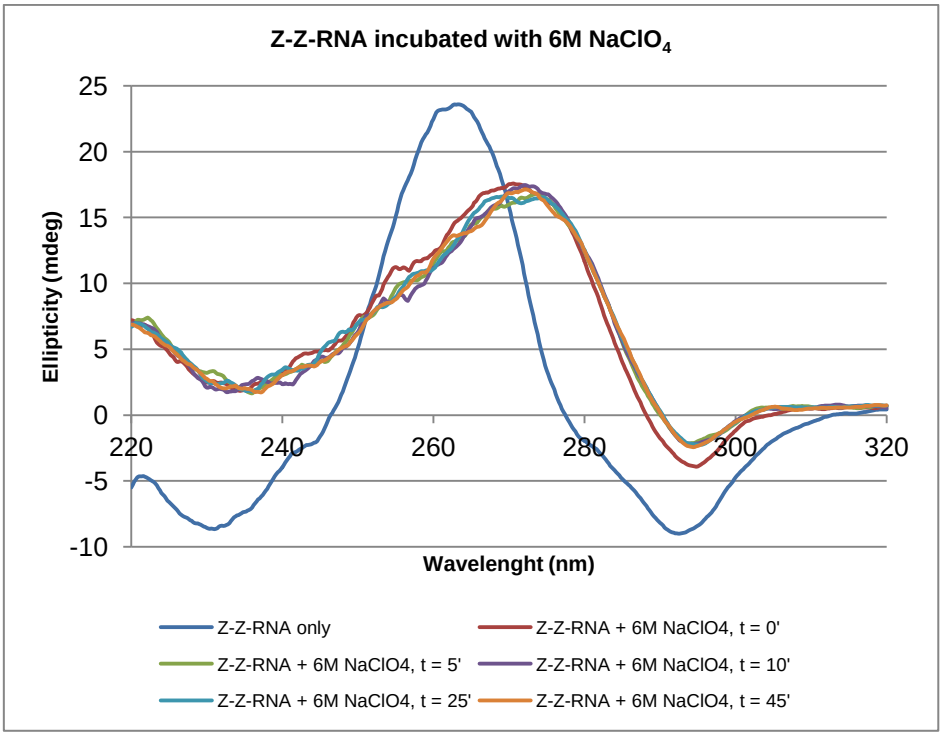

Figure 2.4.5. Z-Z-RNA oligonucleotide incubated with $NaClO_4$.

Evaluation of the conformational change from A to Z-RNA by incubation of the ZZ oligonucleotide with 6M $NaClO_4$.

Incubation of A-Z-RNA oligonucleotide with $Z\alpha_{ADAR1}$ (45ºC) alters the conformation of A-RNA to Z-RNA, as shown in Figure 2.4.4, but only for large incubation times. The CD spectrum (Figure 2.4.5) clearly shows a conformation rearrangement from A to Z-RNA as a result of Z-Z-RNA oligonucleotide incubation with 6 M $NaClO_4$.

Toward the structure determination of A-Z-RNA and Z-Z-RNA bound to $Z\alpha_{ADAR1}$

Several crystals diffracted to high resolution and datasets were collected at synchrotron sources, the data was processed (Table 2.4.1, a).

Table 2.4.1. X-ray diffraction data collection and processing statistics of putative RNA oligonucleotides in complex with $Z\alpha_{ADAR1}$

Parameters/Data sets	**A-Z RNA**	**A-Z RNA**	**Z-Z RNA**
X-ray source	ID14-1 (ESRF)	DLS	ID23-2 (ESRF)
Resolution limits (Å)	37.93 – 1.40 (1.40 – 1.48)[a]	37.56 – 1.55 (1.63 – 1.55)[a]	38.40 – 2.00 (2.11 – 2.00)[a]
Space Group	P3	P3	P3
Cell parameters	a = b = 43.78 Å, c = 28.96 Å α = β = 90º, γ = 120º	a =b = 43.36 Å, c = 28.78 Å α = β = 90º, γ = 120º	a = b = 44.34 Å, c = 29.30 Å α = β = 90º, γ = 120º
R_{merge} (%)	13 (42)[a]	4.7 (13.6)[a]	5.3 (10.5)[a]
B_{factor} ($Å^2$)	7.8	10.5	19.2
R_{pim} (all I^+ & I^-) (%)	5.0 (15.4)[a]	3.6 (10.7)[a]	3.3 (2.3)[a]
Observed reflections	52018 (7536)[a]	20827 (3111)[a]	8412 (1242)[a]
Unique reflections	6478 (913)[a]	8624 (1286)[a]	2400 (352)[a]
Mean((I)/sd(I))	13.9 (4.7)[a]	16.1 (6.2)[a]	15.8 (9.0)[a]
Completeness (%)	99.1 (98.6)[a]	98.1 (99.2)[a]	99.6 (99.6)[a]
Multiplicity	8.0 (8.3)[a]	2.4 (2.4)[a]	3.5 (8.5)[a]
Wavelenght (Ă)	0.93	0.97	0.87

a)

Mathews Coefficient Calculations Solvent Content (%)	
$Z\alpha_{ADAR1}$:dsRNA:	-33.92
$Z\alpha_{ADAR1}$:ssRNA:	5.68
dsRNA	21.40

Autoindexing with Mosflm (Leslie, 2006; Powell, 1999), data scaling with SCALA (CCP4 package) (CCP4, 1994). [a]In parentheses are the statistics for the outer-resolution shell. (a) Mathews Coefficient Calculations based on the $Z\alpha_{ADAR1}$:A-Z-RNA complex (http://csb.wfu.edu/tools/vmcalc/vm.html).

The crystal unit cell dimensions for the putative complexes RNA oligonucleotides with the $Z\alpha_{ADAR1}$ domain are quite small (Table 2.4.1). The values obtained for Matthews coefficient and estimated solvent content considering different possibilities for the crystal of putative $Z\alpha_{ADAR1A}$:Z-

RNA complex are displayed in Table 2.4.1a. The calculated values, only allow for a dsRNA molecule to be present in our crystals, according with the processed experimental data.

Interestingly, the reported unit cell parameters for $Z\alpha_{ADAR1}$:Z-RNA complex (PDB ID 2GXB) are a = 73.60, b = 92.78, c = 50.23 (space group $C222_1$). The three-dimensional structure of this complex shows that a dimer of $Z\alpha_{ADAR1}$ binds a double-helical RNA molecule (Placido et al., 2007).

In order to indentify the molecular species present in our crystals, several crystals of $Z\alpha_{ADAR1}$:A-Z-RNA putative complex were pulled from crystallization droplets, washed in a drop containing the reservoir solution and dissolved in this buffer. This sample was subjected to mass spectrometry (MS) MALDI-TOF analysis. Samples containing the purified protein $Z\alpha_{ADAR1}$ and the A-Z RNA (2 oligonucleotides available) were used as control.

The Zα spectra (Figure 2.4.6c) has a major peak for *m/z* of 7363, as expected, the predicted molecular weight is 7.3 kDa, according to the amino acid sequence.

For the oligonucleotides alone, the expected mass for oligo 1 is 5.38 kDa and for oligo 2 is.5.45 kDa. In Figure 2.4.6b and c, the major peaks correspond to a *m/z* of 5387 and 5461, respectively. The major peaks of the sample containing the dissolved crystals appear in the region of *m/z* 5300 – 5600, with peaks of significant intensity at *m/z* 5368, 5460 and 5522. Therefore, we conclude that most probably our crystals comprise only double-stranded RNA, and no protein is present.

Molecular replacement was done with data collected for crystals of putative $Z\alpha_{ADAR1}$:Z-Z-RNA: using MolRep (Vagin and Teplyakov, 2010), using as a template an RNA molecule and inputing information on our RNA molecule sequence. The obtained solution told us that the X-ray data processed comprised only dsRNA in the A conformation. Model building was carried out (b) with Coot (Emsley and Cowtan, 2004) and one crystallographic refinement with CNS (Brünger et al., 1998; Brunger, 2007) until convergence was reached (R = 0.337, R_{free} = 0.3757). However, since we were interested in having a crystallographic structure from the complexed $Z\alpha_{ADAR1}$:Z-RNA no further refinements were performed. Figure 2.4.7 illustrates what we could see with our data.

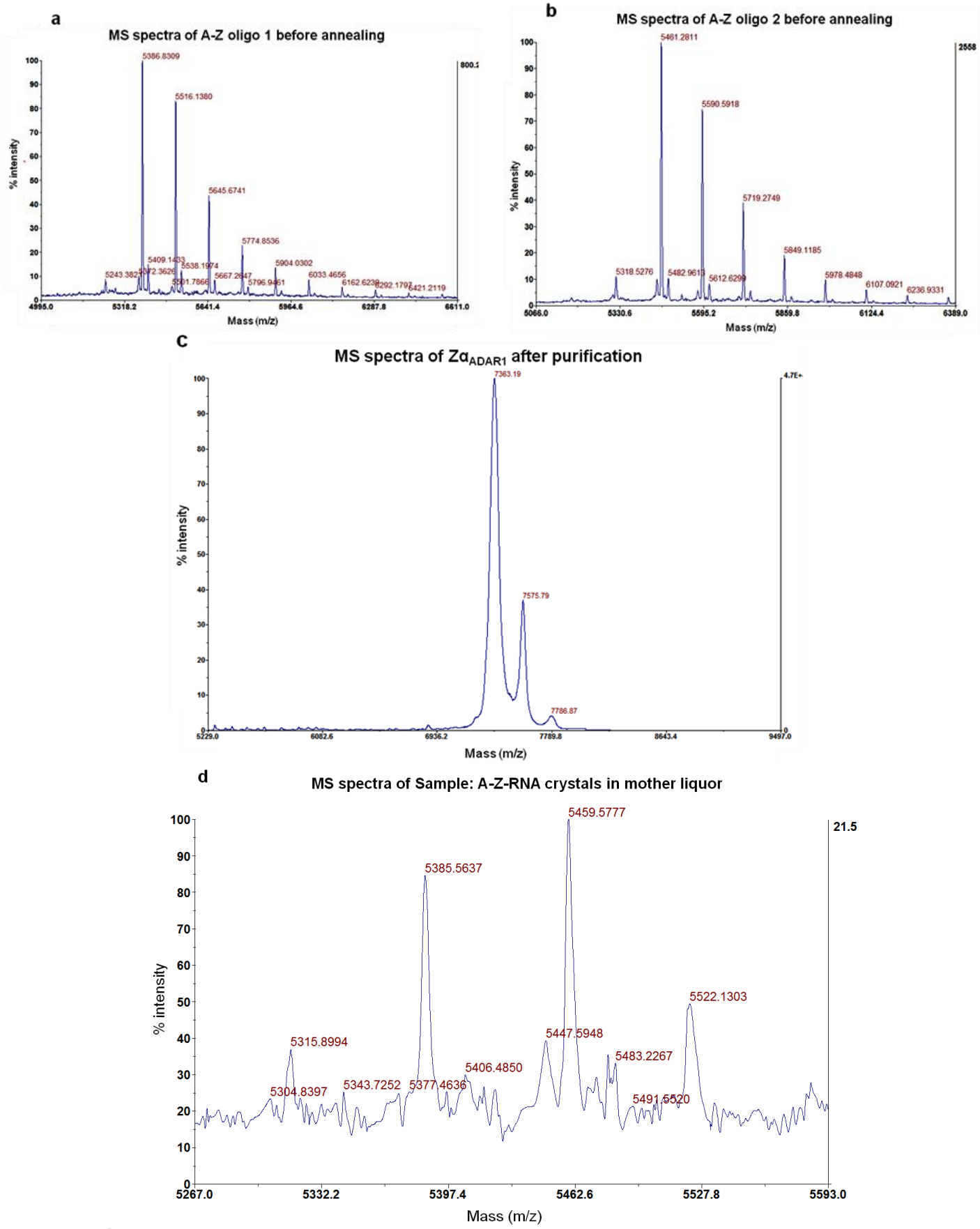

Figure
2.4.6. MS spectra of A-Z oligos (a and b), purified Zα$_{ADAR1}$ (c), and crystals from the A-Z-RNA complex (d).

Data provide by the Mass Spectrometry Laboratory, Analytical Services Unit, Instituto de Tecnologia Química e Biológica, Universidade Nova de Lisboa.

Further processment of the Z-Z-RNA dataset (higher resolution dataset) showed that our crystals only contained dsRNA in the A conformation.

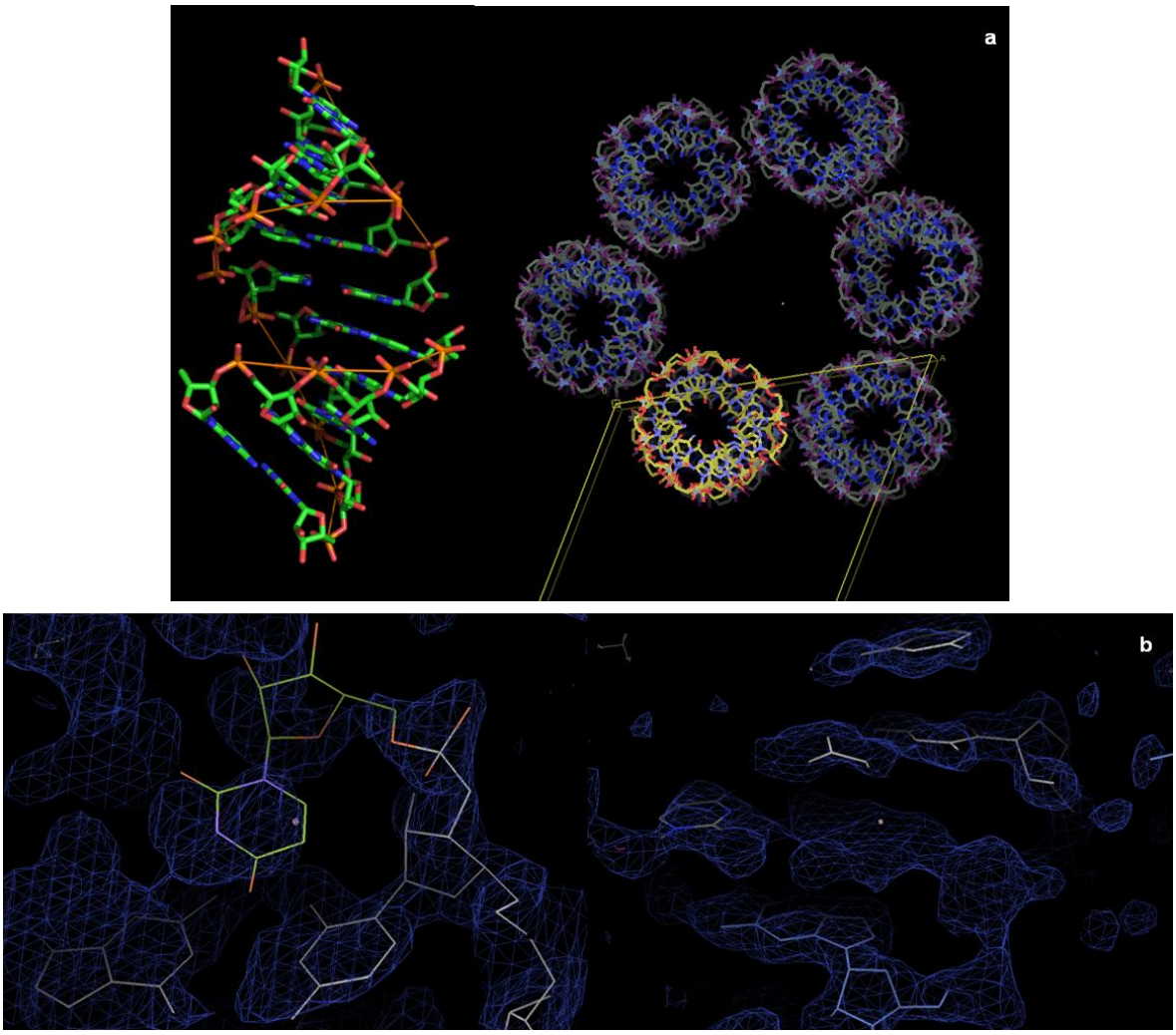

Figure 2.4.7. Data processing of Z-Z-RNA dataset showing A-dsRNA.

Molecular replacement was done with MolRep (Vagin and Teplyakov, 2010) (a). Model building (b) with Coot (Emsley and Cowtan, 2004) and CNS (Brünger et al., 1998; Brunger, 2007) (R = 0.3371 R_{free} = 0.3757).

Structure Determination of a Z-Z DNA Junction Bound by the $Z\alpha_{ADAR1}$ Domain.

Two crystal structures of the same complex between $Z\alpha_{ADAR1}$ and a Z-Z junction forming the duplex sequence $(CG)_3A(CG)_3$, crystallized in slightly different conditions. The best diffracting crystals were obtained initially at pH 7.0 by using Hepes as a buffer, which has been the buffer used historically for $Z\alpha_{ADAR1}$ purification and storage. When a molecule of Hepes was found located in the center of the junction, some crystallization trials of a Hepes-free sample with different buffers were set up in order to clarify the role of such a molecule in junction formation and evaluate to what extent the overall structure is affected by its presence. A second dataset from crystals grown in a Tris buffered solution were obtained, allowing the comparison of both structures.

Whereas the best conditions for the Hepes-containing structure required an initial high throughput robot screening and some efforts in optimization, crystals of the Hepes-free sample were obtained with just minor adjustments in the original conditions. Crystals obtained in both conditions showed similar plate-like morphology and kinetics of formation, belonging to the same orthorhombic $P2_12_12_1$ space group, with similar unit cell dimensions (Table 2.4.2). The quality of the two datasets collected is also equivalent: The first crystal form diffracted to 2.65 Å with an R_{merge} of 9.2%, whereas the Hepes-free one diffracted to 2.8 Å but with a slightly better R_{merge} equal to 8.3%.

Table 2.4.2. Data collection and refinement statistics.

	Hepes-binding	Hepes-free
Beam line	ID23EH2	ID14EH4
Resolution (Å)	47-2.65	106-2.8
Wavelength (Å)	0.87	0.98
R_{merge} (%)	9.2 (53.4)*	8.3 (25.6)†
$I/\sigma I$	12.2 (2.8)*	9.2 (3.1)†
Observed reflections	41,627	27,084
Unique reflections	10,230	7,894
Completeness (%)	99.4 (99.9)*	96.8 (92.2)†
Multiplicity	4.1 (4.1)*	3.4 (3.4)†
Space group	$P2_12_12_1$	$P2_12_12_1$
Cell dimension (Å)	$a = 30.6$, $b = 102.2$, $c = 105.9$	$a = 29.28$, $b = 99.76$, $c = 106.48$
R_{work} (%)	22.9	23.5
R_{free} (%)	28.3	27.1
Mean B factor (protein) (Å^2)	50.4	65.4
Mean B factor (DNA) (Å^2)	37.0	49.1
Mean B factor (solvent) (Å^2)	39.1	50.8

*Values for the outer resolution shell (2.65–2.79 Å).
†Values for the outer resolution shell (2.80–2.95 Å).

Apart from the junction, the two structures are quite similar (Figure 2.4.8). A superimposition of the whole complex would not be meaningful because the DNA molecule is differently kinked at the junction position. Instead, we cut the complex in an equatorial plane to obtain two ternary complexes (two $Z\alpha_{ADAR1}$ molecules binding a six-mere duplex) and superimposed these structures. We obtained an rmsd equal to 1.18 and 0.84 Å by using all 500 of the DNA duplex atoms and 491 atoms of the protein backbone.

Below, a description one of the two complexes is done, with underline the differences when it is appropriate. From now on, we will refer to the Hepes-free complex as the $Z\alpha_{ADAR1}$/Z-Z-DNA structure.

The structure was solved by molecular replacement using the first published $Z\alpha_{ADAR1}/(CG)_3$ structure as the searching model [Protein Data Bank (PDB) ID 1QBJ]. More precisely, to avoid introduction of bias, a minimal model consisting in a single molecule of $Z\alpha_{ADAR1}$ binding a single strand six-mer of Z-DNA was used. Four complexes in the asymmetric unit were found, and we could build the biological unit by reassembling the molecules to form one double-stranded Z-DNA molecule bound by four $Z\alpha_{ADAR1}$ monomers (Figure 2.4.8).

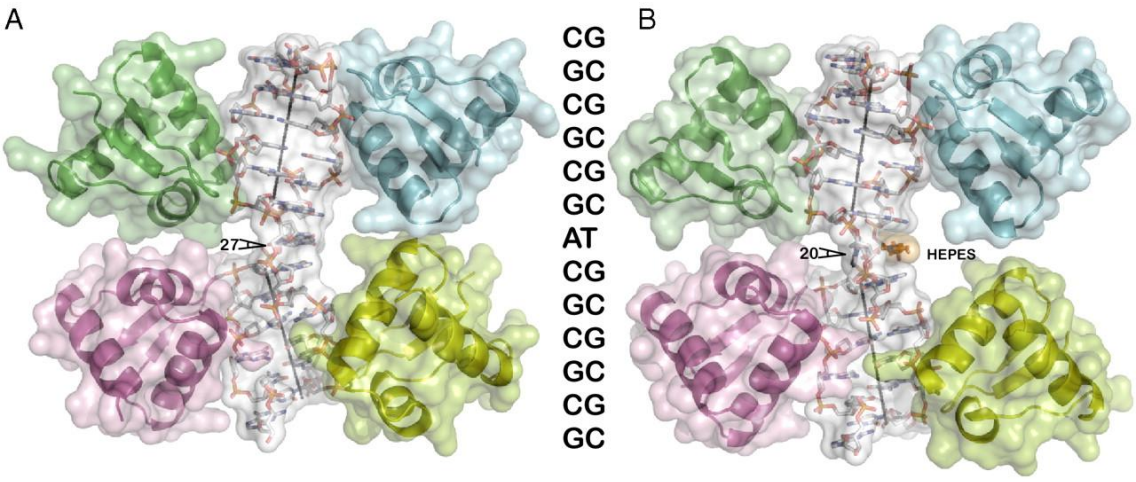

Figure 2.4.8. Overall structure of a Z-Z junction.

The DNA duplex is shown as a skeletal model for the Hepes-free (Left, A) and Hepes (Right, B) structures, respectively, colored according to atom type except for the Hepes molecule (Orange). In both cases four Zα domains are bound to the duplex $(CG)_3A(CG)_3$ DNA oligonucleotide and shown as ribbon diagrams. The molecular surface of each chain is shown transparent. We show aligned the oligonucleotide sequence (Middle). The helical axis for each $(CG)_3$ segment appears as a straight line, and the angle corresponding to the DNA kink is indicated.

Overall Structure and Stoichiometry of the $Z\alpha_{ADAR1}$:$(CG)_3A(CG)_3$ Complex.

Two complementary oligonucleotides were designed to study the structure of a Z-Z junction, consisting in two overhanging bases (AC and GT) at the 5′ followed by two $(CG)_3$ stretches interrupted by an A (T in the complementary strand). Three consecutive CG repeats have been

identified as the minimum binding site for $Z\alpha_{ADAR1}$. The two overhanging bases, even if not visible in most of the previously published structures, are believed to help in crystal packing. The out-of-phase base pair (A-T in our case) should interrupt the Z-DNA helix, because the repeating unit of Z-DNA is a dinucleotide.

It is already known that the protein/DNA stoichiometry is crucial in the crystallization of Z*α*/Z-DNA complexes. To determine the initial conditions for the optimal ratio $Z\alpha_{ADAR1}$ to Z-DNA, some solution experiments by using CD were performed. The CD spectra of left- and right-handed DNA are significantly different (Figure 2.4.9), and by using different protein/DNA ratios we could show that four molecules of $Z\alpha_{ADAR1}$ are required to obtain full conversion of the oligonucleotide to the left-handed conformation (Figure 2.4.9, inset).

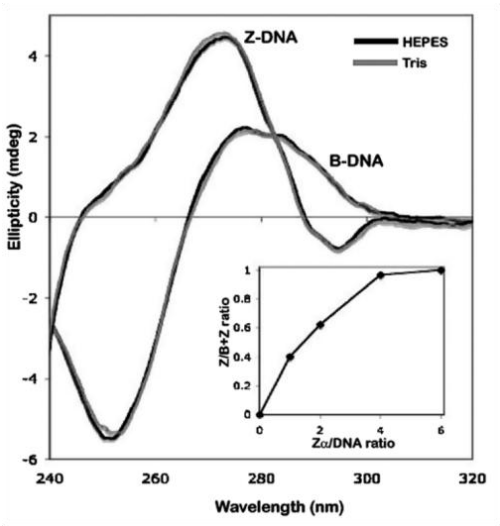

Figure 2.4.9. Circular dichroism spectra of the Z-Z DNA duplex and its titration with Zα.

CD spectra of duplex $(CG)_3A(CG)_3$ as shown for both the right-handed and left-handed form (stabilized by a 4× molar excess of $Z\alpha_{ADAR1}$), in both Hepes (Black Lines) and Tris (Gray Lines) buffered solutions. The inset shows the ratio of Z-DNA over total DNA, during titration with $Z\alpha_{ADAR1}$. The Z-DNA fraction was calculated by assuming it is equal to 0 in the absence of Zα and 1 with a sixfold excess of the protein. Total conversion of the oligonucleotide is obtained with a fourfold excess of $Z\alpha_{ADAR1}$.

Indeed, the same stoichiometry in the crystal structures was found (Figure 2.4.8). Two molecules of $Z\alpha_{ADAR1}$ bind each of the two $(CG)_3$ portions. Overall, the $Z\alpha_{ADAR1}$ domain interaction with the DNA helix is similar to the one described previously for its complex with a single $(CG)_3$ duplex (Schwartz et al., 1999). Not only is the broad surface of interaction the same, but also the intricate network of direct and indirect interactions between protein and DNA is conserved in our structure, as can be noted in (Figire 2.4.10). The Zα monomers show an average rmsd of 0.5 Å (56 C*α* atoms used) when compared to the search model.

Most of the residues involved in the interaction are located in the helix α3 and in the wing, (Figure 2.4.10). They can be divided into van der Waals interacting residues (Pro192 and Pro193), residues interacting directly through hydrogen bonds to the DNA backbone (Thr191, Lys169, Lys170 and Tyr177), and residues whose interaction with DNA is mediated by water

molecules as Trp195. Asn173 is at the same time able to directly bind the DNA and also interact with one of the conserved water molecules. These residues represent the core binding motif of Z-DNA and together with the complementarity of the interacting surface lead to a very high specificity and binding affinity.

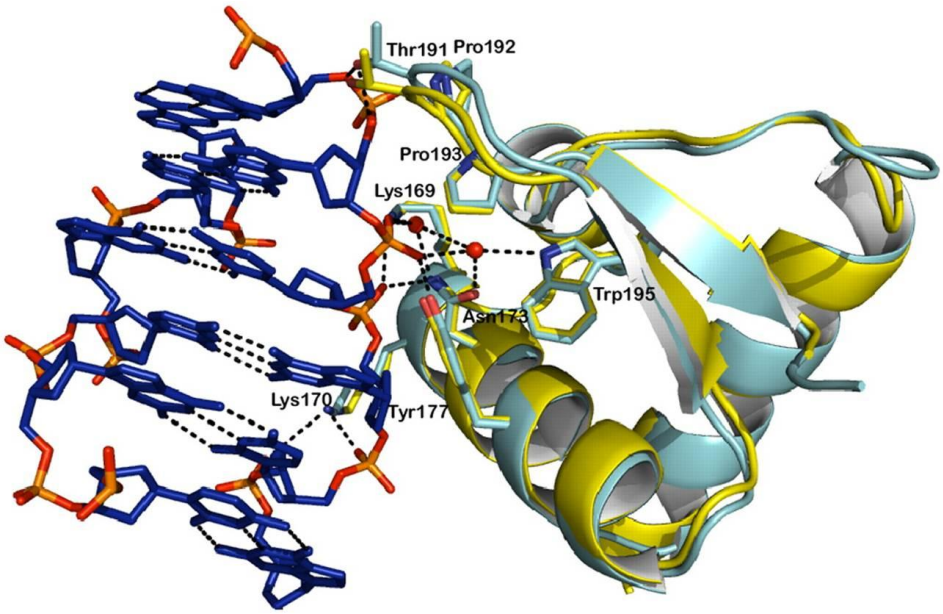

Figure 2.4.10 .Conservation of the protein–DNA interactions in the $Z\alpha_{ADAR1}$:Z-Z DNA complex.

Superimposition of the $Z\alpha_{ADAR1}$ domain from the search model PDB ID 1QBJ (Cyan) and chain C of the Hepes-free structure of the ZZ junction (Yellow). Residues interacting with DNA are shown in stick representation, whereas dotted lines show hydrogen bonds. Side chains involved in interactions with DNA are drawn as sticks and labeled.

Taken separately, the two stretches of six base-pair Z-DNA do not differ significantly from previously published Z-DNA structures. In fact, if we ignore the junction, our structure shows two Z-DNA helices that are close to ideal in conformational parameters (Tables 2.4.3 – 2.4.5). In particular, the slide and the twist parameters are notable because they characteristically alternate between purines and pyrimidines and apparently are in no way affected either by the crystal packing or by the presence of the junction. The unique exception is the adjacent CG pairs to the junction in the Hepes-free structure that show a deformation described in detail later.

Z-DNA possesses a straight helical axis. In our structure the axes of the two CG hexamers form a sharp ~20° angle due to the presence of the junction, resulting in an overall kinked DNA structure. This angle is slightly different in the two structures and equal to 20° in the Hepes structure and 27° in the HEPES-free structure (Figure 2.4.8).

Table 2.4.3. Selected conformational parameters for the Z-Z junction in Tris buffer; DNA conformational parameters as determined by using 3DNA (Lu and Olson, 2003).

Base pair	3′P-5′P (Å)	Opening (°)	Stretch (Å)	H-bonding atoms and distances (Å)		Slide	Twist
1 CG	11.6	0.5	−0.0	O2-N2	2.9	5.4	−6.3
				N3-N1	3.0		
				N4-O6	3.1		
2 GC	14.9	−4.7	−0.1	O6-N4	2.8	−1.3	−49.2
				N1-N3	3.0		
				N2-O2	3.0		
3 CG	11.4	−3.5	−0.2	O2-N2	3.0	5.1	−5.6
				N3-N1	3.0		
				N4-O6	2.9		
4 GC	15.4	6.7	−0.0	O6-N4	3.4	−1.1	−59.4
				N1-N3	3.1		
				N2-O2	2.8		
5 CG	12.8	−6.4	−0.2	O2-N2	3.4	5.3	0.5
				N3-N1	3.3		
				N4-O6	3.1		
6 GC	16.4	−7.7	0.1	O6-N4	3.3	−0.5	−30.5
				N1-N3	3.6		
				N2-O2	3.8		
7 TA	17.9	−92.4	2.3	O4-N6*	2.4*	0.4	−25.2
8 CG	12.3	−1.2	−0.3	O2-N2	2.8	5.1	−2.5
				N3-N1	2.9		
				N4-O6	2.8		
9 GC	15.5	−4.0	−0.3	O6-N4	2.7	−1.4	−51.4
				N1-N3	2.9		
				N2-O2	2.8		
10 CG	11.3	−2.6	−0.4	O2-N2	2.8	5.5	−2.8
				N3-N1	2.8		
				N4-O6	2.7		
11 GC	15.6	−0.8	−0.2	O6-N4	2.8	−1.2	−53.5
				N1-N3	2.9		
				N2-O2	2.8		
12 CG	12.3	−2.7	−0.4	O2-N2	2.8	5.4	−5.9
				N3-N1	2.8		
				N4-O6	2.7		
13 GC	-	5.1	0.0	O6-N4	3.2		
				N1-N3	3.0		
				N2-O2	2.6		

Table 2.4.4. Detailed conformational parameters of a Z-Z junction in Hepes buffer; local base-pair step parameters as calculated by using 3DNA (Lu and Olson, 2003).

	Shift	Slide	Rise	Tilt	Roll	Twist
1 CG	−0.2	5.5	4.0	0.5	−1.3	−5.3
2 GC	−0.3	−1.3	3.2	1.9	−6.8	−47.8
3 CG	−0.03	5.6	3.9	−1.3	−2.7	−7.1
4 GC	0.2	−1.1	3.0	2.7	−6.2	−50.9
5 CG	−0.2	5.0	3.5	−2.8	−1.7	−4.2
6 GC	4.9	2.9	0.2	42.2	−98.4	−114.1
7 TA	-	-	-	-	-	-
8 CG	−0.2	5.3	3.5	−0.2	4.8	−5.0
9 GC	−0.6	−1.2	3.2	0.7	−9.4	−54.6
10 CG	−0.4	5.1	4.5	−1.2	5.2	5.4
11 GC	0.7	−0.5	2.8	0.4	−5.9	−57.3
12 CG	−0.3	5.3	4.0	4.7	−0.0	−3.8
13 GC						

Table 2.4.5. Detailed conformational parameters of a Z-Z junction in Tris buffer; local base-pair step parameters as calculated by using 3DNA (Lu and Olson, 2003).

	Shift	Slide	Rise	Tilt	Roll	Twist
1 CG	–0.2	5.4	3.8	1.7	–4.3	–6.3
2 GC	–0.3	–1.3	3.1	3.0	–9.5	–49.2
3 CG	0.5	5.1	3.9	–0.8	4.4	–5.6
4 GC	–0.5	–1.2	3.4	1.2	–7.3	–59.4
5 CG	–0.3	5.3	3.7	–3.4	–0.3	0.5
6 GC	–3.6	–0.5	3.8	2.2	–15.9	–30.5
7 TA	–2.2	0.4	3.53	7.9	–9.8	–25.2
8 CG	–0.2	5.1	3.76	5.3	–1.8	–2.5
9 GC	0.0	–1.4	3.30	–2.1	–6.8	–51.4
10 CG	0.1	5.5	3.89	–0.2	–1.0	–2.8
11 GC	0.1	–1.2	3.09	–0.1	–5.1	–53.7
12 CG	0.5	5.4	3.80	–2.6	–1.1	–5.9
13 GC						

A Close View of the Z-Z DNA Junction.

Z-Z junctions have already been investigated. In particular, two structural studies have been published suggesting models for the Z-Z junction: An NMR investigation, carried out by Yang and Wang (Yang and Wang, 1997), on a structure containing mismatches at the junction site and in which the Z conformation was induced by organic and inorganic compounds, not by Zα. Another study used diethyl pyrocarbonate and hydroxylamine chemical probing along with molecular modeling to define features of the junction (Johnston et al., 1991). More recent work uses fluorescent modified bases containing 2-amino purine (2AP) to study base stacking at the junction site by fluorescence spectroscopy (Kim et al., 2009). The two older studies suggest that the junction bases remain intrahelical with the NMR study predicting that the junction bases form a reverse Watson–Crick base pair. In contrast, in the more recent study on the basis of 2AP fluorescence, the authors interpreted the data with the junctional bases extruded from the double helix similar to what has been seen for the B-Z junction (Ha et al., 2005). The results show no such base extrusion. However, the base-pair formation at the junction shows differences from the suggested models. These differences are described below.

During the refinement of the first structure (obtained in the presence of Hepes), a feature in the electron density of the junction area adjacent to the well defined base density was noticed (Figure 2.4.11A). An initial raised hypothesis was that this density represented some kind of double conformation of the bases; however, occupancy refinement showed base occupancy close to 1 and their electron density was well defined. Discarding this option, inspecting the crystallization solution composition together with electron density maps, led to a perfectly modeled Hepes molecule. The structure was further refined and the Hepes molecule ended up with a 0.8 occupancy and B factors varying between 30 and 50 $Å^2$ for the ring and slightly higher for the hydroxyl and sulfonate groups (Table 2.4.6). The two bases of the junction show a large

roll and are almost orthogonal to the plane of the previous and next base pair. The A-T pair interacts according to a reverse Watson–Crick geometry because the hydrogen bonding atoms are N_6-O_2 and N_1-N_3, although the N-O hydrogen bond is very weak with a distance between donor and acceptor of 3.5 Å (Figure 2.4.11).

Table 2.4.6. B factors and occupancy of the intercalating Hepes molecule.

Atom	Occupancy	B factor (Å^2)
O_{3S}	0.8	52
S		71
O_{1S}		59
O_{2S}		48
C_{10}		51
C_9		37
N_1		37
C_2		31
C_3		32
N_4		40
C_5		46
C_6		41
C_7		38
C_8		58
O_8		58

The unexpected Hepes ligand, intercalating in a cavity created between the A-T pair and the two C-G pairs before and after the junction (Figure 2.4.11B), seems to restore base stacking because its semiplanar ring is parallel to the planes of the other bases. No other interactions are observed between Hepes and DNA, apart from the interactions between the sulfonate group of the molecule with N4 of C8 and O4′ of T7 and N7 of G6. The junctional bases are almost perpendicular to the rest of the bases and can be accommodated only because of the 20° kink of the helical axis.

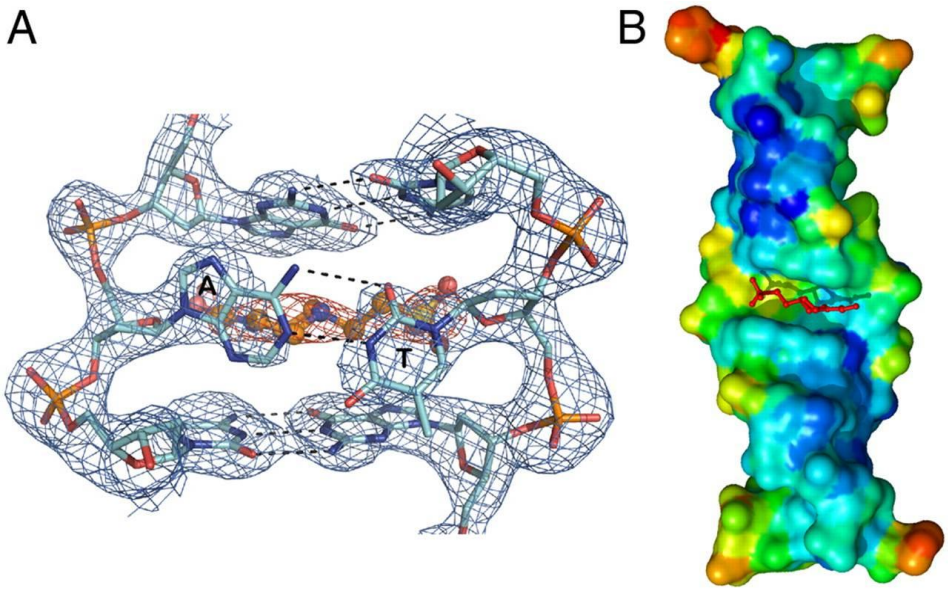

Figure 2.4.11.The Z-Z junction structure in the presence of Hepes.

(A) Electron density of the Z-Z junction contoured at 1σ (Blue); the density for the Hepes molecule is shown orange. Dotted lines represent base-base hydrogen bonds. Note the perpendicular orientation of the A-T reverse Watson–Crick base pair. (B) Surface representation of the $(CG)_3A(CG)_3$ DNA colored according to atom B factors (range blue rigid—red mobile). The Hepes molecule (Stick) is seen intercalating at the junction site. Note the mobility of the thymine at the junction site (Yellow). The region where Zα interacts with DNA is characterized by low B factors (Deep Blue Areas).

Because the observed structure of the Z-Z junction might have been influenced by the intercalation of Hepes, we also determined the structure in Hepes-free conditions. The Hepes-free structure is significantly different at the junction site. Whereas it maintains the kink at the junction, the AT base pair (A7-T7) in this structure lays on a plane that is almost parallel to the plane of the other base pairs (Figure 2.4.12A), and it occupies the position where the Hepes molecule was found in the first structure. The observed kink of the DNA helix in the absence of Hepes is slightly greater (27°), and in this case we find the junction bases located in the helix compression instead of the bulky Hepes molecule. The Hepes-free structure is consistent with aspects of the model predicted by Yang and Wang with the well defined adenine base in *syn* conformation like the preceding G6, maintaining stacking interactions. However, the electron density for the opposing base T7 demonstrates ambiguity, which is best interpreted by the base alternating between *syn* and *anti*conformation. This mobility of T7 is supported from the fact that no optimal hydrogen bonding to A7 on the opposite strand can be formed in any of the alternative conformations. In the *anti* conformation a single hydrogen bond is formed between O4 of T7 to N6 of A7, whereas no hydrogen bonding is observed with T7 in the *syn* conformation. Nevertheless, both conformations of ~0.5 occupancy support partial stacking of this base with the rest of the helix. While stacking is maintained, formation of the junction in the Hepes-free structure also affects the lower G6-C8 base pair (Figure 2.4.12A and Table 2.4.3), resulting in a widening of the helix and hydrogen bonding distances in the range of 3.3–3.8 Å. Interestingly, this helix deformation is asymmetric affecting only one of the two base pairs adjacent to the junction base pairs.

Comparing the Z-Z junction with a B-Z junction

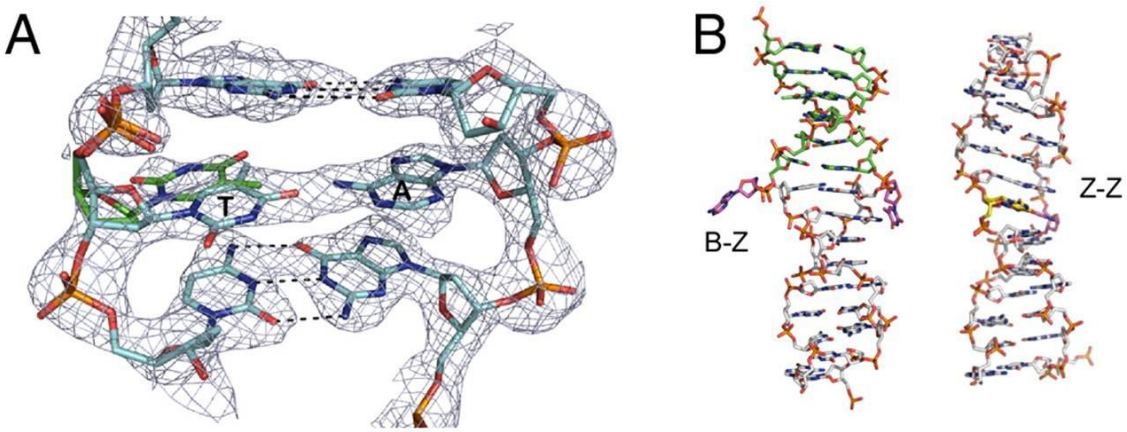

Figure 2.4.12. The Z-Z junction structure and its comparison with a B-Z junction.

(A) Electron density of the Z-Z junction contoured at 1σ. Dotted lines represent base-base hydrogen bonds. (B) Comparison of the Z-Z junction (present work) to the B-Z junction (Ha et al., 2005) PDB ID code 2ACJ.

We determined the crystal structure of a complex between a $(CG)_3A(CG)_3$ DNA duplex and the Zα domain of ADAR1. The $(CG)_3$ parts of the DNA adopt a typical Z-DNA structure, but the overall DNA helix is significantly kinked at the junction. This kink results in the creation of a cavity on one side of the DNA structure and a compression on the opposite side. In the first attempt of structure determination it was found a Hepes molecule occupying the predicted location of the AT base pair with the bases themselves forming a partial base pair surprisingly oriented perpendicular to the plane of the other bases in the DNA. In this way the junction forms a cage for the buffer molecule. Whereas this obviously is a crystallization artifact, it provides significant insight into the dynamic nature of the junction, and it points to the fact that the junction bases are sterically uncomfortable and mobile.

Determining the structure in the absence of Hepes showed that the junction bases can partially stack with the rest of the helix. The adenosine is found in its expected position in the *syn* conformation typical for Z-DNA but breaking the *syn-anti* alternation, whereas the thymine is partially disordered apparently occupying two positions, one in the *syn* and one in the *anti* orientation with occupancy of 0.5 for each orientation. Indeed the pyrimidine of the junction shows the most unfavorable contacts and in solution is expected to shift dynamically between the two conformations.

Unlike the B-Z junction, which by fully extruding the junction bases succeeds in maintaining continuous stacking between the right- and the left-handed helix, bases of the Z-Z junction remain intrahelical and base stacking is partially lost (Figure 2.4.12). Also, unlike the B-Z junction, where only the Z portion is bound by $Z\alpha_{ADAR1}$, in the Z-Z junction both Z-DNA helices are bound by the protein. We have to ask whether unfavorable protein–protein contacts affect the junction structure by not allowing the two 6-mers getting closer through extrusion of the junction bases. Indeed, modeling of $Z\alpha_{ADAR1}$ binding to continuous 12-mer yields protein–protein clashes between Zα molecules. Thus, the presence of Zα might lead to capturing an intermediate state of the junction formation blocking base extrusion and stacking of the two hexamers. On the other hand, there is reasonable agreement of our structure with the model of a Z-Z junction derived from the NMR data. That model was derived from structures with mismatched A-A and T-T pairs at the junction and predicted intrahelical junctional bases. On the basis of the NMR structures, a model was proposed of an AT junction with the bases being in *syn* (A) and *anti* (T) conformation and forming a reverse Watson–Crick base pair. We find the adenosine in the *syn* conformation (χ = 50), whereas the thymidine appears to have more than one conformation. However, in none of the alternative conformations do we observe base pairing, which is in good agreement with the observation that the energetic cost of a Z-Z junction (3.5 kcal/mol) (Johnston et al., 1991) is similar to that of the mismatched junctions. Another important feature of the present structure that is absent in previous models is a partial melting of one of the adjacent CG pairs with hydrogen bonding distances that are more than 0.5 Å longer than the average distances for the other CG base pairs of the helix (Table 2.4.3). The mobility we observe for the T residue is also in good agreement with the chemical reactivity

results of Johnston et al. (Johnston et al., 1991) showing that a corresponding C (in this work the junction was a CG instead of AT) becomes hypersensitive in a Z-Z junction, whereas the N7 of corresponding purine of the junction is shown to be protected as would be expected from our structure. Overall, the Hepes-free structure is in good agreement and explanatory to the available biochemical and NMR data.

Another question is the extent to which the observed angle of bending (27° in the Hepes-free structure) is influenced by the enclosing $Z\alpha_{ADAR1}$ proteins. It can be seen (Figure 2.4.8A) that the two $Z\alpha_{ADAR1}$ molecules on the side of the bend are closer together when the angle is 27°, compared to 20° for the Hepes structure (Figure 2.4.8B). The two $Z\alpha s_{ADAR1}$ are in van der Waals contact, suggesting that they may limit further bending. This observation might support the argument that the observed structure is trapped in an intermediate state. It is clear that this issue can be resolved only by further structural studies, perhaps with fewer $Z\alpha_{ADAR1}$ molecules.

In recent work, base analogs of adenosine (2AP) were used to monitor stacking of bases in different types of junctions using fluorescent spectroscopy. This work suggested the loss of stacking of the adenosine base at a Z-Z junction with a sequence similar to the one described here. Although we do observe loss of base stacking at the junction, this is because of the mobility of the thymine residue. The adenosine residue, however, is not extruded; it is well defined and maintains optimal stacking with the adjacent bases. The reason behind this disagreement is possibly because of the use of Hepes as a buffer in these fluorometric studies that, as we observe in the corresponding structure, results in loss of stacking for the adenosine at the junction. It is also possible that the 2-amino purine substitution in this context alters the properties of the already deformed junction in a way that adenosine becomes more exposed.

2.5. Conclusion

The complexes between $Z\alpha_{ADAR1}$ domain both with Z-DNA and with a small B-Z-DNA junction were already determined. But although these structures took us one step further and a DNA binding role cannot be excluded, all Z-domain carrying proteins with known functionalities are involved in dsRNA recognition and are predominantly cytoplasmic. It is also known that the isoform of ADAR1 containing the domain that binds the Z-form is only expressed in the cytoplasm, where no DNA is suppose to exist, so this domain should actually interact with RNA. The stability of the interaction between $Z\alpha_{ADAR1}$ domain and a small Z-RNA was not enough to clarify all the questions that have been arising on the last years with the new findings on this subject. Also, the binding of the human $Z\alpha_{ADAR1}$ domain to the RNA is expected to be related to the function of the protein of hyper-editing, inserting mutations on the RNA.

Here we show a tentative approach to understand the binding of the $Z\alpha_{ADAR1}$ domain with RNA, by studying two types of possible junctions (A-Z-RNA and Z-Z-RNA) that form upon complex formation, and are the predominant biological signature in nature. However, Z-RNA in complex with $Z\alpha_{ADAR1}$ was not attainable. RNA is less stable and more difficult to handle then DNA, and, of course, Z-RNA formation is not a favored energetic transformation by itself. Even being observable by CD spectroscopy that A-Z-RNA is forming, cocrystallization was not successful.

It is also shown how sequences containing imperfect CpG repeats can adopt the left-handed conformation and tolerate the formation of Z-Z junctions. This finding increases significantly the number of potential Z-forming sequences in genomic DNA. Because Z-forming sequences and CpG repeats are implicated in mammalian genomic instability (Wang et al., 2006) and cancer, the structure presented here provides the basis to understand some of the molecular features that are involved in their mutagenic role. Whereas formation of B-Z and Z-Z junctions increases the exposure of bases to modifying agents with mutagenic effects, the Hepes structure suggests also that a Z-Z junction can be a site for intercalation and a potential target of a number of anticancer drugs that target DNA replication. This intercalation is expected to stabilize the left-handed conformation by restoring base stacking to some extent. Such stabilization may have deleterious effects for cancer cells resulting in lethal DNA rearrangements and may be potentially one of the sources of the anticancer action of intercalating agents.

2.6. References

Adams, P.D., Grosse-Kunstleve, R.W., Hung, L.W., Ioerger, T.R., McCoy, A.J., Moriarty, N.W., Read, R.J., Sacchettini, J.C., Sauter, N.K., and Terwilliger, T.C. (2002). PHENIX: building new software for automated crystallographic structure determination. Acta Crystallogr. D Biol. Crystallogr. *58*, 1948–1954.

Alberts, B. (2009). Essential cell biology (New York: Garland Science).

Alberts, B., Johnson, A., Lewis, J., Raff, M., Roberts, K., and Walter, P. (2002a). Neural Development.

Alberts, B., Johnson, A., Lewis, J., Raff, M., Roberts, K., and Walter, P. (2002b). From DNA to RNA.

Alfano, C., and Studer, M. (2013). Neocortical arealization: Evolution, mechanisms, and open questions. Dev. Neurobiol. *73*, 411–447.

De Anda, F.C., Meletis, K., Ge, X., Rei, D., and Tsai, L.-H. (2010). Centrosome motility is essential for initial axon formation in the neocortex. J. Neurosci. Off. J. Soc. Neurosci. *30*, 10391–10406.

Angevine, J.B., Jr, and Sidman, R.L. (1961). Autoradiographic study of cell migration during histogenesis of cerebral cortex in the mouse. Nature *192*, 766–768.

Arimura, N., and Kaibuchi, K. (2007). Neuronal polarity: from extracellular signals to intracellular mechanisms. Nat. Rev. Neurosci. *8*, 194–205.

Baas, P.W., Black, M.M., and Banker, G.A. (1989). Changes in microtubule polarity orientation during the development of hippocampal neurons in culture. J. Cell Biol. *109*, 3085–3094.

Baird, D.H., Hatten, M.E., and Mason, C.A. (1992). Cerebellar target neurons provide a stop signal for afferent neurite extension in vitro. J. Neurosci. Off. J. Soc. Neurosci. *12*, 619–634.

Balaz, M., Li, B.C., Steinkruger, J.D., Ellestad, G.A., Nakanishi, K., and Berova, N. (2006). Porphyrins conjugated to DNA as CD reporters of the salt-induced B to Z-DNA transition,. Org. Biomol. Chem. *4*, 1865–1867.

Barnat, M., Enslen, H., Propst, F., Davis, R.J., Soares, S., and Nothias, F. (2010). Distinct roles of c-Jun N-terminal kinase isoforms in neurite initiation and elongation during axonal regeneration. J. Neurosci. Off. J. Soc. Neurosci. *30*, 7804–7816.

Barnes, A.P., Solecki, D., and Polleux, F. (2008). New insights into the molecular mechanisms specifying neuronal polarity in vivo. Curr. Opin. Neurobiol. *18*, 44–52.

Bass, R.B., Strop, P., Barclay, M., and Rees, D.C. (2002). Crystal structure of Escherichia coli MscS, a voltage-modulated and mechanosensitive channel. Science *298*, 1582–1587.

Bastmeyer, M., and O'Leary, D.D. (1996). Dynamics of target recognition by interstitial axon branching along developing cortical axons. J. Neurosci. Off. J. Soc. Neurosci. *16*, 1450–1459.

Battaglia, A., Novelli, A., Bernardini, L., Igliozzi, R., and Parrini, B. (2009). Further characterization of the new microdeletion syndrome of 16p11.2-p12.2. Am. J. Med. Genet. A. *149A*, 1200–1204.

Behar, O., Golden, J.A., Mashimo, H., Schoen, F.J., and Fishman, M.C. (1996). Semaphorin III is needed for normal patterning and growth of nerves, bones and heart. Nature *383*, 525–528.

Behe, M., and Felsenfeld, G. (1981). Effects of methylation on a synthetic polynucleotide: the B--Z transition in poly(dG-m5dC).poly(dG-m5dC). Proc. Natl. Acad. Sci. U. S. A. *78*, 1619–1623.

Bellion, A., Baudoin, J.-P., Alvarez, C., Bornens, M., and Métin, C. (2005). Nucleokinesis in Tangentially Migrating Neurons Comprises Two Alternating Phases: Forward Migration of the Golgi/Centrosome Associated with Centrosome Splitting and Myosin Contraction at the Rear. J. Neurosci. *25*, 5691–5699.

Berger, I., Winston, W., Manoharan, R., Schwartz, T., Alfken, J., Kim, Y.G., Lowenhaupt, K., Herbert, A., and Rich, A. (1998). Spectroscopic characterization of a DNA-binding domain, Z alpha, from the editing enzyme, dsRNA adenosine deaminase: evidence for left-handed Z-DNA in the Z alpha-DNA complex. Biochemistry (Mosc.) *37*, 13313–13321.

Berry, M., and Rogers, A.W. (1965). The migration of neuroblasts in the developing cerebral cortex. J. Anat. *99*, 691–709.

Bill, R.M., Henderson, P.J.F., Iwata, S., Kunji, E.R.S., Michel, H., Neutze, R., Newstead, S., Poolman, B., Tate, C.G., and Vogel, H. (2011). Overcoming barriers to membrane protein structure determination. Nat. Biotechnol. *29*, 335–340.

Binda, C., Newton-Vinson, P., Hubálek, F., Edmondson, D.E., and Mattevi, A. (2002). Structure of human monoamine oxidase B, a drug target for the treatment of neurological disorders. Nat. Struct. Biol. *9*, 22–26.

Bjorkblom, B. (2005). Constitutively Active Cytoplasmic c-Jun N-Terminal Kinase 1 Is a Dominant Regulator of Dendritic Architecture: Role of Microtubule-Associated Protein 2 as an Effector. J. Neurosci. *25*, 6350–6361.

Björkblom, B., Ostman, N., Hongisto, V., Komarovski, V., Filén, J.-J., Nyman, T.A., Kallunki, T., Courtney, M.J., and Coffey, E.T. (2005). Constitutively active cytoplasmic c-Jun N-terminal kinase 1 is a dominant regulator of dendritic architecture: role of microtubule-associated protein 2 as an effector. J. Neurosci. Off. J. Soc. Neurosci. *25*, 6350–6361.

Bolla, J.R., Su, C.-C., and Yu, E.W. (2012). Biomolecular membrane protein crystallization. Philos. Mag. Abingdon Engl. *92*, 2648–2661.

Boulder Committee (1970). Embryonic vertebrate central nervous system: revised terminology. The Boulder Committee. Anat. Rec. *166*, 257–261.

Bowie, J.U. (2001). Stabilizing membrane proteins. Curr. Opin. Struct. Biol. *11*, 397–402.

Boyd, D., Schierle, C., and Beckwith, J. (1998). How many membrane proteins are there? Protein Sci. Publ. Protein Soc. *7*, 201–205.

Bracey, M.H., Hanson, M.A., Masuda, K.R., Stevens, R.C., and Cravatt, B.F. (2002). Structural adaptations in a membrane enzyme that terminates endocannabinoid signaling. Science *298*, 1793–1796.

Bradke, F., and Dotti, C.G. (1999). The role of local actin instability in axon formation. Science *283*, 1931–1934.

Brandt, T.A., and Jacobs, B.L. (2001). Both carboxy- and amino-terminal domains of the vaccinia virus interferon resistance gene, E3L, are required for pathogenesis in a mouse model. J. Virol. *75*, 850–856.

Brown, B.A., 2nd, and Rich, A. (2001). The left-handed double helical nucleic acids. Acta Biochim. Pol. *48*, 295–312.

Brown, B.A., Lowenhaupt, K., Wilbert, C.M., Hanlon, E.B., and Rich, A. (2000). The Zα domain of the editing enzyme dsRNA adenosine deaminase binds left-handed Z-RNA as well as Z-DNA. Proc. Natl. Acad. Sci. *97*, 13532–13536.

Brunger, A.T. (2007). Version 1.2 of the Crystallography and NMR system. Nat. Protoc. *2*, 2728–2733.

Brünger, A.T., Adams, P.D., Clore, G.M., DeLano, W.L., Gros, P., Grosse-Kunstleve, R.W., Jiang, J.S., Kuszewski, J., Nilges, M., Pannu, N.S., et al. (1998). Crystallography & NMR system: A new software suite for macromolecular structure determination. Acta Crystallogr. D Biol. Crystallogr. *54*, 905–921.

Buchanan, S.K. (1999). β-Barrel proteins from bacterial outer membranes: structure, function and refolding. Curr. Opin. Struct. Biol. *9*, 455–461.

Burbelo, P.D., Drechsel, D., and Hall, A. (1995). A conserved binding motif defines numerous candidate target proteins for both Cdc42 and Rac GTPases. J. Biol. Chem. *270*, 29071–29074.
Caffrey, M. (2003). Membrane protein crystallization. J. Struct. Biol. *142*, 108–132.
Caffrey, M. (2011). Crystallizing membrane proteins for structure-function studies using lipidic mesophases. Biochem. Soc. Trans. *39*, 725–732.
Caffrey, M., and Cherezov, V. (2009). Crystallizing membrane proteins using lipidic mesophases. Nat. Protoc. *4*, 706–731.
Campbell, K., and Götz, M. (2002). Radial glia: multi-purpose cells for vertebrate brain development. Trends Neurosci. *25*, 235–238.
Carmi, S., Borukhov, I., and Levanon, E.Y. (2011). Identification of widespread ultra-edited human RNAs. PLoS Genet. *7*, e1002317.
CCP4 (1994). The CCP4 suite: programs for protein crystallography. Acta Crystallogr. D Biol. Crystallogr. *50*, 760–763.
Chang, L., Jones, Y., Ellisman, M.H., Goldstein, L.S.B., and Karin, M. (2003). JNK1 is required for maintenance of neuronal microtubules and controls phosphorylation of microtubule-associated proteins. Dev. Cell *4*, 521–533.
Chen, Z., and Cobb, M.H. (2001). Regulation of stress-responsive mitogen-activated protein (MAP) kinase pathways by TAO2. J. Biol. Chem. *276*, 16070–16075.
Chen, C.X., Cho, D.S., Wang, Q., Lai, F., Carter, K.C., and Nishikura, K. (2000). A third member of the RNA-specific adenosine deaminase gene family, ADAR3, contains both single- and double-stranded RNA binding domains. RNA N. Y. N *6*, 755–767.
Chen, G., Sima, J., Jin, M., Wang, K.-Y., Xue, X.-J., Zheng, W., Ding, Y.-Q., and Yuan, X.-B. (2008). Semaphorin-3A guides radial migration of cortical neurons during development. Nat. Neurosci. *11*, 36–44.
Chen, Z., Hutchison, M., and Cobb, M.H. (1999). Isolation of the protein kinase TAO2 and identification of its mitogen-activated protein kinase/extracellular signal-regulated kinase kinase binding domain. J. Biol. Chem. *274*, 28803–28807.
Chen, Z., Raman, M., Chen, L., Lee, S.F., Gilman, A.G., and Cobb, M.H. (2003). TAO (thousand-and-one amino acid) protein kinases mediate signaling from carbachol to p38 mitogen-activated protein kinase and ternary complex factors. J. Biol. Chem. *278*, 22278–22283.
Chenn, A., and McConnell, S.K. (1995). Cleavage orientation and the asymmetric inheritance of Notch1 immunoreactivity in mammalian neurogenesis. Cell *82*, 631–641.
Chilton, J.K. (2006). Molecular mechanisms of axon guidance. Dev. Biol. *292*, 13–24.
Choi, Y.I., Duke-Cohan, J.S., Ahmed, W.B., Handley, M.A., Mann, F., Epstein, J.A., Clayton, L.K., and Reinherz, E.L. (2008). PlexinD1 glycoprotein controls migration of positively selected thymocytes into the medulla. Immunity *29*, 888–898.
Cohen, S.L., and Chait, B.T. (2001). Mass spectrometry as a tool for protein crystallography. Annu. Rev. Biophys. Biomol. Struct. *30*, 67–85.
Corty, M.M., Matthews, B.J., and Grueber, W.B. (2009). Molecules and mechanisms of dendrite development in Drosophila. Development *136*, 1049–1061.
Craig, A.M., and Banker, G. (1994). Neuronal polarity. Annu. Rev. Neurosci. *17*, 267–310.
Dahm, R. (2008). Discovering DNA: Friedrich Miescher and the early years of nucleic acid research. Hum. Genet. *122*, 565–581.
Darnell, J.C., Van Driesche, S.J., Zhang, C., Hung, K.Y.S., Mele, A., Fraser, C.E., Stone, E.F., Chen, C., Fak, J.J., Chi, S.W., et al. (2011). FMRP Stalls Ribosomal Translocation on mRNAs Linked to Synaptic Function and Autism. Cell *146*, 247–261.
Degenhardt, F., Priebe, L., Herms, S., Mattheisen, M., Mühleisen, T.W., Meier, S., Moebus, S., Strohmaier, J., Groß, M., Breuer, R., et al. (2012). Association between copy number variants in 16p11.2 and major depressive disorder in a German case-control sample. Am. J. Med. Genet. Part B Neuropsychiatr. Genet. Off. Publ. Int. Soc. Psychiatr. Genet. *159B*, 263–273.
Deisenhofer, J., Epp, O., Miki, K., Huber, R., and Michel, H. (1985). Structure of the protein subunits in the photosynthetic reaction centre of Rhodopseudomonas viridis at 3|[angst]| resolution. Nature *318*, 618–624.
Desterro, J.M.P., Keegan, L.P., Lafarga, M., Berciano, M.T., O'Connell, M., and Carmo-Fonseca, M. (2003). Dynamic association of RNA-editing enzymes with the nucleolus. J. Cell Sci. *116*, 1805–1818.
Diefenderfer, C., Lee, J., Mlyanarski, S., Guo, Y., and Glover, K.J. (2009). Reliable expression and purification of highly insoluble transmembrane domains. Anal. Biochem. *384*, 274–278.
Dobyns, W.B., and Truwit, C.L. (1995). Lissencephaly and other malformations of cortical development: 1995 update. Neuropediatrics *26*, 132–147.
Dotti, C.G., Sullivan, C.A., and Banker, G.A. (1988). The establishment of polarity by hippocampal neurons in culture. J. Neurosci. *8*, 1454–1468.
Drew, D., Slotboom, D.-J., Friso, G., Reda, T., Genevaux, P., Rapp, M., Meindl-Beinker, N.M., Lambert, W., Lerch, M., Daley, D.O., et al. (2005). A scalable, GFP-based pipeline for membrane protein overexpression screening and purification. Protein Sci. Publ. Protein Soc. *14*, 2011–2017.
Drew, D., Lerch, M., Kunji, E., Slotboom, D.-J., and de Gier, J.-W. (2006). Optimization of membrane protein overexpression and purification using GFP fusions. Nat. Methods *3*, 303–313.
Drew, D., Newstead, S., Sonoda, Y., Kim, H., von Heijne, G., and Iwata, S. (2008). GFP-based optimization scheme for the overexpression and purification of eukaryotic membrane proteins in Saccharomyces cerevisiae. Nat. Protoc. *3*, 784–798.
Drew, D.E., von Heijne, G., Nordlund, P., and de Gier, J.-W.L. (2001). Green fluorescent protein as an indicator to monitor membrane protein overexpression in Escherichia coli. FEBS Lett. *507*, 220–224.
Drew, H.R., Wing, R.M., Takano, T., Broka, C., Tanaka, S., Itakura, K., and Dickerson, R.E. (1981). Structure of a B-DNA dodecamer: conformation and dynamics. Proc. Natl. Acad. Sci. U. S. A. *78*, 2179–2183.
Du, Y., and Zhou, X. (2013). Targeting Non-B-Form DNA in Living Cells. Chem. Rec. *13*, 371–384.
Emsley, P., and Cowtan, K. (2004). Coot: model-building tools for molecular graphics. Acta Crystallogr. D Biol. Crystallogr. *60*, 2126–2132.
Etienne-Manneville, S., and Hall, A. (2002). Rho GTPases in cell biology. Nature *420*, 629–635.
Farkas, L.M., and Huttner, W.B. (2008). The cell biology of neural stem and progenitor cells and its significance for their proliferation versus differentiation during mammalian brain development. Curr. Opin. Cell Biol. *20*, 707–715.
Fenstermaker, V., Chen, Y., Ghosh, A., and Yuste, R. (2004). Regulation of dendritic length and branching by semaphorin 3A. J. Neurobiol. *58*, 403–412.

Ferguson, A.D., McKeever, B.M., Xu, S., Wisniewski, D., Miller, D.K., Yamin, T.-T., Spencer, R.H., Chu, L., Ujjainwalla, F., Cunningham, B.R., et al. (2007). Crystal structure of inhibitor-bound human 5-lipoxygenase-activating protein. Science *317*, 510–512.

Filimonova, M., Gubskaya, V., Davidov, R., Garusov, A., and Nuretdinov, I. (2008). Metal binding induces conversion of B- to the hybrid B-Z-form in natural DNA. Int. J. Biol. Macromol. *43*, 289–294.

Finlay, B.L., and Slattery, M. (1983). Local differences in the amount of early cell death in neocortex predict adult local specializations. Science *219*, 1349–1351.

Forscher, P., and Smith, S.J. (1988). Actions of cytochalasins on the organization of actin filaments and microtubules in a neuronal growth cone. J. Cell Biol. *107*, 1505–1516.

Fu, Y., Comella, N., Tognazzi, K., Brown, L.F., Dvorak, H.F., and Kocher, O. (1999). Cloning of DLM-1, a novel gene that is up-regulated in activated macrophages, using RNA differential display. Gene *240*, 157–163.

Fujii, T., Nakao, F., Shibata, Y., Shioi, G., Kodama, E., Fujisawa, H., and Takagi, S. (2002). Caenorhabditis elegans PlexinA, PLX-1, interacts with transmembrane semaphorins and regulates epidermal morphogenesis. Dev. Camb. Engl. *129*, 2053–2063.

Fukata, M., Nakagawa, M., and Kaibuchi, K. (2003). Roles of Rho-family GTPases in cell polarisation and directional migration. Curr. Opin. Cell Biol. *15*, 590–597.

Geschwind, D.H., and Levitt, P. (2007). Autism spectrum disorders: developmental disconnection syndromes. Curr. Opin. Neurobiol. *17*, 103–111.

Goshima, Y., Ito, T., Sasaki, Y., and Nakamura, F. (2002). Semaphorins as signals for cell repulsion and invasion. J. Clin. Invest. *109*, 993–998.

Götz, M., and Huttner, W.B. (2005). The cell biology of neurogenesis. Nat. Rev. Mol. Cell Biol. *6*, 777–788.

Govek, E.-E., Newey, S.E., and Van Aelst, L. (2005). The role of the Rho GTPases in neuronal development. Genes Dev. *19*, 1–49.

Gregory, W.A., Edmondson, J.C., Hatten, M.E., and Mason, C.A. (1988). Cytology and neuron-glial apposition of migrating cerebellar granule cells in vitro. J. Neurosci. *8*, 1728–1738.

Griffiths, A.J., Miller, J.H., Suzuki, D.T., Lewontin, R.C., and Gelbart, W.M. (2000a). Making recombinant DNA (W. H. Freeman and Company.).

Griffiths, A.J., Miller, J.H., Suzuki, D.T., Lewontin, R.C., and Gelbart, W.M. (2000b). Structure of DNA (W. H. Freeman and Company.).

Gu, C., Rodriguez, E.R., Reimert, D.V., Shu, T., Fritzsch, B., Richards, L.J., Kolodkin, A.L., and Ginty, D.D. (2003). Neuropilin-1 conveys semaphorin and VEGF signaling during neural and cardiovascular development. Dev. Cell *5*, 45–57.

Ha, S.C., Lokanath, N.K., Van Quyen, D., Wu, C.A., Lowenhaupt, K., Rich, A., Kim, Y.-G., and Kim, K.K. (2004). A poxvirus protein forms a complex with left-handed Z-DNA: crystal structure of a Yatapoxvirus Zalpha bound to DNA. Proc. Natl. Acad. Sci. U. S. A. *101*, 14367–14372.

Ha, S.C., Lowenhaupt, K., Rich, A., Kim, Y.-G., and Kim, K.K. (2005). Crystal structure of a junction between B-DNA and Z-DNA reveals two extruded bases. Nature *437*, 1183–1186.

Hall, K., Cruz, P., Tinoco, I., Jr, Jovin, T.M., and van de Sande, J.H. (1984). "Z-RNA"--a left-handed RNA double helix. Nature *311*, 584–586.

Halloran, M.C., and Kalil, K. (1994). Dynamic behaviors of growth cones extending in the corpus callosum of living cortical brain slices observed with video microscopy. J. Neurosci. Off. J. Soc. Neurosci. *14*, 2161–2177.

Hatten, M.E. (2002). New directions in neuronal migration. Science *297*, 1660–1663.

Hays, F.A., Teegarden, A., Jones, Z.J.R., Harms, M., Raup, D., Watson, J., Cavaliere, E., and Ho, P.S. (2005). How sequence defines structure: a crystallographic map of DNA structure and conformation. Proc. Natl. Acad. Sci. U. S. A. *102*, 7157–7162.

Herbert, A., and Rich, A. (1999a). Left-handed Z-DNA: structure and function. Genetica *106*, 37–47.

Herbert, A., and Rich, A. (1999b). Left-Handed Z-DNA: Structure and Function. In Structural Biology and Functional Genomics, E.M. Bradbury, and S. Pongor, eds. (Springer Netherlands), pp. 53–72.

Herbert, A.G., and Rich, A. (1993). A method to identify and characterize Z-DNA binding proteins using a linear oligodeoxynucleotide. Nucleic Acids Res. *21*, 2669–2672.

Herbert, A., Lowenhaupt, K., Spitzner, J., and Rich, A. (1995). Chicken double-stranded RNA adenosine deaminase has apparent specificity for Z-DNA. Proc. Natl. Acad. Sci. U. S. A. *92*, 7550–7554.

Hirokawa, T., Boon-Chieng, S., and Mitaku, S. (1998). SOSUI: classification and secondary structure prediction system for membrane proteins. Bioinformatics *14*, 378–379.

Hopkins, A.L., and Groom, C.R. (2002). The druggable genome. Nat. Rev. Drug Discov. *1*, 727–730.

Horton, A.C., Rácz, B., Monson, E.E., Lin, A.L., Weinberg, R.J., and Ehlers, M.D. (2005). Polarized secretory trafficking directs cargo for asymmetric dendrite growth and morphogenesis. Neuron *48*, 757–771.

Hota, P.K., and Buck, M. (2012). Plexin structures are coming: opportunities for multilevel investigations of semaphorin guidance receptors, their cell signaling mechanisms, and functions. Cell. Mol. Life Sci. CMLS *69*, 3765–3805.

Huangfu, W.-C., Omori, E., Akira, S., Matsumoto, K., and Ninomiya-Tsuji, J. (2006). Osmotic stress activates the TAK1-JNK pathway while blocking TAK1-mediated NF-kappaB activation: TAO2 regulates TAK1 pathways. J. Biol. Chem. *281*, 28802–28810.

Huber, A.B., Kolodkin, A.L., Ginty, D.D., and Cloutier, J.-F. (2003). SIGNALING AT THE GROWTH CONE: Ligand-Receptor Complexes and the Control of Axon Growth and Guidance. Annu. Rev. Neurosci. *26*, 509–563.

Huber, A.B., Kania, A., Tran, T.S., Gu, C., De Marco Garcia, N., Lieberam, I., Johnson, D., Jessell, T.M., Ginty, D.D., and Kolodkin, A.L. (2005). Distinct roles for secreted semaphorin signaling in spinal motor axon guidance. Neuron *48*, 949–964.

Iwata, S., and Chayen NE. Crystallization of Membrane Proteins in Oils. (2003). Methods and Results in Crystallization of Membrane Proteins (Internat'l University Line).

Jabr, F. (2012). Know Your Neurons: The Discovery and Naming of the Neuron.

Jan, Y.-N., and Jan, L.Y. (2010). Branching out: mechanisms of dendritic arborization. Nat. Rev. Neurosci. *11*, 316–328.

Jeanneteau, F., Deinhardt, K., Miyoshi, G., Bennett, A.M., and Chao, M.V. (2010). The MAP kinase phosphatase MKP-1 regulates BDNF-induced axon branching. Nat. Neurosci. *13*, 1373–1379.

Johnston, B.H., Quigley, G.J., Ellison, M.J., and Rich, A. (1991). The Z-Z junction: the boundary between two out-of-phase Z-DNA regions. Biochemistry (Mosc.) *30*, 5257–5263.

Jones, E.G. (1986). Neurotransmitters in the cerebral cortex. J. Neurosurg. *65*, 135–153.

Junge, F., Schneider, B., Reckel, S., Schwarz, D., Dötsch, V., and Bernhard, F. (2008). Large-scale production of functional membrane proteins. Cell. Mol. Life Sci. CMLS *65*, 1729–1755.

Just, M.A., Cherkassky, V.L., Keller, T.A., Kana, R.K., and Minshew, N.J. (2007). Functional and anatomical cortical underconnectivity in autism: evidence from an FMRI study of an executive function task and corpus callosum morphometry. Cereb. Cortex N. Y. N 1991 *17*, 951–961.

Kalil, K., Szebenyi, G., and Dent, E.W. (2000). Common mechanisms underlying growth cone guidance and axon branching. J. Neurobiol. *44*, 145–158.

Kawate, T., and Gouaux, E. (2006). Fluorescence-Detection Size-Exclusion Chromatography for Precrystallization Screening of Integral Membrane Proteins. Structure *14*, 673–681.

Kelleher, R.J., 3rd, and Bear, M.F. (2008). The autistic neuron: troubled translation? Cell *135*, 401–406.

Kelsch, W., Mosley, C.P., Lin, C.-W., and Lois, C. (2007). Distinct mammalian precursors are committed to generate neurons with defined dendritic projection patterns. PLoS Biol. *5*, e300.

Kim, D., Reddy, S., Kim, D.Y., Rich, A., Lee, S., Kim, K.K., and Kim, Y.-G. (2009). Base extrusion is found at helical junctions between right- and left-handed forms of DNA and RNA. Nucleic Acids Res. *37*, 4353–4359.

Kim, U., Wang, Y., Sanford, T., Zeng, Y., and Nishikura, K. (1994). Molecular cloning of cDNA for double-stranded RNA adenosine deaminase, a candidate enzyme for nuclear RNA editing. Proc. Natl. Acad. Sci. U. S. A. *91*, 11457–11461.

Kim, Y.-G., Lowenhaupt, K., Maas, S., Herbert, A., Schwartz, T., and Rich, A. (2000). The Zab Domain of the Human RNA Editing Enzyme ADAR1 Recognizes Z-DNA When Surrounded by B-DNA. J. Biol. Chem. *275*, 26828–26833.

Kim, Y.-G., Muralinath, M., Brandt, T., Pearcy, M., Hauns, K., Lowenhaupt, K., Jacobs, B.L., and Rich, A. (2003). A role for Z-DNA binding in vaccinia virus pathogenesis. Proc. Natl. Acad. Sci. U. S. A. *100*, 6974–6979.

King, I., Tsai, L.T.-Y., Pflanz, R., Voigt, A., Lee, S., Jäckle, H., Lu, B., and Heberlein, U. (2011). Drosophila tao Controls Mushroom Body Development and Ethanol-Stimulated Behavior through par-1. J. Neurosci. Off. J. Soc. Neurosci. *31*, 1139–1148.

Kitsukawa, T., Shimizu, M., Sanbo, M., Hirata, T., Taniguchi, M., Bekku, Y., Yagi, T., and Fujisawa, H. (1997). Neuropilin-semaphorin III/D-mediated chemorepulsive signals play a crucial role in peripheral nerve projection in mice. Neuron *19*, 995–1005.

Kolodkin, A.L., Matthes, D.J., O'Connor, T.P., Patel, N.H., Admon, A., Bentley, D., and Goodman, C.S. (1992). Fasciclin IV: sequence, expression, and function during growth cone guidance in the grasshopper embryo. Neuron *9*, 831–845.

Komiyama, T., and Luo, L. (2007). Intrinsic control of precise dendritic targeting by an ensemble of transcription factors. Curr. Biol. CB *17*, 278–285.

Konur, S., and Ghosh, A. (2005). Calcium signaling and the control of dendritic development. Neuron *46*, 401–405.

Kowalczyk, T., Pontious, A., Englund, C., Daza, R.A.M., Bedogni, F., Hodge, R., Attardo, A., Bell, C., Huttner, W.B., and Hevner, R.F. (2009). Intermediate neuronal progenitors (basal progenitors) produce pyramidal-projection neurons for all layers of cerebral cortex. Cereb. Cortex N. Y. N 1991 *19*, 2439–2450.

Kriegstein, A.R., and Götz, M. (2003). Radial glia diversity: a matter of cell fate. Glia *43*, 37–43.

Kumanogoh, A., and Takamatsu, H. (2012). Regulation of immune cell responses by semaphorins and their receptors. Arthritis Res. Ther. *14*, O45.

Kwan, A.C., Dombeck, D.A., and Webb, W.W. (2008). Polarized microtubule arrays in apical dendrites and axons. Proc. Natl. Acad. Sci. U. S. A. *105*, 11370–11375.

Lee, A.C., and Suter, D.M. (2008). Quantitative analysis of microtubule dynamics during adhesion-mediated growth cone guidance. Dev. Neurobiol. *68*, 1363–1377.

Lehninger, A.L., Nelson, D.L., and Cox, M.M. (2000). Lehninger principles of biochemistry. (New York: Worth Publishers).

Lei, K., Nimnual, A., Zong, W.-X., Kennedy, N.J., Flavell, R.A., Thompson, C.B., Bar-Sagi, D., and Davis, R.J. (2002). The Bax subfamily of Bcl2-related proteins is essential for apoptotic signal transduction by c-Jun NH(2)-terminal kinase. Mol. Cell. Biol. *22*, 4929–4942.

Leng, J., and Salmon, J.-B. (2009). Microfluidic crystallization. Lab. Chip *9*, 24–34.

Leslie, A.G.W. (2006). The integration of macromolecular diffraction data. Acta Crystallogr. D Biol. Crystallogr. *62*, 48–57.

Levanon, E.Y., Eisenberg, E., Yelin, R., Nemzer, S., Hallegger, M., Shemesh, R., Fligelman, Z.Y., Shoshan, A., Pollock, S.R., Sztybel, D., et al. (2004). Systematic identification of abundant A-to-I editing sites in the human transcriptome. Nat. Biotechnol. *22*, 1001–1005.

Liu, J.S. (2011). Molecular genetics of neuronal migration disorders. Curr. Neurol. Neurosci. Rep. *11*, 171–178.

Liu, T., Rohn, J.L., Picone, R., Kunda, P., and Baum, B. (2010). Tao-1 is a negative regulator of microtubule plus-end growth. J. Cell Sci. *123*, 2708–2716.

Liu, Y., Wolff, K.C., Jacobs, B.L., and Samuel, C.E. (2001). Vaccinia virus E3L interferon resistance protein inhibits the interferon-induced adenosine deaminase A-to-I editing activity. Virology *289*, 378–387.

Loll, P.J., Tretiakova, A., and Soderblom, E. (2003). Compatibility of detergents with the microbatch-under-oil crystallization method. Acta Crystallogr. D Biol. Crystallogr. *59*, 1114–1116.

London, M., and Häusser, M. (2005). Dendritic Computation. Annu. Rev. Neurosci. *28*, 503–532.

Long, S.B., Campbell, E.B., and Mackinnon, R. (2005). Crystal structure of a mammalian voltage-dependent Shaker family K+ channel. Science *309*, 897–903.

Lowery, L.A., and Van Vactor, D. (2009). The trip of the tip: understanding the growth cone machinery. Nat. Rev. Mol. Cell Biol. *10*, 332–343.

Lu, X.-J., and Olson, W.K. (2003). 3DNA: a software package for the analysis, rebuilding and visualization of three-dimensional nucleic acid structures. Nucleic Acids Res. *31*, 5108–5121.

Maas, S., Rich, A., and Nishikura, K. (2003). A-to-I RNA editing: recent news and residual mysteries. J. Biol. Chem. *278*, 1391–1394.

Mancia, F., and Hendrickson, W.A. (2007). Expression of recombinant G-protein coupled receptors for structural biology. Mol. Biosyst. *3*, 723–734.

Mao, Y., Ge, X., Frank, C.L., Madison, J.M., Koehler, A.N., Doud, M.K., Tassa, C., Berry, E.M., Soda, T., Singh, K.K., et al. (2009). Disrupted in schizophrenia 1 regulates neuronal progenitor proliferation via modulation of GSK3beta/beta-catenin signaling. Cell *136*, 1017–1031.

Marsh, L., and Letourneau, P.C. (1984). Growth of neurites without filopodial or lamellipodial activity in the presence of cytochalasin B. J. Cell Biol. *99*, 2041–2047.

Martinez Molina, D., Wetterholm, A., Kohl, A., McCarthy, A.A., Niegowski, D., Ohlson, E., Hammarberg, T., Eshaghi, S., Haeggström, J.Z., and Nordlund, P. (2007). Structural basis for synthesis of inflammatory mediators by human leukotriene C4 synthase. Nature *448*, 613–616.

McCarthy, S.E., Makarov, V., Kirov, G., Addington, A.M., McClellan, J., Yoon, S., Perkins, D.O., Dickel, D.E., Kusenda, M., Krastoshevsky, O., et al. (2009). Microduplications of 16p11.2 are associated with schizophrenia. Nat. Genet. *41*, 1223–1227.
McCormick, A.M., and Leipzig, N.D. (2012). Neural regenerative strategies incorporating biomolecular axon guidance signals. Ann. Biomed. Eng. *40*, 578–597.
McCoy, A.J., Grosse-Kunstleve, R.W., Adams, P.D., Winn, M.D., Storoni, L.C., and Read, R.J. (2007). Phaser crystallographic software. J. Appl. Crystallogr. *40*, 658–674.
McManus, M.F., and Golden, J.A. (2005). Neuronal migration in developmental disorders. J. Child Neurol. *20*, 280–286.
Medeiros, N.A., Burnette, D.T., and Forscher, P. (2006). Myosin II functions in actin-bundle turnover in neuronal growth cones. Nat. Cell Biol. *8*, 215–226.
Miao, H.Q., Soker, S., Feiner, L., Alonso, J.L., Raper, J.A., and Klagsbrun, M. (1999). Neuropilin-1 mediates collapsin-1/semaphorin III inhibition of endothelial cell motility: functional competition of collapsin-1 and vascular endothelial growth factor-165. J. Cell Biol. *146*, 233–242.
Micucci, C., Orciari, S., and Catalano, A. (2010). Semaphorins and their receptors in stem and cancer cells. Curr. Med. Chem. *17*, 3462–3475.
Mitsopoulos, C., Zihni, C., Garg, R., Ridley, A.J., and Morris, J.D.H. (2003). The prostate-derived sterile 20-like kinase (PSK) regulates microtubule organization and stability. J. Biol. Chem. *278*, 18085–18091.
Moore, T.M., Garg, R., Johnson, C., Coptcoat, M.J., Ridley, A.J., and Morris, J.D. (2000). PSK, a novel STE20-like kinase derived from prostatic carcinoma that activates the c-Jun N-terminal kinase mitogen-activated protein kinase pathway and regulates actin cytoskeletal organization. J. Biol. Chem. *275*, 4311–4322.
Murray, R.M., Jones, P., and O'Callaghan, E. (1991). Fetal brain development and later schizophrenia. Ciba Found. Symp. *156*, 155–163; discussion 163–170.
Neukirchen, D., and Bradke, F. (2011). Neuronal polarization and the cytoskeleton. Semin. Cell Dev. Biol. *22*, 825–833.
Newstead, S., Ferrandon, S., and Iwata, S. (2008). Rationalizing alpha-helical membrane protein crystallization. Protein Sci. Publ. Protein Soc. *17*, 466–472.
Ng, J.D., Gavira, J.A., and García-Ruíz, J.M. (2003). Protein crystallization by capillary counterdiffusion for applied crystallographic structure determination. J. Struct. Biol. *142*, 218–231.
Ng, J.D., Stevens, R.C., and Kuhn, P. (2008). Protein crystallization in restricted geometry: advancing old ideas for modern times in structural proteomics. Methods Mol. Biol. Clifton NJ *426*, 363–376.
Nishiyama, M., Togashi, K., von Schimmelmann, M.J., Lim, C.-S., Maeda, S., Yamashita, N., Goshima, Y., Ishii, S., and Hong, K. (2011). Semaphorin 3A induces CaV2.3 channel-dependent conversion of axons to dendrites. Nat. Cell Biol. *13*, 676–685.
Noctor, S.C., Flint, A.C., Weissman, T.A., Dammerman, R.S., and Kriegstein, A.R. (2001). Neurons derived from radial glial cells establish radial units in neocortex. Nature *409*, 714–720.
Noctor, S.C., Martínez-Cerdeño, V., Ivic, L., and Kriegstein, A.R. (2004). Cortical neurons arise in symmetric and asymmetric division zones and migrate through specific phases. Nat. Neurosci. *7*, 136–144.
Noctor, S.C., Martínez-Cerdeño, V., and Kriegstein, A.R. (2008). Distinct behaviors of neural stem and progenitor cells underlie cortical neurogenesis. J. Comp. Neurol. *508*, 28–44.
Nordheim, A., and Rich, A. (1983). The sequence (dC-dA)n X (dG-dT)n forms left-handed Z-DNA in negatively supercoiled plasmids. Proc. Natl. Acad. Sci. U. S. A. *80*, 1821–1825.
O'Leary, D.D., Bicknese, A.R., De Carlos, J.A., Heffner, C.D., Koester, S.E., Kutka, L.J., and Terashima, T. (1990). Target selection by cortical axons: alternative mechanisms to establish axonal connections in the developing brain. Cold Spring Harb. Symp. Quant. Biol. *55*, 453–468.
Oliva, A.A., Jr, Atkins, C.M., Copenagle, L., and Banker, G.A. (2006). Activated c-Jun N-terminal kinase is required for axon formation. J. Neurosci. Off. J. Soc. Neurosci. *26*, 9462–9470.
Opekarová, M., and Tanner, W. (2003). Specific lipid requirements of membrane proteins--a putative bottleneck in heterologous expression. Biochim. Biophys. Acta *1610*, 11–22.
Patterson, J.B., and Samuel, C.E. (1995). Expression and regulation by interferon of a double-stranded-RNA-specific adenosine deaminase from human cells: evidence for two forms of the deaminase. Mol. Cell. Biol. *15*, 5376–5388.
Pearlman, A.L., Faust, P.L., Hatten, M.E., and Brunstrom, J.E. (1998). New directions for neuronal migration. Curr. Opin. Neurobiol. *8*, 45–54.
Peck, L.J., Nordheim, A., Rich, A., and Wang, J.C. (1982). Flipping of cloned d(pCpG)n.d(pCpG)n DNA sequences from right- to left-handed helical structure by salt, Co(III), or negative supercoiling. Proc. Natl. Acad. Sci. U. S. A. *79*, 4560–4564.
Perälä, N., Sariola, H., and Immonen, T. (2012). More than nervous: the emerging roles of plexins. Differ. Res. Biol. Divers. *83*, 77–91.
Pinto, D., Pagnamenta, A.T., Klei, L., Anney, R., Merico, D., Regan, R., Conroy, J., Magalhaes, T.R., Correia, C., Abrahams, B.S., et al. (2010). Functional impact of global rare copy number variation in autism spectrum disorders. Nature *466*, 368–372.
Placido, D., Brown, B.A., 2nd, Lowenhaupt, K., Rich, A., and Athanasiadis, A. (2007). A left-handed RNA double helix bound by the Z alpha domain of the RNA-editing enzyme ADAR1. Struct. Lond. Engl. 1993 *15*, 395–404.
Pohl, F.M., and Jovin, T.M. (1972). Salt-induced co-operative conformational change of a synthetic DNA: equilibrium and kinetic studies with poly (dG-dC). J. Mol. Biol. *67*, 375–396.
Poliakov, G.I. (1961). Some results of research into the development of the neuronal structure of the cortical ends of the analyzers in man. J. Comp. Neurol. *117*, 197–212.
Polleux, F., and Snider, W. (2010). Initiating and growing an axon. Cold Spring Harb. Perspect. Biol. *2*, a001925.
Polleux, F., Morrow, T., and Ghosh, A. (2000). Semaphorin 3A is a chemoattractant for cortical apical dendrites. Nature *404*, 567–573.
Popenda, M., Milecki, J., and Adamiak, R.W. (2004). High salt solution structure of a left-handed RNA double helix. Nucleic Acids Res. *32*, 4044–4054.
Potiron, V.A., Roche, J., and Drabkin, H.A. (2009). Semaphorins and their receptors in lung cancer. Cancer Lett. *273*, 1–14.
Poulsen, H., Nilsson, J., Damgaard, C.K., Egebjerg, J., and Kjems, J. (2001). CRM1 Mediates the Export of ADAR1 through a Nuclear Export Signal within the Z-DNA Binding Domain. Mol. Cell. Biol. *21*, 7862–7871.
Powell, H.R. (1999). The Rossmann Fourier autoindexing algorithm in MOSFLM. Acta Crystallogr. D Biol. Crystallogr. *55*, 1690–1695.
Privé, G.G. (2007). Detergents for the stabilization and crystallization of membrane proteins. Methods San Diego Calif *41*, 388–397.

Privé, G.G., Yanagi, K., and Dickerson, R.E. (1991). Structure of the B-DNA decamer C-C-A-A-C-G-T-T-G-G and comparison with isomorphous decamers C-C-A-A-G-A-T-T-G-G and C-C-A-G-G-C-C-T-G-G. J. Mol. Biol. *217*, 177–199.
Rakic, P. (1972). Mode of cell migration to the superficial layers of fetal monkey neocortex. J. Comp. Neurol. *145*, 61–83.
Rakic, P. (1974). Neurons in rhesus monkey visual cortex: systematic relation between time of origin and eventual disposition. Science *183*, 425–427.
Rakic, P. (1990). Principles of neural cell migration. Experientia *46*, 882–891.
Ramón y Cajal, S. (1952). Structure and connections of neurons. Bull. Los Angel. Neurol. Soc. *17*, 5–46.
Ramón y Cajal, S. (1995). Histology of the nervous system of man and vertebrates (New York: Oxford University Press).
Rasmussen, S.G.F., Choi, H.-J., Rosenbaum, D.M., Kobilka, T.S., Thian, F.S., Edwards, P.C., Burghammer, M., Ratnala, V.R.P., Sanishvili, R., Fischetti, R.F., et al. (2007). Crystal structure of the human beta2 adrenergic G-protein-coupled receptor. Nature *450*, 383–387.
Rich, A., and Davies, D.R. (1956). A new two stranded helical structure: polyadenylic acid and polyuridylic acid. J. Am. Chem. Soc. *78*, 3548–3549.
Rich, A., and Zhang, S. (2003a). Z-DNA: the long road to biological function. Nat. Rev. Genet. *4*, 566–572.
Rich, A., and Zhang, S. (2003b). Timeline: Z-DNA: the long road to biological function. Nat. Rev. Genet. *4*, 566–572.
Robert C. Hockney (1994). Recent developments in heterologous protein production in Escherichia coli. Trends Biotechnol. *12*, 456–463.
Rockel, A.J., Hiorns, R.W., and Powell, T.P. (1980). The basic uniformity in structure of the neocortex. Brain J. Neurol. *103*, 221–244.
Romand, S., Wang, Y., Toledo-Rodriguez, M., and Markram, H. (2011). Morphological development of thick-tufted layer v pyramidal cells in the rat somatosensory cortex. Front. Neuroanat. *5*, 5.
Rosário, M., Schuster, S., Jüttner, R., Parthasarathy, S., Tarabykin, V., and Birchmeier, W. (2012). Neocortical dendritic complexity is controlled during development by NOMA-GAP-dependent inhibition of Cdc42 and activation of cofilin. Genes Dev. *26*, 1743–1757.
Rosso, S.B., Sussman, D., Wynshaw-Boris, A., and Salinas, P.C. (2005). Wnt signaling through Dishevelled, Rac and JNK regulates dendritic development. Nat. Neurosci. *8*, 34–42.
Rothenburg, S., Deigendesch, N., Dittmar, K., Koch-Nolte, F., Haag, F., Lowenhaupt, K., and Rich, A. (2005). A PKR-like eukaryotic initiation factor 2alpha kinase from zebrafish contains Z-DNA binding domains instead of dsRNA binding domains. Proc. Natl. Acad. Sci. U. S. A. *102*, 1602–1607.
Sansam, C.L., Wells, K.S., and Emeson, R.B. (2003). Modulation of RNA editing by functional nucleolar sequestration of ADAR2. Proc. Natl. Acad. Sci. U. S. A. *100*, 14018–14023.
Savva, Y.A., Rieder, L.E., and Reenan, R.A. (2012). The ADAR protein family. Genome Biol. *13*, 252.
Schaar, B.T., and McConnell, S.K. (2005). Cytoskeletal coordination during neuronal migration. Proc. Natl. Acad. Sci. U. S. A. *102*, 13652–13657.
Schade, M., Turner, C.J., Kühne, R., Schmieder, P., Lowenhaupt, K., Herbert, A., Rich, A., and Oschkinat, H. (1999). The solution structure of the Zα domain of the human RNA editing enzyme ADAR1 reveals a prepositioned binding surface for Z-DNA. Proc. Natl. Acad. Sci. *96*, 12465–12470.
Schaefer, A.W., Schoonderwoert, V.T.G., Ji, L., Mederios, N., Danuser, G., and Forscher, P. (2008). Coordination of actin filament and microtubule dynamics during neurite outgrowth. Dev. Cell *15*, 146–162.
Schultz, J., Milpetz, F., Bork, P., and Ponting, C.P. (1998). SMART, a simple modular architecture research tool: identification of signaling domains. Proc. Natl. Acad. Sci. U. S. A. *95*, 5857–5864.
Schüz, A., and Palm, G. (1989). Density of neurons and synapses in the cerebral cortex of the mouse. J. Comp. Neurol. *286*, 442–455.
Schwartz, T., Rould, M.A., Lowenhaupt, K., Herbert, A., and Rich, A. (1999). Crystal structure of the Zalpha domain of the human editing enzyme ADAR1 bound to left-handed Z-DNA. Science *284*, 1841–1845.
Schwartz, T., Behlke, J., Lowenhaupt, K., Heinemann, U., and Rich, A. (2001). Structure of the DLM-1-Z-DNA complex reveals a conserved family of Z-DNA-binding proteins. Nat. Struct. Biol. *8*, 761–765.
Serini, G., Maione, F., Giraudo, E., and Bussolino, F. (2009). Semaphorins and tumor angiogenesis. Angiogenesis *12*, 187–193.
Severs, V.-N., and Whiting, J. (2002). Oswald Avery and the story of DNA (Bear, Del.: Mitchell Lane).
Shelly, M., Cancedda, L., Lim, B.K., Popescu, A.T., Cheng, P., Gao, H., and Poo, M. (2011). Semaphorin3A regulates neuronal polarization by suppressing axon formation and promoting dendrite growth. Neuron *71*, 433–446.
Shing, P., and Carter, M. (2011). DNA Structure: Alphabet Soup for the Cellular Soul. In DNA Replication-Current Advances, H. Seligmann, ed. (InTech),.
Sidman, R.L., and Rakic, P. (1973). Neuronal migration, with special reference to developing human brain: a review. Brain Res. *62*, 1–35.
SIDMAN, R.L., MIALE, I.L., and FEDER, N. (1959). Cell proliferation and migration in the primitive ependymal zone: an autoradiographic study of histogenesis in the nervous system. Exp. Neurol. *1*, 322–333.
Simó, S., and Cooper, J.A. (2012). Regulation of dendritic branching by Cdc42 GAPs. Genes Dev. *26*, 1653–1658.
Singer, S.J., and Nicolson, G.L. (1972). The Fluid Mosaic Model of the Structure of Cell Membranes. Science *175*, 720–731.
Smith, H.C., Gott, J.M., and Hanson, M.R. (1997). A guide to RNA editing. RNA *3*, 1105–1123.
Stagi, M., Gorlovoy, P., Larionov, S., Takahashi, K., and Neumann, H. (2006). Unloading kinesin transported cargoes from the tubulin track via the inflammatory c-Jun N-terminal kinase pathway. FASEB J. Off. Publ. Fed. Am. Soc. Exp. Biol. *20*, 2573–2575.
Stevens, T.J., and Arkin, I.T. (2000). Do more complex organisms have a greater proportion of membrane proteins in their genomes? Proteins Struct. Funct. Bioinforma. *39*, 417–420.
Sutton, B.J., and Sohi, M.K. (1994). Crystallization of membrane proteins for X-ray analysis. Methods Mol. Biol. Clifton NJ *27*, 1–18.
Tabet, A.-C., Pilorge, M., Delorme, R., Amsellem, F., Pinard, J.-M., Leboyer, M., Verloes, A., Benzacken, B., and Betancur, C. (2012). Autism multiplex family with 16p11.2p12.2 microduplication syndrome in monozygotic twins and distal 16p11.2 deletion in their brother. Eur. J. Hum. Genet. EJHG *20*, 540–546.
Takahashi, T., Nowakowski, R.S., and Caviness, V.S., Jr (1996). The leaving or Q fraction of the murine cerebral proliferative epithelium: a general model of neocortical neuronogenesis. J. Neurosci. Off. J. Soc. Neurosci. *16*, 6183–6196.
Takahashi, T., Fournier, A., Nakamura, F., Wang, L.H., Murakami, Y., Kalb, R.G., Fujisawa, H., and Strittmatter, S.M. (1999). Plexin-neuropilin-1 complexes form functional semaphorin-3A receptors. Cell *99*, 59–69.

Takamatsu, H., Takegahara, N., Nakagawa, Y., Tomura, M., Taniguchi, M., Friedel, R.H., Rayburn, H., Tessier-Lavigne, M., Yoshida, Y., Okuno, T., et al. (2010). Semaphorins guide the entry of dendritic cells into the lymphatics by activating myosin II. Nat. Immunol. *11*, 594–600.

Tamagnone, L., Artigiani, S., Chen, H., He, Z., Ming, G.I., Song, H., Chedotal, A., Winberg, M.L., Goodman, C.S., Poo, M., et al. (1999). Plexins are a large family of receptors for transmembrane, secreted, and GPI-anchored semaphorins in vertebrates. Cell *99*, 71–80.

Taniguchi, M., Yuasa, S., Fujisawa, H., Naruse, I., Saga, S., Mishina, M., and Yagi, T. (1997). Disruption of semaphorin III/D gene causes severe abnormality in peripheral nerve projection. Neuron *19*, 519–530.

Tararuk, T., Ostman, N., Li, W., Björkblom, B., Padzik, A., Zdrojewska, J., Hongisto, V., Herdegen, T., Konopka, W., Courtney, M.J., et al. (2006). JNK1 phosphorylation of SCG10 determines microtubule dynamics and axodendritic length. J. Cell Biol. *173*, 265–277.

Tavares, I.A., Touma, D., Lynham, S., Troakes, C., Schober, M., Causevic, M., Garg, R., Noble, W., Killick, R., Bodi, I., et al. (2013). Prostate-derived Sterile 20-like Kinases (PSKs/TAOKs) Phosphorylate Tau Protein and Are Activated in Tangle-bearing Neurons in Alzheimer Disease. J. Biol. Chem. *288*, 15418–15429.

Tillo, M., Ruhrberg, C., and Mackenzie, F. (2012). Emerging roles for semaphorins and VEGFs in synaptogenesis and synaptic plasticity. Cell Adhes. Migr. *6*, 541–546.

Tobin, M.J. (2003). April 25, 1953: Three Papers, Three Lessons. Am. J. Respir. Crit. Care Med. *167*, 1047–1049.

Tran, T.S., Rubio, M.E., Clem, R.L., Johnson, D., Case, L., Tessier-Lavigne, M., Huganir, R.L., Ginty, D.D., and Kolodkin, A.L. (2009). Secreted semaphorins control spine distribution and morphogenesis in the postnatal CNS. Nature *462*, 1065–1069.

Trulson, M.O., Cruz, P., Puglisi, J.D., Tinoco, I., Jr, and Mathies, R.A. (1987). Raman spectroscopic study of left-handed Z-RNA. Biochemistry (Mosc.) *26*, 8624–8630.

Tsai, L.-H., and Gleeson, J.G. (2005). Nucleokinesis in Neuronal Migration. Neuron *46*, 383–388.

Vagin, A., and Teplyakov, A. (2010). Molecular replacement with MOLREP. Acta Crystallogr. D Biol. Crystallogr. *66*, 22–25.

Vallee, R.B., Seale, G.E., and Tsai, J.-W. (2009). Emerging roles for myosin II and cytoplasmic dynein in migrating neurons and growth cones. Trends Cell Biol. *19*, 347–355.

Wallin, E., and von Heijne, G. (1998). Genome-wide analysis of integral membrane proteins from eubacterial, archaean, and eukaryotic organisms. Protein Sci. Publ. Protein Soc. *7*, 1029–1038.

Walsh, C.A., Morrow, E.M., and Rubenstein, J.L.R. (2008). Autism and brain development. Cell *135*, 396–400.

Wang, A.H.-J., Quigley, G.J., Kolpak, F.J., Crawford, J.L., van Boom, J.H., van der Marel, G., and Rich, A. (1979). Molecular structure of a left-handed double helical DNA fragment at atomic resolution. Nature *282*, 680–686.

Wang, A.J., Quigley, G.J., Kolpak, F.J., van der Marel, G., van Boom, J.H., and Rich, A. (1981). Left-handed double helical DNA: variations in the backbone conformation. Science *211*, 171–176.

Wang, G., Christensen, L.A., and Vasquez, K.M. (2006). Z-DNA-forming sequences generate large-scale deletions in mammalian cells. Proc. Natl. Acad. Sci. U. S. A. *103*, 2677–2682.

WATSON, J.D., and CRICK, F.H. (1953). Molecular structure of nucleic acids; a structure for deoxyribose nucleic acid. Nature *171*, 737–738.

Weiner, S.J., Kollman, P.A., Case, D.A., Singh, U.C., Ghio, C., Alagona, G., Profeta, S., and Weiner, P. (1984). A new force field for molecular mechanical simulation of nucleic acids and proteins. J. Am. Chem. Soc. *106*, 765–784.

Weiss, L.A., Shen, Y., Korn, J.M., Arking, D.E., Miller, D.T., Fossdal, R., Saemundsen, E., Stefansson, H., Ferreira, M.A.R., Green, T., et al. (2008). Association between microdeletion and microduplication at 16p11.2 and autism. N. Engl. J. Med. *358*, 667–675.

Weiss, L.A., Arking, D.E., Gene Discovery Project of Johns Hopkins & the Autism Consortium, Daly, M.J., and Chakravarti, A. (2009). A genome-wide linkage and association scan reveals novel loci for autism. Nature *461*, 802–808.

Witte, H., and Bradke, F. (2008). The role of the cytoskeleton during neuronal polarization. Curr. Opin. Neurobiol. *18*, 479–487.

Woisard, A., Fazakerley, G.V., and Guschlbauer, W. (1985). Z-DNA is formed by poly (dC-dG) and poly (dm5C-dG) at micro or nanomolar concentrations of some zinc(II) and copper(II) complexes. J. Biomol. Struct. Dyn. *2*, 1205–1220.

Yamasaki, T., Kawasaki, H., Arakawa, S., Shimizu, K., Shimizu, S., Reiner, O., Okano, H., Nishina, S., Azuma, N., Penninger, J.M., et al. (2011). Stress-activated protein kinase MKK7 regulates axon elongation in the developing cerebral cortex. J. Neurosci. Off. J. Soc. Neurosci. *31*, 16872–16883.

Yamauchi, J., Miyamoto, Y., Sanbe, A., and Tanoue, A. (2006). JNK phosphorylation of paxillin, acting through the Rac1 and Cdc42 signaling cascade, mediates neurite extension in N1E-115 cells. Exp. Cell Res. *312*, 2954–2961.

Yang, X.L., and Wang, A.H. (1997). Structural analysis of Z-Z DNA junctions with A:A and T:T mismatched base pairs by NMR. Biochemistry (Mosc.) *36*, 4258–4267.

Yasuda, S., Tanaka, H., Sugiura, H., Okamura, K., Sakaguchi, T., Tran, U., Takemiya, T., Mizoguchi, A., Yagita, Y., Sakurai, T., et al. (2007). Activity-induced protocadherin arcadlin regulates dendritic spine number by triggering N-cadherin endocytosis via TAO2beta and p38 MAP kinases. Neuron *56*, 456–471.

Yoshida, Y. (2012). Semaphorin signaling in vertebrate neural circuit assembly. Front. Mol. Neurosci. *5*, 71.

Zarling, D.A., Calhoun, C.J., Feuerstein, B.G., and Sena, E.P. (1990). Cytoplasmic microinjection of immunoglobulin Gs recognizing RNA helices inhibits human cell growth. J. Mol. Biol. *211*, 147–160.

Zhou, T., Raman, M., Gao, Y., Earnest, S., Chen, Z., Machius, M., Cobb, M.H., and Goldsmith, E.J. (2004). Crystal structure of the TAO2 kinase domain: activation and specificity of a Ste20p MAP3K. Struct. Lond. Engl. 1993 *12*, 1891–1900.

Zihni, C., Mitsopoulos, C., Tavares, I.A., Baum, B., Ridley, A.J., and Morris, J.D.H. (2007). Prostate-derived sterile 20-like kinase 1-alpha induces apoptosis. JNK- and caspase-dependent nuclear localization is a requirement for membrane blebbing. J. Biol. Chem. *282*, 6484–6493.

Ben-Zvi, A., Yagil, Z., Hagalili, Y., Klein, H., Lerman, O., and Behar, O. (2006). Semaphorin 3A and neurotrophins: a balance between apoptosis and survival signaling in embryonic DRG neurons. J. Neurochem. *96*, 585–597.

Chapter 3

General Conclusions

The mammalian neocortex is a unique structure designed for higher cognitive and associative functions. It allows for the high level of advanced behavior in mammals when compared to other animals. From the first exquisite and detailed drawings by Santiago Ramon y Cajal of neuronal connectivity, to the first high-resolution microscopical maps of the human brain, was less than half a century of technological evolution. But even today, the way our brains store, process and retrieve information is still a mystery. Our personality, our reactions to the world, everything that makes us humans comes not only from our DNA but also from the way we are raised, the environment we live in. All comes together in to a complete self, the consciousness of existence.

Through the application of multiple biochemical and biological techniques we elucidated the role of TAOK2α during the mouse brain development. From those studies, we observed multiple phenotypes, compriseing a disregulation of basal dendrite establishing mechanism leading to less complex dendritic arbors when TAOK2α was absent in the cell, while apical dendrites kept their expected complexity. A novel pathway, where Neuropilin 1 (Nrp1), a receptor for the secreted guidance cue Semaphorin 3A (Sema3A), is now known to modulate the formation of basal dendrites through the interaction with TAOK2α, which activates the c-Jun N-terminal kinase (JNK).

Depletion of TAOK2α expression also leads to a migratory defect in the mouse neocortex. TAOK2α is likely to affect actin destabilization, causing a delay in migration: the neuron keeps the ability to migrate, but is unable to navigate the axon due to the impaired substratum selectivity of the growth cone. Since the cortex substratum confers information to the neurons, the slow migration creates a delay in the extrinsic pattern of information, causing neurons to surpass their true final destination, by adjustment they end more superficially than expected.

Our study led us to further understand the biological mechanisms within our brain. It was described, for the first time, an intricate pattern of neuronal development specifically for the specification and maturation of basal dendrites versus apical dendrites. An understanding of the unique physiology and morphology of these neurons is crucial to the elucidation of the mechanisms underlying sophisticated cognitive functions in normal and disease conditions. If inhibiting the expression of TAOK2, as it was described, leads to such marked phenotypes, it is most plausible that it will have an effect in the patophysiology of an individual where the TAOK2 gene happens to be misregulated or absent, most likely, leading to a psychiatric disorder associated with neocortical disconnection, the accepted model mechanism for Autism Spectrum Disorders.

Despite the excitment of our discoverys, the extrapulation to other mammals, specifically humans, of such findings must be taken cautiously. The human brain is much more complex then the mouse brain. The similaritys between the mouse and the human DNA are very high, however, we humans, have very different capabilities and behaviors. The human neocortex is more complex, with a superior degre of convolutions governed by multiple differences

concerning the establishement of neuronal cytoarchitecture when compared to other mammals, denoted by a larger number of neuronal cells present. The findings obtained in our studies, althought extremely valuable, can not be extended to the human brain development. Altogether, assumptions must be taken carefully, as more *in vivo* experiments are needed to establish which other molecules are at play during neuronal maturation.

Membrane protein production and purification is one of the most important remaining frontiers for structural biology research. *h*TAOK2α was used as a model to setup a GFP-based multi-host expression screening towards the purification of eukaryotic integral membrane proteins. The *human*TAOK2α was used as a model to setup a GFP-based multi-host expression screening towards the purification of eukaryotic integral membrane proteins to determine its suitability for large-scale production. The application of a detergent screen since extraction, the first bottleneck of membrane protein purification, will be extremely usefull for production of a stable membrane protein. Our approach is fast and cost effective, applicable to multiple targets simultaneously and will give an estimate yield of expression/purification of different membrane protein constructs and define the suitability for large-scale production of a given target for a specific host. We believe this study is extremely valuable for other researchers working with membrane proteins.

Our study on the Z-DNA/Z-RNA aimed to clarify the role of z conformation in biology. Despite our lack of success with the RNA studies, the produced B-Z-DNA structure helped us to shed new light on the field. First, the structure of B-Z-DNA suggested that the Z conformation of nucleic acids might be more frequent in the genome then previously thought. Such junction requires low energy, as it preserves the integrity of the double helix. So, DNA sequences containing imperfect CpG repeats can easily adopt the left-handed conformation and tolerate the formation of a Z-Z junction.

Due to the fact that CpG stretches, and so Z forming sequences, are frequent in the genome and implicated with mammalian genomic instability, the presented structure provided the basis to understand some of the molecular features that are involved in the mutagenesis related with CpG islands. Z-DNA junctions increase the exposure of bases modifying agents with mutagenic effects and allow the binding of intercalating agents at the junction site. Such agents may stabilize the left-handed conformation and be used, in the future, as anticancer drugs.

Although the structure of this junction provided insights into the biological relevance of the Z form, a lot more remains to be known.

Appendix

A1. OPPF SDS-PAGE gels after purification of overexpressed protein

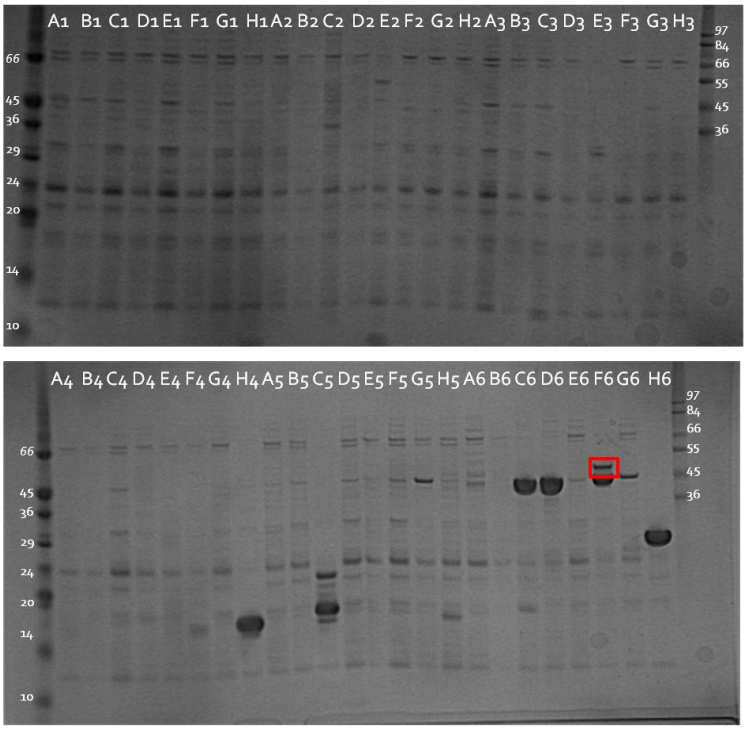

Figure A1.1. SDS-PAGE of overexpressed constructs in E. coli B834 induced with IPTG. F6: 321-370-MBP.

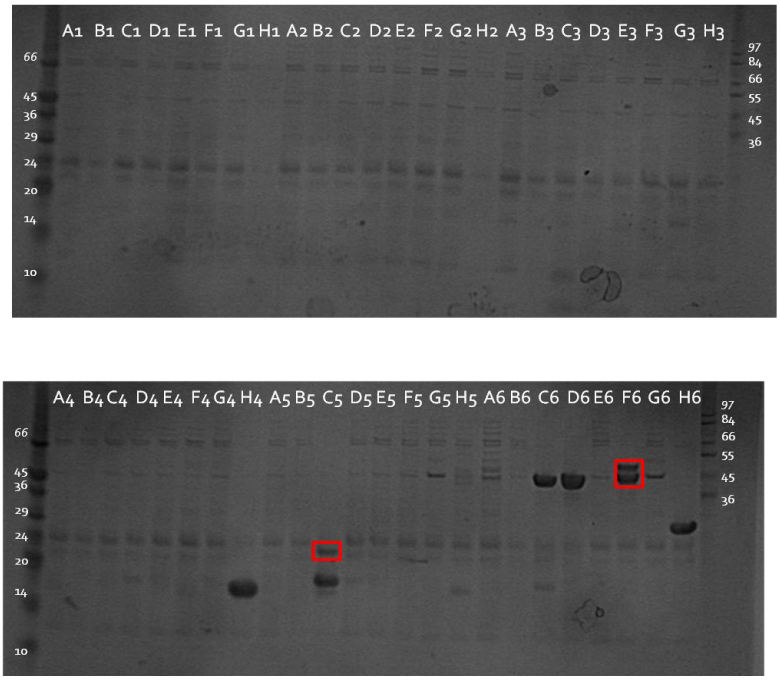

Figure A1.2. SDS-PAGE of overexpressed constructs in E. coli B834 self-induced. C5: 321-370-SUMO3C (18kDa); F6: 321-370-MBP.

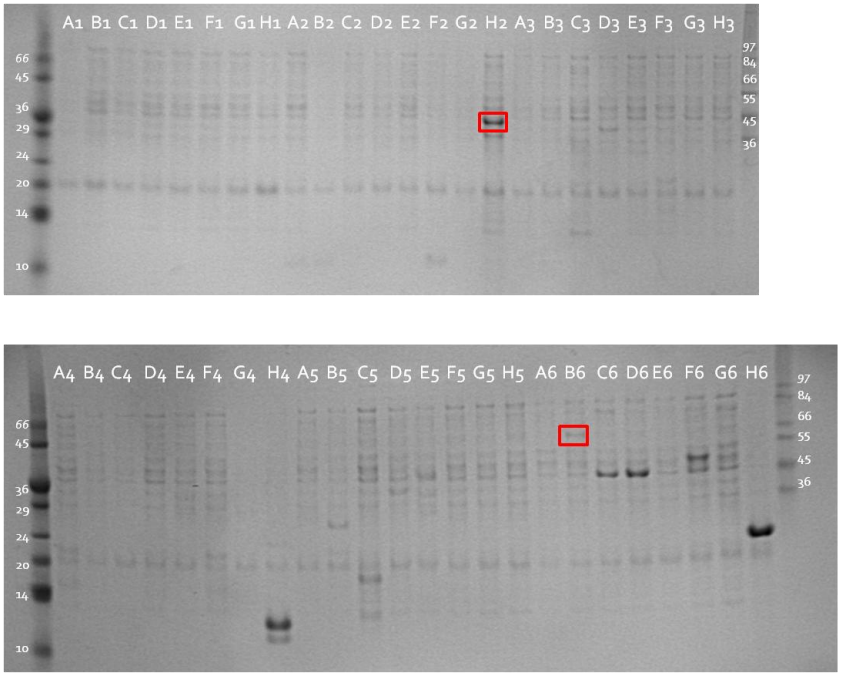

Figure A1.3. SDS-PAGE of overexpressed constructs in E. coli B834 self-induced, insoluble fraction. H2: 2-370 (43 kDa); B6: 595-750-MBP (61 kDa).

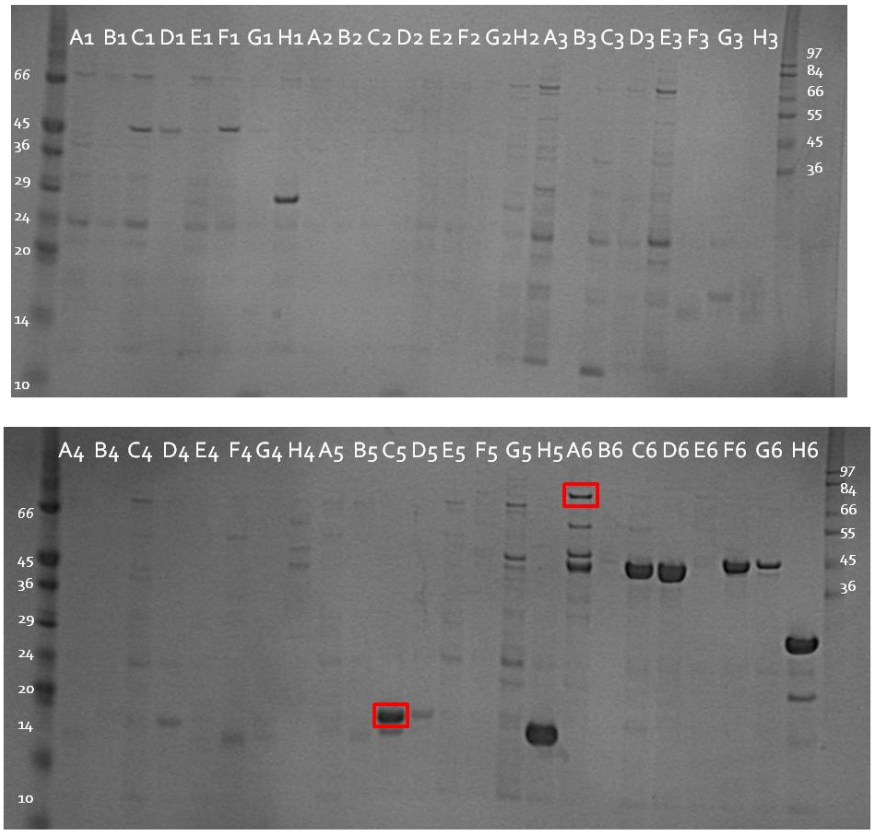

Figure A1.4. SDS-PAGE of overexpressed constructs in E. coli Rosetta induced with IPTG, soluble fraction. C5: 321-370-SUMO3C (18 kDa); A6: hTAO2 460-750-MBP (77 kDa).

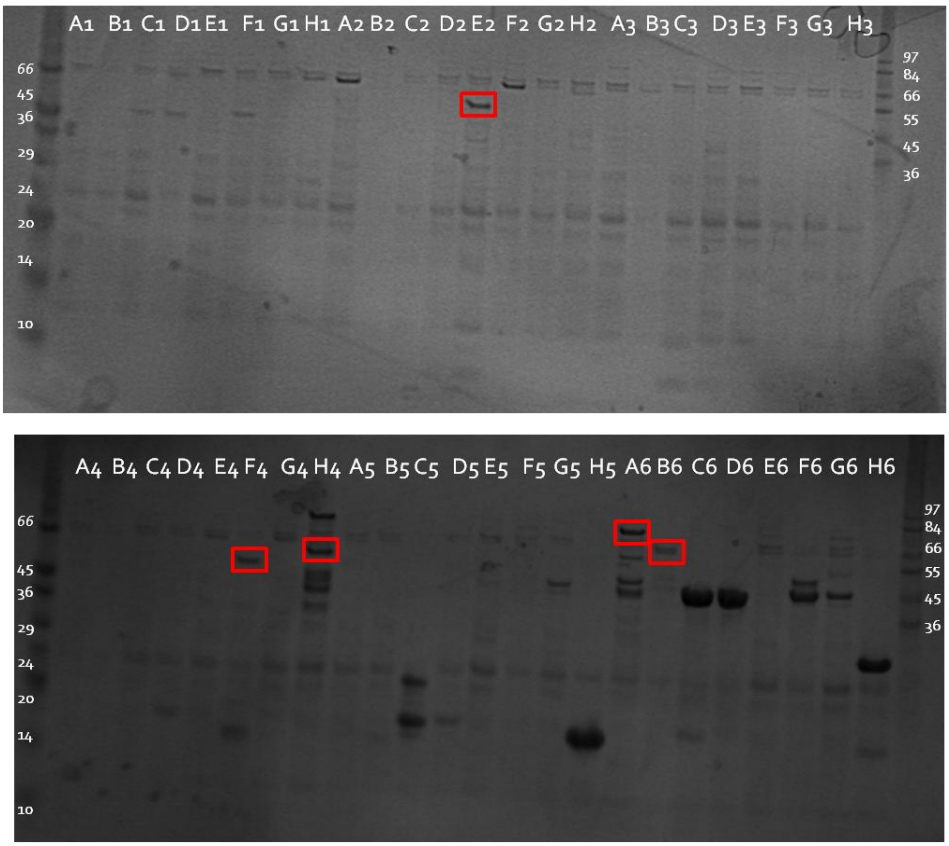

Figure A1.5. SDS-PAGE of overexpressed constructs in E. coli Rosetta self-induced, soluble fraction. E2: 321-750 47Kda; F4: 460-750-SUMO (48 kDa); H4: 2-370-SUMO (54 kDa); A6: 460-750-MBP (77 kDa); B6: 595-750-MBP (61 kDa).

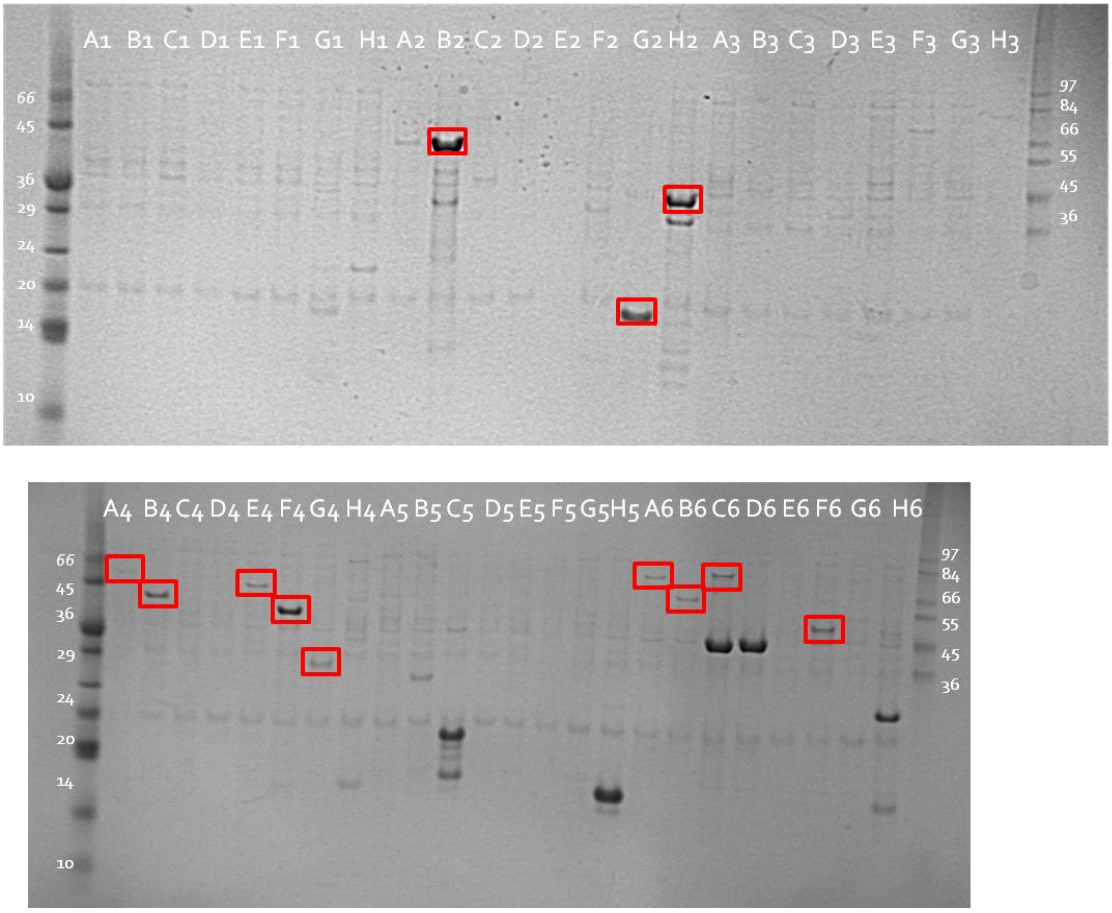

Figure A1.6. SDS-PAGE of overexpressed constructs in E. coli Rosetta self-induced, insoluble fraction. B2: 595-900 (37 kDa); G2: 590-750 (21 kDa); H2: 2-370 (43 kDa); A4: 460-900-SUMO (64 kDa); B4: 595-900-SUMO (48 kDa); E4: 370-750-SUMO (58 kDa); F4: 460-750-SUMO (48 kDa); G4: 595-750-SUMO (32 kDa); A6: 460-750-MBP (77 kDa); B6: 595-750-MBP (61 kDa); C6: 2-370-MBP (84 kDa); F6: 321-370-MBP (47 kDa).

A2. OPPF constructs tested in-house

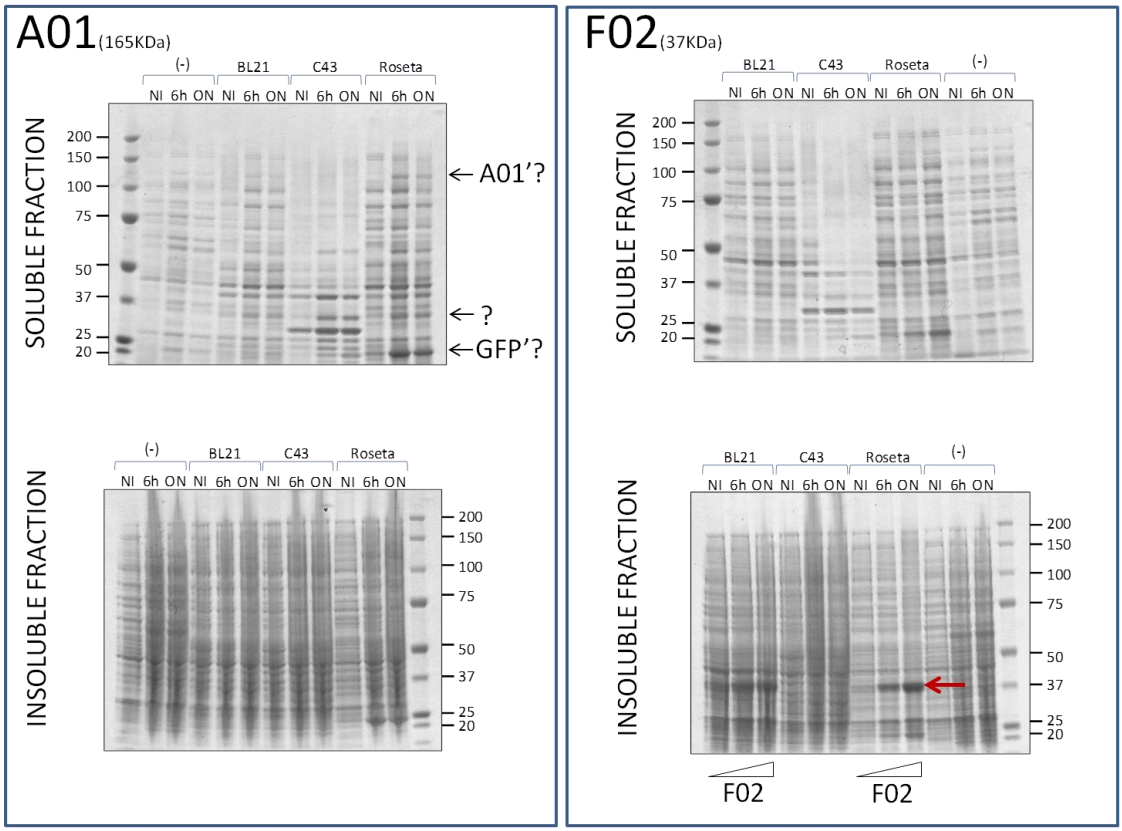

Figure A2.1. Expression tests realizes on OPPF A01 (hTAOK2-GFP) and OPPF F02 (aa 460-750-hTAOK2). SDS-PAGE showing the results for the expressions tests done in *E. coli* strains BL21, C43 and Rosetta with three different induction points – NI, non induced; 6h, 6 hours induction; ON, induction overnight, with IPTG.

A3. Solubilization screen strep-GFP-*h*TAOK2, Hi5 cells

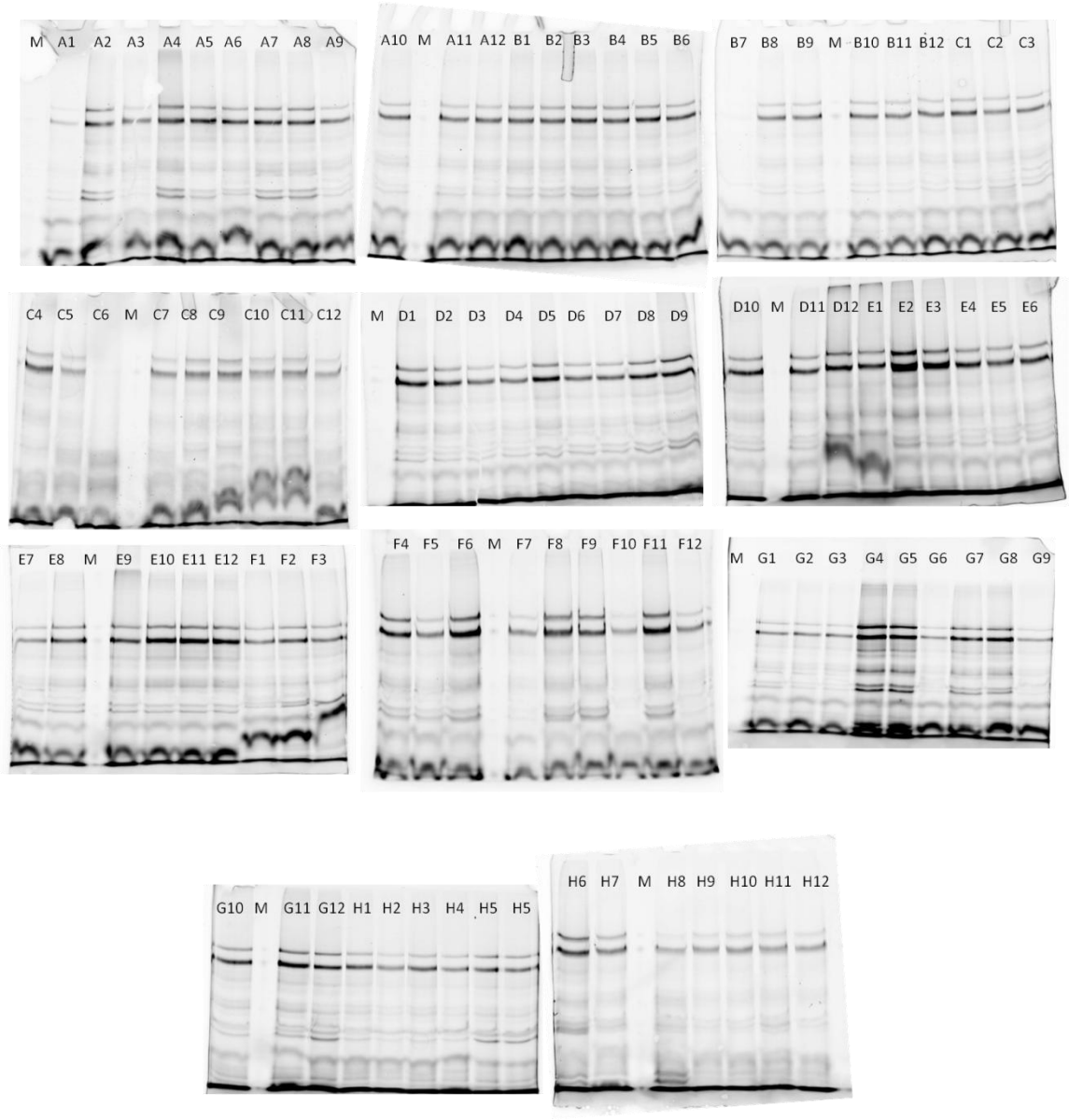

Figure A3.1. Pictures of in-gel fluorescence from SDS-PAGE gels after solubilization test with 96 detergent screen plate (A1 to H12) – soluble fraction. M, molecular weight marker.

A4. Solubilization screen His-GFP-*h*TAOK2, HEK293T cells

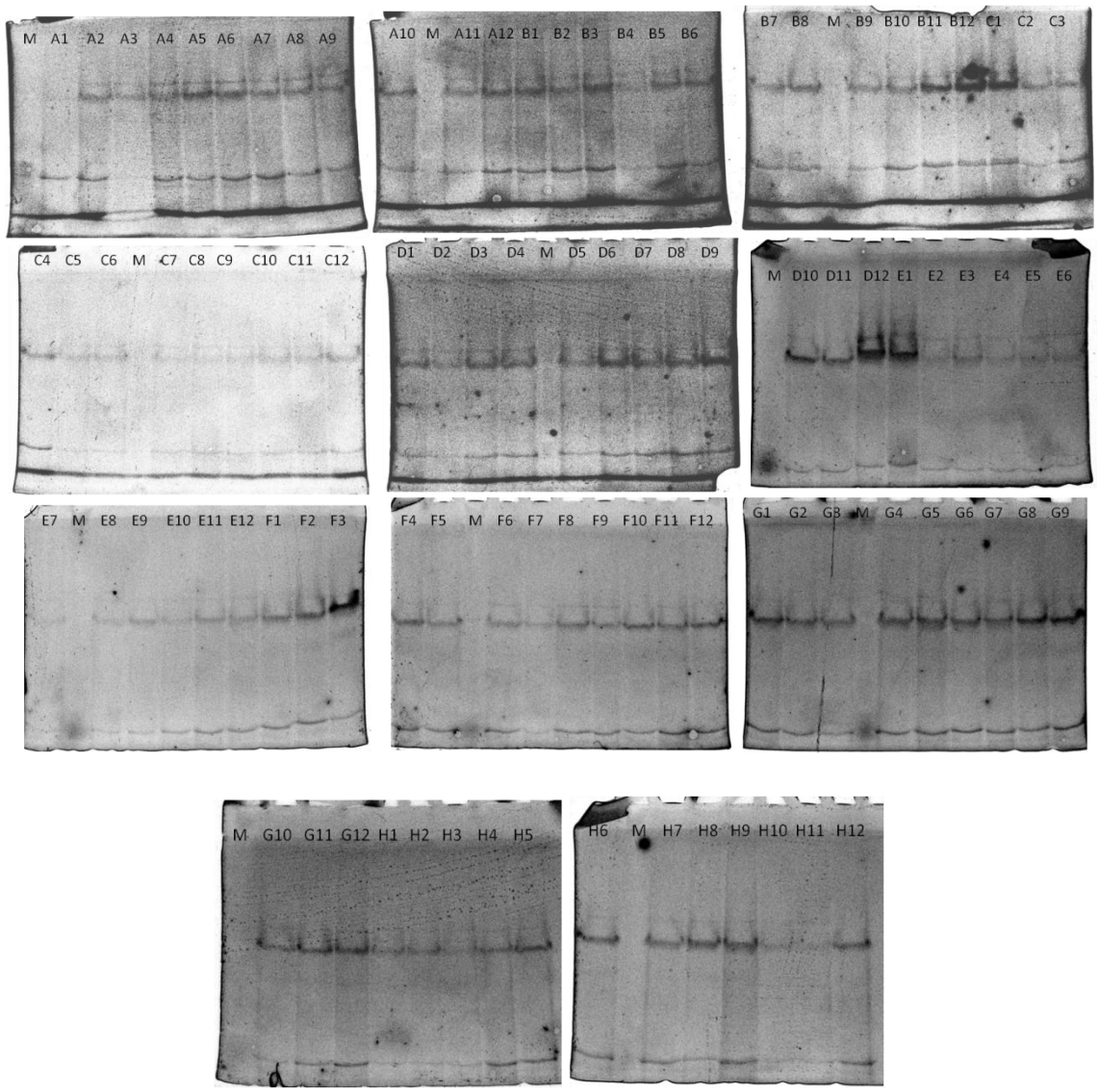

Figure A4.1. Pictures of in-gel fluorescence from SDS-PAGE gels after solubilization test with 96 detergent screen plate (A1 to H12) – soluble fraction. M, molecular weight marker.